GEOCHEMISTRY, GEOLOGY AND GEOCHRONOLOGY OF THE VICTORIO MINING DISTRICT, LUNA COUNTY, NEW MEXICO: LINKING SKARN AND PORPHYRY SYSTEMS TO CARBONATE-HOSTED LEAD-ZINC REPLACEMENT DEPOSITS

New Mexico Bureau of Geology and Mineral Resources
Open-file report 471

By

Kelly M. Donahue

Department of Earth and Environmental Sciences
New Mexico Institute of Mining and Technology
Socorro, New Mexico

THESIS
Submitted as partial fulfillment of the
Requirements for the Degree of
Masters of Science in Geochemistry

Fall 2002

Abstract: The Victorio mining district, southwestern New Mexico, hosts three types of mineral deposits that are spatially related (from the central zone to outer zone): porphyry molybdenum, W-Be-Mo skarn/vein, and carbonate-hosted Pb-Zn replacement deposits. Through geochronology, fluid inclusion microthermometry and gas analysis, and stable isotope analysis a genetic model was developed showing the genetic relationships between the three types of mineral deposits.

The fluid inclusions from the porphyry deposit have a homogenization temperature range of 208 – 315°C and salinities between 2.0 – 11.9 eq. wt% NaCl. The fluid inclusions from the skarn deposits have a range of homogenization temperatures from 180 – 350°C and have salinities 2 – 22.5 eq. wt% NaCl. The carbonate-hosted replacement deposits are slightly lower in temperature and salinity than the skarn and porphyry deposits with a range of homogenization temperatures of 105 – 289°C and salinities <2 – 5 eq., wt% NaCl.

The fluid inclusion and stable isotope analysis indicate an alteration continuum between the porphyry molybdenum, skarn and carbonate-hosted replacements deposits. The sulfur and oxygen isotope data from sulfide and silicate samples and fluid inclusion gas analyses point to a probable magmatic source for the skarn and porphyry mineralization. The sulfide isotope data from the carbonate-hosted replacement deposits also suggest a magmatic component. The carbon and oxygen values from carbonate and silicate samples for the carbonate-hosted replacement deposits indicate a moderate to high degree of interaction between the mineralizing fluid and the host rock.

The mechanisms responsible for the shift in mineralization style between high-temperature porphyry and skarn deposits and low-temperature carbonate-hosted

replacement deposits are most likely boiling and mixing of meteoric and magmatic waters. There is evidence for boiling and fluid mixing in all three mineral deposits, which caused a decrease in temperature and salinity, an increase in pH, and an increase in oxidation state of the mineralizing fluids.

The geochronological results for the Victorio Granite and the skarn alteration minerals indicate that all three mineral deposits formed from one magmatic source at approximately 34.9 Ma. However, there is no direct evidence the mineralization of the three deposits was one continuous event. It is more likely that mineralization took place over an extended period of time with episodic events of brecciation, boiling, fluid mixing, and mineral precipitation as a result of the intrusion of the Victorio Granite.

Acknowledgements:

I wish to thank my advisors and thesis committee members, Dr. Virginia McLemore, Dr. Andrew Campbell, and Dr. William McIntosh for their support, insight, and encouragement. I also would like to thank Dr. Nigel Blamey for his invaluable help with my fluid inclusion gas data and Dr. Matt Heizler for his help with my argon geochronology data. Chris McKee, Lisa Peters, and Rich Esser provided technical support in the XRF and argon geochronology labs. I would like to thank my fellow graduate students: Reyna Abeyta, Gabriel Gomez, Amber McIntosh, Andrew Mioduchowski, Chadwick Spencer, and Amanda Rowe for their insight, help, support, and most importantly listening to me complain. Lastly, I would like to thank my family, friends and former roommates who lived with and supported me through the many years of college and graduate school. A special thanks to my best friend Patti Dorn for sending me the graduate school application for NMIMT and encouraging me to apply.

This project was funded through the New Mexico Bureau of Geology and Mineral Resources, Dr. Peter A. Scholle Director and State Geologist, under the direction of Dr. Virginia McLemore. The use of NMBGMR facilities, resources and the financial support was invaluable. The XRF Lab at NMBMGR a division of NMIMT was partially funded by NSF grant (EAR93-16467). The New Mexico Geochronology Research Lab (NMGRL) provided the argon geochronology analyses for this study. The NMIMT E&ES Stable Isotope Mass Spectromemtry Laboratory provided the isotope work for the carbonate and silicate samples of this study.

Table of contents **Page**

Table of Contents (cont.) **Page**

List of Figures **Page**

List of Figures cont. **Page**

List of Tables **Page**

INTRODUCTION

Location

The Victorio mining district is located within the Basin and Range physiographical province of the southwestern United States, west of Deming in Luna County, New Mexico (Fig. 1). The district has been previously called the Gage and Mine Hill mining districts (McLemore et al., 2000a).

Purpose of study

Numerous studies (Meinert, 1987; Kwak, 1994; Friehauf, 1998) have examined the genetic relationships between various types of mineral deposits to be used in exploration. Skarn deposits and carbonate-hosted replacement deposits have several common aspects, such as, carbonate-host rock lithology and common ore minerals. It is plausible that carbonate-hosted replacements and skarn mineralizing systems are related; and these two systems may be related to porphyry systems (Guilbert and Park, 1986). McLemore and Lueth (1996) identified lead-zinc mineral deposits hosted in carbonate rocks throughout New Mexico (Fig. 2), and further state that in the Silver City and Magdalena areas there maybe economic potential to develop skarns and carbonate-hosted replacement deposits. If a genetic link between carbonate-hosted replacement, skarn, and porphyry deposits can be established, the presence of carbonate-hosted replacement deposits would be an excellent exploration tool for porphyry systems.

Kwak (1994) proposed a model that skarns and carbonate-hosted replacement deposits are genetically related through an alteration continuum. Kwak (1994) proposed that the change from high-temperature ore skarns to lower-temperature carbonate-hosted replacement deposits is the result of the addition of cooler meteoric water; which results

in a decrease in temperature and salinity (Fig. 3). There are several classification schemes for skarn deposits based on depth, process of mineralization, temporal relation to magma emplacement, host-rock type, spatial relation to intrusions, structure, oxidation state, and economic metals (Guilbert and Park, 1986; Kwak, 1994). The skarns in the Victorio mining district are classified as proximal ore skarns (Kwak, 1994). Proximal ore skarns are generally formed within 300 ft of an intrusion due to recrystalization of the host rock by hot, metal-bearing fluids. The presence of serpentine, magnesian pyroxene, phlogopite, talc, and the absence of wollastonite and apatite would classify the Victorio skarns as magnesian (rather than calcic) skarns with both prograde and retrograde mineral assemblages, and high fluorine fugacities (Kwak, 1994). Magnesian skarns tend to be less common and less economic. One possible reason is that $MgCl_2$ is less water soluble under most conditions as compared to $CaCl_2$. Magnesian silicate crystallization restricts the permeability and reduces the ore-forming potential (Kwak, 1994).

Contact-metasomatic skarns reflect the loss of heat from the roof zone of a granitic intrusion and usually predate ore skarns. Contact-metasomatic skarn reactions involve little movement of components since fluid movement is by intergranular static fluid (diffusion) rather than active fluid flow (infiltration) associated with hydrothermal fluids (Kwak, 1994). The products of metasomatic and ore skarns processes are similar making the distinctions between ore formation and alteration products difficult (Kwak, 1994).

Carbonate-hosted replacement deposits are classified as replacements within a carbonate host rock with little to no calc-silicate minerals (Table 1). Carbonate-hosted replacement deposits can be difficult to genetically link to the intrusions responsible for

their formation due to presence of one or more intrusive bodies, structure, and/or distance from the intrusion (Glig, 1996). Spatial association with an intrusion is not conclusive evidence of a genetic relationship (Glig, 1996). However, through mineralogical studies; geochronology, stable isotope, fluid inclusion microthermometry and gas analyses; it may be possible to develop a genetic model for the carbonate-hosted replacement deposits with additional geological information.

The objectives of this study were to determine the genetic relationships between the three different deposit types within the Victorio mining district (Fig. 4), to determine the origins of the mineralizing fluids, and to determine the geologic sequence of events. The three deposit types are separated by several faults, and Quaternary cover so direct geologic relationships between the different deposits cannot be identified through field relationship.

Previous work

Lindgren et al. (1910), first visited the Victorio mining district in 1905 and predicted the development of the district would be short lived. Kottlowski (1960, 1963) mapped the geology of mining district. Thorman and Drewes (1980) and McLemore (unpublished field notes) later remapped the area. Lindgren et al. (1910), Holser (1953), Dale and McKinney (1959), Griswold (1961), Griswold et al. (1989) and McLemore et al. (2000a) described the mineral deposits at the Victorio district. McLemore et al. (2000a) provided geochemical and geochronological studies on the mining district. Lone Mountain Mining Co. and Leonard Resources Co. reports (Heidrick, 1983) evaluated the economic potential of the porphyry and skarn deposits of the Middle Hills. Heidrick (1983) estimated the resources for the skarn deposits to be 57,703,000 tons at a

low grade of 0.215 MoS_2 and 0.142 WO_3, 18,894,000 tons at a middle grade of 0.177 MoS_2 and 0.295 WO_3, 4,065,000 tons at a high grade of 0.214 MoS_2 and 0.356 WO_3, and open-pit resources to be 11,900,000 tons at a grade of 0.076 WO_3. A report for Santa Fe Pacific Mining Co. by Wessel and Maciolek (1989) described the economic potential of the carbonate-hosted replacement deposits of the Mine Hill area. Campbell and Robinson-Cook (1987) studied fluid inclusions in wolframite and quartz from the skarn deposits using an infrared microthermometry technique.

Mining history

A time line showing the significant historical events that took place in the Victorio mining district is illustrated in Figure 5. The Victorio mining district was discovered in the late 1800s by William Kent, William Hyters, and J. L. Doughterty (Griswold, 1961). Production started about 1880 in the carbonate-hosted lead-zinc replacement deposits located at Mine Hill (Fig. 4). The beryllium and tungsten vein and skarn deposits were first discovered in the early 1900s (Griswold, 1961).

The carbonate-hosted replacement deposits of the Mine Hill area are where the largest amounts of ore were extracted in the district (Griswold, 1961). The main metals extracted from these deposits were lead, silver, gold, zinc, and copper, in order of relative importance. Ore from the Rambler mine averaged 12.5% Pb, 3.9% Zn, and gold assays as high as 5.5 ppm (Griswold et al., 1989; McLemore et al., 2000a). Total production was estimated to be 70,000-130,000 short tons of ore mined between 1880 and 1957 for a total worth around $2.3 million (McLemore et al., 2000a). There are numerous mine shafts and prospect pits located on Mine Hill (Fig. 6), many were reclaimed by the Abandoned Mines Land Bureau (AMLB) in 1999. The Chance, Jessie, Rambler, Excess,

and Parole mines exploited the more productive veins of the district (Griswold, 1961). Most of the mines within the Victorio district were developed by shafts with the exception of the Jessie mine, which had two haulage adits (Griswold, 1961). The basic mining methods of stoping included shrinkage and some underhand mining. The width of the stopes ranged from 1 to 20 feet with an average of 4 feet (Griswold, 1961). The replacement lenses outcropped extensively and were mined by trenching. The walls of the stopes were usually strong and timbers were used for support in some rare cases (Griswold, 1961).

Tungsten was produced from 1942 to 1944 from the Tungsten Hill mines of the Middle Hills area (Fig. 5). The skarn deposits were mined through the Irish Rose and Tungsten Hill shafts (Fig. 6) (Griswold, 1961). The ore from Tungsten Hill contained mostly scheelite with minor amounts of galena, smithsonite, and helvite. In 1942, approximately 20,000 short tons of ore at a grade of 1% WO_3 worth nearly $70,000 was produced from the Irish Rose vein claim (Dale and McKinney, 1959).

There are the remains of an old mill foundation near the Rambler mine site. The milling equipment has long since been removed, but Griswold (1961) speculated the method of ore separation was by gravity. There is a small amount of tailings located near the Rambler site suggesting the mill was in operation for only a short time (Griswold, 1961). The majority of the ore was most likely hand sorted and shipped directly to the smelter (Griswold, 1961).

The porphyry molybdenum deposit was discovered during drilling of a geophysical anomaly. Regional gravity surveys conducted by the Santa Fe Mining Company indicated two negative areas. One corresponded to the Victorio Granite (as

discovered through the drilling program) and the other was believed to be a deeper source for the granite (Maciolek, 1989). Gravity (Wynn, 1981) and aeromagnetic (Klein, 1987) maps of the Silver City 1° x 2° quadrangle show no evidence of other anomalies within the vicinity of the Victorio district.

Minor exploration and drilling in the Victorio district began in the 1950s looking for porphyry copper deposits (McLemore et al., 2000a). In 1969–1970 Humble Oil Co. drilled four exploration holes encountering only skarn mineralization. In 1971, Keradamex drilled two holes (K1 and K2, Fig. 7) without encountering any significantly mineralized zones (McLemore et al, 2000a). Asarco (geology), Bethlehem Copper Corp., Donegan and Donegan (IP, resistivity, and deepening K2), Newmont (IP and gravity), Leonard Resources, Southern Union Co. (aeromagnetic, IP and resistivity), and Rosario Exploration (geology and deepening of K2) also drilled exploration holes within the district (Heidrick, 1983; McLemore et al, 2000a). Gulf Minerals Resource Company drilled 71 drill holes between 1977 and 1983 to delineate the porphyry molybdenum deposit (Fig. 7; holes 1-75, A1-3) .

METHODOLOGY

Argon geochronology, fluid inclusion microthermometry and gas analyses, stable isotope analyses, and petrographic studies were used to determine the relationship between the three deposit types in the Victorio mining district. Samples consist of drill core samples from the Gulf Mineral Resource Company core donated to the NMBGMR and samples collected from both the surface and underground mine workings (Fig. 8). Sample type, location, and analyses performed are in Table 2. Petrographic descriptions of thin sections and fluid inclusion thick sections were used to determine the mineral paragenesis.

Drill core from the Victorio district was donated to the NMBGMR by Gulf Minerals Resource Company. Due to a lack of storage space at the NMBGMR and the amount of time allowed for collection, many drill holes were skeletonized by Dr. Virginia T. McLemore. Therefore, not all drill holes are complete and some drill holes were not sampled at all. Few drill holes were sampled from the carbonate-hosted replacement deposits. Dr. McLemore collected samples from within the mines before reclamation and from the mine waste piles on the Middle and Mine Hill areas.

The mineral paragenetic sequences are a combination of work by previous authors with new observations. Griswold (1961) had access to at least parts of several mines on Mine Hill. Wessel and Maciolek (1989) wrote an unpublished company report evaluation of the Mine Hill area for Santa Fe Pacific Mining Company. Heidrick (1983) analyzed the drill core for Gulf Mineral Resource Company and determined the mineral paragenesis and the stages of mineralization. Heidrick's work is referred to for large-scale relationships that could not be determined from the amount of drill core that was

available for this study. Small-scale mineral paragenetic sequences are identifiable with the selection of core for this study.

Argon geochronology

K-feldspar, muscovite, and biotite minerals from the Victorio Granite were analyzed using the $^{40}Ar/^{39}Ar$ dating technique in order to determine the age of mineralization, alteration, and emplacement of the igneous rocks (Table 3). Two samples of the Victorio Granite were dated for this study by analyzing K-feldspar, biotite, and muscovite. Four samples of the skarn alteration were dated by separating K-feldspar, biotite, and muscovite minerals associated with sulfide minerals (Table 3).

A summary of the analytical results is in Table 4. The core samples were crushed and sieved to the 40-mesh fraction size. The biotite and muscovite were separated using a magnetic separator. Biotite, muscovite, and K-feldspar mineral grains were hand picked and examined under a binocular microscope to eliminate samples with possible contamination. Muscovite and biotite grains from the Victorio Granite used for argon dating are original magmatic minerals, as opposed to alteration products. The muscovite and biotite grains separated for age dating were between 1 to 3 mm in size (Fig. 9). The alteration muscovite minerals visible in thin section were less than 50 microns in size (Fig. 9). The considerable difference in size between the magmatic and alteration micas makes it unlikely that alteration products were dated.

The mineral grains were ultrasonically cleaned in distilled water, weighed, and wrapped in copper foil packets. The sample packets were encapsulated in silica vacuum tubes and in-vacuo irradiated for 24 hours at the University of Michigan nuclear reactor. The Fish Canyon Tuff sanidine flux monitor, with an assumed age of 27.84 Ma, was

irradiated along with the mineral separates. The samples were incrementally heated in a double-vacuum molybdenum resistance furnace. The gas extracted was analyzed by a MAP 215-50 mass spectrometer operating in the electron multiplier mode. The measured isotopic ratios were corrected for interference reactions, system blanks and mass discrimination (Table 4).

A plateau age is defined as the three or more contiguous gas fractions equaling at least 50% of the total ^{39}Ar released and overlapping in age within a $\pm 2\sigma$ analyzed uncertainty. All age data are calculated using the decay constants and isotopic abundances listed in Steiger and Jager (1977). The closure temperatures for biotite and muscovite are assumed to be 300°C and 350°C (Harrison et al, 1985; McDougall and Harrison, 1998). Due to the highly variable and large range of closure temperatures for K-feldspar, it was inappropriate to assign a closure temperature without knowing the diffusion characteristics of K-feldspar samples.

Fluid inclusions

Two procedures were used to analyze the fluid inclusions in the Victorio samples. The first, microthermometry, is a nondestructive method of heating and freezing the sample. The second method, quadrupole mass spectrometry, is a destructive method of crushing fluid inclusion samples. Fluid inclusion samples were chosen based upon the location within the district and quality of the sample. Whenever possible, multimineralic samples were chosen to obtain coexisting temperature measurements. Once suitable samples were chosen, the samples were then cut into thick-section billets and sent to Quality Thin Sections in Tucson, AZ to be made into doubly polished fluid inclusion sections.

Fluid inclusion microthermometry

Fluid inclusion size, shape, and distribution were examined using standard microscopic techniques. In order to determine the inclusion paragenesis, the methods outlined by Roedder (1981) to classify inclusions as, primary, secondary, or psuedosecondary were used. Another concern was necking down of fluid inclusions. In order to prevent measuring inclusions that had necked down, isolated inclusions were selected rather than clusters of inclusions. Microthermometry measurements were made on a Linkham TH-600 heating/freeze stage. An automatic temperature controller was used to manipulate the rate of heating and freezing during analysis. The system was calibrated using standard fluid inclusion H_2O and CO_2-H_2O slides. The H_2O water standard was measured before each session, and the CO_2 standard was measured before each session with liquid-CO_2 filled inclusions. The precision of the temperature measurements is ± 0.2°C for measurements of –56.6°C to 0°C and ± 1°C for temperatures between 0°C and 300°C. During measurements the temperature rate was typically lowered to 0.1 °C per minute for freezing measurements and 1°C per minute for heating measurements to compensate for errors caused by thermal gradients.

Fluid inclusion gas analysis

Eight samples were analyzed in a quadrupole gas mass spectrometer (QMS) to measure the gas content within the fluid inclusion samples (Table 2). Samples were selected based on the type of deposit each sample represented and the number of primary inclusions within each sample. The samples were crushed to a 40-mesh size using a mortar and pestle. The grains were then cleaned in a solution of 10% sodium hydroxide and heated on a hot plate for an hour to remove any organic contaminates on the surface

of the grain. The samples were then rinsed in deionized water and dried in an oven at 100°C for over an hour. Three samples were placed within the quadrupole mass spectrometer extraction line and heated over night with the vacuum pump on to draw out any air.

To analyze the vapor within the fluid inclusions, a modified quadrupole mass spectrometer was used for rapid real-time analysis of the gas composition. A Balzer model QMG 125 QMS with a secondary electron multiplier (SEM) detector was used to analyze the fluid inclusion gases. The ion source was set to 100 EV and the SEM operated at 1900 volts. Each sample was crushed at least ten times or until there was no sample left. The volatiles in atomic mass units (AMU) were measured for He, CH_4, H_2O, N_2, O_2, H_2S, Ar, CO_2, SO_2 and hydrocarbons. The results from each crush were displayed on a real-time computer graphical display. The peak intensity was integrated and the background values were subtracted from the peak area using an equal number of counts before and after the peak.

Stable isotopes

Carbon and oxygen isotopes

Thirty samples from drill core and surface outcrop of calcite and limestone were analyzed for carbon and oxygen stable isotopes (Table 2). The drill core samples consisted of vein calcite and limestone from both the carbonate-hosted replacement and skarns deposits. Drill hole GVM 21 was sampled at somewhat regular intervals to determine how the stable isotopes change with alteration and depth. Samples were crushed to a –40/+80 mesh and 10 milligrams of sample was added to carbonate sample vessels with phosphoric acid. The samples were pumped for four hours to remove excess

water and atmospheric gases. The samples were allowed to react over night in a water bath set at 47°C. The CO_2 gas resulting from the reaction of the carbonate rocks was extracted and cleaned through a series of cold traps. Once the gases were analyzed, acid fractionation factors were calculated using a set of standards to compensate for the loss of an oxygen atom during the process of the carbonate reaction

$$(Mg, Ca)CO_3 + \text{acid} \rightarrow CO_2 + H_2O + Ca^{2+}.$$

Oxygen isotopes

The sample preparation for oxygen stable isotope analysis involved grinding the sample to a –40/+80 mesh size. The quartz grains were hand picked, 12 milligrams was weighed out, and funneled into metal sample vessels. The sample vessels were loaded into the silicate extraction line and pumped for several hours to remove the atmospheric gases. Once the extraction line had been pumped down, chlorine trifluoride gas reagent was added to the extraction line, heated to over 450°C and the samples were reacted for eight hours to release the oxygen gas. The oxygen gas was run through a series of cold traps to remove reagent and other condensable gases. The oxygen gas reacted with a hot carbon rod to produce CO_2 gas. Silica standards were used to calibrate the mass spectrometer and to test for sample preparation errors.

Sulfur isotopes

Samples of sulfide minerals taken from drill core were crushed to a fine powder and sent to the University of Indiana for stable isotope analysis. Sulfur isotope results are significant because sulfides are ore minerals while quartz and carbonate samples are gangue minerals. Sulfur isotopes can serve as an indicator of geochemical environment and the type of fluid present during mineralization.

GEOLOGIC SETTING

Southwestern New Mexico was affected by several major geologic events, since Late Jurassic-Early Cretaceous time. The Victorio district was part of a regional north-northwest-trending uplift know as the Laramide Burro-Florida uplift that formed as a result of compression during the subduction of the Farallon plate (Mack and Clemons, 1988) (Fig. 10). The zone of compression extends from El Paso, Texas to the west toward Las Vegas, NV, and is called the Cordilleran orogenic belt. High-angle faults and thrust faults along pre-existing structures were suitably orientated to accommodate displacement during subduction compressive shortening (Hodgson, 2000). The structure and stratigraphy of the Laramide geology suggests a two-stage event with the first being a late-Cretaceous block uplift and the second a Paleocene-Eocene left-lateral convergent wrenching (Hodgson, 2000). The Lower Cretaceous and older sedimentary rocks in the Victorio district underwent compression during the Laramide orogeny. This caused deformation in the form of folding, thrusting and local detachment along the Precambrian basement (Griswold, 1961).

New Mexico experienced a surge of igneous activity during the Tertiary due to a period of extension. Starting at 40-35 Ma and persisting for at least 18 Ma, extensive intermediate-silicic calc-alkaline volcanism and associated plutonism occurred throughout much of New Mexico and Arizona (McLemore et al. 2000b; McIntosh and Bryan, 2000). Several volcanic fields (Fig. 11) extend from Colorado south into Mexico (McIntosh and Bryan, 2000). The Victorio mining district is located between the Mogollon-Datil and Boot Heel volcanic fields and is close to many calderas (Fig. 11, 12).

There are several igneous intrusive and extrusive rocks that were erupted during the mid- to late-Tertiary within the Victorio mining district (Fig. 13, 14a, b).

Stratigraphy

The rocks in the Victorio Mountains consist of Proterozoic rocks, Ordovician to Cretaceous sedimentary rocks, and Tertiary igneous rocks, overlain by unconsolidated Quaternary alluvium, sand and gravels (Fig. 13).

The Proterozoic rocks consist of quartzo-feldspathic gneiss and amphibolite that are only found in the drill core (McLemore et al., 2000a). The quartzo-feldspathic gneiss consists of metamorphosed siltstone, sandstone, and arkose layers. The amphibolite ranges between a fine-grained foliated biotite schist composed of plagioclase, hornblende, and biotite to a coarse-grained diabase.

The Bliss Formation (Cambrian-Ordovician) is approximately 90 – 150 feet thick (Fig. 14a), is not exposed at the surface in the district, and lies uncomfortably on the Proterozoic rocks (Thorman and Drewes, 1980). The basal conglomerate of the Bliss Formation consists of subrounded to subangular clasts of the Proterozoic rocks and quartz pebbles in a fine-grained matrix. The next 5 to 10 feet above the conglomerate are typically a clean orthoquartzite. The upper part of the Bliss Formation consists of two lithologies, a silty quartzite and a limy to dolomitic siltstone. The majority of the skarn deposits are found in the uppermost units of the Bliss Formation and El Paso Group.

The oldest rocks that are exposed at the surface are the limestones and dolomites of the El Paso Group (Ordovician). The El Paso Group is approximately 450 – 500 feet thick (Fig. 14a) and is comprised of three members (oldest to youngest), the Hitt Canyon, McKelligan, and Padre Formations. The lowest member, Hitt Canyon, is the most

readily recognized and mapped lithology of the El Paso Group. This unit consists of brown, wavy, thin-bedded dolostones or dolomitic limestones containing sandy, shaley, and silty beds. Thin beds of carbonate sequences are interbedded within massive gray limestone and dolomite beds of the Hitt Canyon (Griswold, 1961). Locally, the El Paso Group contains gastropods, cephalopods, and algal masses (Kottlowski, 1960).

The Montoya Group (Ordovician) lies conformably over the El Paso Group and consists of fine- to medium-grained limestones and dolostones that are approximately 270 - 340 feet thick (Fig. 14a) (Griswold, 1961). The four formations of the Montoya Group are the Cable Canyon Sandstone, Upman Dolomite, Aleman Formation, and Cutter Dolomite. The Cable Canyon Sandstone is a fine-grained quartz sandstone to a sandy limestone. The Upman Dolomite contains medium bedded, dark gray dolostones and characteristically contains crinoids. The Aleman Formation is a medium bedded, dark gray dolostone with interbedded chert nodules. The Cutter Dolomite is a thinly bedded, gray dolostone to a dolomitic limestone with shaley interbeds (Kottlowski, 1960; Thorman and Drewes, 1980).

The Fusselman Dolomite (Silurian) conformably overlies the Montoya Group and is approximately 900 feet thick (Fig. 14a) in the Victorio Mountains (Kottlowski, 1960; Griswold, 1961). The Fusselman Dolomite consists of dolostones that contain chert, minor amounts of coral, and locally abundant brachiopods. The Fusselman Dolomite is made up of four informal members, lower gray, lower black, upper tan, and upper black. The lower gray unit consists of a gray, sandy dolostone. The lower black unit is a dark gray to black, dolostone containing abundant coral and minor amounts of chert. The

upper tan and upper black members are massive dolostones. The upper half of the Fusselman Dolomite has abundant chert beds.

There is an angular unconformity that separates the marine Paleozoic rocks from the Lower Cretaceous rocks (McLemore et al, 2000a). The Bisbee Group (Cretaceous) consists of interbedded conglomerate, sandstone, calcarenite, and mudstone that range from 500 to 600 feet thick (Fig. 14b) (Griswold, 1961). The Bisbee Group was correlated to the Hell-to-Finish and U-Bar formations in Arizona based on rare fossils, lithologies and stratigraphic sections by Lucas et al. (2000). Overlying the Bisbee Group are a sequence of dacite flows and breccias approximately 720 to 915 feet thick (Fig. 14b). The dacite flows and breccias are overlain by sedimentary rocks that Lawton and Clemons (1992) correlated to the Lobo Formation.

The main ridge of the Victorio Mountains consists of Tertiary volcanic rocks called the Victorio Peak dacite (Thorman and Drewes, 1980), which lies uncomformably upon the Lobo Formation. The dacite consists of flow breccias, tuffs, and dacite lavas approximately 900 to 1500 feet thick (Fig. 14b). Thorman and Drewes (1980) assigned a 41.7 ± 2 Ma age (zircon-fission track) to a dacite breccia of the Victorio Peak dacite. This is a minimum age for this unit.

The Victorio Granite is medium- to coarse-grained, porphyritic granite consisting of feldspar, biotite, ± muscovite, and quartz, with trace amounts of molybdenite, pyrite, scheelite, apatite, garnet, fluorite, and zircon (Appendix D-1) (McLemore et al, 2000a). There appears to be two generations of muscovite mineralization in the granite. One generation is primary (Fig. 9a, b) while the other generation is probably hydrothermal alteration of feldspars minerals (Fig. 9e, f). The primary muscovite is course grained and

well crystallized, while the alteration muscovite minerals are more fine-grained and less crystallized. The primary biotites in the granite were partially replaced by chlorite, sericite, and/or muscovite (Fig. 9c, d). The sericite/muscovite alteration of the granite is only visible in thin section and is not extensive as some samples show little or no alteration.

The granite intruded into Proterozoic metamorphic rocks and the Bliss Formation. The Victorio Granite contains Mg-rich garnets with inclusions of Hf-rich zircons, and Th-, U- and Y-rich allanite and fluorite (McLemore et. al, 2000a). There are several rhyolite dikes that branch off the main granitic body. Sills and dikes of andesite, basalt, dacite, and rhyolite intrude the carbonate rocks. The altered Irish Rose rhyolite porphyry dike (Tr) (Fig. 13, 14) is nearly flat-lying and intruded the limestones and dolostones near the Irish Rose mine (McLemore et al, 2000a).

The Victorio Granite is an A-type granite (Fig. 15), peraluminous to metaluminous, and plots in syn-collision to within-plate granite fields (Fig. 16, 17) (Pearce et al., 1984). A-type magmas are generated by fractionation of a mantle-derived basalt, interaction between mantle-derived magmas and continental crust and, the re-melting of a terrain from which a previous melt has been extracted (Eby, 1990). The fact that the Victorio Granite samples do not plot within a clearly defined tectonic-chemical field indicates the tectonic setting of the Victorio Granite is more complicated then a simple subduction or rifting model.

The Tungsten Hill breccia pipe (Tib) is exposed in the Middle Hills between the Main Ridge and Victorio Mountains faults and cuts through Paleozoic and Cretaceous

rocks in the district. It consists of angular fragments of granite, andesite, rhyolite, marble, limestone, conglomerate, and sandstone. Within the weathered surface exposure of the breccia, rounded granite clasts are found that indicate the breccia pipe is younger than the Victorio Granite. Locally the breccia pipe is cut by quartz veins with pyrite and possibly molybdenite veins (McLemore et al, 2000a). There are no direct cross-cutting relationships exposed or described in drill core between the breccia pipe and skarn zones (Heidrick, 1983). However, quartz, albite, muscovite, and fluorite with disseminated scheelite/powellite, helvite, molybdenite, and base-metal sulfides are both clasts and matrix supported minerals found within the breccia pipe (Heidrick, 1983). A rhyolite dike intruded the breccia pipe and has a zircon fission track age of 24.8 Ma (Thorman and Drewes, 1980). The dike could be older and related to the granite since fission track ages are minimum ages and rarely coincide with intrusion ages.

A fine-grained, light gray, aplite dike parallels the North fault of Mine Hill and is exposed only in the Excess and Rambler mines. The dike is highly altered with albite and orthoclase in a quartz-rich groundmass and a fine-grained sugary texture. The dike probably intruded during or just prior to mineralization of Mine Hill (Griswold, 1961). Mineralized veins within the adjacent Fusselman Dolomite end abruptly against the dike and do not extend into the dike indicating emplacement prior to mineralization. However, the presence of pyrite and chalcopyrite disseminated in the dike suggests some mineralization occurred during the dike emplacement.

Structural geology

Rocks exposed in the Victorio Mountains dip gently to moderately to the north or south with offsetting faults (Fig. 13, 14). The sedimentary rocks in the area are folded

and faulted locally (Griswold, 1961). Faults are well to moderately exposed in some places in the district, but difficult to trace due to thick alluvial cover. There is an east to west fault that divides the Middle Hills from the Main Ridge called the Main Ridge fault. This fault is not very well exposed due to Quaternary cover. The saddle between the Middle Hills and the Main Ridge is characterized by near vertical faults (Fig. 14a) that occur on either side of the low point.

The steeply-dipping Victorio Mountains fault is exposed in both the East and Middle Hills. Locally the fault is sinuous and consists of numerous steeply-dipping splays (McLemore et al, 2000a). The Victorio Mountains fault has been interpreted by previous authors to be a strike-slip fault or a polyphase normal fault (Thorman and Drewes, 1980), and as a reverse fault (Kottlowski, 1960; Griswold, 1961). The preferred interpretation for this study is that the Victorio Mountain fault is a polyphase normal fault as shown in the cross section (Fig. 14a).

Mine Hill is cut by numerous faults (Griswold, 1961). The Mine Hill fault strikes N50-70°E and forms the northern boundary of Mine Hill. The Mine Hill fault cuts mineralized veins in both the Excess and Rambler mines (Griswold, 1961). The southern side of Mine Hill is bounded by the South fault, which strikes N70-75°E. Faults on the north side of Mine Hill tend to dip north similar to the Mine Hill fault, while faults on the south side of Mine Hill tend to dip to the south or east similar to the South fault. There are many pre-ore faults that strike N40-80°E and are filled with barren quartz. One of the more prominent pre-ore faults is the Crest fault. The Crest fault is 2300 feet long and is cut by younger mineralized faults. Many of the mines on Mine Hill occur along silicified and mineralized north-northeast faults.

The Fusselman Dolomite, which is nearly 900 feet thick on Mine Hill, has been almost completely removed north of Mine Hill (Fig. 14a). It is found as surface exposure in the Middle Hills bounded by thrust faults (McLemore et. al, 2000a). It is possible that strike-slip movement along the faults north of Mine Hill caused the removal of the Fusselman Dolomite. Alternatively, the abrupt thinning of the Fusselman Dolomite may be due to post-Silurian erosion on the south edge of the Burro uplift (McLemore et al. 2000a). Unfortunately, there is very little surface exposure to identify the possible causes of the removal of the Fusselman Dolomite.

Alteration

There are four types of alteration that are found in the Victorio mining district: contact-metasomatic non-mineralized skarn, silicification (veins and jasperoids), sericitic/argillic, and carbonate recrystallization (McLemore et al., 2000a).

Contact-metasomatic non-mineralized skarn

The contact-metasomatic alteration produced skarns in the carbonate rocks of the district and appears to be related to the rhyolite and mafic dikes and sills and the Victorio Granite (McLemore et al., 2000a). The most intense amount of contact-metasomatic alteration occurs in the Middle Hills area, with decreasing amounts of contact-metasomatic alteration towards the south.

Typically, the contact-metasomatic skarn alteration displays a sequence of mineral assemblages starting with anhydrous minerals assemblages (prograde) then later hydrous, volatile-rich mineral assemblages (retrograde). The sequence change from prograde to retrograde is in response to decreasing temperatures and changes in fluid chemistry such as fluid mixing (Kwak, 1994). Superimposed on the prograde mineral

assemblages are later retrograde assemblages. Metasomatic alteration and ore-forming events produce similar mineralogies making a distinction between the separate alteration stages difficult. Metasomatic alteration usually predates the ore-forming processes. Permeability in the host rock at first usually follows sedimentary contacts or fractures and faults. As crystallization progresses, a decrease in host-rock volume creates more open space for later mineralization. There is the possibility that earlier karsting events created open spaces within the carbonate rocks before the first stages of mineralization (Young, 1992).

Limestone skarn mineralogy consists of grossularite or andradite, wollastonite, tremolite, epidote, and Ca-Fe pyroxenes (Guilbert and Park, 1986). Sample GVM 21 1581.1 (Appendix D-2) illustrates this type of mineralogy. The mineral assemblage from the center of the veinlet outward is calcite, grossular garnet, and epidote, to altered limestone. Dolomite skarns consist of magnesium-rich minerals such as, serpentine, diopside, and humite-chondrodite minerals (Guilbert and Park, 1986). Sample GVM 21 1168.2 (Appendix D-3) shows this mineral assemblage, with calcite, chondrodite, pyrite, chlorite, serpentine, and diopside. The mineralogy of the Victorio skarns displays both types of alteration because both lithologies are present in this area.

Silicification

Two types of silicification occur in the Victorio district, quartz veins and jasperoids. Massive quartz veins occur in pre-ore forming faults at Mine Hill and Middle Hills. There are multiple episodes of both barren quartz veins and quartz associated with other minerals as illustrated by sample GVM 18 1651 (Appendix D-4). The silicification occurs within veins and joints along the Victorio Mountain fault. Silica replacements

occur within carbonate units along bedding planes and within replacement breccias McLemore et al., 2000a). There is a close association between the silicification and mineralization of the carbonate-hosted replacement deposits (McLemore et al., 2000a).

Sericitic/argillic alteration

The sericitic/argillic alteration is mostly confined to the Victorio Granite and other igneous intrusions in the district. The alteration consists of sericite, adularia, chlorite, and clay minerals replacing primary igneous minerals (Fig. 9c, d). Nearly all of the mafic rocks in the district have some amount of sericitic/argillic alteration (McLemore et al., 2000a). Minor amounts of quartz veining and iron staining commonly occur with the sericitic/argillic alteration (McLemore et al., 2000a). The porphyry and skarn deposits are slightly altered, and the alteration appears to have occurred during the post-mineralization stage. The porphyry sample GVM 21 1499 (Appendix D-5) shows chlorite and muscovite with iron-staining rims that may have some amounts of sericitic/argillic alteration. Sample GVM 41 1925.5 (Appendix D-6) has a clay alteration layer and sericitic alteration of the pyrite-muscovite layer as well.

DESCRIPTION OF MINERAL DEPOSITS

There are three deposits types at the Victorio mining district, but only two of these types of mineral deposit were mined; the carbonate-hosted lead-zinc replacement deposits (Mine Hill) and the W-Be-Mo skarns (Middle Hills) (Fig. 4). The porphyry molybdenum deposit is not economic due to the low grade and the depth of the deposit, and therefore was never exploited.

Porphyry molybdenum deposit

The Victorio deposit is described as a porphyry-type molybdenum deposit, instead of a Climax-type deposit (Table 5). The Victorio deposit has a higher Cu:Mo ratio then Climax-type deposits as Climax-type deposits typically have little to no associated copper (Cox and Singer, 1986). Within the highest grade zone, the porphyry deposit is altered to actinolite that is being replaced by secondary biotite and phlogopite (Heidrick, 1983). Veins cutting the porphyry deposit consist of quartz-pyrite with associated chalcopyrite, sphalerite, pyrrhotite, galena, and molybdenite (Heidrick, 1983). Within the main porphyry ore body early quartz-biotite-molybdenite-pyrite ± magnetite veins are cut by stock-work quartz-molybdenite ± muscovite and pyrite-fluorite-scheelite-magnetite veins (Heidrick, 1983). The porphyry deposit in drill core samples consists of quartz phenocrysts in a fine-grained whitish-pink feldspar matrix with quartz-molybdenite veins (GVM 21 1862 Appendix D-7, GVM 21 1493.5 D-8).

W-Be-Mo Ore Skarns

The Irish Rose vein strikes north with a dip that ranges from 50° to 70° E, and was discovered during the early production of the district. The vein ranges in width from 0.5 to 3 feet and averages 1.5 feet in thickness. The vein was mined through an inclined

shaft approximately 125 feet deep, several pits and trenches (Griswold, 1961). The alteration mineral assemblages of the Irish Rose skarn vein consists of milky white to colorless quartz, white to yellowish muscovite, limonite, pyrite, wolframite, and beryl (Griswold, 1961). Ore minerals include helvite, wolframite, scheelite, molybdenite, galena, sphalerite, and beryl (McLemore et al., 2000a).

Griswold (1961) refers to a "tactite zone" of irregular altered lenses within the Montoya and El Paso formations. The "tactite zone" refers to metasomatism of the carbonate-host rock, and could simply be referred to as skarn. These zones consists of grossularite, tremolite, pyroxene, idocrase, phlogopite, fluorite, and quartz. The main ore minerals were helvite and scheelite mined for beryllium and tungsten respectively. Helvite and scheelite are only present in minor amounts in the vicinity of the Irish Rose vein. Helvite is only found within the skarn zones while scheelite occurs as disseminations and veins (Griswold, 1961).

The mineral assemblages in the skarns are dependant upon the host lithology, and even members within a single formation will have different mineral assemblages. Therefore, a discussion of each lithological group/formation/member described from drill core observations gives a more accurate description of the skarn alteration and mineralization.

Alteration and mineral deposits in the Precambrian rocks

The Precambrian amphibolite unit (Ya; Fig. 14a) within the Victorio district has a vein alteration mineral assemblage consisting of quartz, quartz-molybdenite, chlorite-pyrite, chlorite-pyrite-scheelite, and other mineral assemblages of quartz, chlorite, pyrite, pyrrhotite, magnetite, muscovite, molybdenite, scheelite, powellite, fluorite, beryl, K-

feldspar, and albite occurring as veins and veinlets (Heidrick, 1983). Skarn minerals within the Precambrian amphibolite consists of 20 – 135 feet of 0.2% Mo +WO_3 with 15-20% vein frequency, whereas the quartzo-feldspathic gneiss has much lower grades and vein frequencies (Heidrick, 1983). Skarn minerals within the quartzo-feldspathic gneiss (Ygn) consists of stockwork quartz-molybdenite, quartz-albite, quartz-pyrite veins with rare fluorite and muscovite and grades much lower than 0.2% Mo + WO_3 (Heidrick, 1983).

Alteration and mineral deposits in the Bliss Formation

Within the Bliss Formation, the three major lithological units exhibit differences in the amounts of Mo-W, vein thickness, and vein frequencies (McLemore et al., 2000a). Veins in the Bliss sandstone peripheral to the skarn deposits are weakly developed consisting of quartz, calcite, fluorite, albite, biotite, sericite, pyrite, molybdenite, and scheelite. Areas in the Bliss sandstone that show weak to no skarn veins are underlain by the Precambrian quartzo-feldspathic gneiss suggesting the Precambrian footwall influences mineralogy (Fig. 14a; Heidrick, 1983).

Skarn mineralization within the Bliss calcium-poor othroquartzite facies consists almost entirely of small veinlets (0.01-0.2”) with rare scheelite and disseminated molybdenite (McLemore et al, 2000a). Mostly, the skarn minerals are disseminated or restricted to the quartz veinlets. Sample GVM 41 2073.1 (Appendix D-9) is from the Bliss othroquartzite sandstone member, and consists of a quartz-molybdenite-magnetite vein cutting through the altered quartzite host rock with disseminated pyrite. There is no scheelite or powellite present when observed using a UV light.

The silty glauconitic facies of the Bliss Formation has slightly higher calcium values and correspondingly higher tungsten values (McLemore et al., 2000a). Vein frequency and thickness is greater in the silty glauconitic unit than in the othroquartzite facies. The veins in the silty glauconitic facies are more contiguous and thicker. The molybdenite mineralization is mainly vein controlled while the scheelite is disseminated (Heidrick, 1983).

The high vein frequency and thickness (1.0–1.5 inches) in the silty limestone facies of the Bliss sandstone is most likely related to higher calcium values within this unit (Heidrick, 1983). Molybdenite minerals are mostly vein controlled with some dissemination (McLemore et al., 2000a). Scheelite is mainly disseminated and is visible under UV light. The main stage of mineralization that cuts through the Bliss Formation is predominately quartz-molybdenite with or without albite, pyrite, magnetite, and scheelite. Samples GVM 65 1902.8 (Appendix D-10) and GVM 21 1297 (Appendix D-11) exhibit this kind of mineralogy.

Alteration and mineral deposits in the El Paso Group

In the El Paso Group, the interbedded units of dolomite, dolomitic limestone, sandy dolostone, dolomitic sandstone, limestone, and cherty limestone have produced a varied mineral assemblage with overprinting of one or more metamorphic or pyrometasomatic events (Heidrick, 1983). The Hitt Canyon fine- to medium-grained dolostone and limestone is the most important ore-bearing unit of the El Paso Group (Heidrick, 1983). Minor amounts of garnet, tremolite, idocrase, and wollastonite occur at the base of the Hitt Canyon in drill holes outside of the main ore body (Heidrick, 1983). Certain strata within the Hitt Canyon Formation peripheral to the main ore body are

completely converted to skarn with diopside being the main calc-silicate mineral being replaced by tremolite, muscovite, fluorite, and actinolite (Heidrick, 1983).

Within the El Paso Group the Hitt Canyon Formation has a distinctive alteration pattern referred to in drill logs as ribbon rock (Heidrick, 1983). This alteration consists of a mottled texture of irregular dark to pale green patches. In the ribbon rock alteration massive diopside is replaced by tremolite, muscovite, chlorite, and actinolite. The main stage of mineralization in the Hitt Canyon ribbon rock is characterized by disseminated scheelite and molybdenite filling in between diopside grains. The lower Hitt Canyon ribbon rock contains abundant quartz-albite-molybdenite-tungsten-pyrite veins (Heidrick, 1983). The molybdenite is fine to coarse grained and is found more or less equally in both veins and disseminations similar to the silty facies of the Bliss sandstone. Sample GVM 18 1651 (Appendix D-4) is from the lower Hitt Canyon Formation of the El Paso Group with the mottled ribbon rock texture. The mottled light and dark green texture consists of diopside being replaced by tremolite and chlorite. Mineralization in this sample is a quartz-molybdenite vein that is cross cut and offset by a barren quartz vein.

The skarn lies within a fluidized megabreccia above a zone of normal faults with large blocks of steeply dipping El Paso altered marbles and ribbon-rock (Heidrick, 1983). There is a high frequency of brecciation and faulting in this area as well (Heidrick, 1983). The skarn within this zone consists of vein-controlled and disseminated scheelite, molybdic-scheelite, huebnerite, and helvite with minor amounts of molybdenite and beryl. Dominant vein mineralogy is idocrase, fluorite, muscovite, red garnet, and pyrite with minor amounts of scheelite, huebnerite, helvite, albite, beryl, and rhodocrosite, with

little or no quartz (Heidrick, 1983). Sample GVM 17 1420 illustrates the mineral assemblages for the dominant ore veins (Appendix D-12)

Carbonate-hosted replacement deposits

Deposits include replacements and veins in carbonate rocks. The Victorio carbonate-hosted replacement deposits are typically predominately lead and zinc with copper, silver, and gold as by-products, with little to no calc-silicate minerals (McLemore et al., 2000a). The main ore minerals produced were galena, smithsonite, cerussite, and anglesite with rare amounts of sphalerite and chalcopyrite. Gangue minerals include quartz, calcite, and secondary iron- and manganese-oxides. Gold and silver minerals are rarely recognizable (McLemore et al., 2000a). The width of the mineralized lenses range from a maximum of 20 feet wide to tiny fracture fillings (Griswold, 1961).

The carbonate-hosted replacement deposits are not fracture filling deposits, but replacement lenses in the host sedimentary rock that consists predominately of quartz. Carbonate-hosted replacement deposits are structurally (along faults or fractures) or lithologically (at boundaries between chemically or mechanically different lithologies) controlled (Glig, 1996). The carbonate-hosted replacement deposits within the Victorio district are classified as high-temperature (>300°C) carbonate-hosted replacement deposits and not Mississippi-Valley type deposits due to the high temperature and low salinity of the Victorio carbonate-hosted replacement deposits (Table 6). Typical temperatures of formation for Mississippi Valley deposits ranges from 50° to 225°C and have no direct spatial association with igneous intrusive bodies. (Titley, 1996). High-temperature carbonate-hosted replacement deposits occur distal to coeval intermediate to

felsic intrusions within back-arc environments are typically Mesozoic to Tertiary in age (Glig, 1996).

The majority of the mines are located on the west side of Mine Hill (Fig. 6). Of the known ore bodies within Mine Hill, there are two different replacement deposits orientations. Replacement deposits occurring along faults and fractures striking N30-65° E and dip steeply to the northeast and replacement deposits striking almost due north and dip steeply to the east (Griswold, 1961). The most productive replacement deposits are those that occur along faults striking to the northeast. The Chance, Jessie, Parole, Excess and Rambler mines exploited these types of deposits. The only productively mined replacement deposits that strike north were in the Excess and Rover mines (Griswold, 1961), probably a result of the many intersections with the northeast trending replacements in these mines. There is evidence of both pre- and post-mineralization movement along the fault systems on Mine Hill (Griswold, 1961).

MINERAL PARAGENESIS

The general paragenetic sequence of events at the Victorio mining district was determined by observations from drill core, petrographic studies, and work by previous authors (Fig. 18). Three stages of alteration and mineralization include, pre-mineralization, mineralization, and post-mineralization. The pre-mineralization stage is characterized by the contact-metasomatic alteration, silicification, sericitic alteration, and the deposition of some disseminated sulfides. The mineralization consists of three substages and is discussed below with respect to the host lithology. The last stage is characterized by post-mineralization alteration and oxidation.

W-Mo-Be Skarn mineralization

The variation of mineralogy due to different host lithologies and overprinting presents difficulties in determining a specific paragenetic sequence for the skarn deposit, therefore looking at the lithological units separately gives a better paragenetic sequence for the skarn deposit. The general paragenetic sequence of the skarn vein mineral within the Bliss Formation units starts with the first appearance of barren quartz veins (Appendix D-13, D-14). Quartz-molybdenite veins with or without albite, pyrite, magnetite and scheelite cut the barren veins. Late-stage veins contain muscovite, albite, beryl, fluorite, orthoclase, dolomite, and molybdenite. These veins are usually quartz-poor and contain traces of bismuthinite and galenobismutite (Heidrick, 1983).

In the El Paso Group there is evidence of an early contact metasomatic event followed by a later pyrometasomatic overprinting (Heidrick, 1983). Veins within the El Paso Group contain at least four and as many as 12 minerals in a multitude of combinations. Nearly all veins contain muscovite, fluorite and calcite with other

minerals such as, garnet, diopside, idocrase, chondrodite, tremolite, epidote, talc, scheelite, molybdic scheelite, powellite, sphalerite, pyrite, pyrrhotite, magnetite, wolframite, galena, galenobismutite, chalcopyrite and tetrahedrite (Heidrick, 1983). Veins in the El Paso adjacent to and within the Tungsten Hill breccia pipe usually contain mixtures of these minerals with more abundant wolframite, helvite, pyrite, sphalerite, and fluorescent calcite (Heidrick, 1983). The last stage of the mineralization of the middle and upper El Paso Group is divided into two distinct vein assemblages (Heidrick, 1983). One assemblage is alkali-rich containing muscovite, albite, fluorite, helvite, pyrite, scheelite, and molybdenite, for examples, sample GVM 21 1490 (Appendix D-15). The second assemblage consists of thick veins of quartz, muscovite, pyrite, fluorite, beryl, calcite, molybdenite, bismuthinite, galenobismutite, wolframite, sphalerite, and helvite, for example, GVM 2 553 (Appendix D-16).

Carbonate-hosted replacement mineralization

The carbonate-hosted replacement deposits were nearly completely mined out and underground workings were not accessible, so very few samples exist. Literature pertaining to the Mine Hill deposits has little details about mineral paragenesis. Sample E109 1940 (Appendix D-17) contains sphalerite-galena-pyrite with intergrown quartz in an altered host rock. Samples VIC 67-99 and VIC 149-99 (Appendix D-18, D-19) possibly represents what Griswold (1961) described as the non-oxidized ore. The paragenetic sequence in Figure 18 is based upon these few samples and the limited literature reports.

RESULTS

Geochronology

Previously, McLemore et al. (2000a) dated two samples of the Victorio Granite, GG1 2225 and GVM A1 2741 (Fig. 19), with inconclusive results. The K-feldspars for both samples have saddle-shaped age spectra with minimum values of approximately 30 Ma and final values between ~50 to 70 Ma. (Fig.19). The K-feldspars results contain steps that are both younger and older than the coexisting biotite minerals. The complexity of the GG1-2225 age spectrum (Fig. 19) may be the result of excess argon. Some saddle-shaped age spectra are indicative of a K-feldspar that has retained excess argon trapped in anion sites that degas at high temperatures (Foster et al., 1990). The age spectrum for sample GVM A1- 2741 (Fig. 19) is a more common age spectrum that is not typically the result of excess argon, but instead could represent an 50 Ma granite that experienced a loss of argon by a re-heating event at ~30 Ma. The biotite age spectra are relatively flat lying with approximate ages of 35 Ma. The biotite results could be interpreted as either the age of the granite emplacement or the results could represent the re-setting of the biotite minerals in response to a re-heating event. The preliminary data by McLemore et al. (2000a) indicated two different possible ages for the intrusion of 35 Ma (from biotite mineral separates) or 70 Ma (from K-feldspar mineral separates). The study did not have enough information to distinguish between these two possible ages for the granite, therefore dating more samples from the Victorio Granite was necessary in this study.

Victorio Granite

A total of six mineral separates of biotite, muscovite, and K-feldspar were analyzed using the $^{40}Ar/^{39}Ar$ step-heating technique (Table 3). A summary of the argon geochronology results is in Table 4. The age spectra for all the mineral separates of the Victorio Granite samples GVM 15 2402 and GVM 9 2056 are shown in Figure 20. The slightly older portions of the GVM 9 2056 biotite age spectrum in the first and last few heating steps (Appendix A-1) could be the result of excess argon (Foster et al., 1990). The older apparent ages for these steps could be attributed to excess argon or ^{39}Ar recoil. The biotite age spectrum for GVM9 2056 has a plateau age of 35.24±0.09 Ma (Table 4) and an integrated age of 36.81± 0.06 Ma. The muscovite results for GVM 9 2056 do not appear to contain excess argon (Appendix A-2). The age spectrum has a plateau age of 34.99 ± 0.09 Ma (Table 4).

The GVM 15 2402 biotite age spectrum has a calculated age of 33.84± 0.12 Ma (Table 4). A forced plateau for steps E-I yielded a calculated age of 33.99± 0.17 Ma (Appendix A-1). The complexity of the age spectrum could be due to either excess argon or to mineral inclusion contamination within the biotite minerals. The first few heating steps of the age spectrum are anomalously old and may contain excess ^{40}Ar (Appendix A-1). The last three heating steps have low K/Ca values and the ages for these steps decreases at first then increases again. The low K/CA ratio for the last three steps could indicate contamination by inclusions of a potassium-poor mineral that degasses at higher temperatures, such as pyroxene. The muscovite GVM15 2402 age spectrum does not have the same sort of complexity as the biotite results for this sample (Appendix A-2). The plateau age of the muscovite is 34.67 ± 0.07 Ma.

The K-feldspar results are more difficult to interpret than the mica data. The gas from K-feldspar sample for GVM 9 2056 was catastrophically lost during analysis before the furnace had reached over 1200°C, therefore the age spectra for this sample does not represent the entire analysis (Appendix A-3). The K-feldspar age spectra for GVM 15 2402 (Appendix A-3) is complex making the results difficult to interpret. The first few steps were measured twice at the same temperature to clean the gas. This was done to remove the excess argon with the first measurement in order to obtain a more accurate second measurement. The overall appearance of the K-feldspar spectrum closely resembles a saddle-shaped age spectrum that contains excess argon in large-diffusion domains (Foster et al., 1990).

Skarn alteration

Four alteration samples associated with sulfide minerals were dated to determine the age of mineralization (Table 4). The samples selected had both datable minerals and sulfide minerals that could be paragenetically related. The samples are most likely from the first and second sub-stages of the paragenetic sequence (Fig. 18).

The results from sample GVM 21 1278 (Fig. 21) are similar to the results of the Victorio Granite (Fig. 20). The plateau age calculated from the GVM 21 1278 biotite (Appendix A-4) is 35.80 ± 0.19 Ma (Table 4). The K-feldspar from sample GVM 21 1278 (Appendix A-4) displays the same saddle-shaped age spectrum as the K-feldspar samples from the Victorio Granite with an integrated age of 74.79 ± 0.16 Ma. The skarn alteration mica samples have relatively undisturbed age spectra. Sample GVM 21 1490 muscovite (Fig. 22) has a plateau age of 34.83 ± 0.2 Ma. Sample GVM 41 1925.5

muscovite (Fig. 22) has a plateau age of 34.91 ± 0.17 Ma. The GVM 59 1702 biotite (Fig. 23) had a plateau age of 35.57 ± 0.10 Ma.

Fluid Inclusions

Fluid inclusions, which range in size from < 2 μm to 40μm, were found in quartz, calcite, fluorite, and garnet from mineralization sub-stages 1-3 of the paragenetic sequence (Fig. 18). There are three different types of inclusions found within the Victorio district, 1. primary and secondary two-phase liquid-vapor inclusions (Fig. 24), 2. primary and secondary three-phase liquid-vapor CO_2-rich inclusions (Fig. 25), and 3. secondary three-phase inclusions with solid mineral phases (Fig. 26). Some samples contain both primary inclusions that are two-phase liquid-rich inclusions, as well as, three phase liquid-CO_2 rich inclusions. The types of fluid inclusions are categorized as follows:

Type Ia – liquid + vapor, >50% liquid
Type Ib – liquid + vapor, >50% vapor
Type IIa – liquid + $liquid_{CO2}$ + $vapor_{CO2}$, >50% liquid
Type IIb – liquid + $liquid_{CO2}$ + $vapor_{CO2,}$ >50% $liquid_{CO2}$ + $vapor_{CO2}$
Type IIc - $liquid_{CO2}$ + $vapor_{CO2}$
Type III - liquid + vapor + solid.

Microthermometry

The results of the fluid inclusion microthermometry analysis (Appendix B) are summarized in Table 7. Salinity, mole percent CO_2, critical pressure and temperatures, and other fluid parameters were calculated from the microthermometry measured data using the Flincor computer program (Brown, 1989). Primary skarn temperatures ranged from 171 - 360°C and had salinities fall between <1 to 25.6 eq. wt% NaCl. The barren quartz veins (sub-stage 2) found near the skarn mineral veins had temperatures that between 199– 340°C with salinities of 3.1 to10.97 eq. wt% NaCl. Porphyry quartz

(sub-stage 1) primary temperatures ranged from 179 - 325°C with salinities of 2.0 – 11.2 eq. wt% NaCl.

The primary fluid inclusions results taken from the carbonate-hosted replacement deposit sample E109 ranged in temperature from 151 – 257°C and had salinities of 10 to 19 eq. wt% NaCl (sub-stage 2). The Mine Hill vuggy quartz samples from the Rambler mine area and silicified veins from Mine Hill (sub-stage 3) ranged in temperature from 109 - 350°C and had salinities all below 5 eq. wt% NaCl.

Brief discussion of the fluid inclusion microthermometry analytical techniques

The precision of the measurements for the fluid inclusion heating and freezing stage (1.0°C and 0.2°C) is much better than the standard deviation for the Victorio samples. The ranges of temperatures for primary inclusions in a single sample can be large. Sample GVM 41 1925.5 primary inclusions have a range of temperatures of 246 to 360°C and a standard deviation of 33°C. This variation in the data (standard deviation of 33°C) cannot be attributed to errors in temperature determinations. The variation could be attributed to the measurement of inclusions that have had post-entrapment modifications, such as necking down. However, precautions were taken to avoid measuring inclusions that showed signs of post-entrapment modifications by measuring isolated inclusions instead of clusters of inclusions.

Fluid inclusion gas analysis

The gas concentrations for the eight fluid inclusion gas samples are listed in Appendix C. All eight samples contain varying concentrations of He, CH_4, H_2O, N_2, O_2, H_2S, Ar, CO_2, SO_2 and complex hydrocarbons. This is a relatively new technique, however the results from the fluid inclusion gas analysis can be used to determine the

composition of the vapor phase, the origins of the fluid, and fluid temperature assuming that the vapor is in equilibrium with the hydrothermal waters.

Stable Isotopes

Stable isotopes help to determine the origin of the mineralizing fluids, which is an important part of a genetic model. There are two methods of determining the $\delta^{18}O$ and δD values for the hydrothermal mineralizing fluids. One involves a direct measurement of the fluid itself either from a geothermal area or from fluid inclusions. Fluid inclusion measurements can be problematic because they may incorporate secondary inclusions that do not represent the mineralizing fluid. The other method to determine the isotopic composition of the water is analyzing the stable isotopic composition from the mineral assemblages. This indirect technique has the advantage over the direct techniques of using the actual vein minerals to determine the water that was in equilibrium with the minerals during formation. However, this technique requires a correction for fractionation. Using the temperature of formation and the appropriate fractionation factors, the composition of the mineralizing fluid in equilibrium with the mineral assemblage during formation can be determined (Taylor, 1974). The indirect technique of calculating fluid compositions from mineral values was used for this study.

In order to help determine the origins of the mineralizing fluids, sulfide, silicate, and carbonate samples from the second and third sub-stages of the paragenetic sequence were analyzed for their stable isotope composition. Carbon and oxygen isotope values were obtained from calcite and carbonate rocks. Oxygen isotopes were determined from quartz. Sulfur isotopes were determined from pyrite, sphalerite, molybdenite, and galena.

Carbon and oxygen from carbonates

The skarn calcite samples ranged from –2.2 to – 5.0‰ $\delta^{13}C$, and 11.3 to 20.8‰ $\delta^{18}O$ (Table 8). The skarn limestone samples had a range of –2.0 to –5.1‰ $\delta^{13}C$ and 9.2 to 20.4‰ $\delta^{18}O$. The carbonate-hosted replacement deposits ranged from –1.6 to –9.1‰ $\delta^{13}C$ and 14.3 to 23.6‰ $\delta^{18}O$. The results of the carbonate isotope analysis were reproducible to within 1.2‰ for carbon and 1.0‰ for oxygen as calculated from duplicate samples.

Oxygen from silicates

Quartz samples from the Victorio Granite, breccia pipe, porphyry, skarn, and carbonate-hosted replacement deposits were analyzed for oxygen isotopes (Table 9). The $\delta^{18}O_{qtz}$ values for the quartz samples ranged from 7.7 to 17.8‰ (Fig. 27). The $\delta^{18}O_{H2O}$ values were calculated using estimated average homogenization temperatures from fluid inclusions analyses and the quartz-water fractionation factor from Zheng (1993). The calculated $\delta^{18}O_{H2O}$ values ranged from –2.3 to 5.3‰ (Fig. 28) The results of the silicate analysis were reproducible to within 0.4‰ for oxygen as calculated from duplicate samples.

Sulfur from sulfides

Six samples had more than one sulfide mineral that could be separated. The sulfur isotope values (Table 10) for the pyrite-molybdenite mineral pairs are nearly equal in each sample, this indicates that the system was near equilibrium during deposition. Unfortunately, these results could not be used for geothermometry because pyrite and molybdenite exhibit little fractionation at temperatures higher than 200°C (Taylor, 1974).

A histogram of the sulfur results (Fig. 29) shows that nearly all of the values for all mineral types fall between 3 to 7‰. One exception, GVM 41 1925.5 pyrite sample has a value of –11.2 ‰. The sulfide isotope results were reproducible to within 0.1‰ as calculated from duplicate samples. The homogenization temperatures from fluid inclusions were used to calculate the H_2S in equilibrium with the mineral samples. The majority of the $\delta^{34}S_{H2S}$ values calculated using the equations for each mineral listed in Campbell and Larson (1998) fall within the range of 1.0‰ to 6.9‰ regardless of the mineralogy (Fig. 30). The homogenization temperatures used to calculate the H_2S values for this study were measured on gangue minerals, and therefore may not represent the temperature of the sulfide minerals. The sulfides and the quartz gangue minerals are coexisting, but not necessarily co-genetic. Campbell and Robinson-Cook (1987) found the homogenization temperatures for wolframite minerals were higher than quartz minerals from the Victorio district and the fluids were compositionally different even though there was no evidence for non-co-genetic deposition in hand sample. The study by Campbell and Robinson-Cook (1987) determined the fluid homogenization temperature in wolframite to be 280-380°C and quartz temperatures of 141-320°C. The results of this study indicated there was a significant difference between the temperature of formation for the wolframite and quartz crystals.

DISCUSSION

Age of the Victorio Granite and skarn alteration

The Victorio Granite argon geochronology results of this study (Fig. 20) are similar to the results of McLemore et al. (2000a) (Fig. 19). The Victorio Granite ages (Appendix A) have two possible interpretations. The first is the K-feldspar ages (Fig. 20) represent the true age of the granite (~ 70 Ma), the complexity of the K-feldspar age spectra represents the cooling history of the granite plus the effects of excess ^{40}Ar, and the mica dates are a result of a re-heating event at approximately 30 Ma. The second scenario is that the mica dates (Fig. 20) represent the correct age of the granite and the K-feldspar results (Fig. 20) are due to excess argon.

To determine if the K-feldspar results could represent the thermal history of the Victorio Granite, a time-temperature history model was constructed. However, the model did not accurately coincide with the observed geochronology results (Fig. 31). Both the biotite and muscovite have similar dates, but different closure temperatures (~300°C for biotite and ~350°C for muscovite from McDougall and Harrison, 1998). If the mica age spectra represented a loss of argon due to re-heating, then the biotites (with a lower closure temperature) should be younger than the muscovites. However, there is no systematic difference in the mica age results as shown on an age probability diagram (Fig. 32). The granite would have to cool rapidly in order to reset both mica minerals to the same approximate age and still retain the older age portion of the age spectra. The thermal model for the K-feldspar results do not show a rapid cooling event (Fig. 31) and therefore do not coincide with the mica results.

The saddle-shape of the K-feldspar age spectrum (Appendix A-3) indicates the presence of excess argon (Foster et al., 1990). The K-feldspars could have trapped multiple excess argon components. If the multiple trapped argon components are located in different diffusion domains that degas at different temperatures, the resulting age spectra could be difficult to interpret (Heizler and Harrison, 1988). There is minor excess argon in the biotite samples (Appendix A-1) and a small amount in the muscovite samples (Appendix A-2) as well.

The age probability diagram (Fig. 32) (Dieno and Potts, 1990) shows there is no systematic age difference for the Victorio Granite mica samples. The age probability diagram shows that sample GVM 15 2402 biotite results fall outside the cluster of the other age results. The small variation in the ages for the four mica samples could due to ^{39}Ar recoil if the samples are slightly chloritized, loss of ^{40}Ar after the emplacement of the granite, or due to excess argon from mineral or fluid inclusions. A flat age spectra does not eliminate the possibility of excess argon in a biotite or muscovite sample. Mica samples heated in a furnace do not diffuse argon like feldspar samples. Therefore, mica age spectra do not indicate the presence of excess argon like feldspar samples would with a saddle-shaped age spectra. The three mica results were combined using a weighted average, excluding sample GVM 15 2402 biotite, and the age of 34.9 ± 0.05 Ma was assigned to the granite. The age of the Victorio Granite is important in constructing the genetic model for the Victorio mining district.

The geochronology results of the skarn alteration minerals are consistent with the mica data from the Victorio Granite samples. The K-feldspar sample from the alteration GVM 21 1278 (Fig. 21) has a similar saddle-shaped age spectra as the Victorio Granite

K-feldspar samples (Fig. 20). The K-feldspar age could be the result of excess argon. There is little literature on the presence of excess argon in hydrothermal fluids. Richards and McDougall (1990) found evidence of excess argon in sericite and roscoelite minerals associated with gold mineralization in the Pogera gold deposit. There was no speculation as to the source of the excess argon. However, the conclusion was drawn that the mineralization was linked to the intrusion (Richards and McDougall, 1990). Therefore, it is possible the K-feldspar from the skarn alteration sample could be from a hydrothermal fluid. The other possibility is the K-feldspar is from a pegmatite that occurred before the skarn mineralization. The evidence that disagrees with this hypothesis is that the biotite samples with an age of 35.8 Ma are on the outside of the vein (Appendix D-20). Another piece of evidence to support the K-feldspar being part of the skarn deposit is that the molybdenite is incorporated into the K-feldspar layer of the vein (Appendix D-20). Since there is no proof the K-feldspar is from a pegmatite, the K-feldspar is considered to be part of the skarn alteration and the complexity of the age spectra is attributed to the effect of excess argon.

Ages of the four mica skarn alteration samples are similar to the results of the Victorio Granite. The muscovite samples are slightly younger than the biotite samples (Fig. 32). This could be the result of recoil caused by chloritization of the biotite minerals. The age of the skarn alteration was calculated using a weighted average of all four mica results to be 35.4 ± 0.07 Ma. However, if the biotite results are excluded based on the possibility of recoil or excess argon effecting the ages, then the age calculated from only the muscovites is 34.9 ± 0.09 Ma for the skarn alteration.

The results of the argon geochronology analysis indicates the age of the Victorio Granite and the age of the skarn alteration minerals are similar. The igneous whole-rock geochemistry results show that the Victorio Granite samples are similar in chemistry to other igneous rocks of southwestern New Mexico (Fig. 16). The chemistry of the Victorio igneous rocks are different from the older Laramide copper porphyries of the Chino and Tyrone districts or the Laramide intrusions from the Lordsburg district (Fig. 17). The geochemical data supports the interpretation that the age of the Victorio Granite is 34.9 Ma, not of Laramide age. Four different areas of the Victorio Granite sampled for geochemistry and argon geochronology have similar results, which suggests the granite is one granitic body not several intrusions emplaced over time.

Depth of alteration/mineralization

The original depth of the deposits during mineralization must be considered in ascertaining the pressure. Two methods were used to estimate the pressure during mineralization, the first was a stratigraphic reconstruction and the second was calculated from the fluid inclusion microthermometry measurements using the Flincor computer program. To determine the maximum amount of lithostatic pressure during the time of mineralization within the Victorio Mountain district, a geologic reconstruction of the stratigraphic section was used to determine the rock overburden. The minimum estimated thickness for each unit was taken to be the current thickness of these units.

The minimum calculated thickness accounted for the presence of the units between the Bliss Formation and the Victorio Peak Dacite dated at 41.7 Ma by Thorman and Drewes (1980). From the cross section (Fig. 14a), only the units from the Montoya Group to the Victorio Peak dacite could have been thicker than the minimum estimated

thickness. The El Paso and Bliss Formations are conformable and probably did not erode from the time of mineralization to the present day; so it is not necessary to estimate an additional thickness for these units. The cross section and the drill core from GVM 6 (Fig. 14a) indicate the unit corresponding to the Hidalgo Formation (Tka) directly overlies the Bisbee Formation. This could be interpreted to mean the Bisbee Formation was exposed at the surface when the Hidalgo Formation was deposited. This would constrain the stratigraphic reconstruction to only the carbonate units currently present in the Victorio Mountains. It is possible that the carbonate units south of the Main Ridge fault (Fig. 14a) were thicker and there were possibly other units present that have since eroded as there are no volcanic rocks overlying these units to indicate what units were at the surface during the time of mineralization. However, it is difficult to estimate the possible thickness of rock in the southern portion of the district with no other evidence.

Therefore, the possible thickness of these units present during a 35 Ma mineralizing event is not much greater than the minimum estimated thickness of 6000 feet. This estimate takes into account the possibilities that the volcanic rocks and the Bisbee, Fusselman, and Montoya groups could have been significantly eroded or sheared away between 35 Ma and the present. The Victorio Peak Dacite (which correlates to the Rubio Peak Formation) is 1800 feet thick a few miles south in the Bisbee Hills well (Lawton and Clemons, 1992). The U-Bar and Hell-to-Finish formations are over 750 feet thick in the Little Hatchet Mountains (Lucas and Lawton, 2000). It is possible that erosion since the time of mineralization at approximately 35 Ma has removed several hundreds of feet from the surface, therefore an estimated thickness of 8000 feet is an

attempt to compensate for the unknown amount of rock in estimating a maximum depth during mineralization.

Pressure

The depth estimates of between 6000 to 8000 feet roughly corresponds to 600 to 800 bars under lithostatic pressure. The pressures calculated for fluid inclusion samples containing liquid-CO_2 using the Flincor program (Brown and Lamb, 1986) were much higher than the pressures calculated using the stratigraphic reconstruction technique. The pressures calculated using Flincor ranged from 1 to approximately 4 kbar, an estimated depth under lithostatic pressure of 10,000 to 40,000 feet.

One possible source of error is the estimation of volume percent CO_2. If the estimation of volume percent CO_2 is too low then the corresponding pressure calculated would be too high. Also, the composition of the fluid may not be pure CO_2, this could effect the calculation of pressure by the Flincor program. Gas analysis of fluid inclusion volatiles showed the samples containing high concentrations of CO_2 also contained high concentrations of hydrocarbons (Appendix C). The presence of hydrocarbons could effect the calculation of pressure using the Flincor program since the vapor is not pure CO_2 gas. The CO_2 volume was estimated visually. The presence of hydrocarbons that are indistinguishable from CO_2 could have made the visual estimation incorrect.

Another theory to explain the difference in the pressures calculated from Flincor and the pressure estimated from the stratigraphic reconstruction, is the deposits were over pressured. If the deposit formed in a system with accumulating pressures caused by a pressure cap, then the results of the fluid inclusions analysis would not necessarily need to correlate to the lithostatic pressure calculated. The mole percent of CO_2/N_2 for the

fluid inclusion gases (Fig. 33) indicates high amounts of CO_2 in six of the samples. Total gas mole percents over 1.5% is an indication of boiling and over 20% is an indication of a gas cap (Fig. 33) (Norman et al., 2002). The presence of the intrusive breccias and brecciation associated with both the carbonate-hosted replacement and skarn deposits are supporting evidence of an over pressurized system. As a result of the disagreement of the two techniques used to calculate pressure and possible evidence of boiling (discussed below), no pressure corrections were applied to any of the fluid inclusion results.

Boiling

There is evidence that boiling occurred episodically during the formation of the skarn deposits. Evidence of boiling in the Victorio samples includes primary vapor-rich inclusions in the skarns, however this may be extreme necking down. Fluid inclusions with dominant vapor phases were found in all porphyry and skarn samples, but there were very few vapor dominant inclusions in the carbonate-hosted replacement deposits. The granite and breccia pipe samples did not have any vapor dominant fluid inclusions.

The carbonate-hosted replacement deposits sample Vic 601, from the Rambler shaft area, contained both liquid-vapor water inclusions and liquid-CO_2 inclusions. The trapping of two separate phases is more substantial evidence of boiling as the process of necking down would not separate out the CO_2-phase completely. At the Rambler shaft there is another sign that boiling was occurring, bladed quartz. Bladed quartz is the dissolution of calcite followed by the precipitation of quartz during boiling. As a fluid boils after calcite precipitates, the release of CO_2 gas causes calcite to dissolve. The temperature drop causes the precipitation of quartz to fill the open cavities created by the

removal of calcite. Campbell and Robinson-Cook (1987) concluded that the system depositing the quartz was effervescent with CO_2, citing the coexistence of vapor-rich inclusions with liquid-CO_2 inclusions.

Boiling can concentrate the aqueous components by the loss of water, affect the oxygen and sulfur fugacities, and cause a pH change by the loss of CO_2 (Reed and Spycher, 1984). Metal sulfide and metal chloride complexes can be broken by the loss of volatile anions during boiling (Cunningham, 1978). Boiling causes the removal of volatile components (CO_2, H_2S, CH_4, SO_2, H_2) that are responsible for the oxidation-reduction and acid-base equilibrium of a solution (Drummond and Ohmoto, 1985). The solubility of sulfides can be decreased by the partitioning of H_2S into the vapor phase (Cunningham, 1978). Pressure drops can cause boiling to occur. At shallow depths in highly faulted areas, a sudden change from lithostatic to hydrostatic pressure is likely, and results in an explosive loss of volatile components from the magma body (Cunningham, 1978). Boiling can cause a significant drop in temperature, which affects mineral solubilities (Drummond and Ohmoto, 1985). The effect of lowering the temperature is two fold. For a given amount of water, considerably more gas is partitioned into the vapor phase at lower temperatures (Drummond and Ohmoto, 1985). Mineral solubility is higher at elevated temperatures for most minerals, resulting in precipitation at lower temperatures (Drummond and Ohmoto, 1985). Reed and Spycher (1984) indicated both boiling and dilution alter the chemical characteristics of a hydrothermal fluid.

Temperature of alteration/mineralization

The homogenization temperatures obtained from the fluid inclusion microthermometry analyses are minimum temperatures. The average temperatures for the three deposits as determined through the fluid inclusion microthermometry results are listed in Table 7 for primary and secondary fluid inclusions. The temperatures of the skarn deposits are lower than typical skarn temperatures, however the fluid inclusion temperatures were measured on gangue minerals that are from the second and third sub-stage of the paragenetic sequence of the skarn deposits.

When attempting to obtain isotope temperatures for the E109 1942 sulfide mineral pairs, the calculated temperatures were over 4000°C. A plausible explanation is that minor amounts of sulfides are intergrown in the pyrite, sphalerite, and galena. Photomicrograph pictures illustrate how mineral samples from E109 are not monomineralic. A photomicrograph of a pyrite cube (Fig. 34) shows the sample has inclusions of chalcopyrite and sphalerite and Figure 35 shows that the galena has streaks of pyrite intergrowths.

Fluid chemistry

Certain constraints on the chemistry and evolution of the fluid can be determined using the geologic, mineralogic, isotopic, and fluid inclusion evidence in conjunction with published experimental and theoretical geochemical data. Fluid inclusion and stable isotope evidence suggests a dynamic and constantly changing physical and chemical environment. Fluid inclusion and stable isotope analyses were mostly of gangue minerals (quartz, calcite), which may have precipitated over a long period of time during mineralization.

The porphyry and skarn minerals were deposited from a low to moderate salinity (0.02 – 25.6 eq. wt. % NaCl) fluid at a temperature range of 171 - 360°C that shows evidence of boiling and cooling. The porphyry and skarn fluids contained high concentrations of gases (Fig. 33). The carbonate-hosted replacement deposits minerals were deposited from slightly lower salinity (0.8 – 19.3) and lower temperature (109 – 350 °C) fluids that show evidence of boiling and cooling; with lower concentrations of gases. The high amounts of complex hydrocarbons found in the fluid inclusion vapor phase are believed to be derived from the carbonate host rocks or trapped hydrocarbons within the basin. The porphyry sample has the highest concentrations of hydrocarbons (Fig. 36). The skarn and siliceous veins from the carbonate-hosted replacement deposits have lower hydrocarbon concentrations, and the breccia and sample E109 from the carbonate-hosted replacement deposit have very low concentrations of hydrocarbons (Fig. 36). This change in hydrocarbon concentrations between the three deposits could reflect changing water/rock ratios or mixing with another fluid. The porphyry intrusion would have most likely caused a high-temperature convective cell with a high degree of fluid interacting with the carbonate country rock incorporating more hydrocarbons. As the temperature decreased away from the fluid source, the fluid would have less interaction with the surrounding rock. Also, mixing of meteoric water that does not contain hydrocarbons would decrease the concentration.

The vein mineralogy for all three deposits types consists mostly of quartz suggesting a high concentration of silica in the mineralizing fluids. Although the presence of quartz suggests a stable pH of the mineralizing fluid, the pH actually may have shifted over the duration of the mineralization (Reed and Spycher, 1985). This is

because temperature decreases control the precipitation of quartz not changes in pH (Reed and Spycher, 1985). The pH of the mineralizing fluid can be estimated using the vein mineralogy for each deposit. The pH of the mineralizing fluids must initially be at least slightly acidic in order to consume even a small amount of carbonate host-rock before equilibrating with calcite and ending the reaction (Lu et al., 1991). During the main stages of mineralization, sulfide minerals such as pyrite, pyrrhotite, and chalcopyrite will begin to precipitate producing an acidic mineralizing fluid (Lu et al, 1991). The pH also can be constrained by the replacement of K-feldspar by muscovite and the absence of kaolinite indicates a slightly to moderately acidic pH, but not strongly acidic (Barton, 1984).

Evidence of boiling in the three deposit types indicates a possible increase in fluid pH by the degassing of CO_2 as the following reaction illustrates (Reed and Spycher, 1985).

$$HCO_3^-{}_{(aq)} + H^+{}_{(aq)} \rightarrow H_2O_{(aq)} + CO_{2(g)}$$

The increase in pH has greater significance in the precipitation of sulfides than the decrease in temperature (Reed and Spycher, 1985).

The porphyry, skarn, and carbonate-hosted replacement deposits all contain pyrite. The skarn deposits contain chalcopyrite, magnetite, and trace amounts of pyrrhotite. The carbonate-hosted replacement deposits contain galena and sphalerite. These mineral assemblages have some implications on the oxygen and sulfur fugacities. The absence of other sulfide minerals can somewhat constrain the possible fluid chemistry. The mineral assemblages of pyrite, with trace amounts of pyrrhotite, and the absence of bornite constrains the oxygen fugacity to be below log $fO_2 = -36$ (Fig. 37).

The absence of alunite constrains the pH to be above 3.5 and because K-feldspar is present but not abundant, the maximum pH is estimated to be approximately 6. The potassium mineral stability boundaries constrain the pH values since few ore-forming fluids have molalities that fall outside the range of 0.001 to 1 moles K^+/kg H_2O (Ohmoto, 1972). The potassium concentrations plotted on Figure 37 range between 0.001 to 0.1 moles K^+/kg H_2O. Fixing the temperature at 250°C (Barton, 1984), the oxygen fugacity is estimated between log fO_2 = -36 to -42 (Fig. 37). The mineral assemblages used to constrain the oxygen fugacity also can be used to constrain the sulfur fugacity to be between log fS_2 = -9 to –14 (Fig.38). The estimated oxygen fugacity values were added to Figure 38 and resulted in the shaded region shown.

In the Victorio district, Heidrick (1983) indicated there is evidence of both molybdenum-poor and molybdenum-rich scheelite that can be seen by the difference in scheelite fluorescence color. The molybdenum-rich scheelite (greater than 10% molybdenum) fluoresces a cream to amber yellow while the molybdenum-poor scheelite (less than 5 - 10% molybdenum) fluoresces a blue color (Greenwood, 1943). The presence of both molybdenum-rich and molybdenum-poor scheelite in the porphyry and skarn deposits suggests the oxygen and sulfur fugacities fluctuated during skarn mineralization (Hsu and Galli, 1973). Scheelite precipitation also is dependent on temperature. Molybdenum-rich scheelite + pyrrhotite + pyrite veins are stable at higher temperatures than molybdenite-poor scheelite + molybdenite + quartz + pyrite veins at lower temperatures (Ishiyama et al., 2000) indicating the temperature also changed during the mineralization of the porphyry and skarn deposits.

The fluid chemistry of the carbonate-hosted replacement deposit mineralizing fluid can be estimated using the same techniques. The pH of the fluid can be estimated by using the sulfide minerals; pyrite, trace amounts of pyrrhotite, and magnetite indicate the fluid was neutral to acidic (Fig. 37). However, the lack of potassium-bearing minerals does not constrain the pH as well as for the skarn mineralizing fluids. The presence of primary Fe-, Mn- and Cu-oxides and Cu-carbonates indicates that the carbonate-hosted replacement fluids were more oxidizing than the skarn fluids. The fluid inclusion gas analysis for the Rambler sample (Mine Hill area) has H_2S/SO_2 ratio typically less than one that indicates a more oxidizing environment (Appendix C).

Source of fluids

The oxygen stable isotope analyses indicate the mineralizing fluids had a magmatic source component (Fig. 27 and 28). The quartz-water fractionation factor from Zheng (1993) was used to calculate the water values during the time of mineral deposition (Fig. 28) using the temperatures obtained through the fluid inclusion study. Water values were not calculated for the granite since the igneous quartz would not have been in equilibrium with a hydrothermal fluid during formation. The skarn mineral results (9.1 – 11.8‰, Table 9) fall within the range of igneous rock of 6 to 11‰ (Taylor, 1974). The $\delta^{18}O$ of the breccia mineral samples (11.8 and 13.2 ‰, Table 9) are slightly above the typical igneous rocks, however, the range for igneous rocks can be as high as 15‰ (Campbell and Larson, 1998). The carbonate-hosted replacement deposits range from 15.4 to 17.8‰ (Table 9) and fall between the ranges of igneous rocks and limestones.

The calculated $\delta^{18}O_{H2O}$ values for the porphyry samples are between 0 – 4‰, representing meteoric to magmatic fluids. The calculated waters for the skarn samples are between –1 and 4‰, representing meteoric to magmatic fluids. The calculated water values for the carbonate-hosted replacement deposits range between 2 – 7‰, just slightly outside the range of magmatic fluids. The quartz samples from the breccia pipe $\delta^{18}O_{H2O}$ values are between -3 to 0‰, at just about meteoric water values. All of the calculated waters for the porphyry and skarn samples fall outside of the magmatic water values. The calculated waters indicate a possible mixing between magmatic and meteoric fluids. This presumably represents meteoric waters that were enriched either by the addition of magmatic water or through the interaction with isotopically heavy carbonate rocks. The carbonate-hosted replacement deposit waters are even more enriched, perhaps reflecting a higher degree of interaction with the carbonate host rock.

The sulfur stable isotope analyses indicate that majority of the mineral samples fall within a similar range of 2.9 to 6.8‰ (Fig. 29). One sample falls outside this range (-11‰, sample GVM 41 1925.5). However, the calculated $\delta\ ^{34}S$ values do not fall within the range of magmatic sulfur of 0‰ ± 2‰ (Campbell and Larson, 1998). Sulfur speciation must be considered in order to determine the correct equilibrium equation to calculate the fluid origin. The results from the fluid inclusion gas analysis indicate that six of the eight samples have H_2S/SO_2 ratios greater than one. Samples GVM 41 1925.5 and Rambler have ratios less than one indicating a more oxidizing environment, which could have affected the sulfur speciation.

The calculated $\delta^{34}S$ values plot within a similar range of values for different temperatures (Fig. 30) indicating a similar fluid deposited the molybdenite and pyrite in

the skarn deposits and pyrite, galena, and sphalerite in the carbonate-hosted replacement deposit. However, the calculated δS^{34} fluid values fall outside the magmatic sulfur range. One explanation is that under oxidizing conditions a magmatic fluid could range up to +5‰ (Ohmoto, 1972). Another possibility is the temperatures used to calculate the δS^{34} values were estimated too low. At higher temperatures the fractionation factors between the mineral and calculated fluid values become smaller. Therefore, the $\delta^{34}S$ of the fluid would be closer to the $\delta^{34}S$ measured from the minerals.

The one skarn sample that is not within the range of the remaining skarn samples (GVM 41 1925.5 pyrite, -11.2‰) could be the result of sedimentary pyrite from within the host carbonate rock or the sample may contain more than one type of sulfur species. The fluid inclusion gas analyses for sample GVM 41 1925.5 show there are higher concentrations of SO_2 than H_2S gas. However, the XRD results for sample GVM 41 1925.5 show no presence of sulfate minerals. The gas analyses show that the fluid depositing pyrite from sample GVM 41 1925.5 was becoming oxidized, and resulted in lighter sulfide sulfur isotopic values. The oxidation of H_2S could be the result of mixing of hydrothermal fluids with oxygen-bearing ground water (Ohmoto and Goldhaber, 1997).

A comparison of ratios of N_2/Ar and CO_2/CH_4 (Fig. 39) and N_2/Ar and Ar/He (Fig. 40) of the fluid inclusion gas samples indicates that the majority of the samples fall outside of the magmatic water region, and fall in the regions of shallow meteoric and crustal waters (Norman and Moore, 1997). The definitions of these fields based on the gas ratios are still subject to change since this is a new technique. However, this evidence does suggests that the porphyry, skarn, and carbonate-hosted replacement

deposits contained some amount of meteoric water. The general trend is the porphyry, skarn, and carbonate-hosted replacement deposits samples do not plot within any one field, but overlap in both the meteoric and magmatic water fields (Fig. 39, 40). The breccia pipe and the E109 carbonate-hosted replacement samples plot in the crustal waters field (Fig. 39). This could indicate a high degree of interaction with the carbonate-host rocks in these samples incorporating more CH_4 than in the other samples. The hydrocarbon results indicate a changing water/rock ratio (Fig. 36). The predominate gas for porphyry, skarn, and siliceous veins from the carbonate-hosted replacement samples is CO_2 (Fig. 36). The CO_2-dominated fluid inclusion gas assemblages are typical of porphyry-type deposits (Norman and Sawkins, 1987).

Limestone isotopic alteration

The limestone and calcite isotope results from the Victorio district indicate carbon and oxygen values change simultaneously for both the carbonate-hosted replacement and skarn deposits (Fig. 41). Surface limestone samples (VIC 601 and VIC 612) plot in the range of unaltered limestone; 0 ± 3‰ for carbon and 20 to 30‰ for oxygen (Hoefs, 1997). Samples GVM 21 1581.1 and E109 1973 have been altered by different amounts. This could be the result of two different altering fluids or the same fluid at different temperatures.

Drill hole GVM 21 was sampled at regular intervals in order to determine if the isotopic signature changed with increased alteration. Since carbonate rocks do not demonstrate typical silicate alteration, then another method to determine the pattern of alteration was necessary. Analyzing the isotopic composition of the limestones was used to see if it was possible to determine if a limestone sample had been altered.

The carbon and oxygen isotope values co-vary (Fig. 42), indicating some of the limestones have been altered. The change in the isotopic value correlates to the amount of metal content (Fig. 43 and 44). Samples with high metal concentrations are altered. Oxygen and carbon values decrease from typical limestone values with an increase in the metal concentrations (Fig. 43 and 44). Some samples have altered values and low metals concentrations (Table 11), but this may be due to the method of assaying. The assay results were calculated by adding the assay results for an interval of 100 feet for the corresponding carbonate sample from within that interval. The interval of 100 feet was chosen because the assay data ranged between 10 and 100 foot intervals. This method of calculating the metal concentration may dilute some sample results, however, it was the best means of comparing the metal concentrations that was available. For example, GVM 21 317 has a low concentration of molybdenum, but has altered values for oxygen and carbon. The metal concentration may have been diluted by adding together a large section of core. Another explanation is the way in which the fluid traveled through the host rock during mineralization. The result of waters passing within the region of sample GVM 21 317, but not depositing metals, would cause a high degree of alteration but a low concentration of metals. The limestones could have been altered to dolomite previous to the time of mineralization as well.

Genetic models

There are three possible models to explain the origins of the mineralization in the Victorio mining district. The first is that all three deposits formed at different times from different fluids. The second is the skarns and porphyry deposits are genetically related, but that the carbonate-hosted replacement deposits formed at a different time from

different fluids. The third model is that all three deposits were formed from a single mineralizing event.

Theory I: Not genetically related

It is unlikely that all three deposits are not related to each other. Microprobe evidence indicates garnets from the Victorio Granite and skarn deposits are similar in chemistry (McLemore et al., 2000a). Based on microprobe qualitative analysis and chemical mapping data both low- and high-Mn garnets are present in the Victorio Granite and skarn mineral deposits (McLemore et al., 2000a). Garnets from both the granite and the skarn deposits contain fluorite inclusions suggesting the skarn deposits formed from a high-F fluid (McLemore et al. 2000a). The porphyry molybdenum deposit appears to be spatially linked to the Victorio Granite as observed in the cross sections (Fig. 14b). The porphyry and skarn deposits are very similar in temperature, salinity, pH, oxidation, and sulfidation conditions. It is probable that the porphyry and skarn deposits are genetically related.

Theory II: Carbonate-hosted replacement deposits not related to skarn and porphyry systems

The sulfur isotopes from the sulfide minerals indicate the source of the sulfur for the skarn and carbonate-hosted replacement deposits possibly contained some amount of magmatic fluid (Fig. 30). The sulfur values fall outside the range of magmatic sulfur, however the values probably represent a magmatic fluid interacting with the carbonate host rock. The oxygen isotope data could be interpreted to be a meteoric fluid interacting with either the carbonate host rock or a magmatic fluid (Fig. 27). For the theory that the carbonate-hosted replacement deposits are not related to the porphyry and skarn deposits,

then another source of magmatic fluid other than the Victorio Granite must be identified. No other intrusions have been located in the vicinity of the Victorio mining district, as supported by regional geophysical data (Maciolek, 1989). The source of the magmatic fluid cannot be at a large distance because the amount of rock the fluid would interact with along the flow path would affect the isotopic signature, decrease the temperature, and affect the pH of the fluid. Therefore, a source for the carbonate-hosted replacement mineralizing fluids must be found within a reasonable distance from the deposit itself.

Another possibility is the emplacement of more than one granitic source. The Victorio Granite could represent several different igneous pulses instead of one contiguous granitic body. However, the age dating and whole rock geochemistry supports that the Victorio Granite is one igneous intrusion. The age dates come from four different drill holes located throughout the mining district, GVM 9, 15, A1, and GG1 (Fig.7). All four samples show similar biotite and K-feldspar age spectra with a biotite age approximately 34.9 Ma and a complicated K-feldspar age spectra that yields no specified age (Fig. 19 and 20). The geochemistry of these granite samples cluster together (Fig. 17). The similar chemistry and age results of the granite samples from these four drill holes indicates there is only one granitic intrusion in the Victorio district. These results indicate the Victorio Granite is probably the source for the carbonate-hosted replacement deposits mineralizing fluids.

Theory III: Genetically related deposits

Other workers (McLemore, 1998, McLemore et al, 1999; Friehauf, 1998) have suggested that porphyry systems are related to skarn and carbonate-hosted replacement deposits. Meinert (1987) indicates the skarns at the Groundhog mine in southwestern

New Mexico are related to the manto carbonate-hosted replacement deposits within the Central mining district. Kwak (1994) shows a continuum from skarn deposits to carbonate-hosted replacement deposits (Fig. 3). This model indicates that the addition of meteoric water results in change in deposition style. However, it is likely that dilution by meteoric water alone would not cause the change in mineral deposition, boiling also would have a significant effect on the fluid chemistry.

The fluid inclusion gas data indicate the fluid composition of the porphyry, skarn, and carbonate-hosted replacement deposits overlap between magmatic and meteoric fields (Fig. 39, 40). The sulfur and oxygen isotope data indicate a meteoric fluid mixed with magmatic fluid (Fig. 28, 30). The fluid inclusion gas analysis and carbonate isotope data indicate the fluid interacted with the carbonate host rock (Fig. 36, 42).

The porphyry and skarn fluid inclusion data for the Victorio district are similar in temperature and salinity (Table 7). The carbonate-hosted replacement deposits are lower in salinity but have similar temperatures to the skarn and porphyry systems (Fig. 3). The change in fluid chemistry could be the result of significant amounts of boiling and mixing with shallow meteoric oxidizing fluids.

ECONOMIC POTIENTIAL

The majority of the production for the district came from the carbonate-hosted replacement deposits on Mine Hill. There was speculation by previous authors (Griswold, 1961; Wessel and Maciolek, 1989) that the deposits continued beyond Mine Hill and that there was a possible skarn system at depth. In order to determine the grades and possible extent of any mineral deposits on Mine Hill, additional deeper drilling and new geological investigations of the skarn and carbonate-hosted replacement deposits is recommended. The previous mining activities have exploited the majority of the shallow deposits and further development of the district would have to be accomplished through underground mining. The porphyry molybdenum and skarn deposits have estimated resources of over 50 millions tons of ore at a low grade of approximately 0.2% WO_3 + MoS_2 (Heidrick, 1983). The low grades of the porphyry and skarn deposits are uneconomic for underground mining. Aggregate from the limestone quarry at the Middle Hills and mineral collecting, for minerals such as wolframite, garnet, and beryl (Dunbar and McLemore, 2000), are the most economically favorable resources in the Victorio district in the near future.

CONCLUSIONS

The evidence supports the theory that the three different deposit types in the Victorio district are all related and are the product of the magmatic fluids from the Victorio Granite mixing with meteoric fluids. The similar age results for the Victorio Granite and the skarn alteration minerals and the lack of another igneous intrusion in the district indicate that all three mineral deposits formed from one magmatic source at approximately 34.9 Ma (Table 4). The whole-rock geochemistry of the igneous rocks in the Victorio district is similar to other igneous intrusions of the same age in southwestern New Mexico (Fig. 12, 16). However, there is no direct evidence that the mineralization of the three deposits was one continuous event. It is more likely mineralization took place over an extended period of time with episodic events of brecciation, boiling, fluid mixing, and mineral precipitation.

The simultaneous emplacement of the Victorio Granite and the porphyry-molybdenum deposit resulted in the skarn formation. The skarn deposits formed in at least three stages. The first stage resulted in contact-metasomatic alteration in response to the intrusion of the Victorio Granite and porphyry system (Fig. 18). The second stage involved the deposition of scheelite-molybdenite-quartz ± other minerals (sub-stage 1, Fig. 18) from a weak- to moderately-acidic (Fig. 37), oxidizing fluid. The last stage involved retrograde mineralization resulting in the precipitation of quartz, calcite, sulfides, and other minerals (sub-stage 2, Fig. 18). The last mineralogical event in response to the emplacement of the Victorio Granite was the deposition of the carbonate-hosted replacement deposits involving the precipitation of sulfides with minor gold and

silver minerals (sub-stage 3, Fig. 18) and a high degree of silicification from an oxidizing, moderately acidic, low salinity fluid.

The evidence points to an alteration continuum between the porphyry molybdenum, skarns, and carbonate-hosted lead-zinc replacements deposits within the Victorio mining district. The stable isotope and fluid inclusion gas data point to a magmatic fluid mixing with a meteoric fluid for the skarn and porphyry deposits. Sulfur stable isotopes of minerals from the carbonate-hosted replacement deposits indicate a possible magmatic component to the mineralizing fluid (Fig. 30). The carbon and oxygen values from carbonate and silicate samples from the carbonate-hosted replacement deposits indicate a moderate to high degree of interaction between the mineralizing fluid and the carbonate host rock (Fig. 28, 42).

The mechanisms responsible for the shift in mineralization style between high-temperature porphyry and skarn deposits and lower-temperature carbonate-hosted replacement deposits are most likely boiling and mixing between meteoric and magmatic waters. The evidence from the fluid inclusion and stable isotope data for boiling and fluid mixing in all three mineral deposits. The fluid inclusion gas analysis indicates the porphyry, skarn, and carbonate-hosted replacement deposits were boiling during mineralization (Fig. 33). Boiling and fluid mixing caused a decrease in temperature and salinity, an increase in pH, and an increase in oxidation state of the mineralizing fluids causing the change from high-temperature porphyry and skarn deposits to low-temperature carbonate-hosted replacement deposits.

FURTHER RESEARCH

In the interest of better describing the fluid forming conditions of the three mineral deposits types, a further fluid inclusion study targeting ore minerals should be conducted. A study of the stable isotopic composition of the fluid inclusion should be helpful in determining the source of the mineralizing fluids. Hydrogen stable isotopes from the fluid inclusions and also from hydrous minerals when plotted along with oxygen values can determine the fluid origins more effectively.

Further geochronological dating of the igneous intrusions, the porphyry molybdenum deposit, and the volcanic rocks at the surface would result in a better understanding of the timing of events in the district. Geochronological and geochemical analyses of other intrusions throughout southwestern New Mexico would help to determine if the K-feldspar results of the Victorio Granite are anomalous or part of a trend. Microprobe analysis of the K-feldspars in the granite and skarn alteration to determine the location of the excess argon are needed to explain the age spectra for these samples.

References cited:

Barton, P. B., Jr., 1984, Redox reactions in hydrothermal fluids, *in* Berger, B. R., and Bethke, P. M., ed., Fluid-mineral equilibria in hydrothermal systems: Society of Economic Geologists, Reviews in Economic Geology. 1, p. 99-114.

Blamey, N., and Norman, D. I., 2002, New Interpretations of geothermal fluid inclusion volatiles: Ar/He and N2/Ar ratios - A better indicator of magmatic volatiles, and equilibrium gas geothermometrers (abstr.): Proceedings from the Twenty-seventh Workshop on Geothermal Reservoir Engineering, Stanford University, Stanford, California, January 28-30, 2002.

Brown, P. E., 1989, FLINCOR; a microcomputer progra for the reduction and investigation of fluid-inclusion data: American Mineralogist, v. 74, no. 11-12, pg. 1390-1393.

Brown, P. E., and Lamb, W. M., 1986, Mixing H_2O-CO_2 in fluid inclusions; Geobarometry and Archean gold deposits: Geochemica et Cosmochemica Acta, v. 50, p. 847-852.

Campbell, A., and Robinson-Cook, S., 1987, Infrared fluid inclusion microthemometry on coexisting wolframite and quartz: Economic Geology, v. 82, p. 1640-1645.

Campbell, A. and., Larson, P.B., 1998, Introduction to stable isotope applications in hydrothermal systems: Reviews in Economic Geology, v. 10, p. 173-193.

Cox, D. P., and Singer, D. A., 1986, Mineral deposit models: U.S. Geological Survey, Bulletin 13, 379 p.

Cunningham, C. G., 1978, Pressure gradients and boiling as mechanisms for localizing ore in porphyry systems: Journal of Research of the U. S. Geological Survey, v. 6, no. 6, p. 745-754.

Dale, V. B., and McKinney, W. A., 1959, Tungsten deposits of New Mexico: U. S. Bureau of Mines, Report of Investigation 5517, 72 p.

Deino, A., and Potts, R., 1990, Single-crystal $^{40}Ar/^{39}Ar$ dating of the Olorgesailie Formation, Southern Kenya Rift: Journal of Geophysical Research, v. 95, no. 6, p. 8453 – 8470.

Dunbar, N. W. and McLemore, V. T., 2000, Preliminary mineralogy of the Victorio district, New Mexico, New Mexico Geology, v. 22, no. 1., p.12 – 13.

Drewes, H., 1991, Description and development of the Cordilleran orogenic belt in the southwestern United States, U. S. Geological Survey, Professional Paper 1512, 92p.

Drummond, S. E., and Ohmoto, H., 1985, Chemical evolution and mineral deposition in boiling hydrothermal systems: Economic Geology, v. 80, p. 126-147.

Eby, G. N., 1990, The A-type granitoids: A review of their occurrence and chemical characteristics and speculations on their petrogenesis: Lithos, v. 26, p. 115-134.

Foster, D. A., Harrison, T. M., Copeland, P., and Heizler, M. T., 1990, Effects of excess argon within large diffusion domains on K-feldspar age spectra: Geochemica et Cosmochimica Acta, v. 54, p. 1699-1708.

Friehauf, K. C., 1998, Cu-Au massive replacement ore of the Bingham (UT), Bisbee (AZ) and Superior (AZ) districts, a petrographic comparison of late-stage porphyry-related ores in carbonate rocks, (abstr.): Geological Society of America, 1997 Annual meeting Abstracts with Programs, v. 29, p. 446.

Glig, H. A., 1996, Fluid inclusion and isotope constraints on the genesis of high-temperature carbonate-hosted Pb-Zn-Ag deposits: Society of Economic Geologists, Special Publication no. 4, p. 501-514.
Greenwood, R., 1943, Effect of chemical impurities on scheelite fluorescence: Economic Geology, v. 34, no. 1, p. 56-64.
Griswold, G. B., 1961, Mineral deposits of Luna County, New Mexico: New Mexico Bureau of Mines and Mineral Resources, Bulletin 72, p. 69 - 93.
Griswold, G. B., Boy, R., Olson, R. R., and Zrinscak, P, 1989, Reconnaissance gold geochemical survey of five selected areas in southwestern New Mexico: New Mexico Bureau of Geology and Mineral Resources, Open File Report, OF-357, 19 p.
Guilbert, J. M., and Park C.F., Jr., 1986, The geology of ore deposits: New York, NY, W. H. Freeman and Company, 985 p.
Harrison, T. M., Duncan, I., and McDougall, I., 1985, Diffusion of (super 40) Ar in biotite; temperature, pressure and compositional effects: Geochimica et Cosmochimica Acta, v. 49, no. 11, p. 2461-2468.
Heidrick, T., 1983, Victorio Project Geologic Report: unpublished report for the Gulf Mineral Resources Company, on file at New Mexico Bureau of Mines and Mineral Resources archives, 141 p.
Heizler, M. T., and Harrison, H. T., 1998, Multiple trapped argon isotope components revealed by $^{40}Ar/^{39}Ar$ isochron analysis: Geochemica et Cosmochemica Acta, v. 52, p. 1295-1303.
Hodgson, S. A., 2000, Structural geology and Laramide tectonics of the Little Hatchet Mountains, southwestern New Mexico; *in* Lawton, T. F., McMillian, N., J., and McLemore, V. T. eds., Southwest Passage: New Mexico Geologic Society, Guidebook 51, p. 109-117.
Hoefs, J. H., 1997, Stable isotope geochemistry: London, England, Springer-Verlag, 199 p.
Holser, W. T., 1953, Beryllium minerals in the Victorio Mountains, Luna County, New Mexico: American Mineralogist, v. 38, p. 599-611.
Hsu, L. C., and Galli, P. E., 1973, Origin of the scheelite-powellite series of minerals: Economic Geology, v. 68, p. 681-696.
Ishiyama, D., Fuchino, T., Kaneko, K., Mizuta, T., and Fujikawa, O., 2000, Tungsten mineralization of the Ohkawame molybdenite deposit in Kuji City, Iwate Prefecture, Japan: Journal of Mining College, Akita University, Series A; Mining Geology, v. 8, no. 3, p. 105-127.
Klein, D. P., 1987, Aeromagnetic map of the Silver City 1 degree by 2 degrees quadrangle, New Mexico and Arizona: U.S. Geological Survey, Miscellaneous Investigation Series Map, I-1310, scale: 1:250,000.
Kottlowski, F. E., 1960, Summary of Pennsylvanian sections in southwestern New Mexico and southeastern Arizona: New Mexico Bureau of Mines and Mineral Resources, Bulletin 66, 187 p.
Kottlowski, F. E. , 1963, Paleozoic and Mesozoic stratigraphy of southwestern and south-central New Mexico: New Mexico Bureau of Mines and Mineral Resources, Bulletin 79, 100 p.
Kwak, T., A.P., 1994, Hydrothermal alteration in carbonate-replacement deposits: Ore skarns and distal equivalents, *in* Lentz, D. R., ed., Alteration and alteration

processes associated with ore-forming systems: Geological Association of Canada, Short Course notes, v. 11, p. 381-402.
Lawton, T. F., and Clemons, R. E., 1992, Klondike basin; late Laramide depocenter in southern New Mexico, New Mexico Geology, V. 14, no. 1, p. 1-7.
Lindgren, W., Graton, L. C., and Gordon, C. H., 1910, The ore deposits of New Mexico: U.S. Geological Survey Professional Paper 68, 361 p.
Lu, C., Reed, M, and Mirsa, K. C., 1991, Zinc-lead skarn mineralization at Tin Creek, Alaska: Fluid inclusions and skarn forming reactions: Geochemica et Cosmochemica Acta, v. 56, p. 109-119.
Lucas, S. G., and Lawton, T. F., 2000, Stratigraphy of the Bisbee Group (Jurassic-Cretaceous), Little Hatchet Mountains, New Mexico; *in* Lawton, T. F., McMillian, N., J., and McLemore, V. T. eds., Southwest Passage: New Mexico Geological Society Guidebook 51, p. 175-194.
Lucas, S. G., Estep, J. W., and, Anderson B. G., 2000, Lower Cretaceous stratigraphy and biostratigraphy in the Victorio Mountains, Luna County, New Mexico, *in* Lucas, S. G., ed., New Mexico's fossil record 2: New Mexico Museum of Natural History and Science Bulletin 16, p. 63-72.
Maciolek, J. B. 1989, Interpretation of geophysical data for Victorio Mountains: unpublished mining company report for Santa Fe Mining Company, on file at the New Mexico Bureau of Geology and Mineral Resources, 47 p.
Mack, G. H., and Clemons, R. E., 1988, Structural and stratigraphic evidence for the Laramide (early Tertiary) Burro uplift in southwestern New Mexico; *in* Mack, G. H., Lawton, T. F., and Lucas, S. G., eds. Cretaceous and Laramide Tectonic Evolution of Southwestern New Mexico: New Mexico Geologic Society Guidebook 39, p. 59-66.
McDougall, T., and Harrison, T. M., 1998, Geochronology and Thermalchronology by the $^{40}Ar/^{36}Ar$ method: New York, NY, Oxford University Press, 212 p.
McIntosh, W. C., and Bryan, C., 2000, Chronology and geochemistry of the Boot Heel Volcanic Field, New Mexico; *in* Lawton, T. F., McMillian, N., J., and McLemore, V. T. eds., Southwest Passage: New Mexico Geologic Society, Guidebook 51, p. 157-174.
McLemore, V. T., 1998, Insights into origin of carbonate-hosted Ag and Pb-Zn replacement deposits in the Black Range, Sierra and Grant Counties, New Mexico (abstr): New Mexico Geology, v. 20, no. 2, p. 49.
McLemore, V. T., 2001, Silver and gold in New Mexico: New Mexico Bureau of Geology and Mineral Resources, Resource Map 21, 60 p.
McLemore, V. T., and Lueth V. W., 1996, Lead-Zinc deposits in carbonate rocks in New Mexico: Special Publication, Society of Economic Geologists, no. 4, p. 264-276.
McLemore, V. T., Donahue, K., Breese, M., Jackson, M. L., Arbuckel, J., and Jones, G., 2001, Mineral-resources assessment of Luna County, New Mexico, New Mexico Bureau of Geology and Mineral Resources, Open File Report 459, 153 p.
McLemore, V. T., Dunbar, N., Heizler M. T., Donahue, K., 2000a, Geology and mineral deposits of the Victorio mining district, Luna County, New Mexico-Preliminary observations; *in* Lawton, T. F., McMillian, N., J., and McLemore, V. T. eds., Southwest Passage: New Mexico Geologic Society, Guidebook 51, p. 267-278.
McLemore, V. T., McIntosh, W. C., and Appelt, R., 2000b, Volcanic stratigraphic, geochemistry, and structure of the Steeple Rock district, Grant County, New

Mexico, and Greenlee County, Arizona; *in* Lawton, T. F., McMillian, N., J., and McLemore, V. T. eds., Southwest Passage: New Mexico Geologic Society, Guidebook 51, p. 127-140.

McLemore, V. T., Munroe, E. A., Heizler, M. T., and McKee, C, 1999, Geochemistry of the Copper Flat porphyry and associated deposits in the Hillsboro mining district, Sierra County, New Mexico: Journal of Geochemical Exploration, v. 67, no. 1-3167-189.

Meinert, L. D., 1987, Skarn zonation and fluid evolution in the Groundhog mine, Central mining district, New Mexico: Economic Geology, v. 82, no. 3, p. 523-545.

Muehlberger, W. R., 1980, Texas lineament revisited; *in* Dickerson, P. W., and Hoffer, J. M., eds., Trans-Pecos Region: New Mexico Geological Society, Guidebook 31, p. 113-122.

North, R. M., and McLemore, V. T., 1986, Silver and Gold occurences in New Mexico: New Mexico Bureu of Mines and Mineral Resources, Resource Map 15, scale 1:1,000,000, 32 p.

Norman, D. I., and Moore, J. N., 1997, Gaseous species in fluid inclusions: A tracer of fluids and indicator of fluid processes; *in* Proceedings of the XIVth European current research on fluid inclusions: v. 14, p. 243-244.

Norman, D. I., and Sawkins, F. J., 1987, Analysis of volatiles in fluid inclusions by mass spectrometry: Chemical Geology, v. 61, p. 1 - 10.

Norman, D. I., Blamey, N., and Moore, J. N., 2002, Interpreting geothermal processes and fluid sources from fluid inclusion organic compounds and CO_2/N_2 ratios; *in* Proceedings from the Twenty-seventh Workshop on Geothermal Reservoir Engineering: Stanford University, Stanford, California, January 28-30, 2002, p. 234-242.

Ohmoto, H., 1972, Systematics of sulfur and carbon isotopes in hydrothermal ore deposits: Economic Geology, v. 67, no. 5, p. 551-578.

Ohmoto, H., and Goldhaber, M. B., 1997, Sulfur and carbon isotopes: *in* Barnes, H. L., ed., Geochemistry of hydrothermal ore deposits: New York, John Wiley and sons, p. 517-612.

Pearce, J. A., Harris, N. B., and Tindle, A. G., 1984, Trace element discrimination diagrams for the tectonic interpretation of granitic rocks: Journal of Petrology, v. 24, p. 956-983.

Reed, M., and Spycher, N, 1984, Calculation of pH and mineral equilibrium in hydrothermal waters with application to geothermometry and studies of boiling and dilution: Geochimica et Cosmochimica Acta, v. 48, p. 1479-1492.

Reed, M., and Spycher, N, 1985, Boiling, cooling, and oxidation in epithermal systems: A numerical modeling approach; *in* Berger, B. R., and Bethke, P. M., ed., Geology and Geochemistry of epithermal systems, Society of Economic Geologists, Reviews in Economic Geology, v. 2, p.249-272.

Richards, J. P., and McDougall, I., 1990, Geochronology of the Pogera gold district, Papua New Guinea; resolving the effects of excess argon on K-Ar and $^{40}Ar/^{39}Ar$ age estimates for magmatisim and mineralization: Geochemica et Cosmochemica Acta, v. 54, no. 5, p. 1397-1415.

Roedder, E., 1981, Origin of fluid inclusions and changes that occur after trapping: Mineralogical Association of Canada Short Course Handbook, v. 6, p. 101-137.

Samson, S. D., and Alexander, E. C., Jr., 1987, Calibration of the interlabratory $^{40}Ar/^{39}Ar$ dating standard, MMhb-1: Chemical Geology, v. 66, no. 1-2, p. 27-34.

Steiger, R. H., and Jager, E., 1977, Subcommision on geochronology: Convention on the use of decay constants in geo- and cosmochronology: Earth and Planetary Science Letters, v. 36, p. 359-362.

Taylor, H. P., Jr, 1974, The Application of oxygen and hydrogen isotope studies to problems of hydrothermal alteration and ore deposition: Economic Geology, v. 69, p. 843-883.

Thorman, C. H., and Drews, H., 1980, Geologic map of the Victorio Mountains, New Mexico: U. S. Geological Survey, Misc. Field Map, MF-1175, scale 1:24,000.

Titley, S. R., 1996, Characteristics of high temperature carbonate-hosted replacement ores and some comparisons with Mississippi Valley-type ores: Society of Economic Geologists, Special Publication, no. 4, p. 244-254.

Wessel, G. R., and Maciolek, J., 1989, An evaluation of the Mine Hill area, Victorio Mountains, Luna county, New Mexico: Potential for undiscovered metallic mineralization: unpublished report on file at the New Mexico Bureau of Geology and Mineral Resources archives. 52 p.

Whalen, J. B., Currie, K. L., and Chappell, B. W., 1987, A-type granites; geochemical characteristics, discrimination and petrogenesis: Contributions to Mineralogy and Petrology, v. 95, no. 4, p. 407-419.

White, W. H., Bookstrom, A. A., Kamilli, R. J., Ganster, M. W., Smith, R. P., Ranta, D. E., and Steininger, R. C., 1981, Character and origin of Climax-type molybdenum deposits: Economic Geology, 75th Anniversary Volume, p. 270-316.

Wynn, J. C., 1981, Complete Bouger gravity anomaly map of the Silver City 1 degree by 2 degrees quadrangle, New Mexico-Arizona: U.S. Geological Survey, Miscellaneous Investigation Series Map I-1310-C, scale: 1:250,000.

Young, L. M., 1992, Devonian cave fillings and breccias at the Fusselman Dolomite-Percha Shale contact, Silver City area, New Mexico, Geological Society of America, Abstracts with Programs, v. 24, no. 7, p. 55.

Zheng, Y. F., 1993, Calculation of oxygen isotope fractionation in anhydrous silicate minerals: Geochemica et Cosmochemica Acta, v. 57, no. 5, p. 1079-1091.

Table 1. Classification of carbonate hosted mineral deposits in New Mexico as defined by Cox and Singer (1986), McLemore and Lueth (1996), and McLemore (2001).

NMBGMR Classification	USGS Classification (Model Number)	Commodities Present
Porphyry Cu, Cu-Mo (±Au) (75–50 Ma)	Porphyry copper (17, 20c, 21a)	Cu, Mo, Au, Ag
Laramide Cu and Pb-Zn skarn (75–50 Ma)	Skarn (18a, 18c, 19a)	Au, Ag, Cu, Pb, Zn
Porphyry Mo (±W)	Porphyry Mo-W (16, 21b)	Mo, W, Au, Ag
Mo-W-Be contact-metasomatic deposits	W-Be skarns (14a)	Mo, W, Be, Pb, Zn, Cu
Carbonate-hosted Pb-Zn (Cu, Ag) replacement	Polymetallic replacement (19a)	Pb, Zn, Cu, Ag

Table 2. Location and analyses preformed on each sample. The sample number refers to the drill hole number (GVM 2) followed by the depth of the sample measured from the top of the drill hole (553) in feet. Age= argon geochronology analysis, FI micro = fluid inclusion microthermometry, FI gas = fluid inclusion gas analysis, sulfur = sulfur isotope analysis, oxygen = oxygen isotope analysis, CO2 = carbonate isotope analysis, XRD = x-ray diffraction analysis. Latitude and longitude are reported in decimal degrees.

sample number	type of sample	latitude	longitude	age	FI micro	FI gas	sulfur	oxygen	CO2	XRD
GVM 2 554	skarn	32.1852	108.1053		X		X			
GVM 2 1499	porphyry	32.1852	108.1053		X					
GVM 2 900	skarn	32.1852	108.1053						X	
GVM 7 1823.3	barren qtz	32.1852	108.1001		X			X		
GVM 8 819.8	skarn	32.1828	108.1045						X	
GVM 8 1889	barren qtz	32.1828	108.1045		X	X				
GVM 8 2250	granite	32.1828	108.1045		X			X		
GVM 8 2297	granite	32.1828	108.1045				X			
GVM 9 881.5	skarn	32.1792	108.1002						X	
GVM 9 2056	granite	32.1792	108.1002	X						
GVM 15 2337	granite	32.1852	108.1097		X			X		
GVM 15 2402	granite	32.1852	108.1097	X			X			
GVM 21 65	skarn	32.1845	108.1028						X	
GVM 21 93	skarn	32.1845	108.1028						X	
GVM 21 215.5	skarn	32.1845	108.1028						X	
GVM 21 317	skarn	32.1845	108.1028						X	
GVM 21 439	skarn	32.1845	108.1028						X	
GVM 21 532	skarn	32.1845	108.1028						X	
GVM 21 715	skarn	32.1845	108.1028						X	
GVM 21 867.5	skarn	32.1845	108.1028						X	
GVM 21 960	skarn	32.1845	108.1028						X	
GVM 21 1065	skarn	32.1845	108.1028						X	
GVM 21 1152	skarn	32.1845	108.1028						X	
GVM 21 1168.2	skarn	32.1845	108.1028		X	X	X			
GVM 21 1278	skarn	32.1845	108.1028	X	X		X			X
GVM 21 1297	skarn	32.1845	108.1028		X		X			
GVM 21 1488	skarn	32.1845	108.1028						X	
GVM 21 1490	porphyry	32.1845	108.1028	X			X			
GVM 21 1493.5	porphyry	32.1845	108.1028		X	X				
GVM 21 1518.1	porphyry	32.1845	108.1028						X	
GVM 41 1925.5	skarn	32.1896	108.1069	X	X	X	X		X	X
GVM 41 2073.10	porphyry	32.1896	108.1069		X			X		

Table 2 continued.

sample number	type of sample	latitude	longitude	age	FI micro	FI gas	sulfur	oxygen	CO2	XRD
GVM 59 1702	skarn	32.1848	108.1099	X	X	X	X			X
GVM 65 1902	skarn	32.1880	108.1075		X					
GVM A3 2007	skarn	32.1887	108.1070		X	X	X	X		
VIC 12-99	skarn vein	32.1897	108.1038		X	X				
VIC 67-99	silica vein from Mine Hill	32.1983	108.0926						X	
VIC 69-99	silica vein from Mine Hill	32.1983	108.0926						X	
VIC 149-99	silica vein from Mine Hill	32.1785	108.0921		X					
Vic 601	silica vein from Mine Hill	32.1783	10.0917		X				X	
VIC 603	limestone	32.1753	108.0935						X	
VIC 604	calcite vein	32.1924	108.1020						X	
VIC 605	breccia	32.1924	108.1020		X			X		
VIC 608	limestone	32.1898	108.1076						X	
VIC 611	limestone	32.1879	108.1057						X	
VIC 612	limestone from quarry	32.1889	108.0856						X	
BRECCIA	breccia vuggy qtz	32.1924	108.1020		X					
Rambler	silica vein from Mine Hill	32.1783	108.0917		X	X				
E109 1019	drill core from Mine Hill	32.1766	108.0941						X	
E109 1935	drill core from Mine Hill	32.1766	108.0941		X				X	
E109 1942	drill core from Mine Hill	32.1766	108.0941		X	X	X			
E109 1973	drill core from Mine Hill	32.1766	108.0941						X	

Table 3. Summary of the argon geochronology samples. Depth reported in feet from the top of the drill hole.

Sample number	deposit	latitude	longitude	depth (ft)	mineral	associated sulfides
GVM 15 2402	granite	32.1852	108.1097	2402	K-feldspar	none
GVM 15 2402	granite	32.1852	108.1097	2402	muscovite	none
GVM 15 2402	granite	32.1852	108.1097	2402	biotite	none
GVM 9 2056	granite	32.1792	108.1002	2056	K-feldspar	none
GVM 9 2056	granite	32.1792	108.1002	2056	muscovite	none
GVM 9 2056	granite	32.1792	108.1002	2056	biotite	none
GVM 21 1278	skarn	32.1845	108.1028	1278	K-feldspar	moly w/trace pyrite
GVM 21 1278	skarn	32.1845	108.1028	1278	biotite	moly w/trace pyrite
GVM 21 1490	skarn	32.1845	108.1028	1490	muscovite	moly and pyrite
GVM 41 1925.5	skarn	32.1896	108.1069	1925.5	muscovite	pyrite
GVM 59 1702	skarn	32.1848	32.1848	1702	biotite	molybdenite

Table 4. Summary of the argon geochronology results for the Victorio Granite and skarn deposit. No assigned age = no geologically significant age was obtained from the geochronology results. Results listed in millions of years. References McLemore = McLemore et al., (2000a).

Sample number	mineral	plateau age (Ma)	integrated age (Ma)	MSWD	assigned age	Reference
GG1 2225	K-feldspar		76.73 ± 0.36		no assigned age	McLemore
GG1 2225	biotite	35.09±0.08	35.31 ± 0.21		35.09±0.08	McLemore
GVM A1 2741	K-feldspar		44.19 ± 0.21		no assigned age	McLemore
GVM A1 2741	biotite	35.27±0.41	35.52 ± 0.12		35.27±0.41	McLemore
GVM 15 2402	K-feldspar		70.31 ± 0.22	none	no assigned age	this study
GVM 15 2402	biotite	33.84±0.12	33.99 ± 0.17	3.7 **	33.84±0.12	this study
GVM 15 2402	muscovite	34.67±0.07	34.83 ± 0.16	1.5	34.67±0.07	this study
GVM 9 2056	K-feldspar		55.2 ± 0.40	none	no assigned age	this study
GVM 9 2056	biotite	35.24±0.09	36.81 ± 0.29	2.5**	35.24±0.09	this study
GVM 9 2056	muscovite	34.99 ± 0.09	35.5±0.16	3.0	34.99 ± 0.09	this study
GVM 21 1278	K-feldspar	53.2 ± 3.4	74.79 ± 0.16	none	no assigned age	this study
GVM 21 1278	biotite	35.8 ± 0.19	36.69 ± 0.26	0.6**	35.8±0.19	this study
GVM 21 1490	muscovite	34.83 ± 0.20	35.07 ± 0.22	3.1	34.83±0.20	this study
GVM 41 1925.5	muscovite	34.91 ± 0.17	34.98 ± 0.20	4.2**	34.91±0.17	this study
GVM 59 1702	biotite	35.57 ± 0.10	35.68 ± 0.19	0.8	35.57±0.10	this study

Sample preparation and irradiation:

The mineral separates were prepared using standard handpicking techniques.

The separates were loaded into a machined Al disc and irradiated for 24 hours at the University of Michigan Neutron flux monitor Fish Canyon Tuff sanidine (FC-1). Assigned age = 27.84 Ma (Deino and Potts, 1990) equivalent to Mmhb-1 at 520.4 Ma (Samson and Alexander, 1987).

Instrumentation:

Mass Analyzer Products 215-50 mass spectrometer on line with automated all-metal extraction system.

Samples were step-heated with a Mo double-vacuum resistance furnace. Heating duration 8 minutes

Reactive gases removed by a 6 minute reaction with 2 SAES GP-50 getters, 1 operated at ~450°C and 1 at 20°C. Gas also exposed to a W filament operated at ~2000°C and a cold finger operated at -140°C.

Analytical parameters:

Electron multiplier sensitivity averaged 5.48 $x10^{-16}$ moles/pA.

Total system blank and background averaged:

40Ar = 4.32 x 10-15 mol 38Ar = 8.64 x 10-18 mol

39Ar = 1.728 x 10-17 mol 37Ar = 8.64 x 10-18 mol

36Ar = 2.16 x 10-17 mol

J-factors determined to a precision of ± 0.1% by CO_2 laser-fusion of 4 single crystals from each of 6 radial positions around the irradiation tray.

Correction factors for interfering nuclear reactions were determined using K-glass and CaF_2 and are as follows:

$(^{39}Ar/^{37}Ar)_{Ca}$ = 0.00078±0.00003, $(^{36}Ar/^{37}Ar)_{Ca}$ = 0.00028±0.00001, $(^{40}Ar/^{39}Ar)_{K}$ = 0.0266±0.0021

Age calculations:

Total gas age and error calculated by weighting individual steps by the fraction of ^{39}Ar released.

Plateau age or preferred age calculated for the indicated steps by weighting each step by the inverse of the variance.

MSWD values are calculated for n-1 degrees of freedom for plateau age. ** MSWD outside 95% confidence interval

Decay constants and isotopic abundances after Steiger and Jäger (1977).

All final errors reported at ±2σ, unless otherwise noted.

Table 5. Comparison of Climax-type and porphyry-Mo deposits. The Victorio deposit is classified as a porphyry Mo deposit under this classification scheme. Data taken from Cox and Singer (1986)*, Guilbert and Park (1986)+ and White et al. (1981)‡.

	Climax-type	Porphyry Mo deposit
Rock type	Granite-rhyolite*	Tonalite, granodiorite, and monzonite
Host rock geochemistry	High-silica, porphyritic granitic, alkaline intrusions+	typically calc-alkaline, porphyritic intrusions+
Texture	Porphyry, aplitic groundmass‡	Porphyry, fine aplitic groundmass‡
Age range	Mid-Tertiary‡	Mesozoic to Tertiary‡
Depositional environment	Multi-stage hypabayssal intrusions*	Orogenic belt, calc-alkaline intrusive rocks*
Tectonic setting	Extensional craton, related to subduction	Numerous faults‡
Associated deposits	Ag-based veins, fluorspar, rhyolite-hosted Sn deposits‡	Porphyry-Cu, Cu skarns, volcanic hosted- Cu-As-Sb deposits‡
Mineralogy	Molybdenite + fluorite ± K-feldspar ± pyrite ± wolframite ± cassiterite ± topaz*	Molybdenite + pyrite ± scheelite ± chaclopyrite ± argentian tetrahedrite*
Alteration	Intense quartz and quartz + K-feldspar related to subduction*	Potassic outward to propylitic, phyllic, and argillic overprint*
Ore controls	Stockwork ore zone over small stocks, multiphase intrusions and mineralization‡	Stockwork in felsic porphyry and in surrounding country rock‡
Geochemical signature	Mo, Sn, W, and Rb anomalies above ore zone Pb, Z, F, U anomalies in wall rock*	Zoning outward and upward from Mo + Cu + W to Zn + Pb, + Au + Ag*
Average ore grade	0.3 - 0.5% MoS_2 Cu: Mo ratio 1:100 to 1:50‡	0.1 - 0.2 MoS_2 Cu:Mo ratio 1:30 to 1:1‡

Table 6. Comparison of carbonate-hosted replacement deposits and Mississippi Valley-type deposits. Information was taken from Guilbert and Park (1986) †, Glig (1996)‡, Titley (1996)*, Cox and Singer (1986) [#], McLemore (2001)¥, and North and McLemore (1986).

	Carbonate-hosted Pb-Zn replacement	Mississippi-Valley type
Rock type	dolostone, dolomitized limestone*	dolostone, dolomitized limestone*
Texture	fine- to coarse-grained open-space fillings	fine- to coarse-grained open-space fillings
Depositional environment	possibly related to intrusions†	result of connate-water circulation†
Tectonic setting	no constraint, possible association with intrusions†	basin margins, stable craton†
Associated intrusions	distal to intermediate to felsic intrusion‡	not associated with igneous activity*
Mineralogy	galena, sphalerite, pyrite, chalcopyrite*	galena, sphalerite, barite, fluorite*
Alteration	silicification, carbonate recrystalization*	silicification, pyritization, dolomitization*
Temperature	250°C to 400°C average 300°C‡	50 to 225°C average 120°C‡
Salinity	2 to 60 wt% NaCl‡	15 to 30 wt% NaCl‡
Ore Controls	structure and/or lithology‡	structure and/or lithology‡
Overall Average grade	4.3% Cu, 5.1% Pb, 3.9% Zn, <193g/ton Ag[#]	4% Zn, 1.2% Pb, 4.7 g/ton Ag[#]
Average size	1.8 million tones[#]	35 million tones[#]
New Mexico Average grade	5 -30% Pb +Zn, variable Ag, Au rare¥	very few deposits in New Mexico¥

Table 7. Summary of all fluid inclusion results. Figure below illustrates the classification used to identify the fluid inclusion type.

Fluid inclusion results for the Victorio district

Deposit	Type	Size Range	Th range	Th ave	Salinity range	Salinity ave
Carbonate-hosted replacement	Ia, IIa, IIb, IIc	<2 – 15μ	109 - 350	213	0.8 - 19.3	8.8
Mine Hill siliceous veins	Ia, IIa, IIb, IIc	<2 – 10μ	109 - 350	217	0.8 - 4.1	2.1
E109 non-oxidized	Ia	<2 – 5μ	151 - 257	209	10.2 - 19.3	12.9
Skarn	Ia, Ib, IIa, IIb, III	<2 – 40μ	171 - 360	242	0.02 - 25.6	6.6
Barren qtz veins	Ia, Ib, IIa, IIb	<2 – 40μ	199 - 340	278	3.1 – 10.9	5.9
Porphyry	Ia, Ib, IIa, IIb	<2 – 10μ	179 - 325	255	2.0 - 11.2	6.1

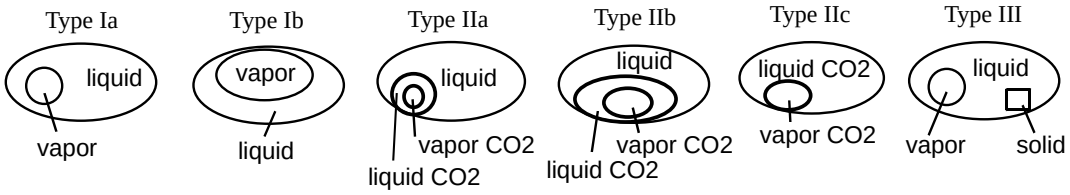

Table 8. Carbon and oxygen values from carbonate rocks. Results are listed in per mil. 13C = carbon value, 18O corr = oxygen value corrected for acid fractionation. CALC = calcite, LIME = limestone samples. Errors calculated from duplicate samples for the carbonate samples is approximately 1.2‰ for carbon and 1.0‰ for oxygen.

Sample/ Deposit type	13C	18O corr
carb-hosted limestone		
carb-hosted calcite		
VIC 67-99 CALC	-9.1	21.2
VIC 69-99 CALC	-5.8	18.9
E109 1935 CALC	-2.0	15.3
E109 1019 CALC	-2.4	22.1
E109-1973 CALC	-5.4	14.4
E109 1973 LIME	-5.2	14.7
E109 1935 LIME	-1.3	22.1
E109 1973 LIME	-4.7	15.4
E109 1019 LIME	-1.6	23.5
skarn limestone		
skarn calcite		
GVM 41 1925.5 CALC	-2.2	17.5
GVM 9 881.5 CALC	-4.9	20.8
GVM8 819.8 CALC	-5.0	11.3
GVM2 900B CALC	-4.6	20.5
GVM 9 881.5 LIME	-2.0	20.4
GVM 21 drill hole skarn deposit		
GVM 21 1581.1 LIME	-3.6	9.3
GVM 21 1518 LIME	-4.0	11.4
GVM 21 960 LIME	-2.9	15.4
GVM 21 1152 LIME	-5.4	8.3
GVM 21 715 LIME	-5.1	8.5
GVM 21 317 LIME	-4.1	9.8
GVM 21 532 LIME	-2.4	16.8
GVM 21 867.5 LIME	-1.3	20.8
GVM 21 439 LIME	-3.2	11.6
GVM 21 1065 LIME	-5.5	7.8
GVM 21 1488 LIME	-6.5	7.2
GVM 21 65 LIME	-1.6	18.1
GVM 21 215.5 LIME	-2.8	15.8
GVM 21 93 LIME	-3.6	13.6
surface limestone		
surface calcite		
VIC 601 LIME	-0.6	23.4
VIC 612 LIME	-0.6	21.3
VIC 611 LIME	-1.8	19.5
VIC 603 LIME	-1.0	25.6
VIC 604 CALC	-5.3	11.2
VIC 608 CALC	-5.7	15.1

Table 9. Oxygen isotopes from silicate samples. Results are listed in per mil. Th = average homogenization temperature used in water calculation, 18O is measured oxygen value, MIN-H_2O = fractionation between mineral and calculated water, H_2O = calculated water value, qtz = quartz. Errors calculated from duplicate samples were approximately 0.4‰ for oxygen.

sample	deposit type	18O	Th	MIN-H_2O	H_20
GVM 7 1823.3 qtz	skarn barren qtz	8.6	250	9.0	-0.4
GVM 8 1889 qtz	skarn barren qtz	10.6	320	6.4	4.2
GVM 21 1490 qtz	skarn	11.8	250	9.0	2.9
GVM 59 1702 qtz	skarn	8.9	225	10.2	-1.3
GVM A3 2007 qtz	skarn	8.0	250	9.0	-1.0
GVM 41 2037.1 qtz	skarn	8.6	275	7.9	0.7
GVM 41 1925.5 qtz	skarn	10.1	290	7.4	2.7
GVM 21 1297qtz	skarn	9.1	230	9.9	-0.8
VIC 12-99 qtz	skarn	10.4	250	9.0	1.4
GVM 2 1499 qtz	porph	10.6	300	7.0	3.6
GVM 21 1493.5 qtz	porph	9.7	250	9.0	0.7
GVM 8 2250 qtz	granite	8.0	300	7.0	1.0
GVM 15 2337 qtz	granite	7.7	300	7.0	0.7
VIC 149-99 qtz	carb-hosted replc	15.4	225	10.2	5.3
RAMBLER qtz	carb-hosted replc	17.8	150	15.5	2.3
VIC 149-99 qtz	carb-hosted replc	16.8	225	10.2	6.6
BRECCIA qtz	breccia	13.2	150	15.5	-2.3
vic 605 qtz	breccia	11.8	200	11.6	0.2

Table 10. Sulfur isotope results from sulfide minerals. Results listed in per mil. Th = average fluid inclusion temperature used to calculate water values in Celsius and Kelvin, delta-H_2S = fractionation value for each mineral and the calculated fluid, H_2S = the calculated fluid value, PY = pyrite, MO = molybdenite, GA = galena, SPH = sphalerite. Errors calculated from duplicate samples were within 0.1‰.

Sample	delta 34S	Th	Th Kelvin	delta-H_2S	H_2S
GVM 2 554 PY	2.9	181	454	1.9	1.0
GVM 8 2297 PY	5.0	240	513	1.5	3.5
GVM 21 1168.2 PY	4.2	193	466	1.8	2.4
GVM 21 1278 PY	6.3	281	554	1.3	5.0
GVM 21 1297 PY	5.0	200	473	1.8	3.2
GVM 21 1490 PY	5.0	280	553	1.3	3.7
GVM 41 1925.5 PY	-11.2	287	560	1.3	-12.5
GVM A3 2007 PY	5.4	190	463	1.8	3.5
E109 1942 PY	4.8	195	468	1.8	3.0
GVM 8 2297 MO	5.1	240	513	1.7	3.4
GVM 15 2402 MO	5.1	250	523	1.6	3.5
GVM 21 1278 MO	4.7	281	554	1.5	3.2
GVM 21 1297 MO	5.9	200	473	2.0	3.9
GVM 41 1925.5 MO	5.2	287	560	1.4	3.8
GVM 59 1702 MO	4.6	225	498	1.8	2.8
GVM 65 1902.5 MO	6.8	250	523	1.6	5.2
GVM A3 2007 MO	5.4	190	463	2.1	3.3
E109 1942 GA	4.0	195	468	-2.9	6.9
E109 1942 SPH	4.5	195	468	0.4	4.0

Table 11. Assay data from the drill core of GVM 21. Interval = the interval of core used to calculate the total Mo and Wo concentrations, feet = total footage used in calculating the metal concentrations, Mo = concentration of molybdenum in ppm, Wo = concentration of tungsten in ppm. The metal concentrations were calculated by adding the metal assay values over the entire core interval of 100 feet for the corresponding carbonate sample from within that interval.

Sample number	interval	feet	Mo (ppm)	Wo (ppm)
GVM 65	58-100	42	1	120
GVM 93	58-100	42	1	120
GVM 215.5	200-300	100	70	530
GVM 317	300-400	100	156	1100
GVM 439	400-500	100	111	305
GVM 532	500-600	100	324	3680
GVM 715	700-800	100	5141	8306
GVM 867.5	800-900	100	298	356
GVM 960	900-1000	100	378	445
GVM 1065	1000-1100	100	924	280
GVM 1152	1100-1200	100	2645	6420
GVM 1488	1400-1500	100	3577	5670
GVM 1518	1500-1600	100	4846	7120

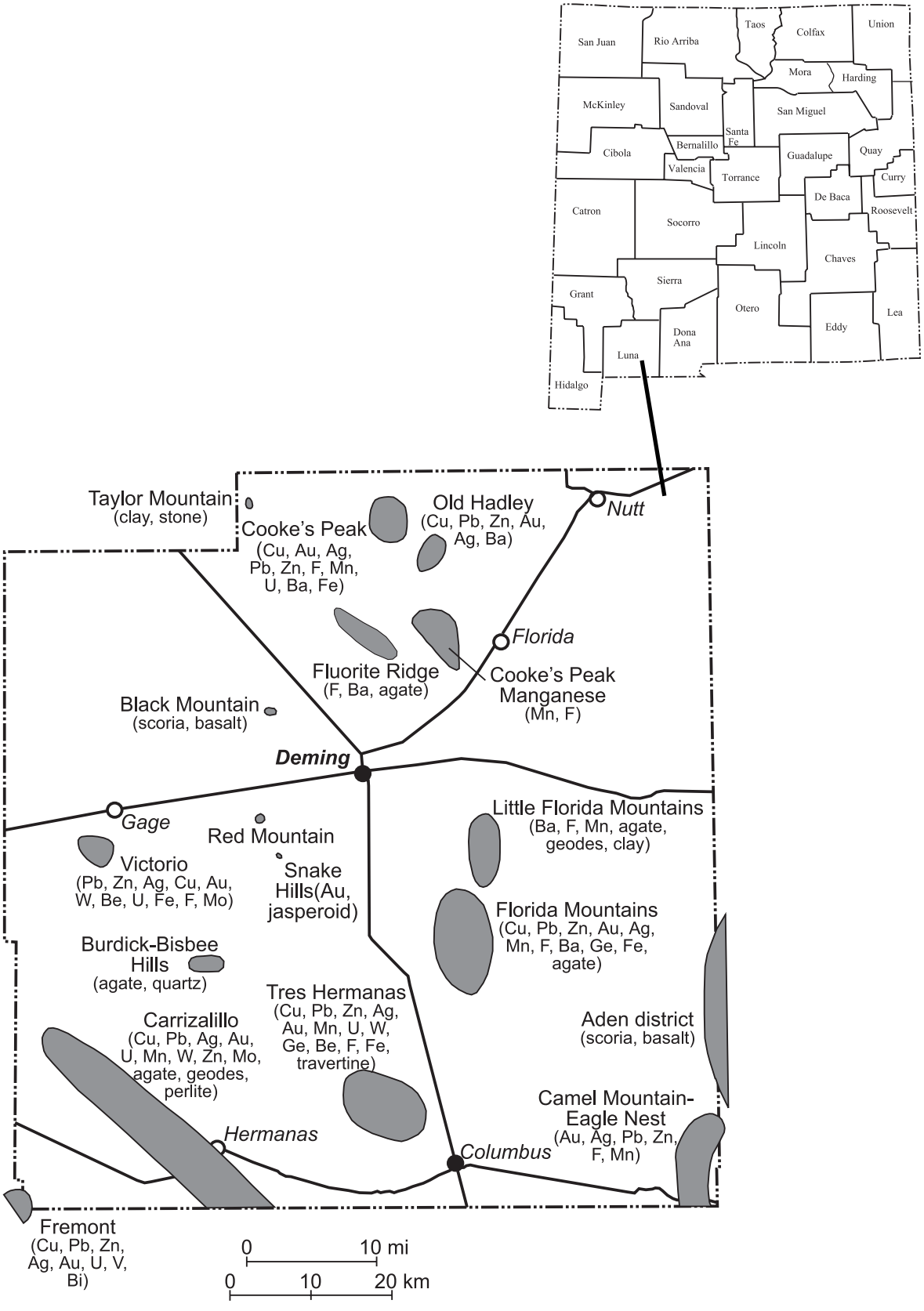

Figure 1. Map showing the location of the Victorio and other mining districts and the commodities present for Luna County, New Mexico (modified from McLemore et al., 2001).

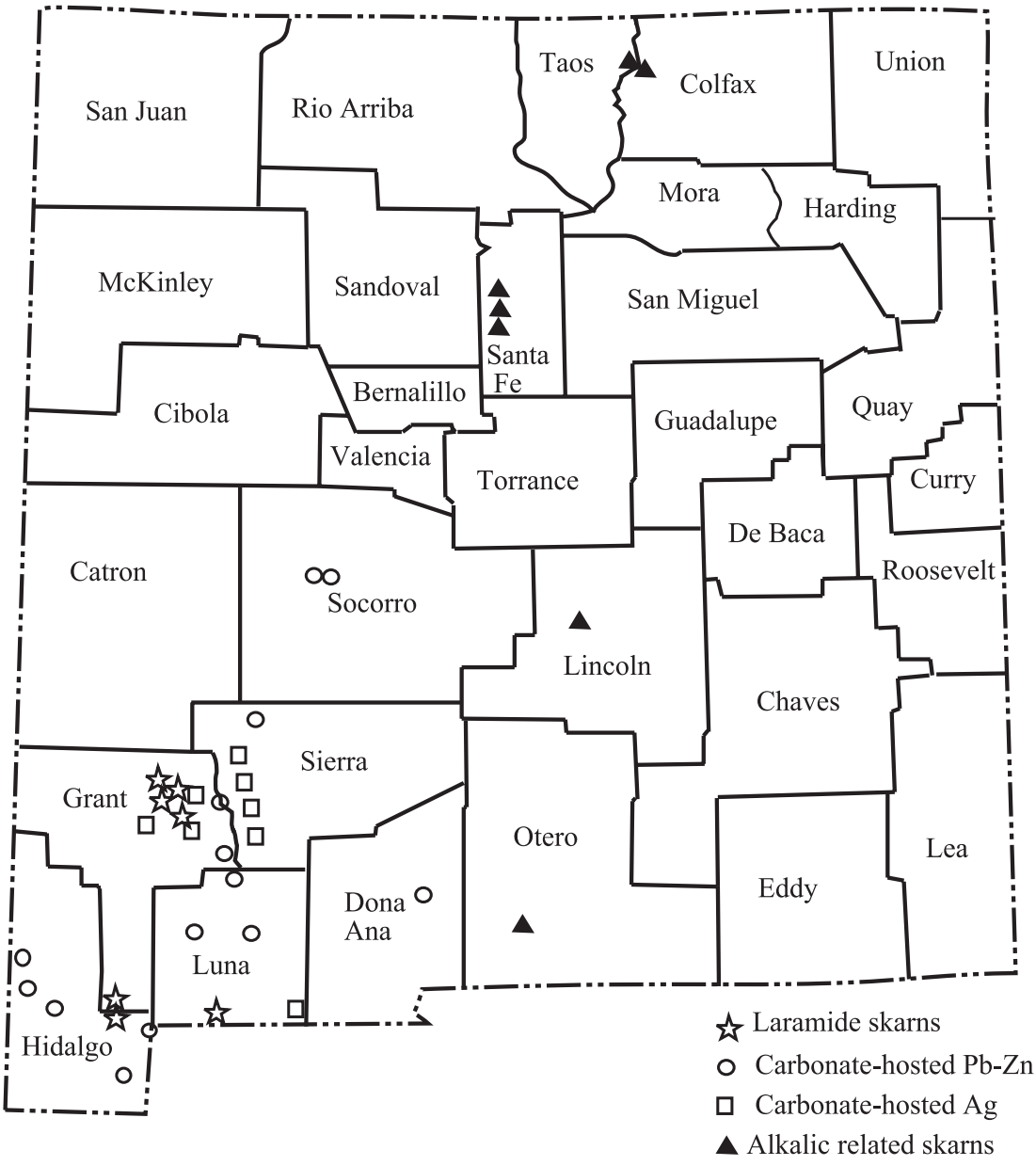

Figure 2. Map showing the lead-zinc carbonate-hosted deposits for New Mexico (modified from McLemore and Lueth, 1996). A correlation between porphyry and carbonate-hosted replacement deposits could prove to be a useful tool for porphyry exploration throughout New Mexico.

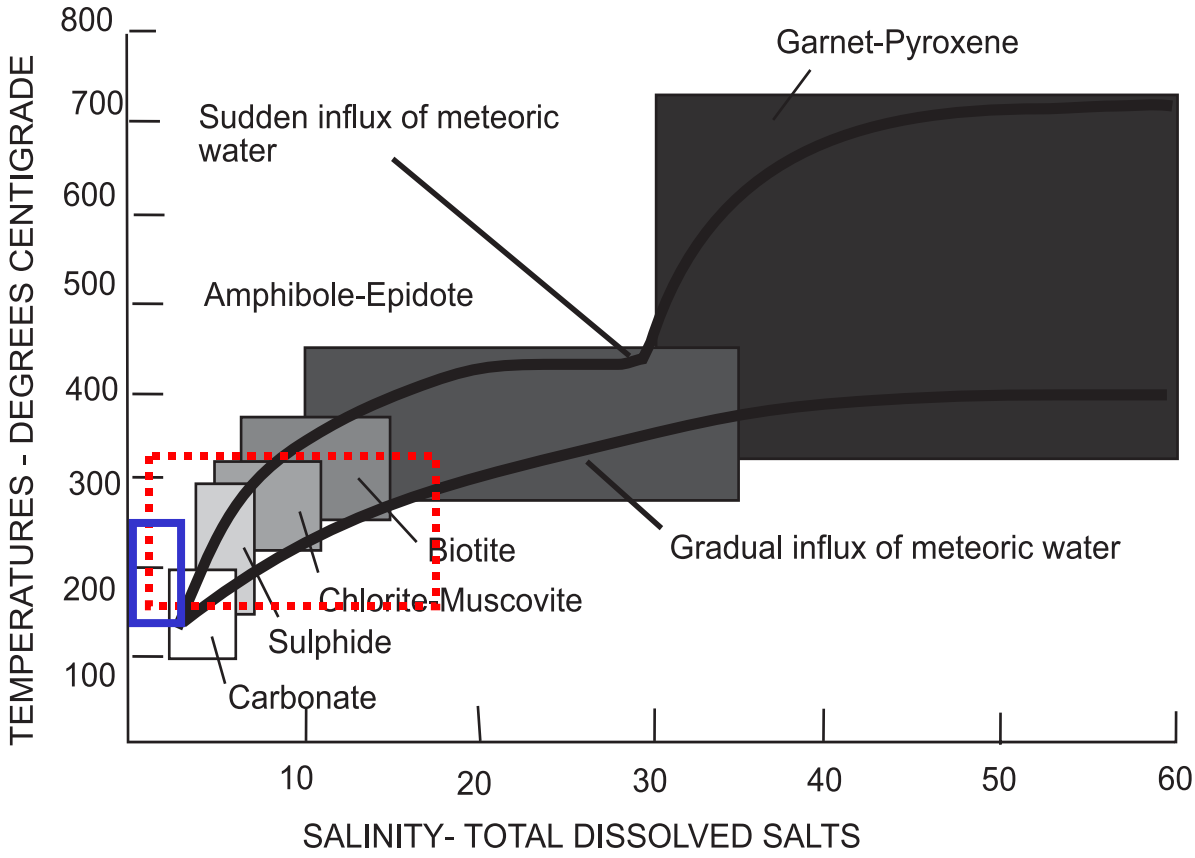

Figure 3. Model showing an alteration continuum between carbonate-hosted replacement and skarn deposits (Kwak, 1994). The dashed box represents the Victorio skarn primary fluid inclusion results and the solid box represents the carbonate-hosted replacement primary fluid inclusion results. Fluid inclusion results are summarized in Table 7 and reported in Appendix B.

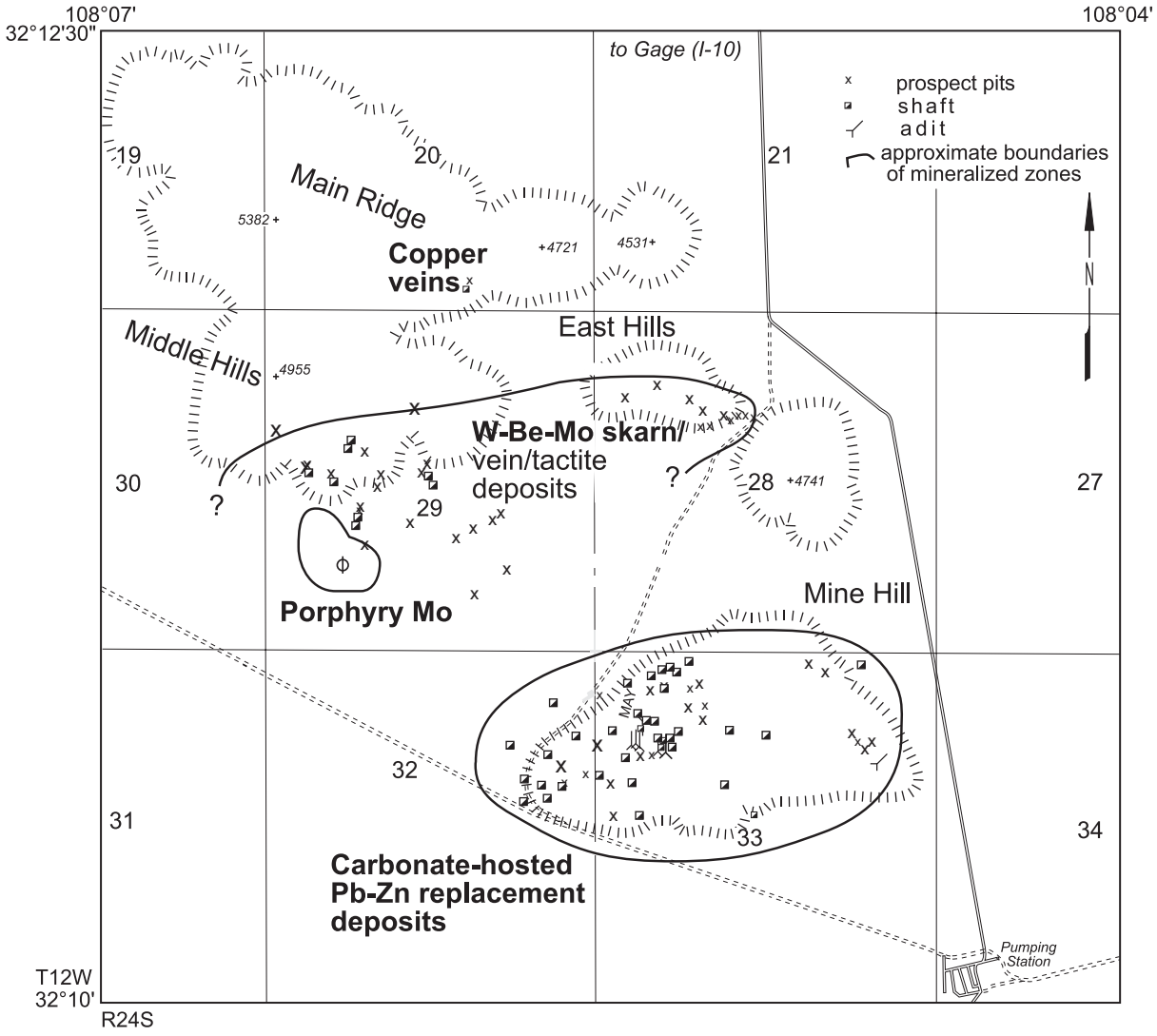

Figure 4. Map showing location and alteration zoning of the Victorio mining district mineral deposits (modified from McLemore et al, 2000a). Zoning of the Victorio district from the central core outward consists of porphyry-Mo, skarn vein, and carbonate-hosted replacement deposits.

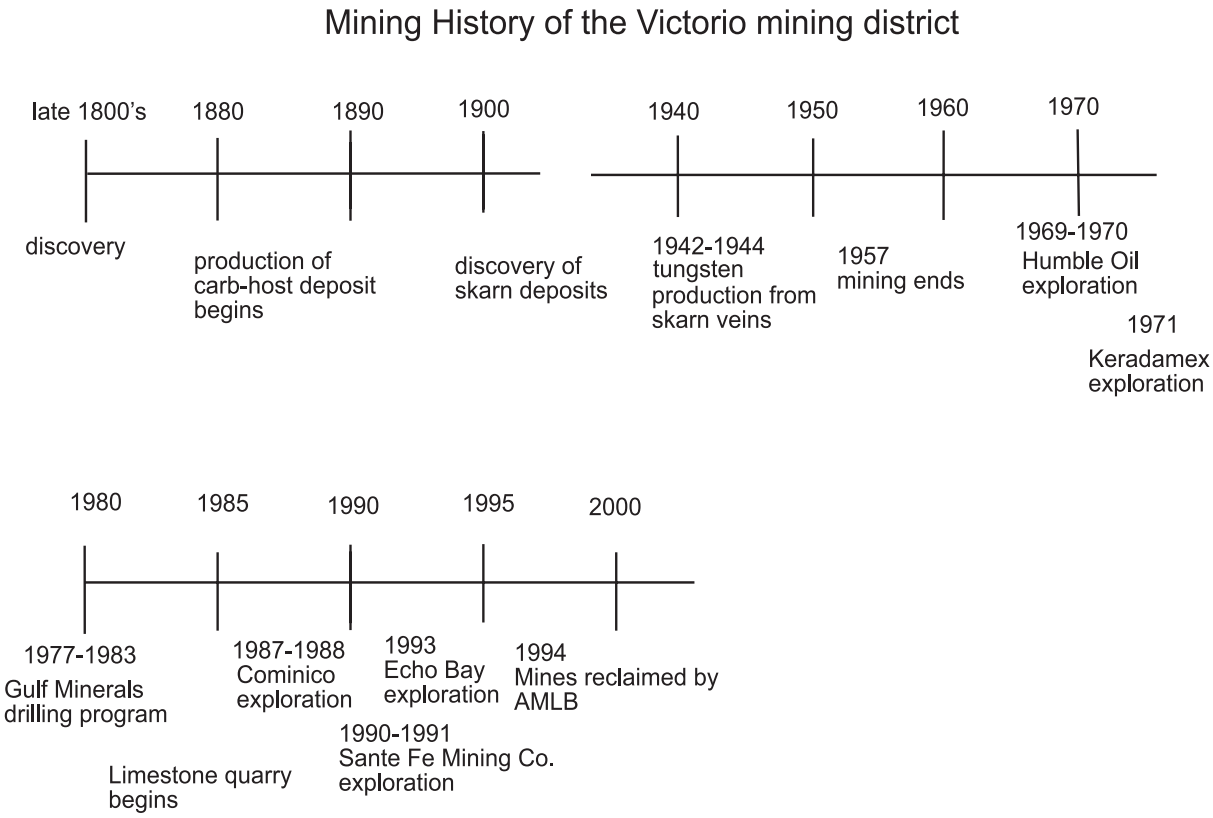

Figure 5 . A time line of significant events in the Victorio mining district history showing the deposits and exploration by various mining companies.

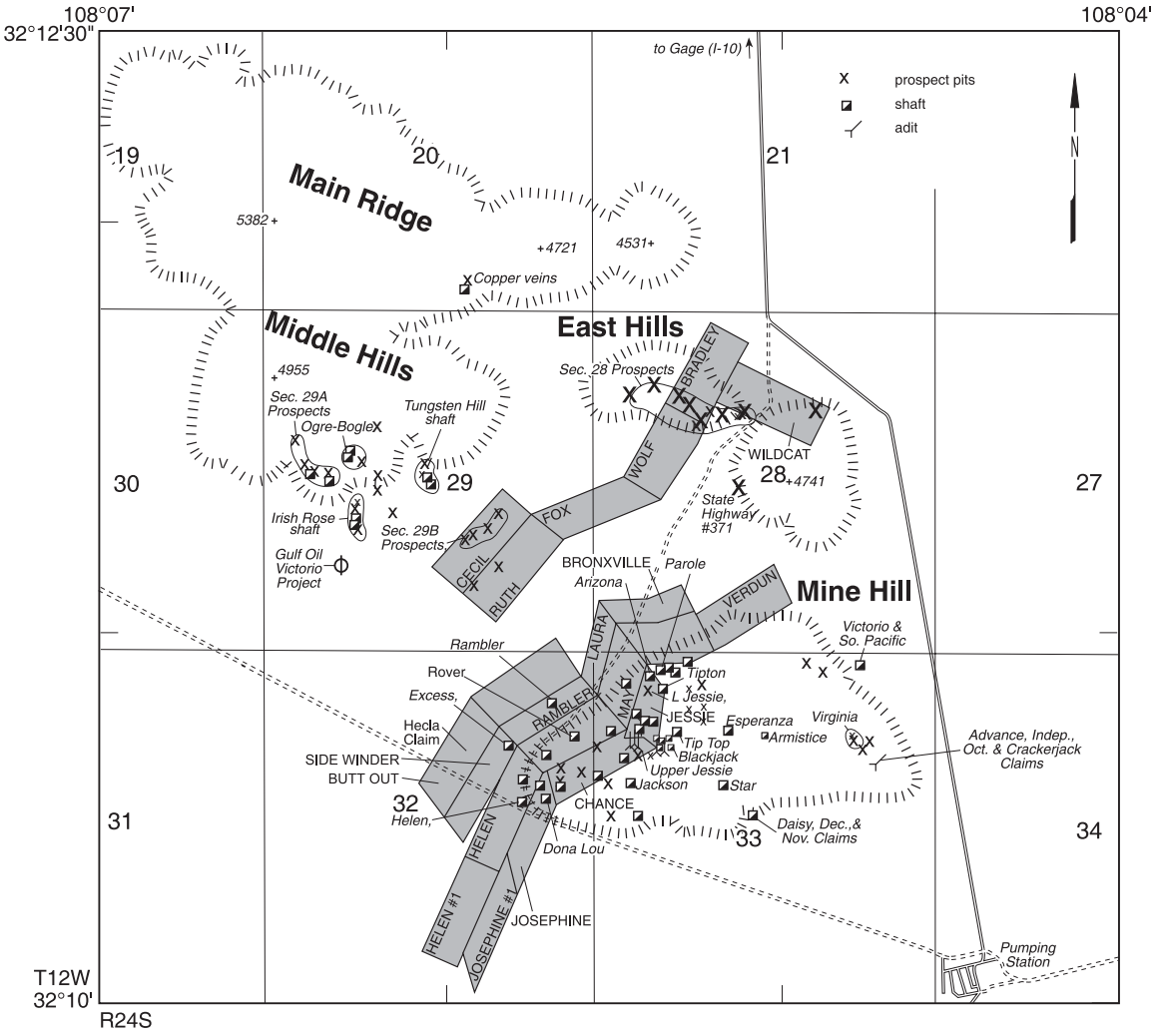

Figure 6. Map showing location of mines and claims locations in the Victorio mining district (modified from McLemore et al., 2000a). The shaded areas represent mining claims. The majority of the mines and claims are found on Mine Hill exploiting the carbonate-hosted replacement deposits.

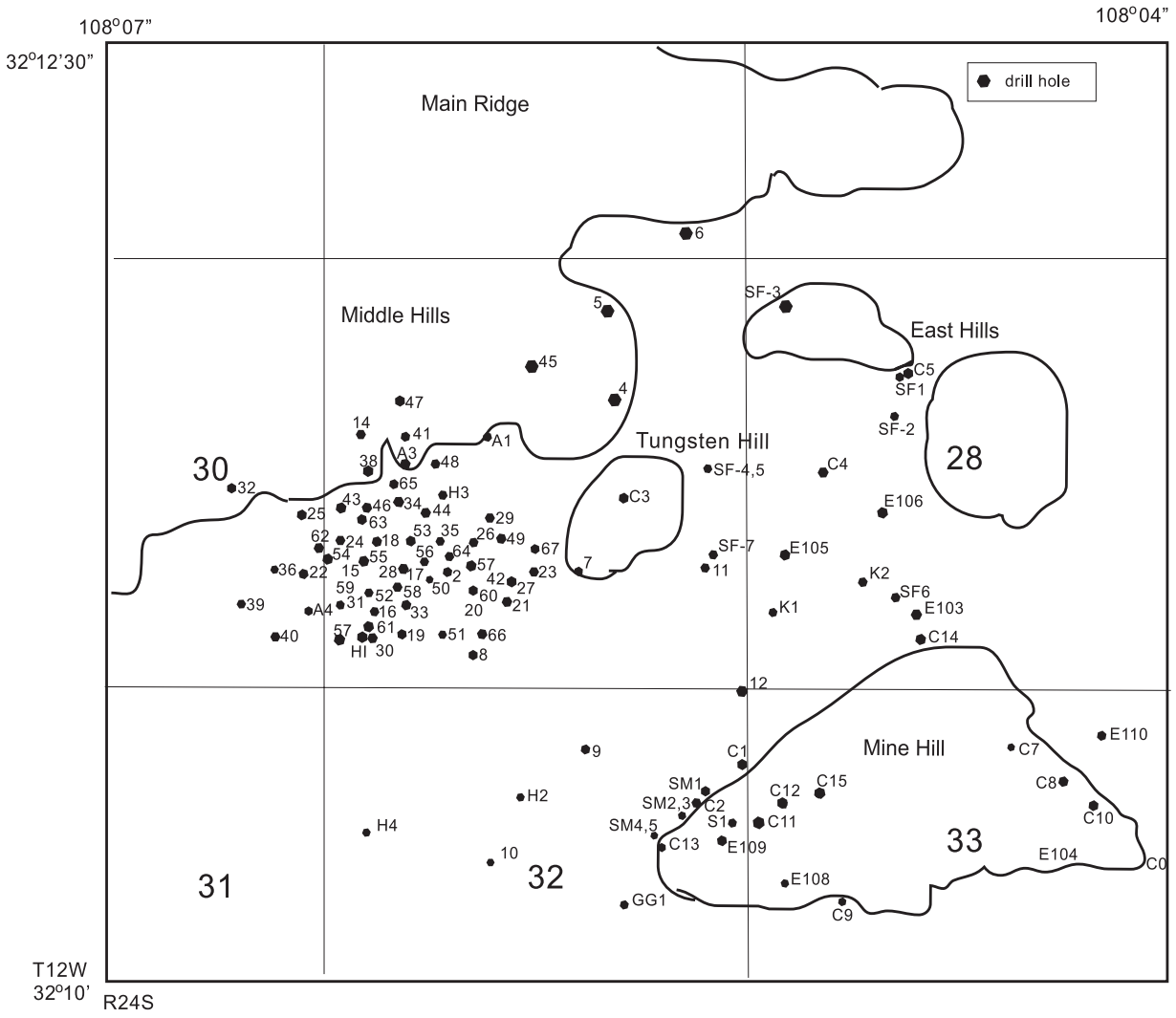

Figure 7. Location of drill holes in the Victorio mining district. C = Cominco American Resources., SF and SM = Sante Fe Mining Co., E = Eco Bay Mining Co., H = Humble Oil, K = Keradamex, numbered drill holes without a prefix = Gulf Mineral Resources Company

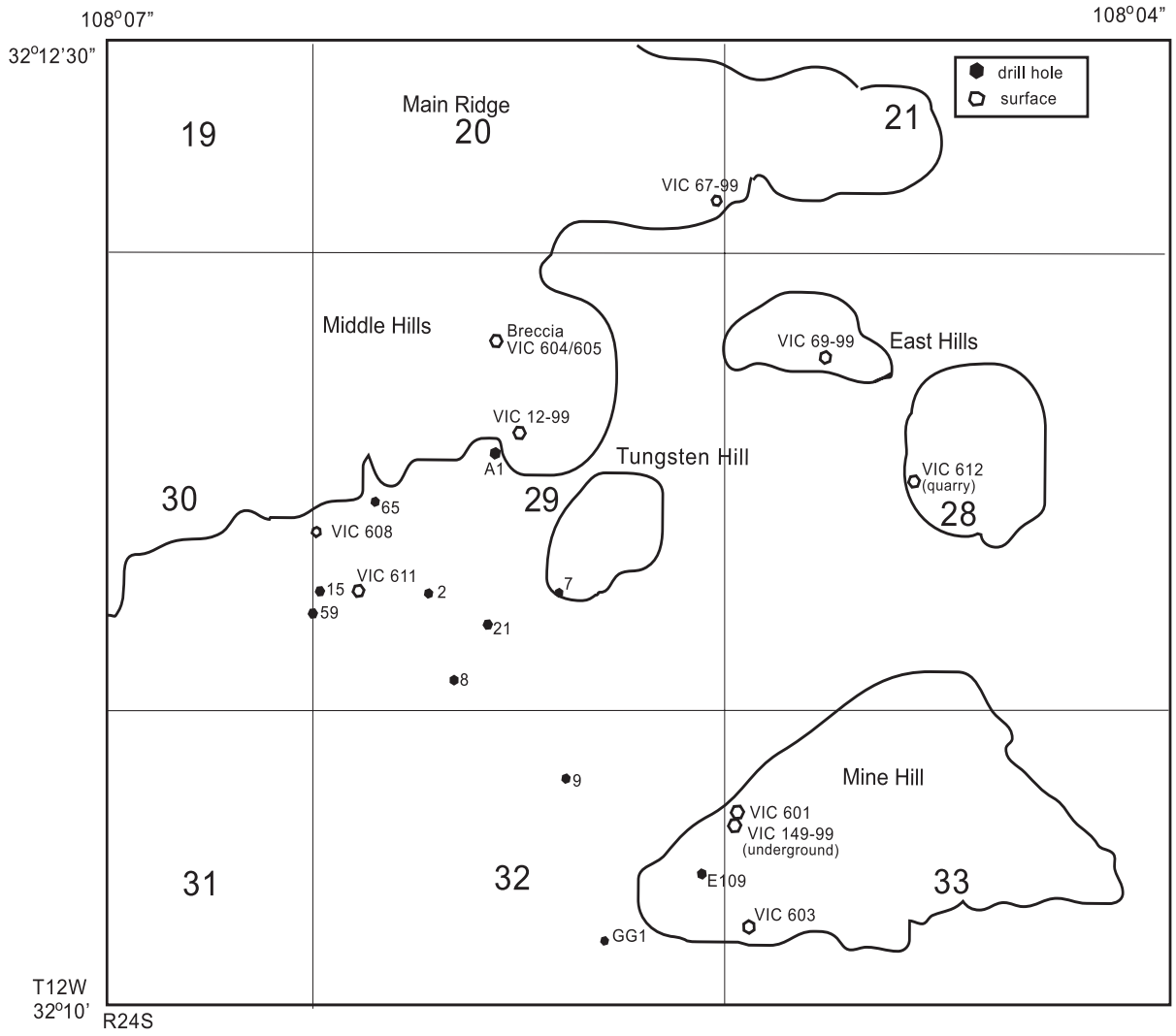

Figure 8. Location of samples listed in Table 2. Open circles indicate surface samples, closed circles indicate drill core samples.

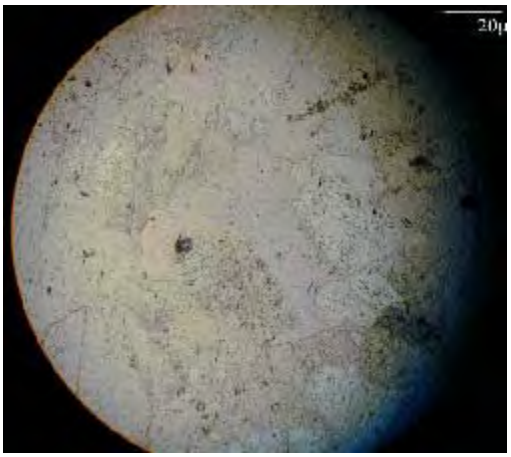

a. GVM 15 2402 in plain light

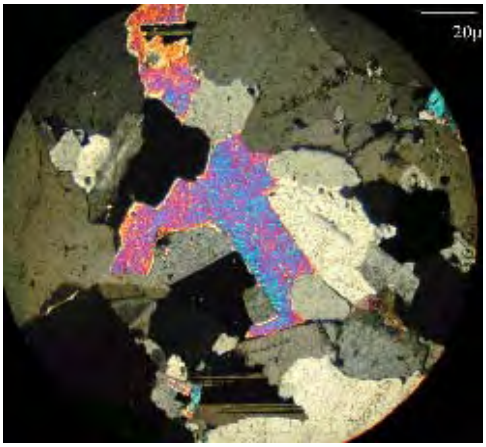

b. GVM 5 2402 in polarized light

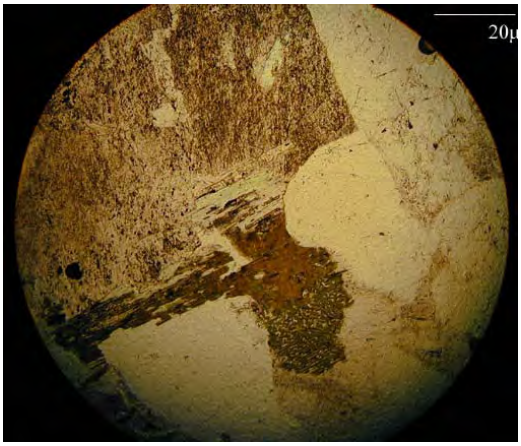

c. GG1 2225 in plain light

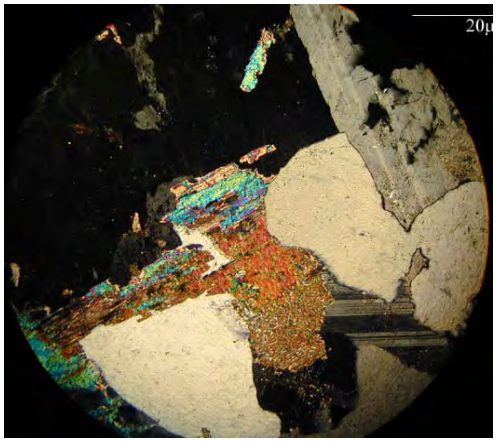

d. GG1 2225 in polarized light

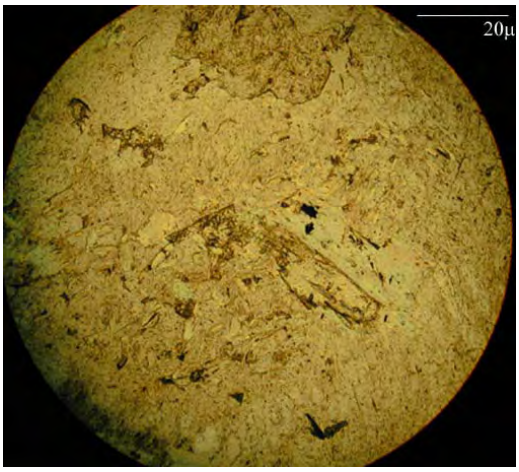

e. GVM 61 1876 in plain light

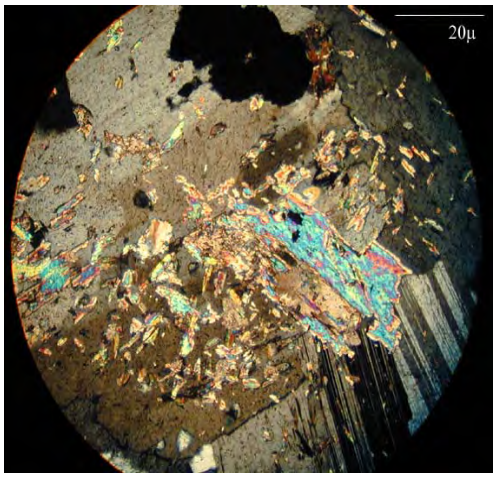

f. GVM 61 1876 in polarized light

Figure 9. Photomicrograph showing the mica mineralization in the Victorio Granite samples; a, b.) photomicrograph from sample GVM 15 2402 showing coarse-grained muscovite. c, d.) photomicrograph from sample GG1 2225 showing the alteration of a coarse-grained biotite mineral, e, f.) photomicrograph showing the muscovite alteration in the granite samples. Alteration muscovites are significantly smaller than igneous muscovites and biotites. Micas have been altered to sericite, chlorite, and muscovite.

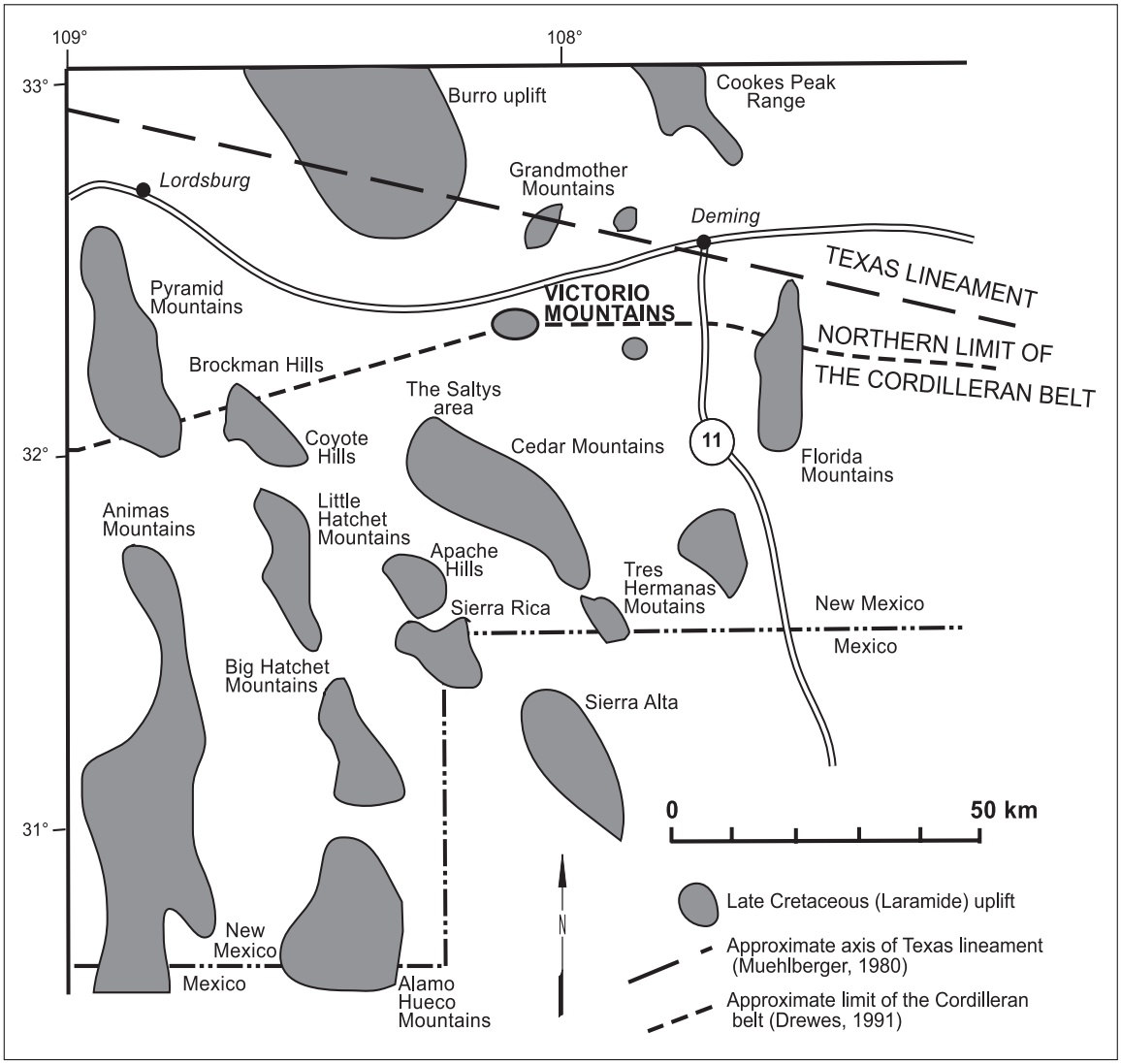

Figure 10. Map of southwestern New Mexico showing the regional structural elements (modified from McLemore et al., 2000a). The Victorio mining district has been effected by several geologic events that resulted in the characteristic Basin and Range structures.

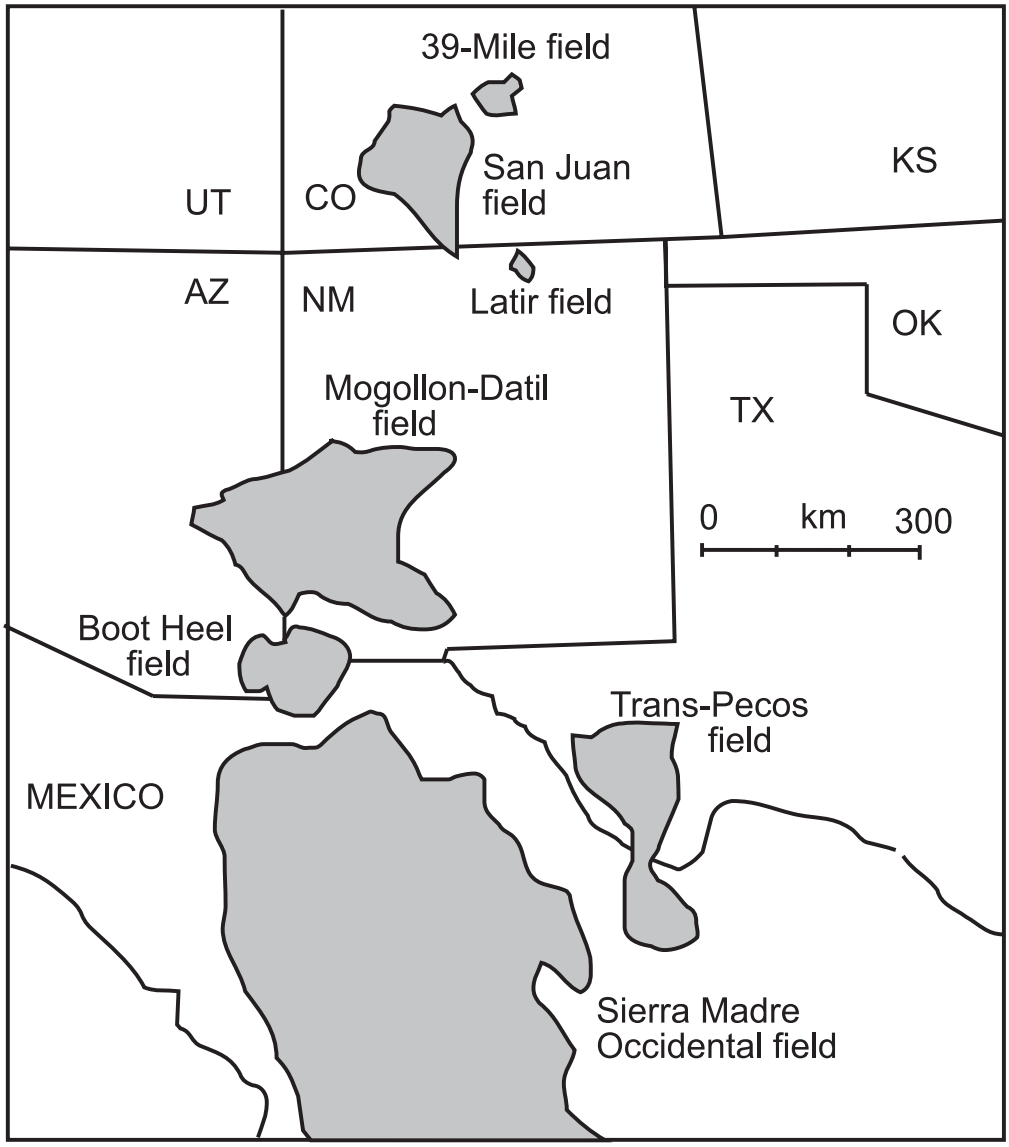

Figure 11. Map showing the location and proximity of the major volcanic fields in the southwestern United States and northern Mexico (modified from McIntosh and Bryan, 2000).

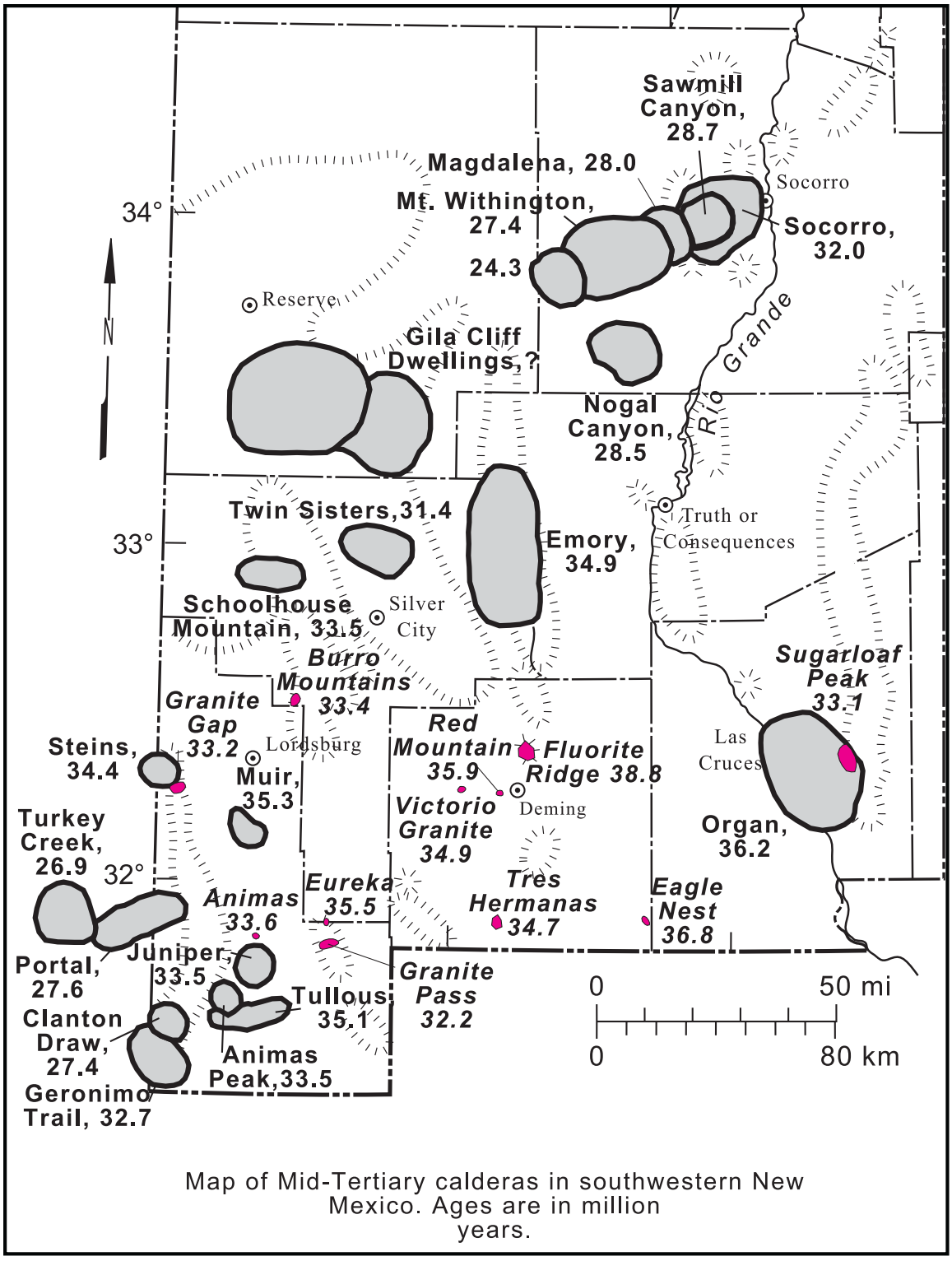

Figure 12. Map of calderas and igneous intrusions for southwestern New Mexico (from McLemore et al., 2001). Dark gray shapes are intrusive bodies, light gray shapes are caldera boundaries. The Victorio Granite has a argon geochronology date consistent with other granites within southwestern New Mexico.

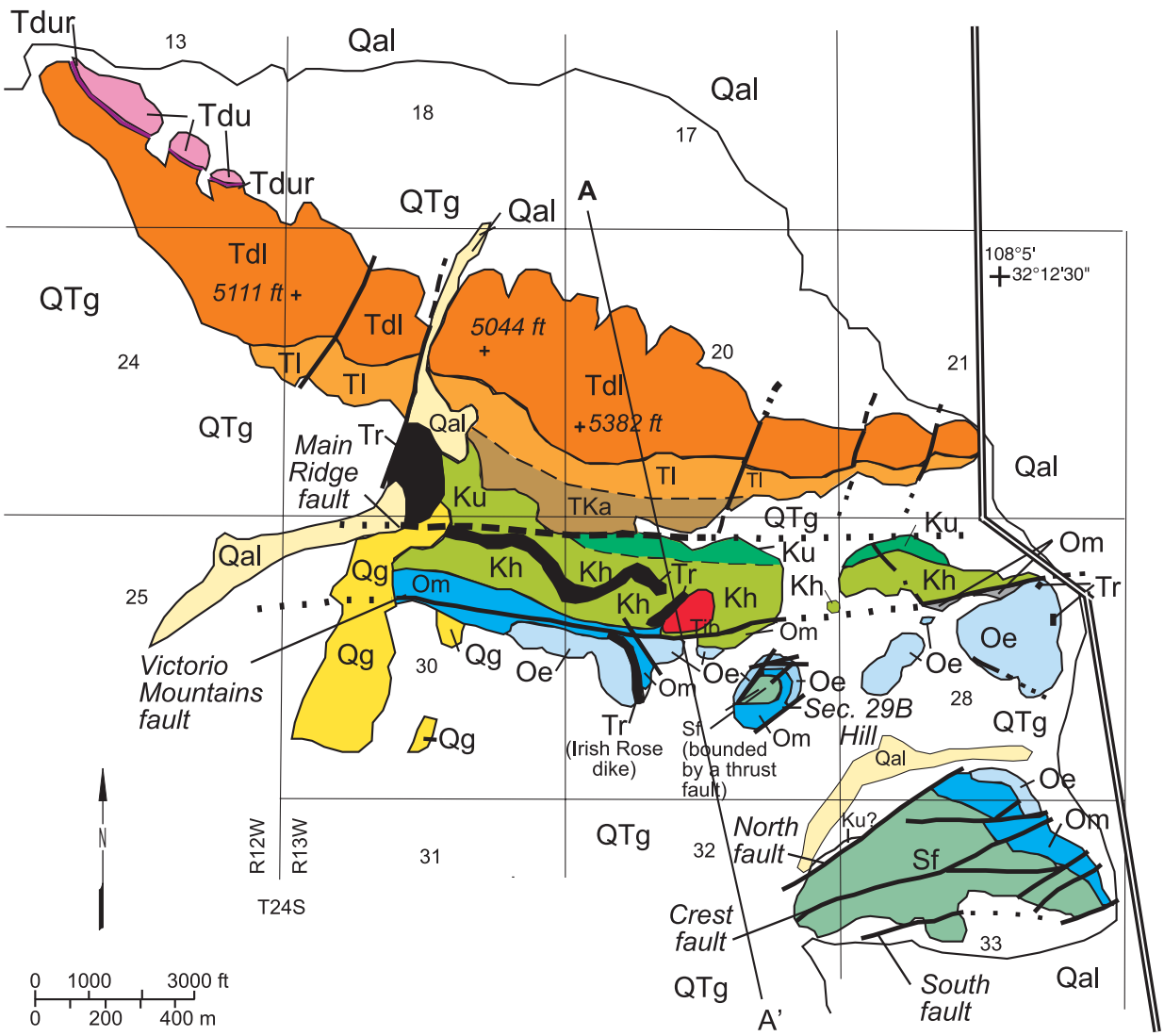

Figure 13. Simplified regional geologic map of the Victorio Mountains area (modified from McLemore et al., 2000a). Lithological descriptions listed in Figure 14b. Cross section line A-A' shown in Figure 14a.

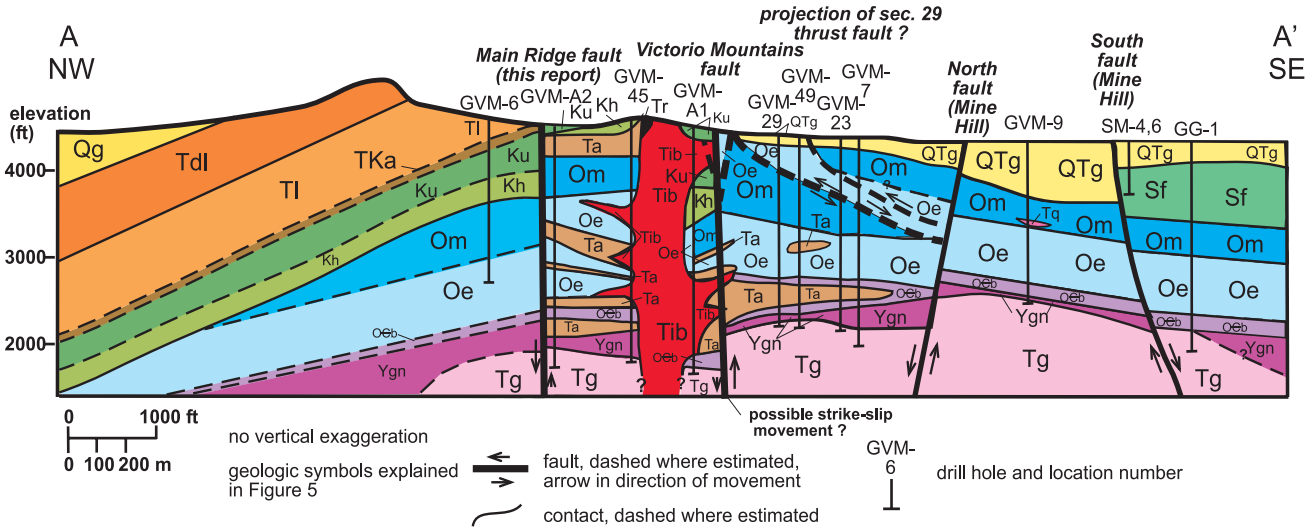

Figure 14a. Geologic cross section through the Victorio Mountains area (modified from McLemore et al, 2000a). Lithological descriptions listed in Figure 14b.

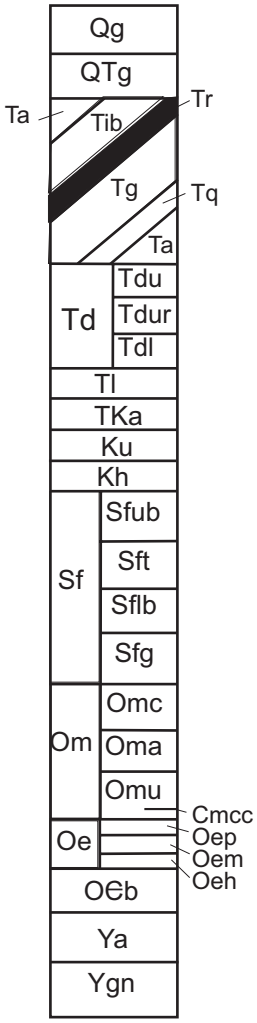

Estimated Thickness		
10-200 ft	Qg	alluvial deposits
	QTg	gravels
	Ta	basalts, andesite sills and dikes
	Tib	Tugnsten Hill breccia pipe
	Tr	rhyolite, dacite dikes
	Tg	Victorio Granite
	Tq	quartz latite/rhyolite
900-1500 ft	Td	Victorio Peak dacite
	Tdu	upper unit
	Tdur	ash-flow tuff
	Tdl	lower unit
630-825 ft	Tl	Lobo Formation
720-915 ft	TKa	dacite flows and breccias (Hidalgo Formation?)
550-600 ft	Kb	Bisbee Formation
	Ku	U-bar Formation
	Kh	Hell-to-finish Formation
30-900 ft	Sf	Fusselman Formation
	Sfub	upper black
	Sft	upper tan
	Sflb	lower black
	Sfg	lower gray
270-340 ft	Om	Montoya Group
	Omc	Cutter Dolomite
	Oma	Aleman Formation
	Omu	Upman Dolomite
	Omcc	Cable Canyon Sandstone
450-500 ft	Oe	El Paso Group
	Oep	Padre Formation
	Oem	McKelligan Formation
	Oeh	Hitt Canyon Formation
90-150 ft	OCb	Bliss Formation
	Yg	granite
	Ya	amphibolie
	Ygn	quartzo-feldspathic gneiss

Figure 14b. Stratigraphic section and explination of units for the Victorio Mountains district (modified from McLemore et al, 2000a). Estimated thickness is in feet.

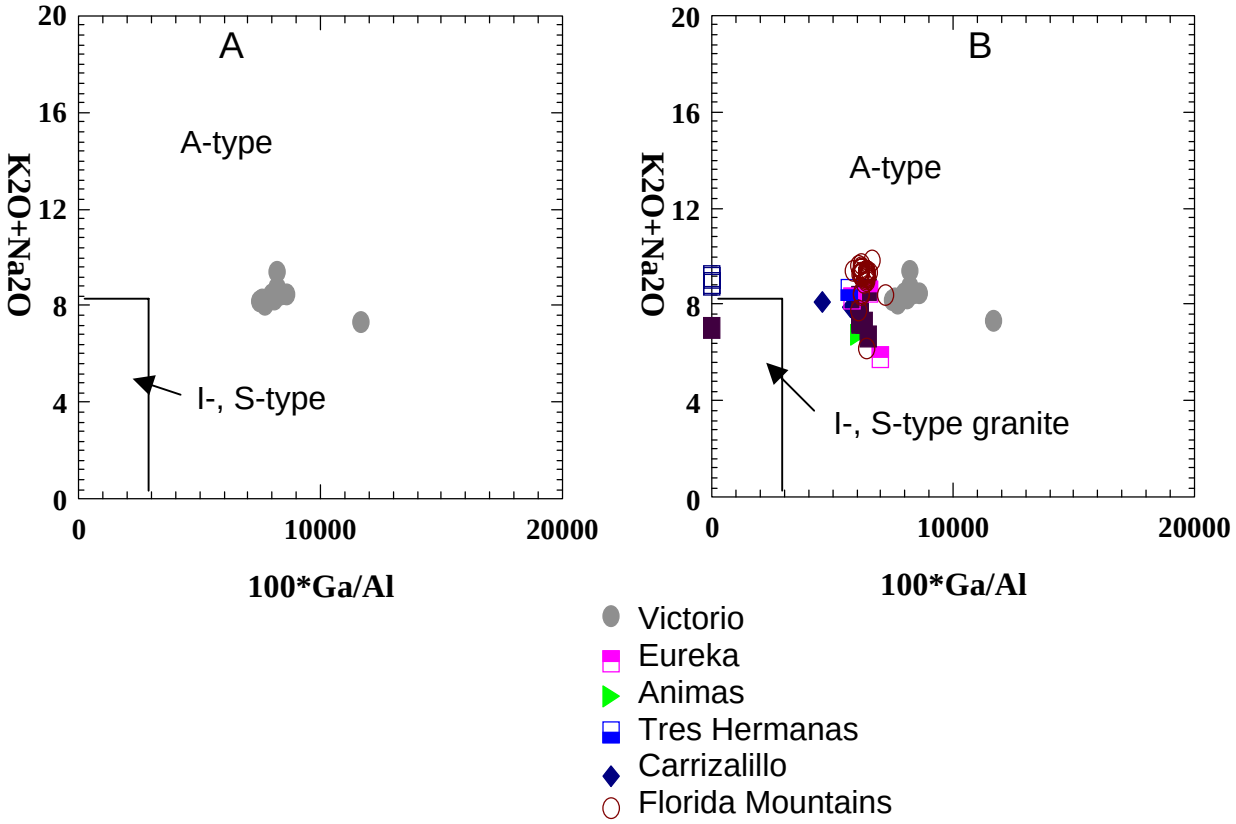

Figure 15. A. Plot of geochemistry of the Victorio Granite and B. other granites from southwestern New Mexico on a geochemical diagram differentiating between A-, I-, and S-type granites (Whalen et al., 1987). Data is from McLemore et al. (2001).

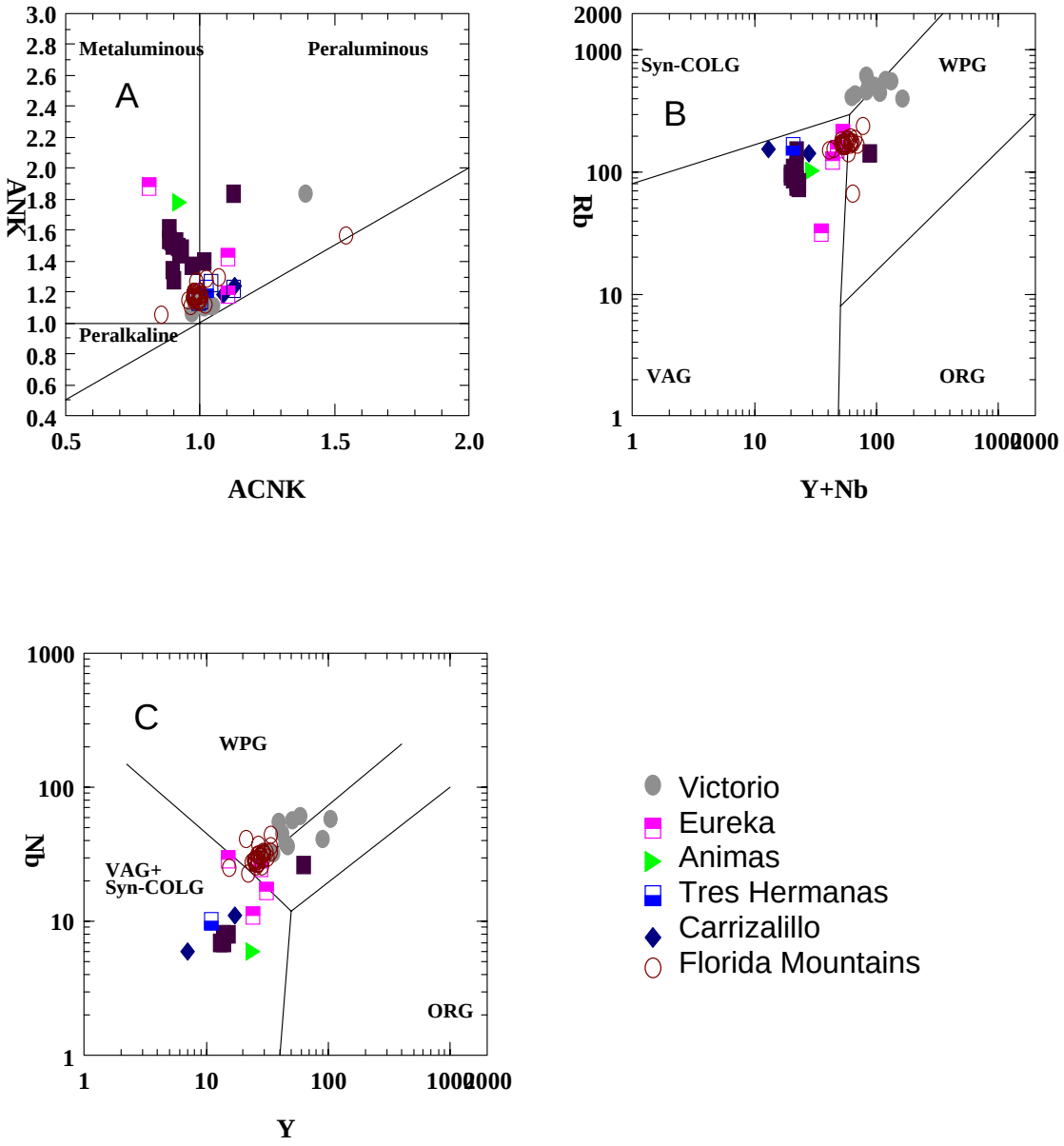

Figure 16. Plot of geochemistry from granites (data from McLemore et al., 2001) throughout New Mexico including the Victorio Granite. A. Aluminum content diagram. B. and C., Tectonic setting diagrams from Pearce et al. (1984). Syn-COL = syn-collision granites, WPG = within plate granites, VAG = volcanic arc granites, ORG = orogenic granites. Most of these granites are located on Figure 12.

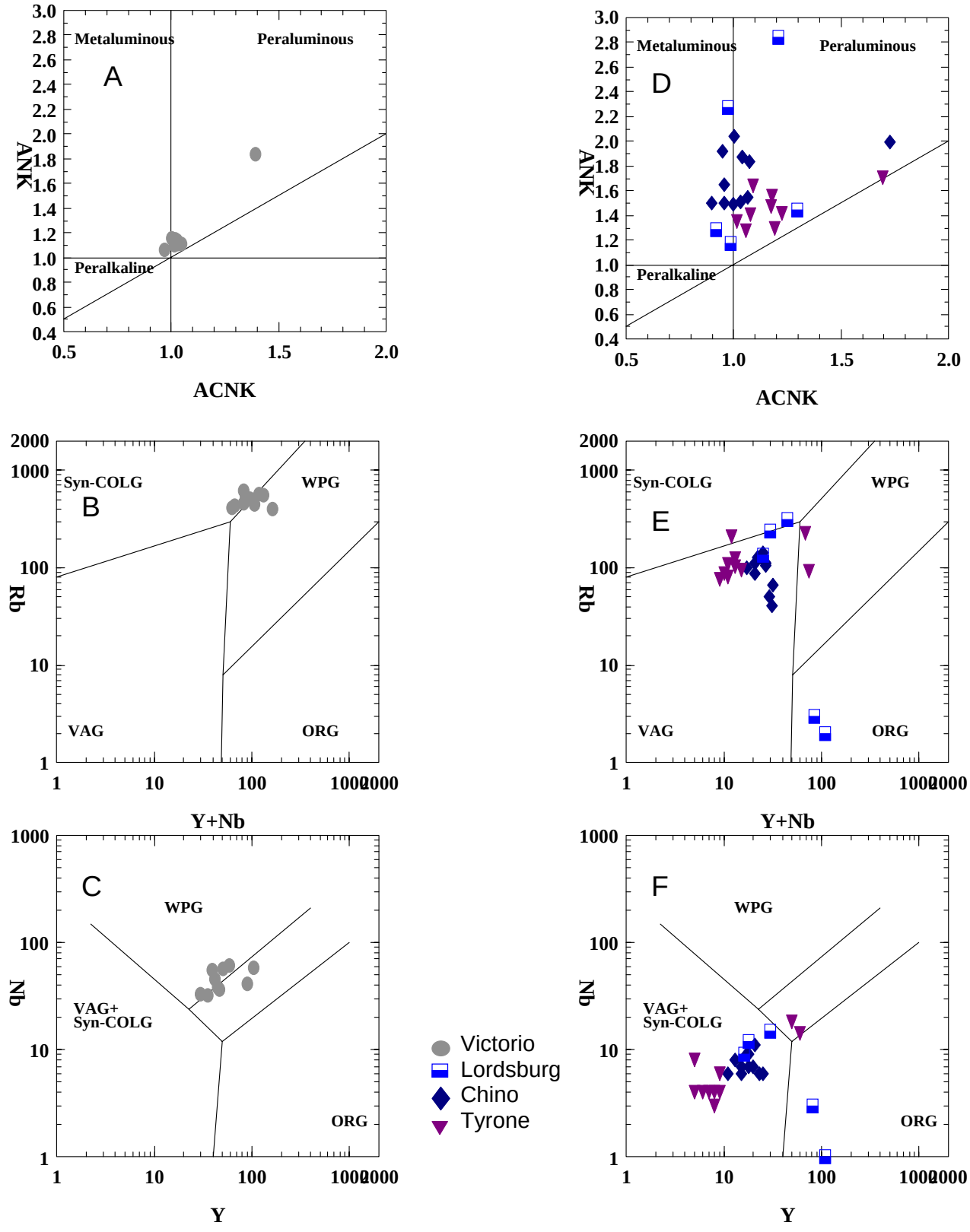

Figure 17. Plot of geochemistry from porphry and Laramide polymetalic vein deposits (data from V. T. McLemore, written communication) throughout New Mexicocompared to the Victorio Granite. A. , D. Aluminum content diagram. B. , C., E., and F., Tectonic setting diagrams from Pearce et al. (1984). Syn-COL = syn-collision granites, WPG = within plate granites, VAG = volcanic arc granites, ORG = orogenic granites.

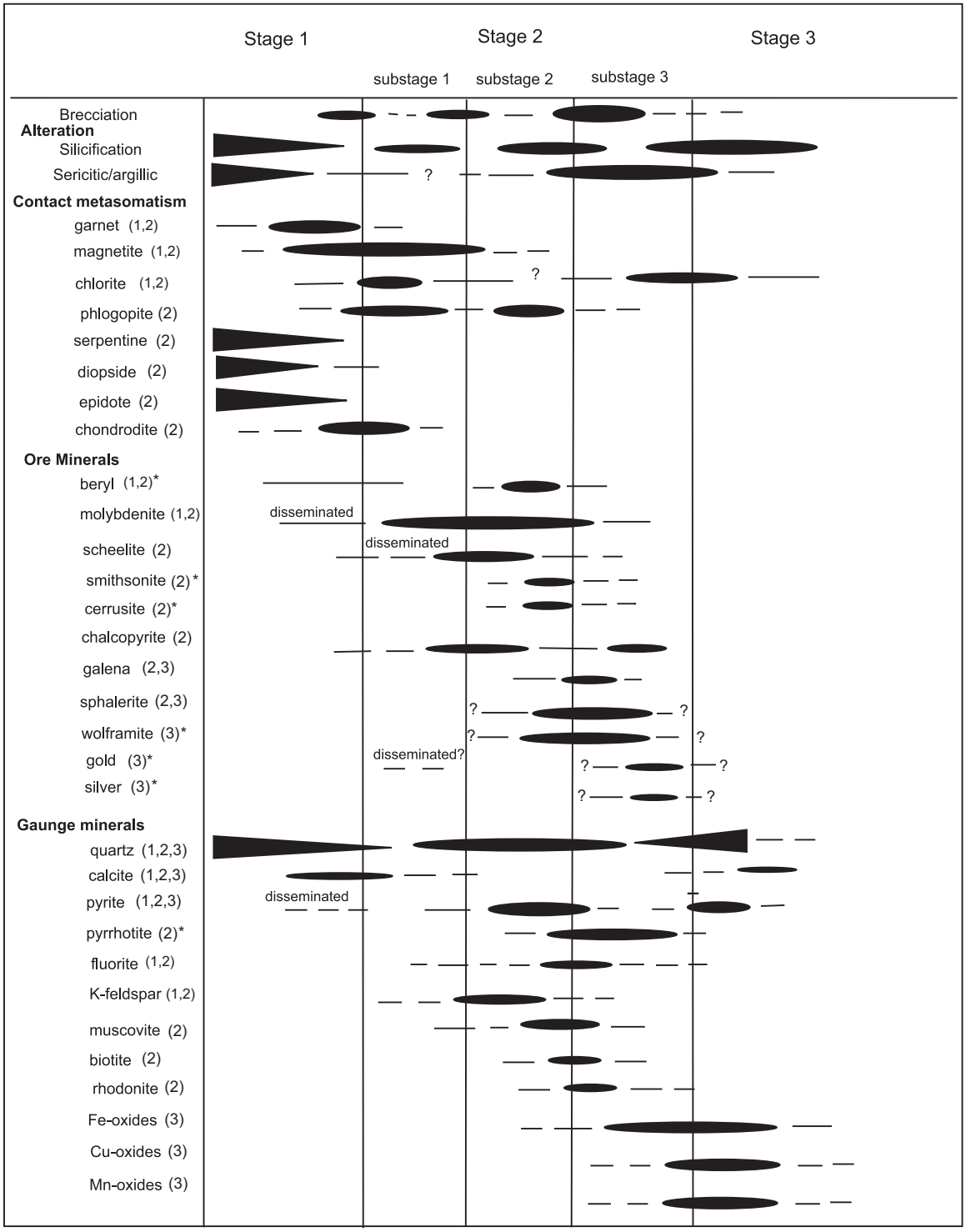

Figure 18 . Relative paragenetic sequence for the Victorio mining district showing the mineral relationships and alteration events. The paragenetic sequence is for all three types of deposits. 1 = porphyry Mo , 2 = skarn, 3 = carbonate-hosted replacement deposit, * = mineral not seen in drill core relative paragenesis taken from literature (Heidrick, 1983). Core samples in Appendix D were used to determine paragenesis .

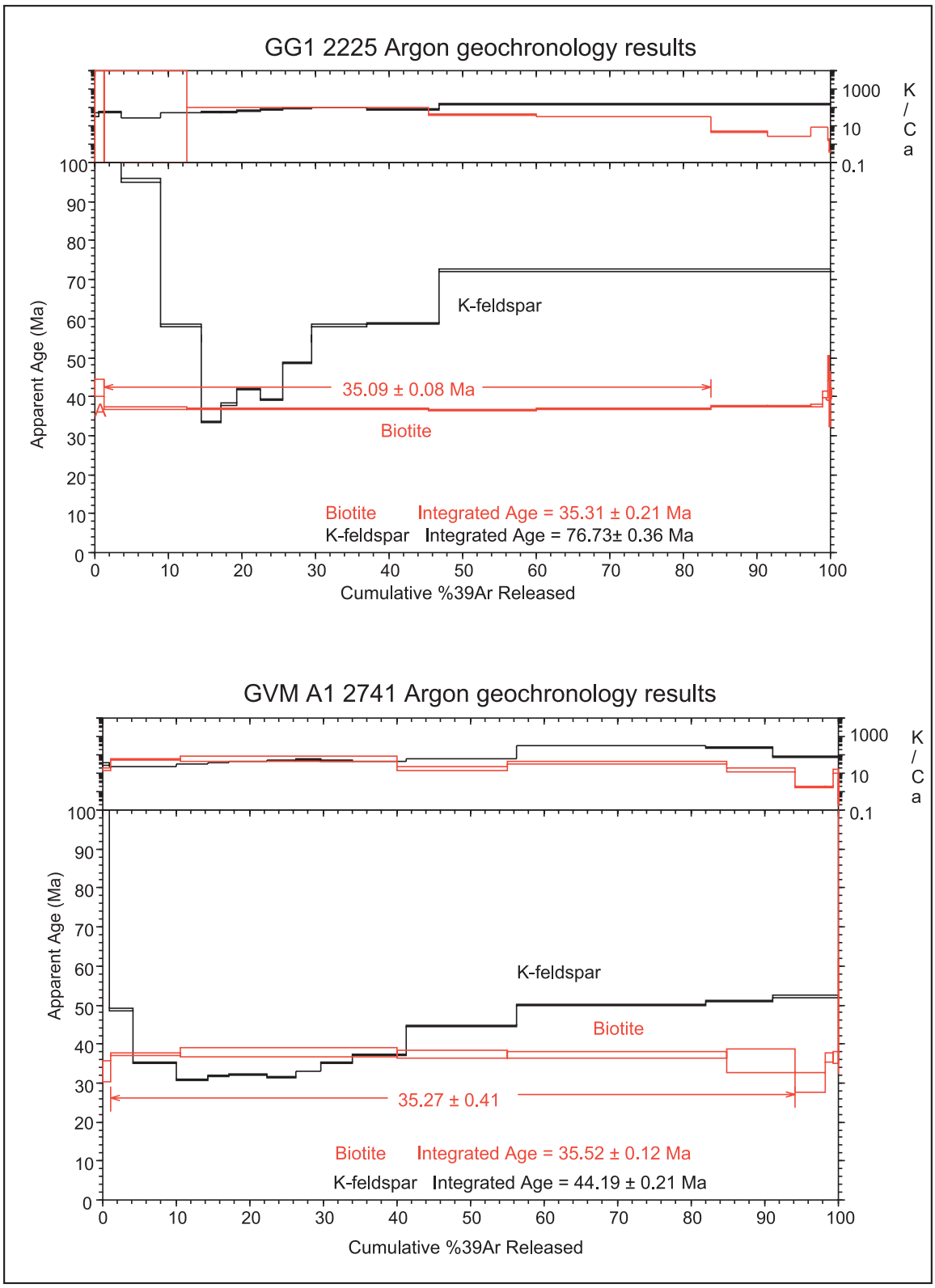

Figure 19. Argon geochronology results for the Victorio Granite samples GG1 2225 and GVM A1 2741 modified from McLemore et al. (2000a). The black age spectra are the K-Feldspar results, the red age spectra are the biotite results.

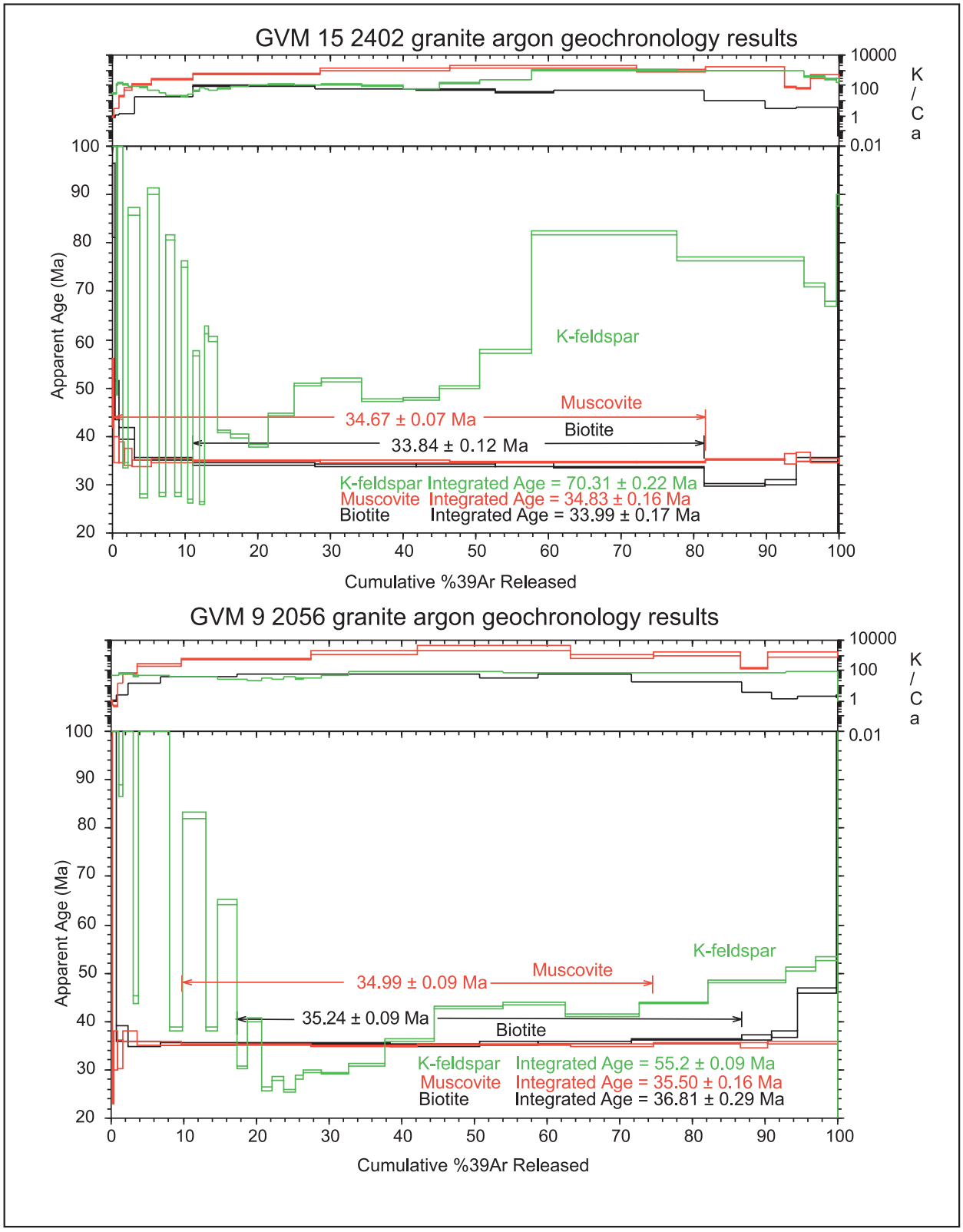

Figure 20. Argon geochronology results for the Victorio Granite samples GVM 15 2402 and GVM 9 2056. The green age spectra are the K-Feldspar results, the red age spectra are the muscovite results and the black age spectra are the biotite results. Sperately plotted age spectra results for each mineral can be found in Appendix A.

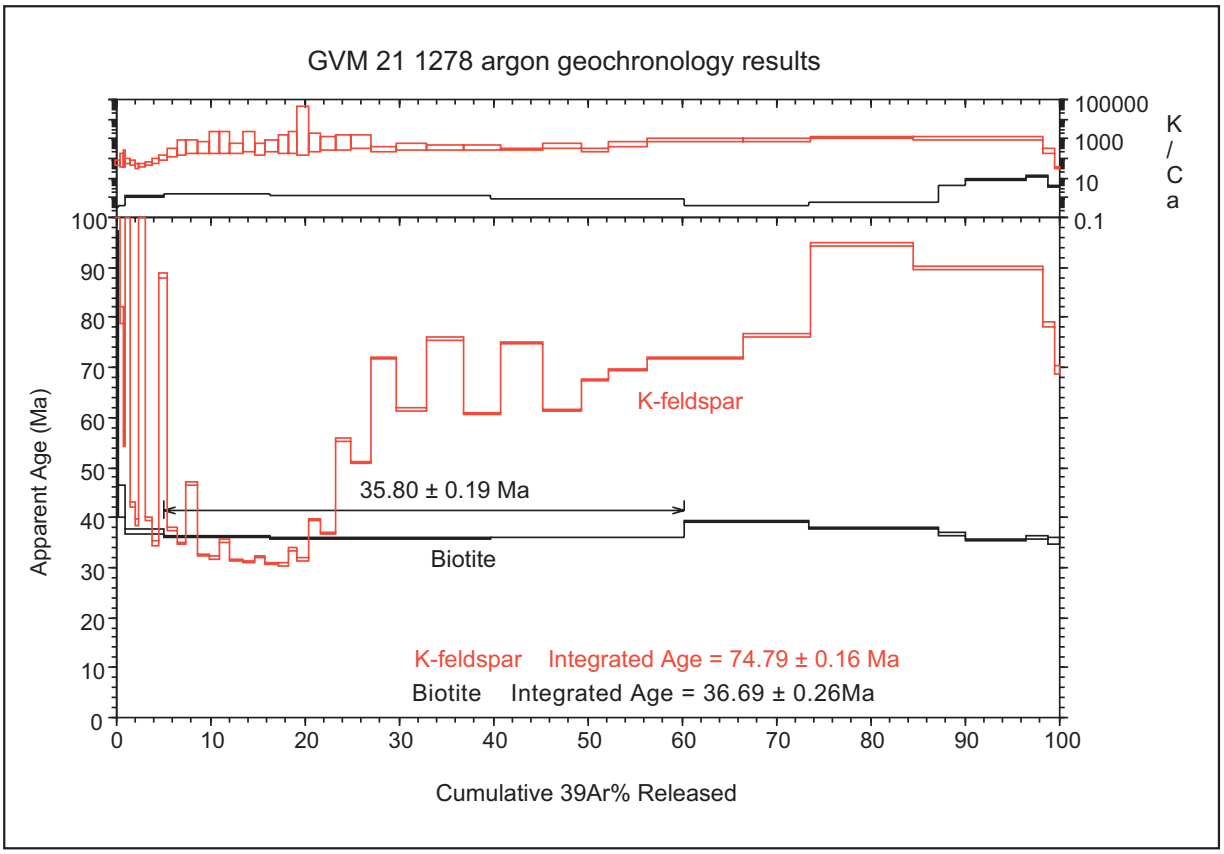

Figure 21. Age spectra for sample GVM 21 1278 K-feldspar and biotite. The K-feldspar age spectrum is shown in red, the biotite age spectrum is shown in black. The full results of the argon geochronology analysis are listed in Appendix A.

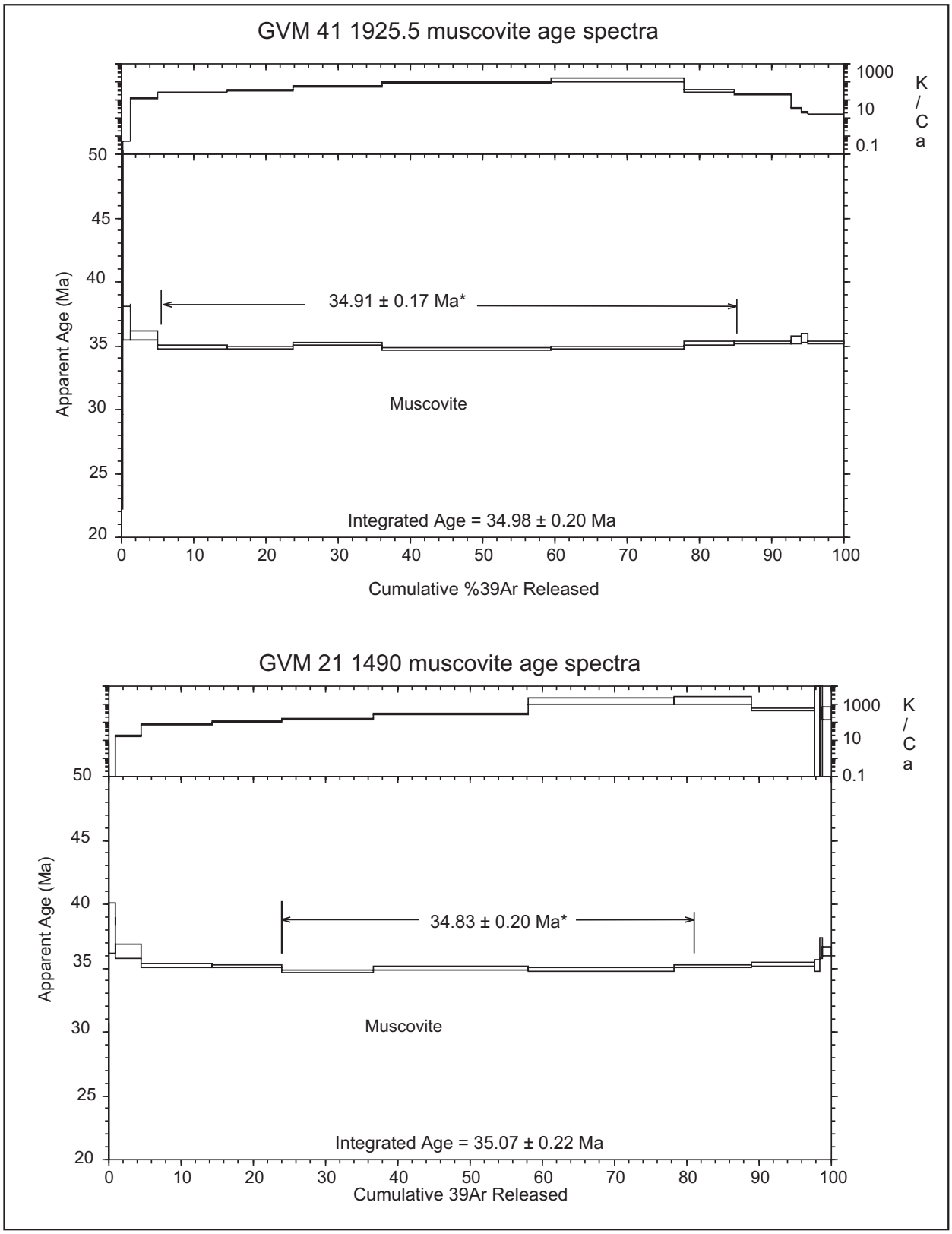

Figure 22. Age spectra for samples GVM 41 1925.5 and GVM 21 1490 muscovite mineral samples.

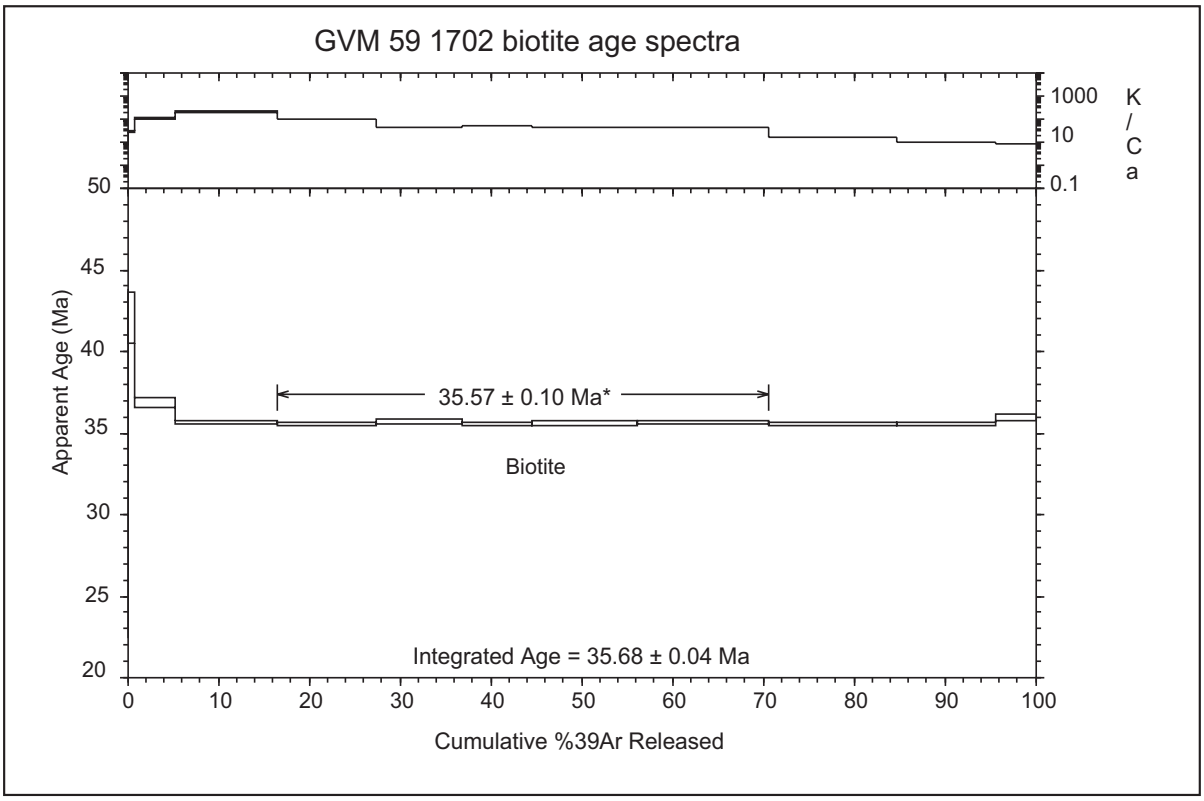

Figure 23. Age spectra for GVM 59 1702 biotite mineral sample.

Figure 24. Photomicrograph of a plane of secondary liquid + vapor (type Ia) fluid inclusions in a quartz crystal from sub-stage 3 of the mineralization stages. The photograph shows clusters of secondary inclusions that may have experienced post entrapment modifications.

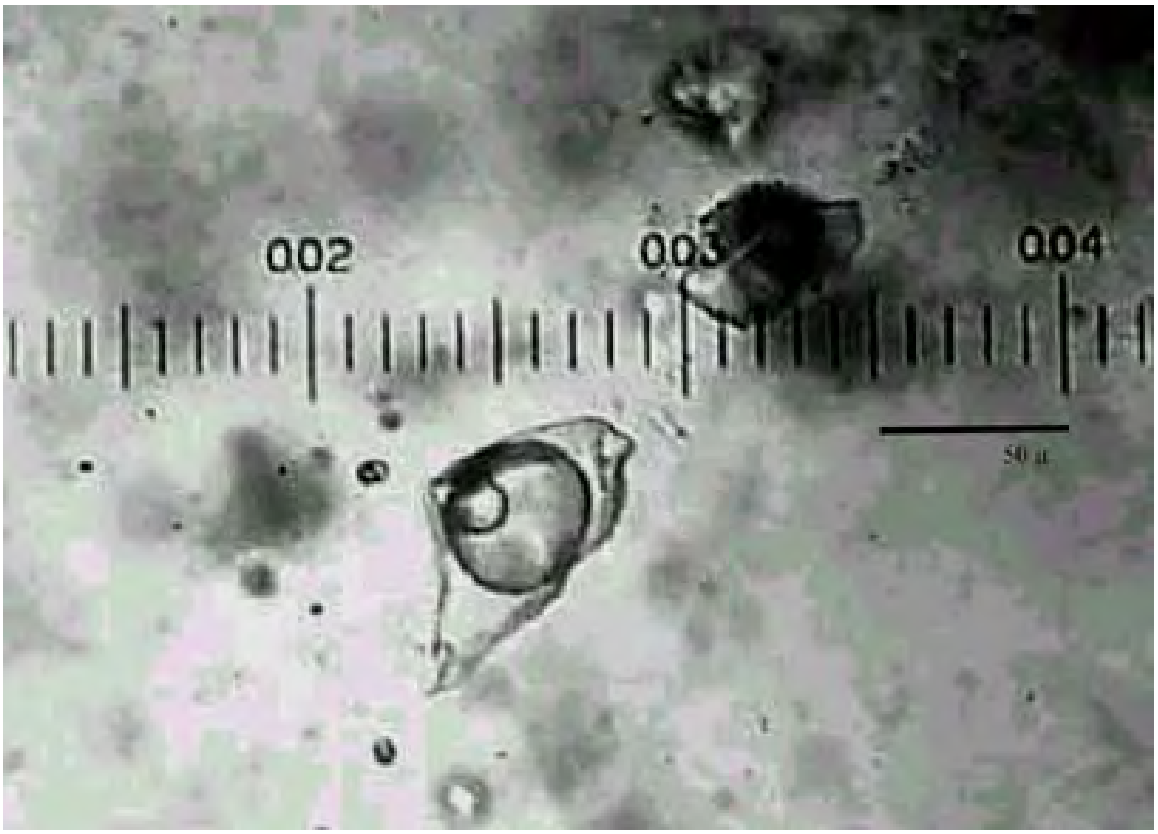

Figure 25. Photomicrograph of a primary fluid inclusion that contains liquid CO_2 + vapor CO_2 + liquid (type IIb) in a quartz crystal from sub-stage 2 of the mineralization stages.

Figure 26. Photomicrograph of a group of secondary fluid inclusions that contain an unidentified solid + liquid + vapor (type III) in a fluorite crystal from sub-stage 3 of the mineralization stages. The photo shows a range of ratios between solid to liquid for each inclusion.

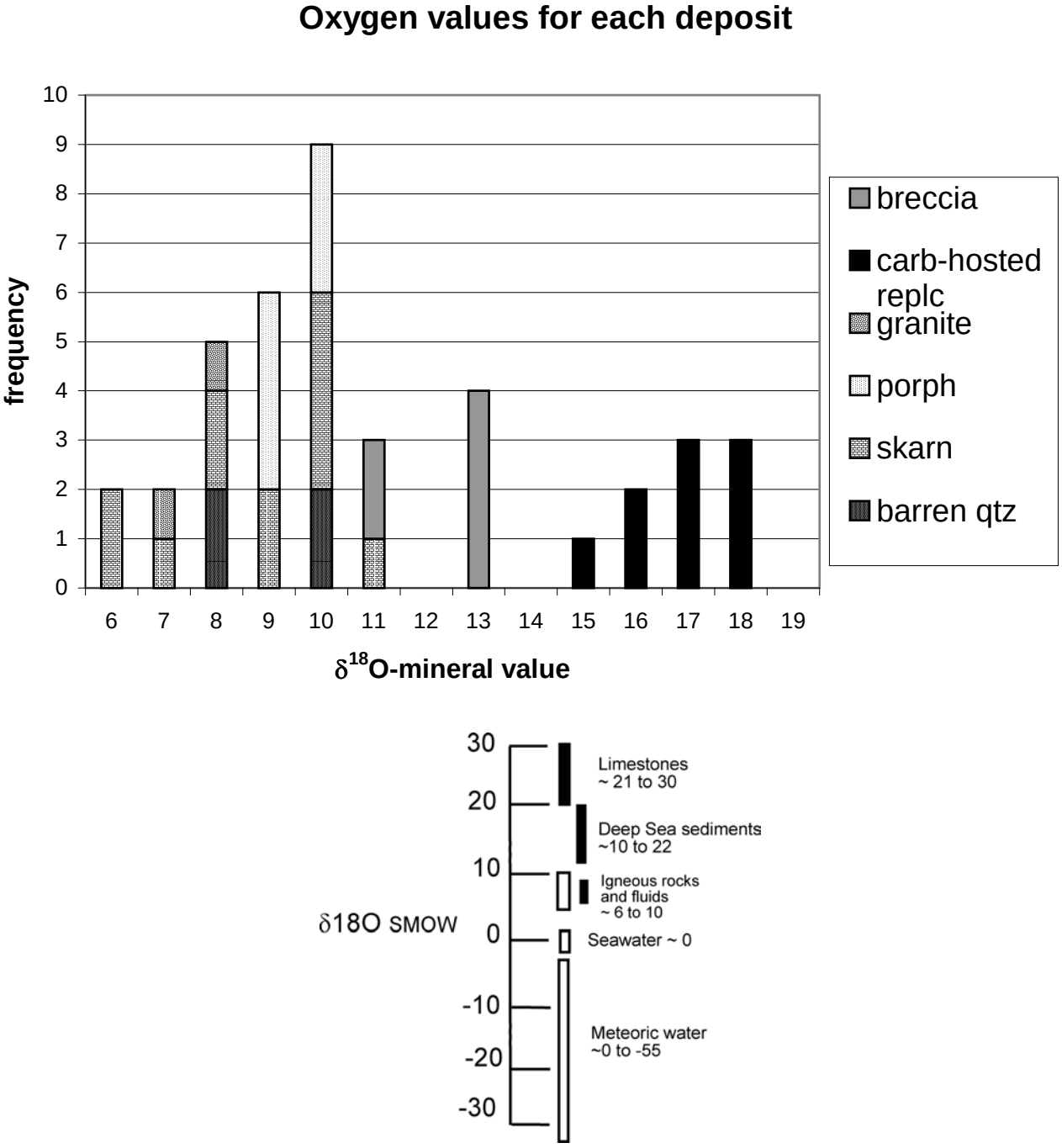

Figure 27. Histogram of $\delta^{18}O$ values for each mineral deposit, the breccia pipe vuggy quartz, and Victorio Granite samples. The oxygen values are mineral values and do not represent fluid values. Ranges of water and rock values are modified from Campbell and Larson (1998).

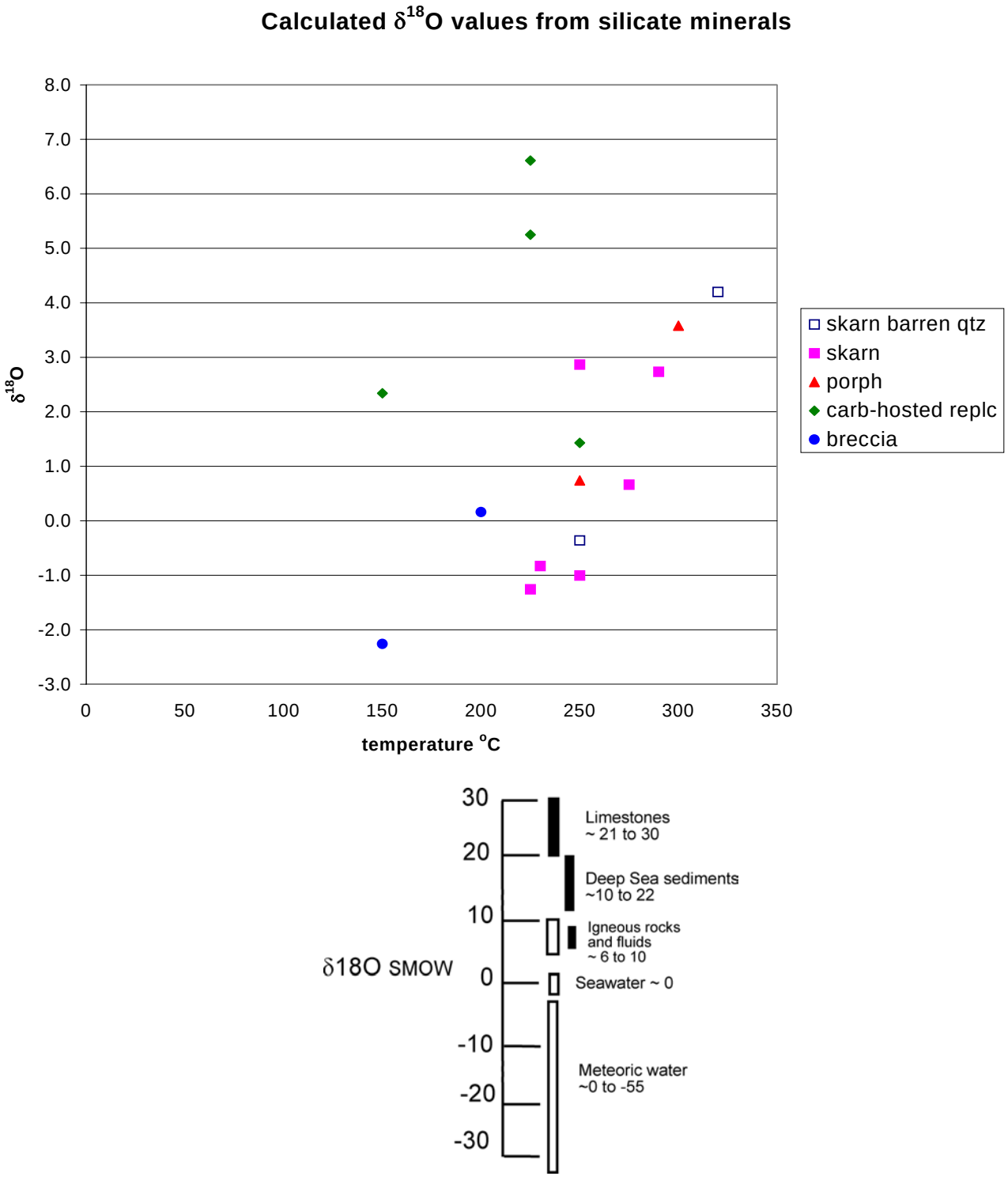

Figure 28. Calculated water values for silicate stable isotopes for each mineral deposit, the breccia pipe, and the Victorio Granite. The values have been calculated using equilibrium equations for quartz and water from Zheng (1993). Ranges of water and rock values modified from Campbell and Larson (1998).

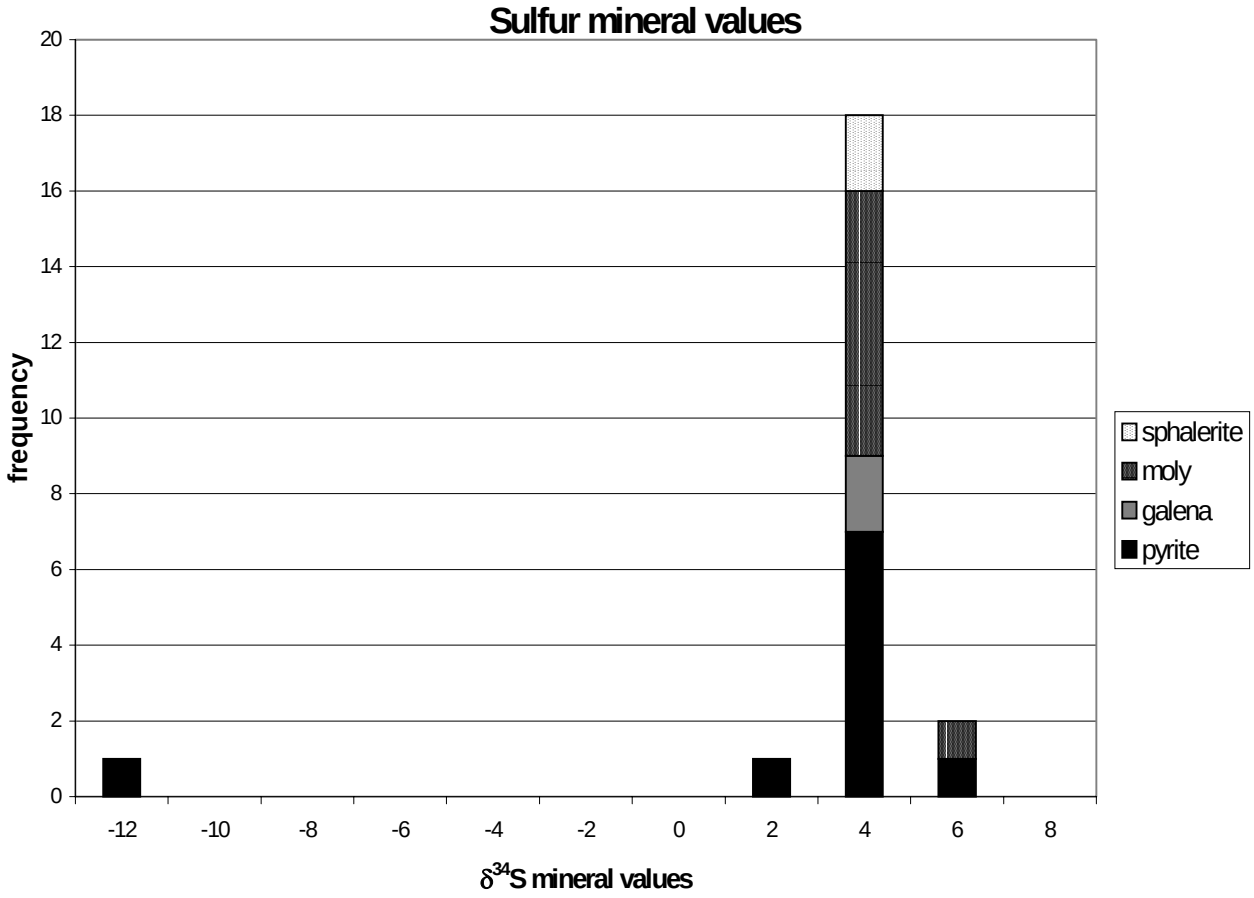

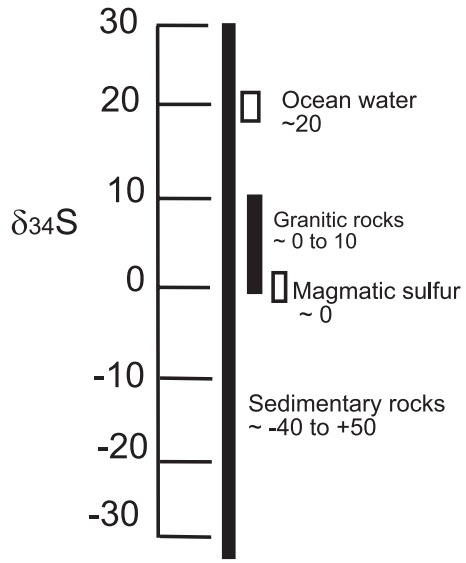

Figure 29. Histogram of $\delta^{34}S$ sulfur values from the skarn and carbonate-hosted replacement deposits with reference to the mineral sample type. Values are mineral values and do not represent the mineralizing fluids. Sulfur fluid and rock ranges modified from Hoefs (1997).

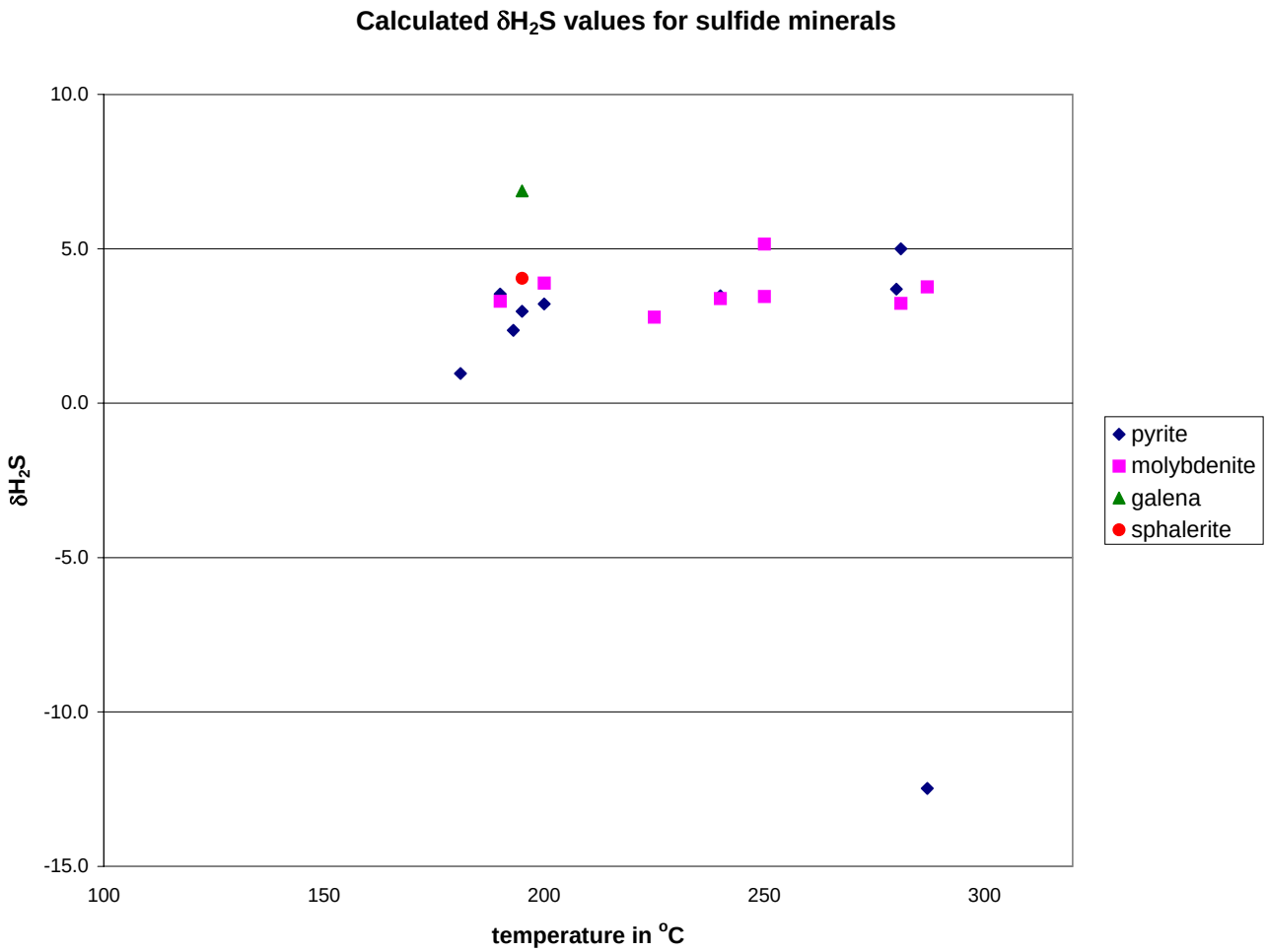

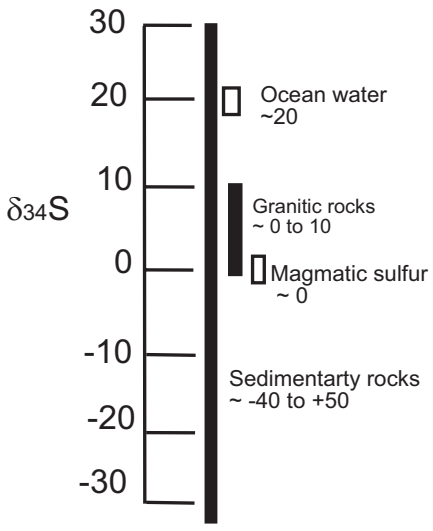

Figure 30. Calculated H_2S-mineral fluid values from the skarn and carbonate-hosted replacement deposits calculated for each corresponding temperature. Temperatures used to calculate H_2S values were average fluid inclusion homogenization temperatures for each sample. Sulfur fluid and rock ranges modified from Hoefs (1997).

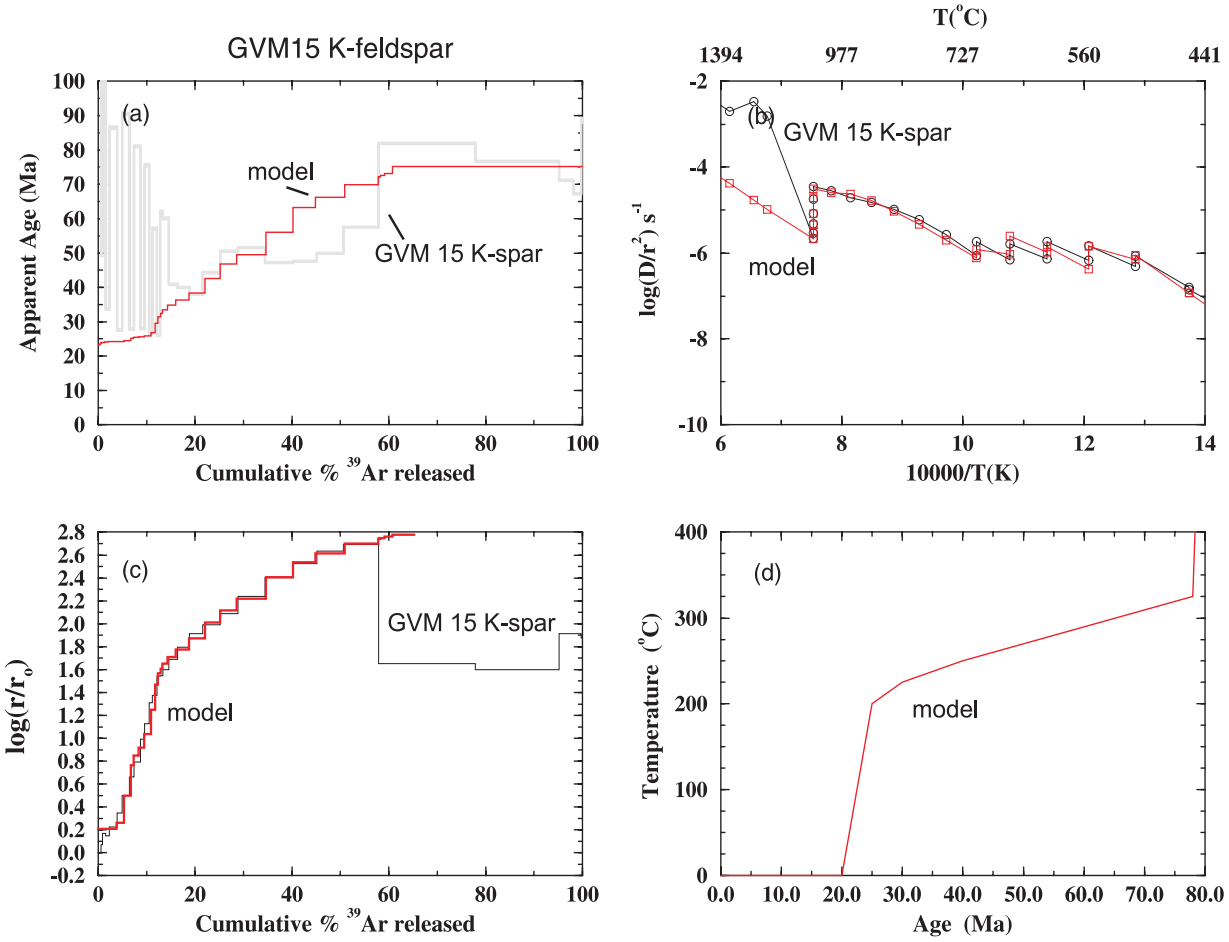

Figure 31. A. The results of the multidomain diffusion model of the GVM 15 2402 K-feldspar results (McDougall and Harrison, 1998). The red outline is the computer generated model. B. An Arrhenius diagram of the K-feldspar results and the computer model shows the model closely resembles the rate of diffusion characteristics of the samples. C. A log (r/r_o) plot versus the cumulative percent release of ^{39}Ar. This plot compares the laboratory argon transport with the data from the K-feldspar sample. D. The thermal model of the results showing the best-fit line for the time-temperature history of the K-feldspar sample. The model shows that the granite would have remained at approximately 300°C for a relatively long period of time. This does not fit with the scenario that the micas were re-heated then quickly cooled at ~30 Ma.

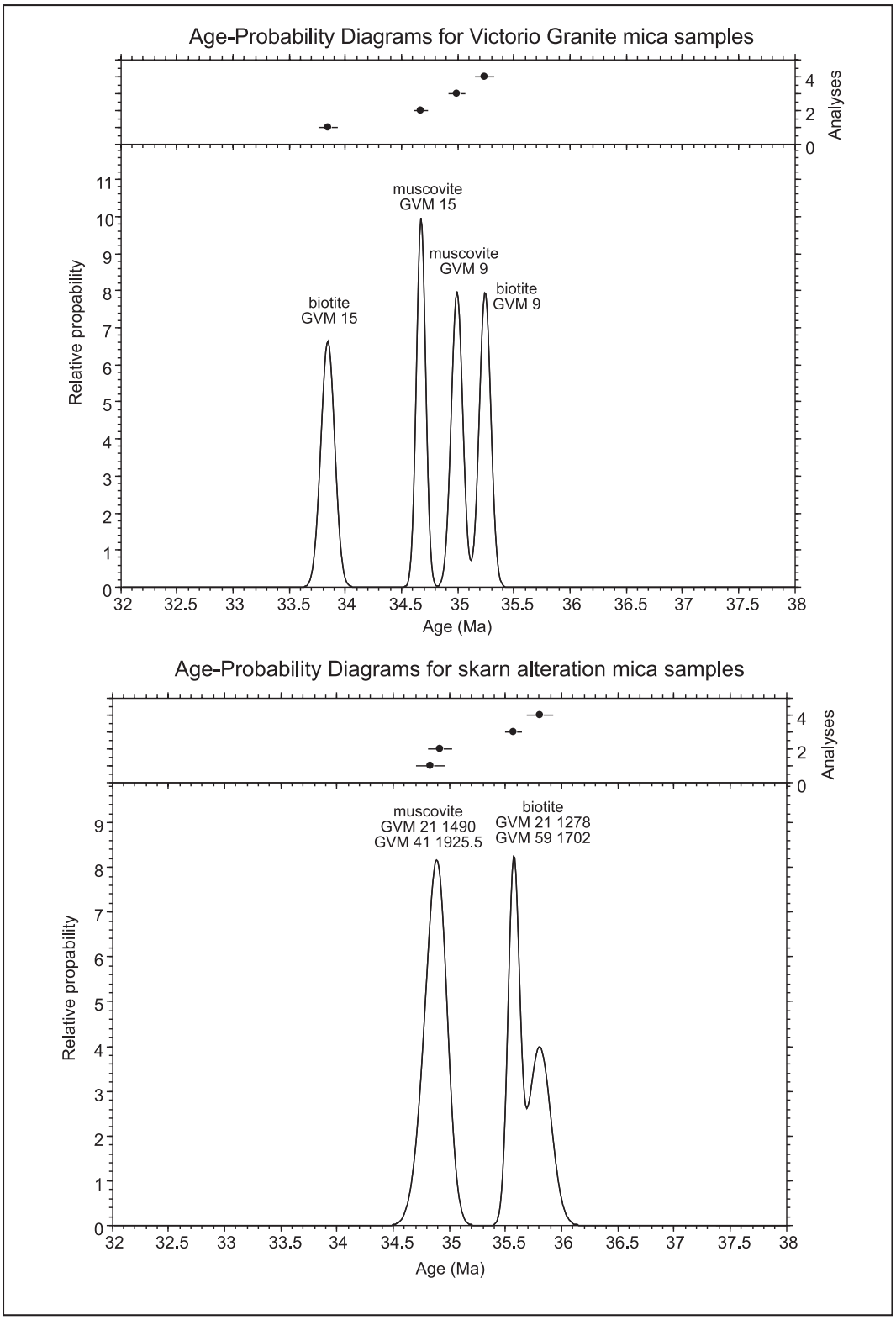

Figure 32. Relative age probability diagram for the Victorio Granite and skarn alteration argon geochronology results. The Victorio Granite results indicate no systematic difference in age between the muscovite and biotite granite results. The skarn alteration results indicate the muscovites have younger apparent ages than the biotites. The Victorio Granite biotite result for GVM 15 was excluded from the calculation of the age.

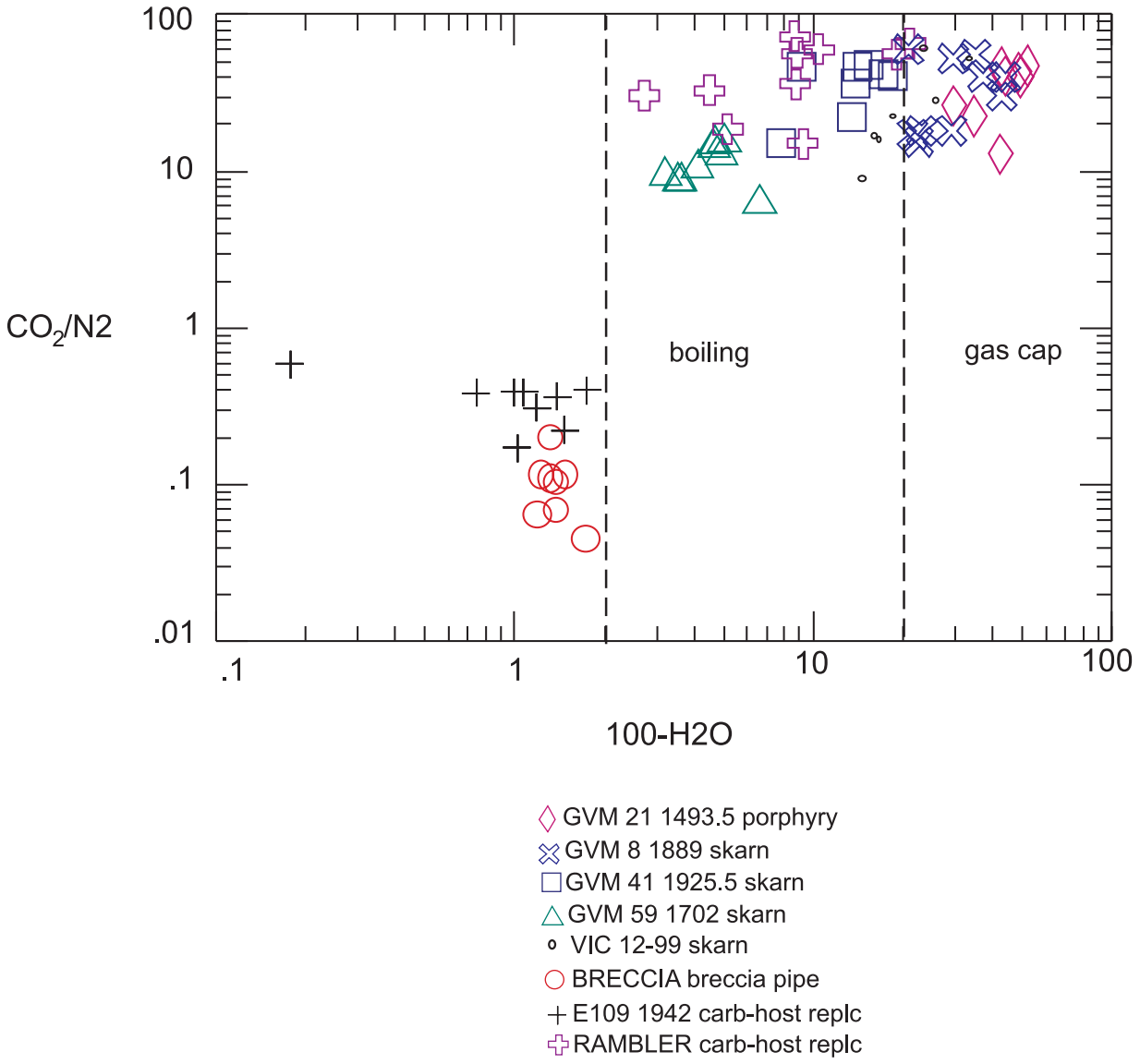

Figure 33. Plot of CO_2/N_2 vs. total gas percent of the results from the fluid inclusion gas analysis (Appendix C). Lines for gas cap and boiling boundaries from Norman et al. (2002). This graph illustrates that six of the eight of the Victorio samples fall within the boiling and condensation (gas cap) regions as a result of over pressuring system.

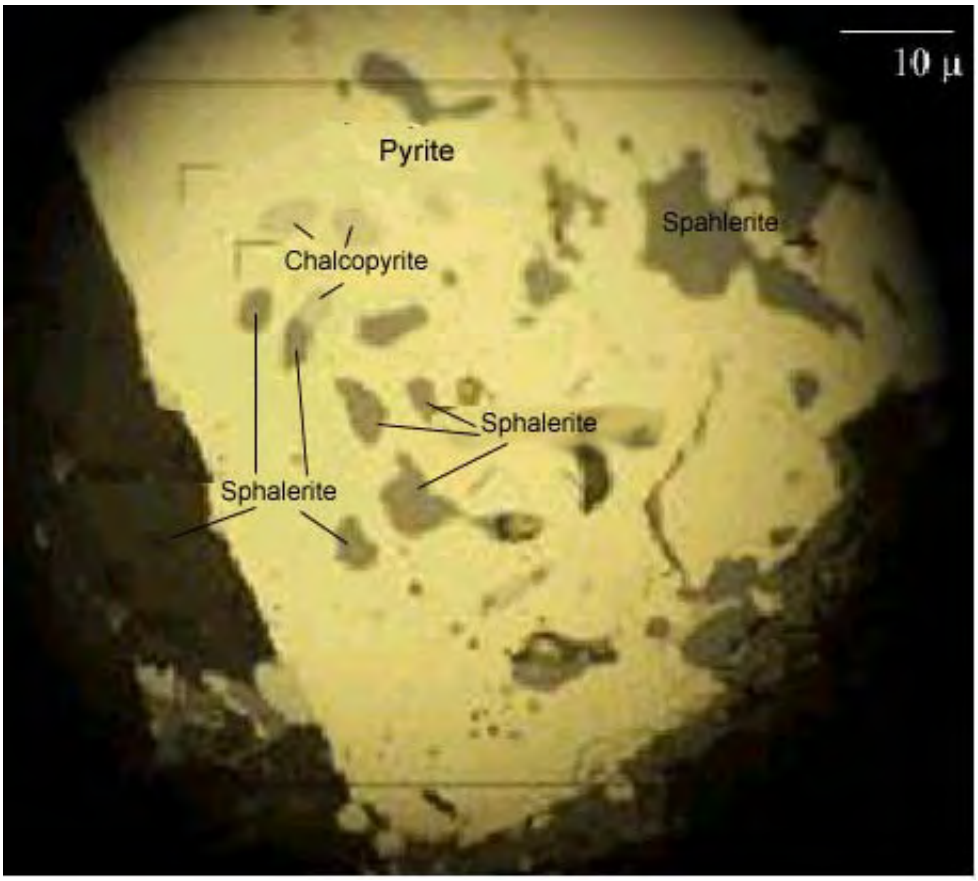

Figure 34. Photomicrograph of a pyrite cube surrounded by sphalerite from sample E109 1942 with chalcopyrite and sphalerite inclusions. The sulfide inclusions affected the ability to calculate the formation temperature from the sulfur isotope data.

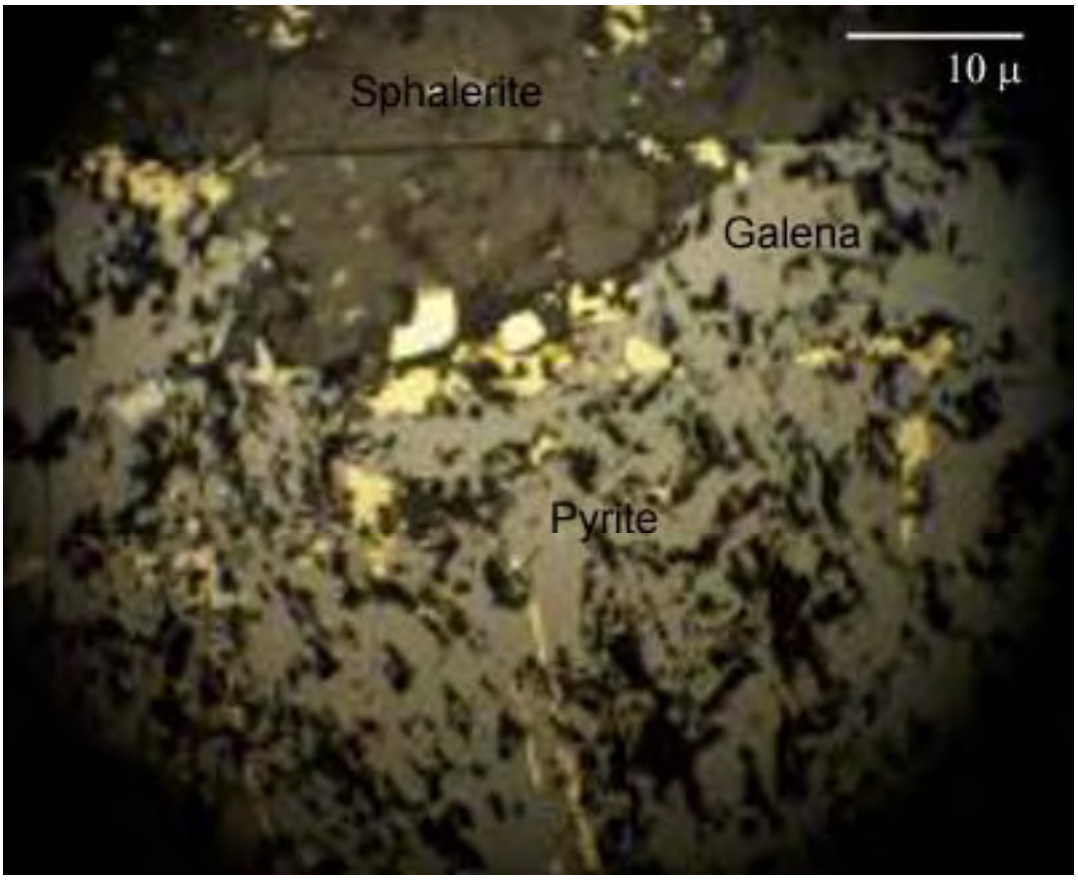

Figure 35. Photomicrograph of galena and sphalerite with pyrite inclusions and streaks of pyrite. The sulfide inclusions affected the ability to calculate the formation temperature from the sulfur isotope data.

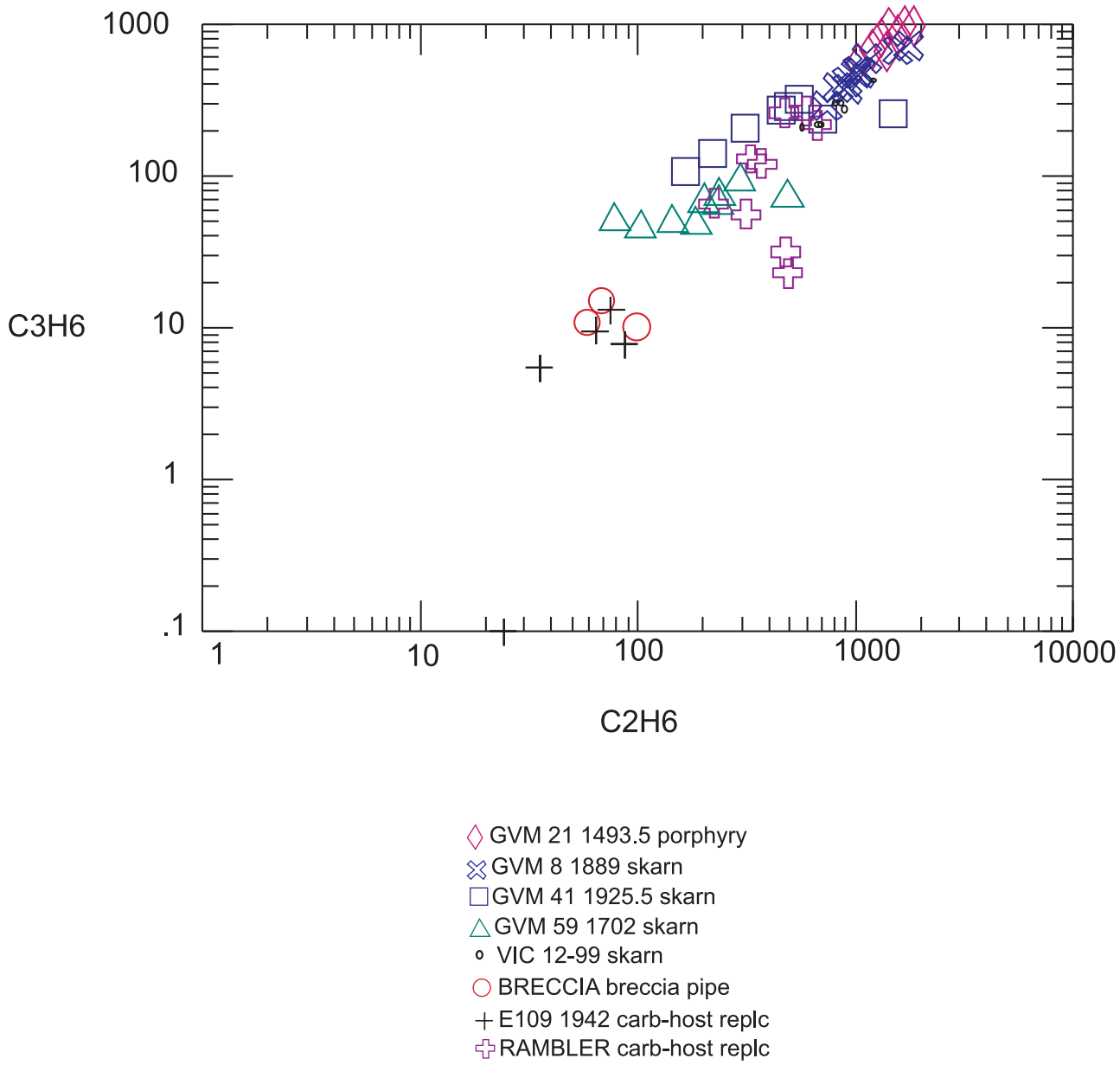

Figure 36. Graph showing the strong correlation of hydrocarbons and deposit type from the fluid inclusion gas analysis. The complex chain hydrocarbons are found in both the skarn and carbonate-hosted replacement deposits. The change in hydrocarbon concentrations could be due to a change in water/rock ratio or dilution by meteoric water.

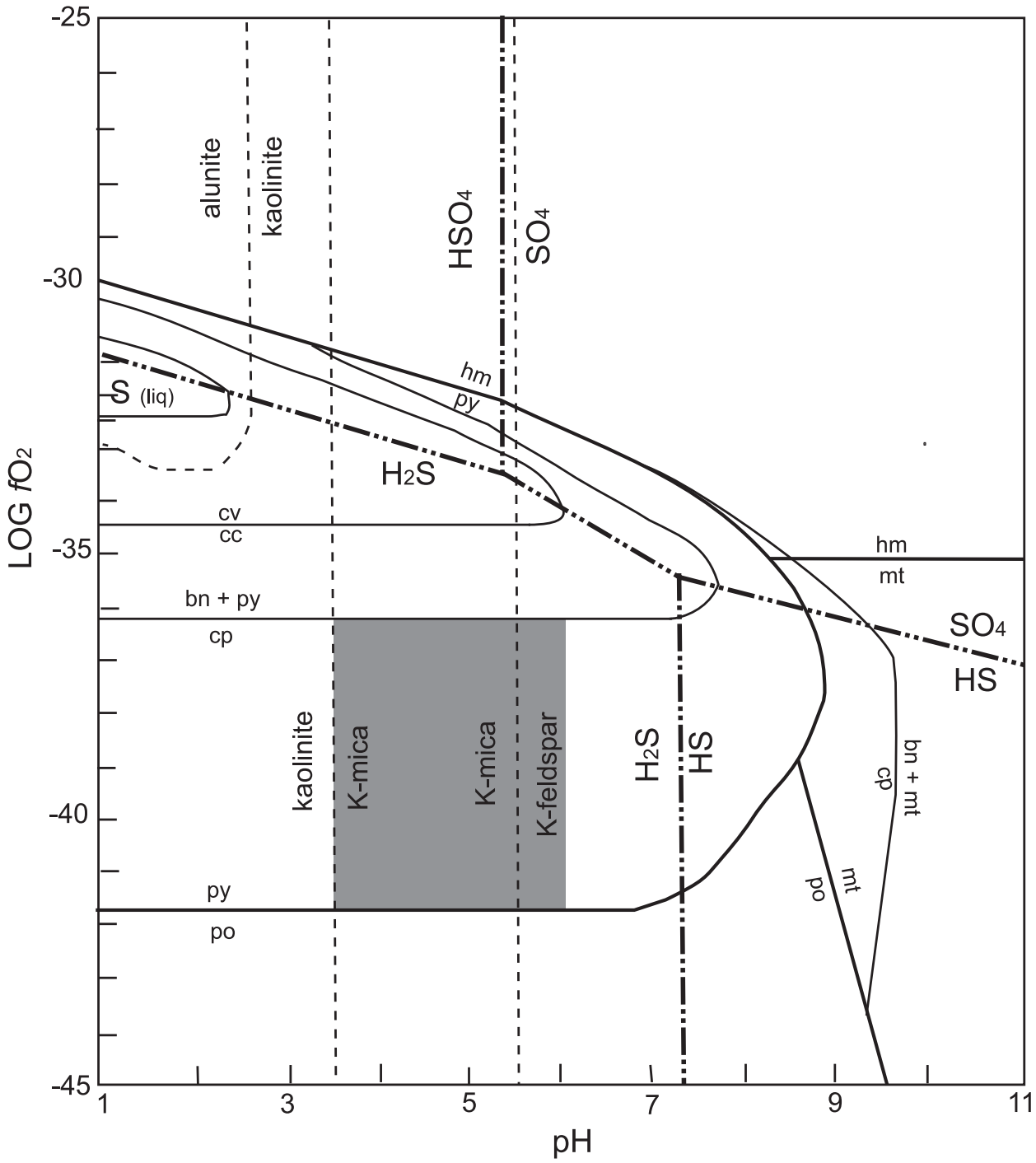

Figure 37. Mineral stability diagram showing the relationship between sulfide minerals, oxygen fugacity and pH at 250°C (modified from Barton, 1984). Log $a_{(K+)}$ = -1.5, muscovite-K-feldspar boundary at K^+ = 0.001 moles/kg H_2O and kaolinite-muscovite boundary at K^+ = 0.1 moles/kg H_2O. bn - bornite, cc-chalcocite, cp - chalcopyrite, py - pyrite, po - pyrrhotite, hm - hematite, mt - magnetite, cv -covelite. Shaded area represents the mineral assemblages and stability fields for the skarn deposits.

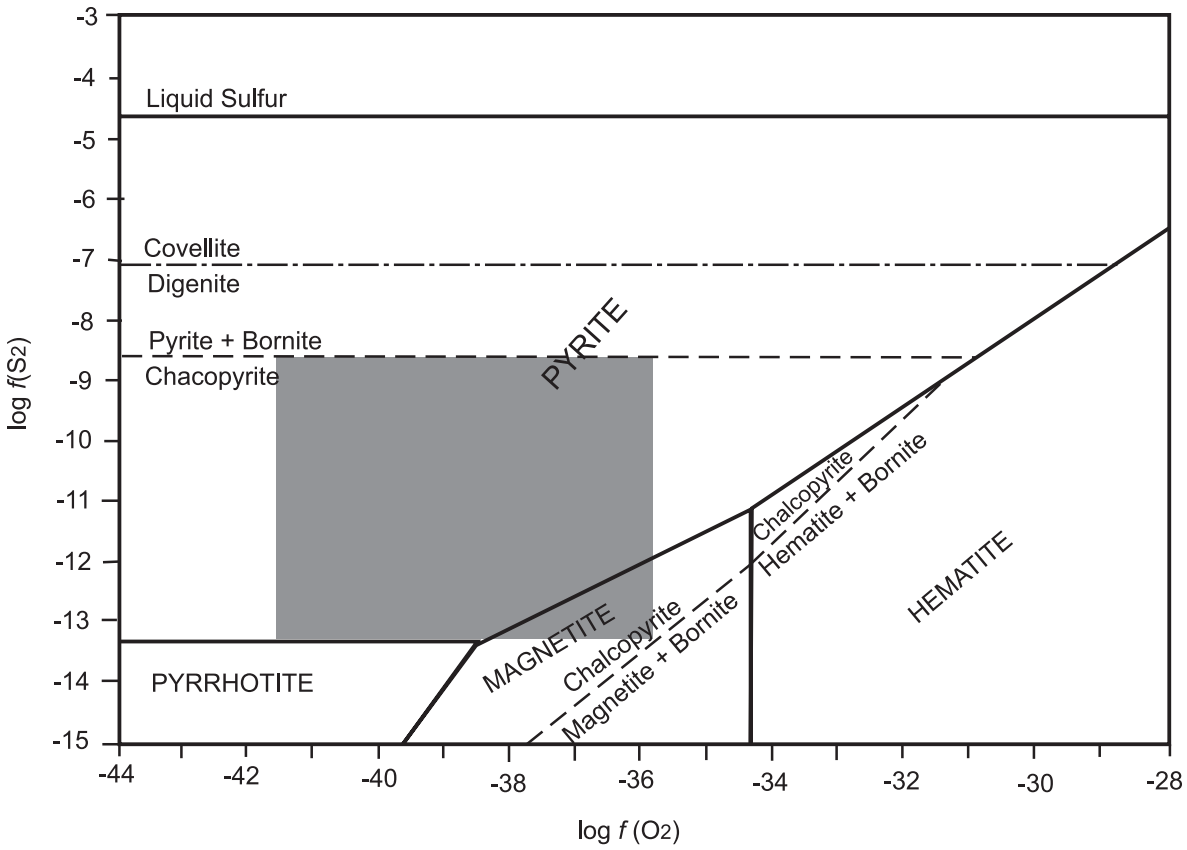

Figure 38. Mineral stability fields at 250º C for sulfide minerals (modified from Barton, 1984). The box represents the mineral assemblages present together in the skarn deposits. The oxygen fugacities from Figure 37 were applied to this graph to deliniate the shaded region.

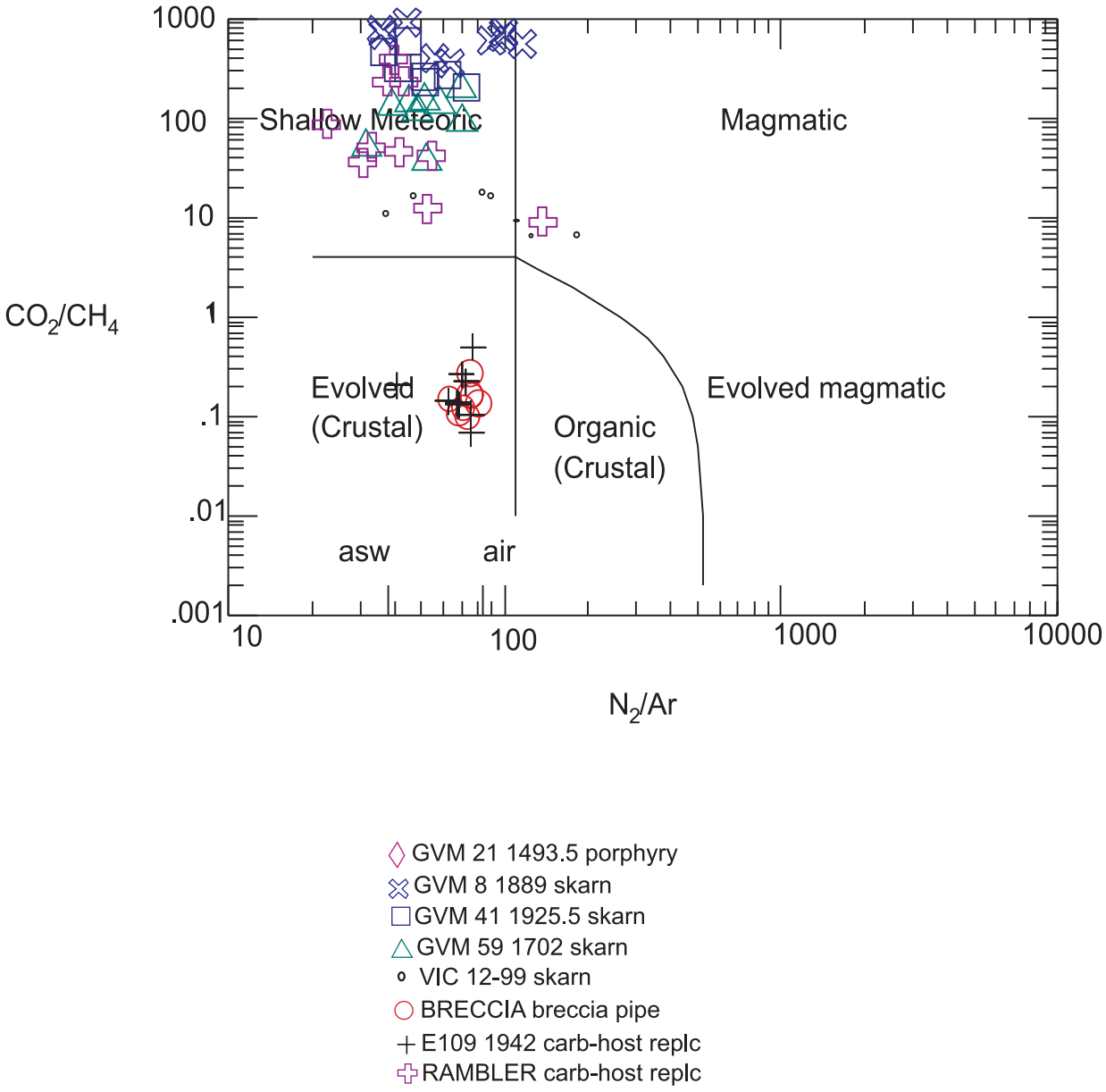

Figure 39. Fluid inclusion gas analysis results of CO_2/CH_4 vs. N_2/Ar showing the possible origins of the fluids. The fluid origin fields defined in Norman and Moore (1997).

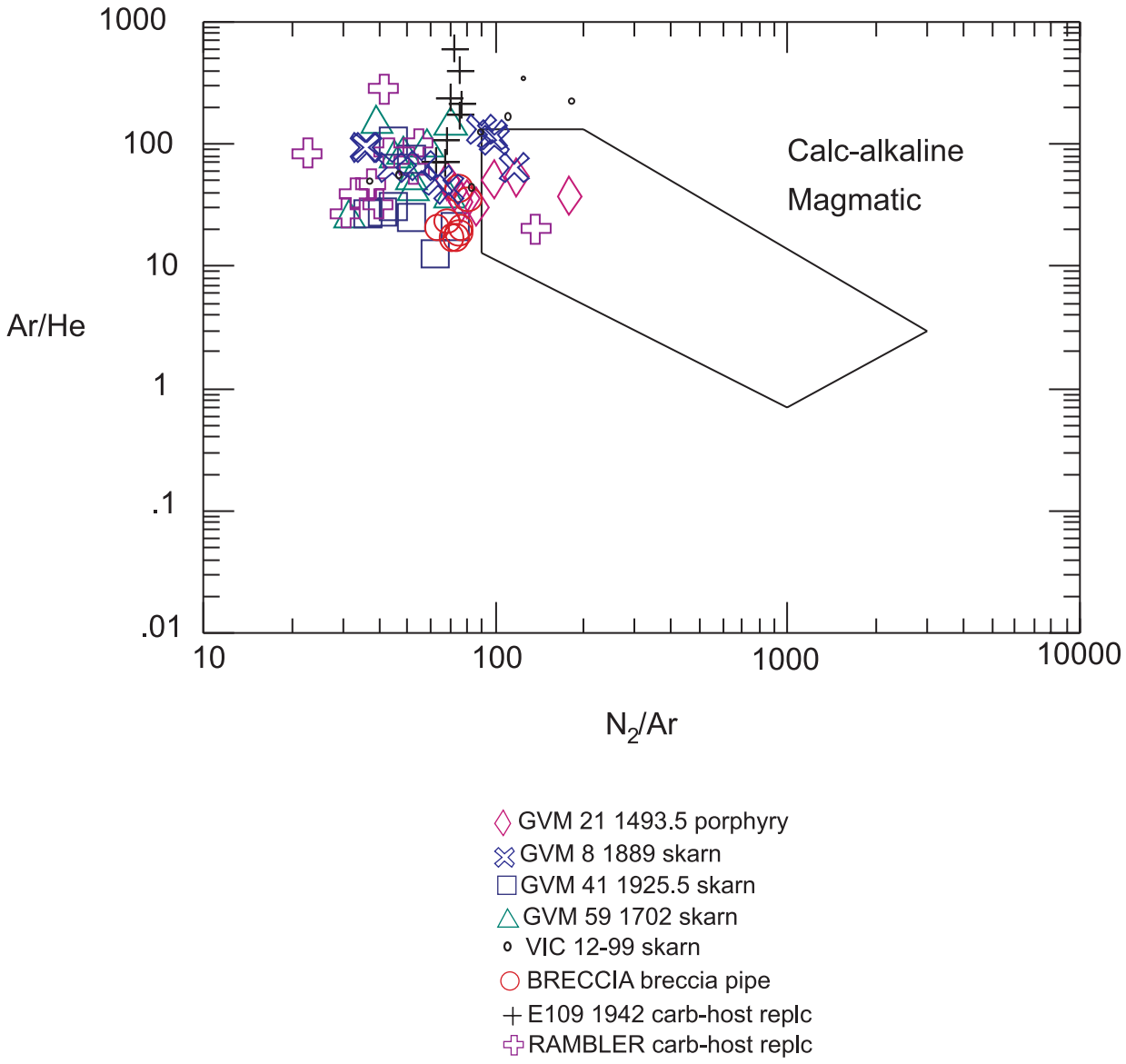

Figure 40. A plot of fluid inclusion gas analysis results ratios Ar/He vs. N_2/Ar showing the majority of the Victorio samples fall on the boundary and just outside the magmatic water box. Magmatic water box defined from Blamey and Norman (2002).

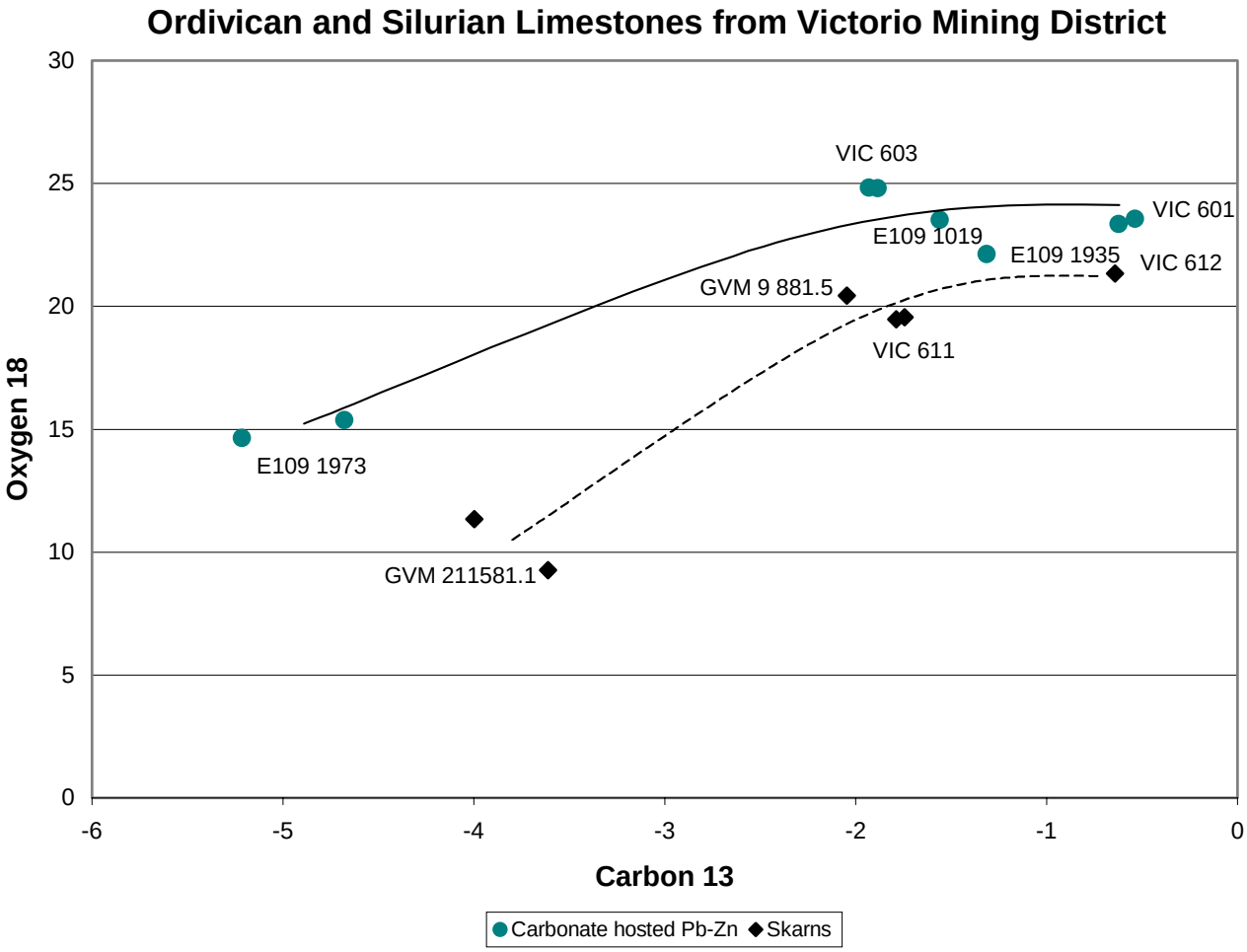

Figure 41. Carbon and oxygen isotope values from carbonate rocks showing different alteration trends between skarn and carbonate-hosted replacement deposit samples. VIC 601 and VIC 612 represent unaltered limestone samples. The trend lines shift different amounts from unaltered limestone.

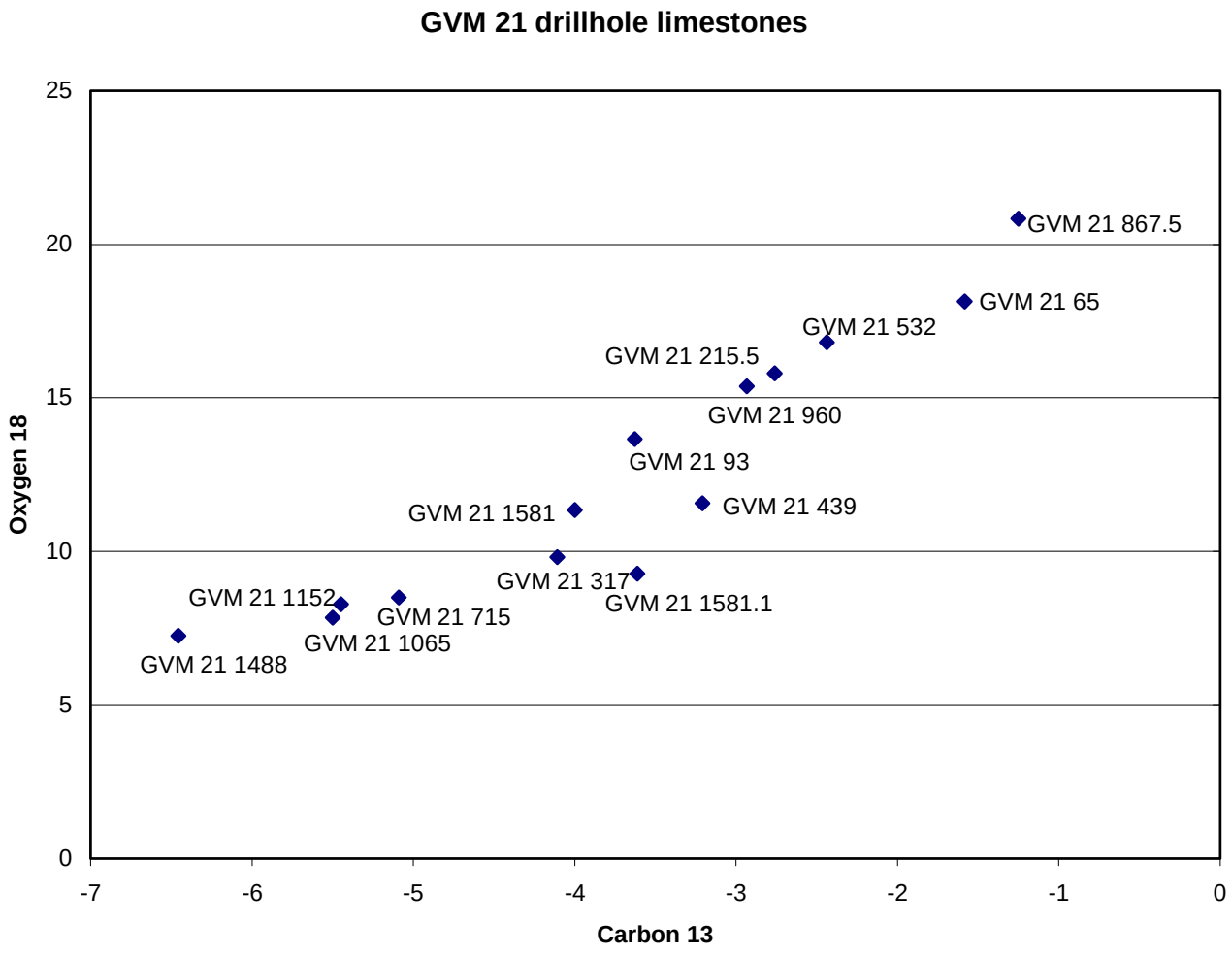

Figure 42. Carbon and oxygen stable isotope values from carbonate samples. There is no correlation between the oxygen and carbon isotope values and depth. The label is the drill hole GVM 21 drill hole followed by the depth from the top of the drill hole.

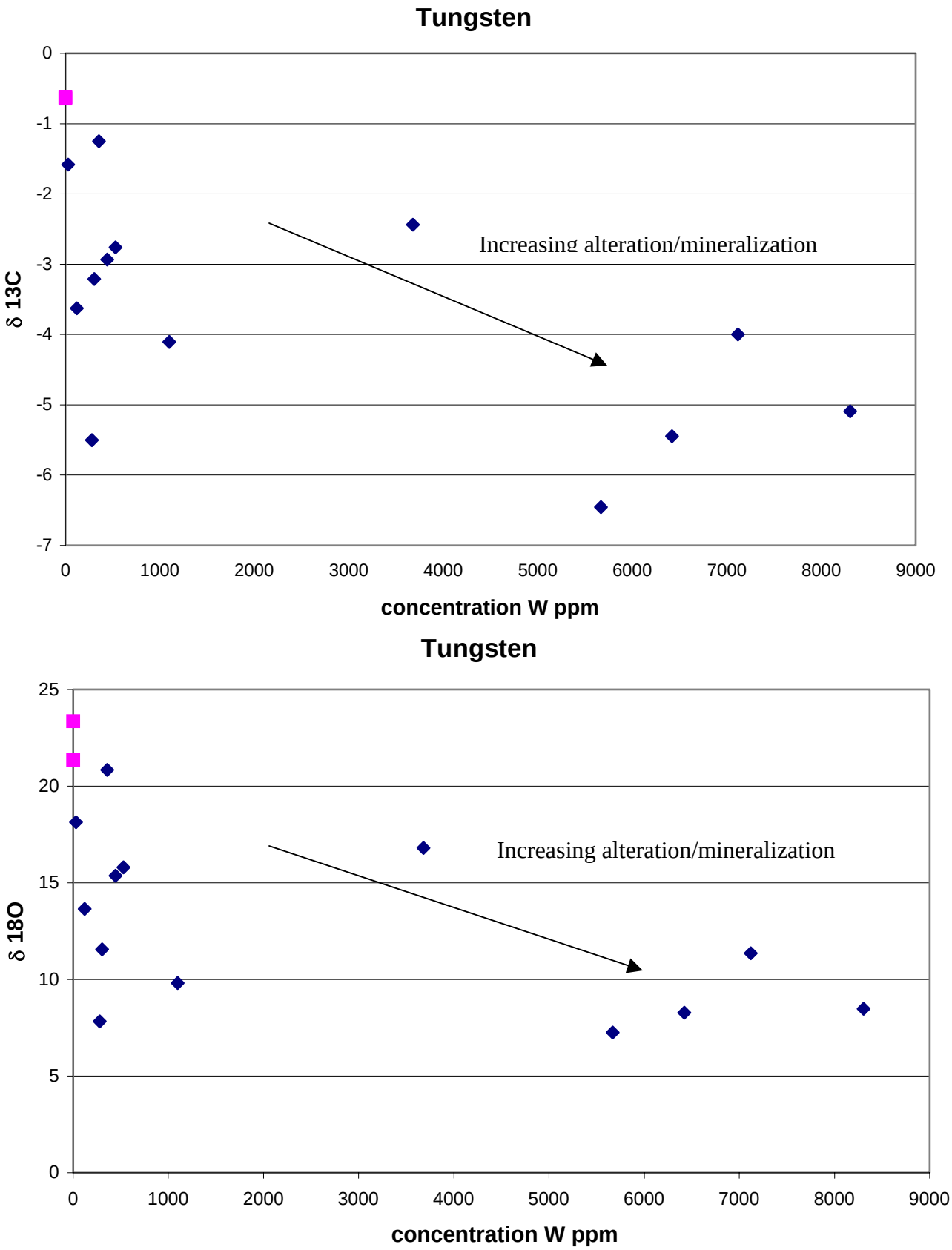

Figure 43. Carbon and oxygen isotope values versus tungsten concentrations. Concentrations are listed in ppm, isotopic values are listed in per mil. The squares represent unaltered limestone values. The metal concentrations are listed in Table 12.

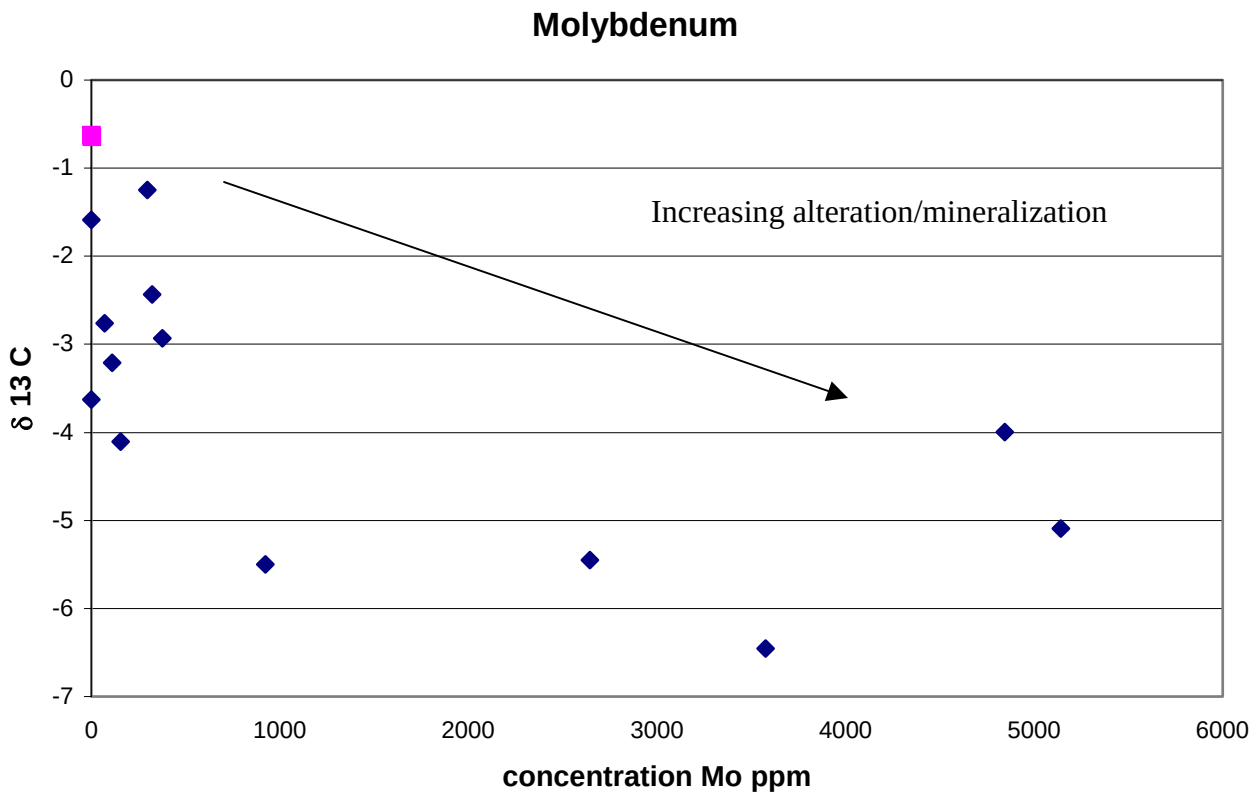

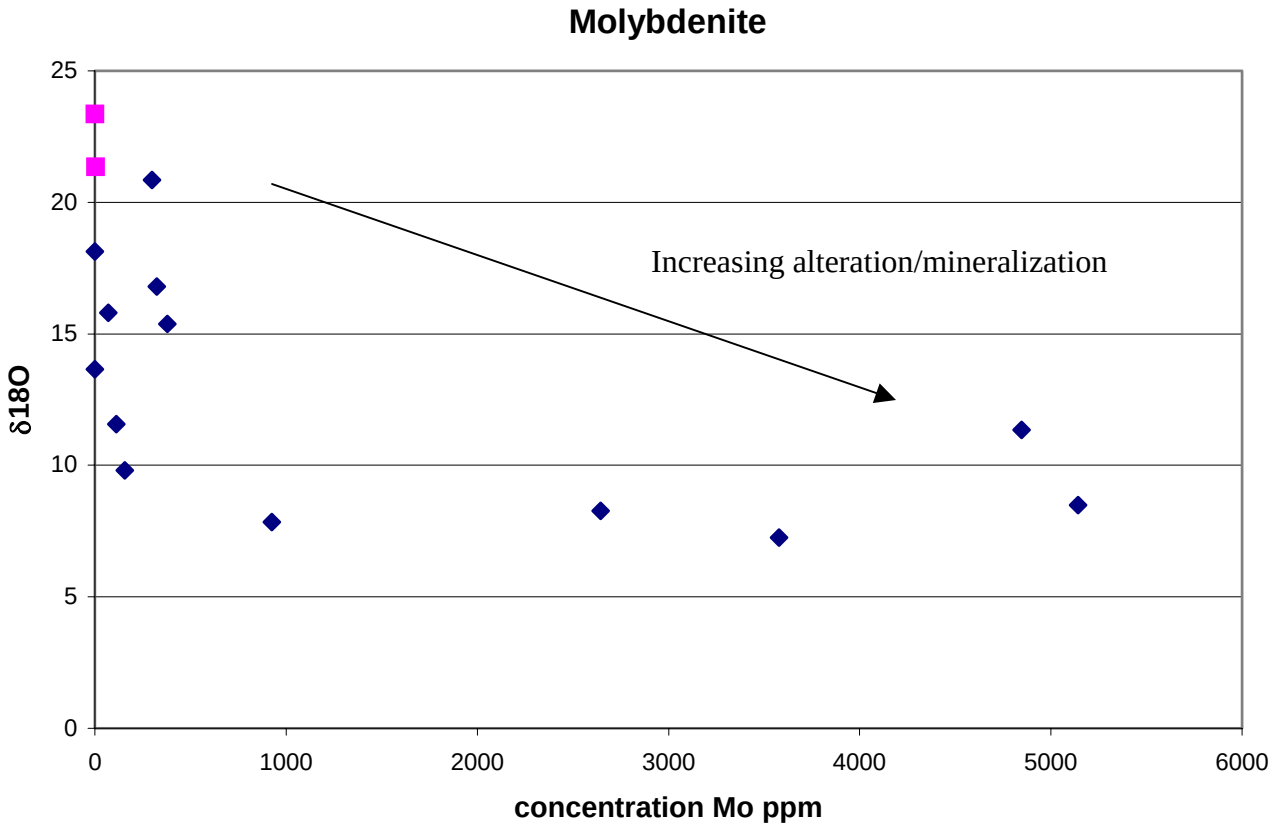

Figure 44. Carbon and oxygen isotope values versus molybdenum concentration. Concentrations are listed in ppm, isotopic values are listed in per mil. The squares represent unaltered limestone values. The metal concentrations are listed in Table 12.

Appendices

Appendix A. Argon geochronological analyses.
Appendix B. Fluid inclusion microthermometry analyses
Appendix C. Fluid inclusion gas analyses
Appendix D. Sample photographs

Appendix A. 1. Argon geochronology analyses for the Victorio Granite K-feldspar. No age assigned to this sample because of complexity of the age spectrum (Appendix A-3).

ID	Temp (°C)	$^{40}Ar/^{39}Ar$	$^{37}Ar/^{39}Ar$	$^{36}Ar/^{39}Ar$ (x 10^{-3})	$^{39}Ar_K$ (x 10^{-15} mol)	K/Ca	Cl/K (x 10^{-3})	$^{40}Ar^*$ (%)	^{39}Ar (%)	Age (Ma)	±2s (Ma)
GVM15 Pack8:124, K-feldspar											
A	510	340.4	0.0191	231.8	4.35	26.8	6.2	79.9	0.6	1230.8	3.6
B	510	11.72	0.0049	13.18	1.99	103.4	0.49	66.5	0.9	49.92	0.75
C	560	32.47	0.0043	24.01	4.76	119.6	0.53	78.1	1.5	157.50	0.67
D	560	6.872	0.0047	5.364	5.60	109.2	0.059	76.6	2.3	33.83	0.27
E	610	17.74	0.0062	13.76	11.5	82.2	0.64	76.9	3.9	86.45	0.38
F	610	5.263	0.0073	3.233	7.61	69.6	0.074	81.4	4.9	27.58	0.17
G	660	18.33	0.0122	13.54	10.7	41.9	0.90	78.0	6.4	90.56	0.32
H	660	5.187	0.0167	2.839	6.83	30.5	0.27	83.3	7.4	27.84	0.18
I	710	16.25	0.0254	11.70	9.77	20.1	0.93	78.6	8.7	81.02	0.31
J	710	5.069	0.0255	2.396	5.59	20.0	0.48	85.6	9.5	27.93	0.20
K	760	15.09	0.0281	10.76	6.94	18.1	1.2	78.8	10.5	75.54	0.31
L	760	4.653	0.0204	1.726	4.49	25.0	0.30	88.5	11.1	26.53	0.21
M	810	11.06	0.0127	7.110	6.77	40.1	0.76	80.8	12.0	57.07	0.30
N	810	4.496	0.0080	1.445	4.83	63.4	0.20	89.9	12.7	26.05	0.20
O	860	12.29	0.0101	8.692	4.10	50.7	0.97	78.9	13.3	61.89	0.37
P	910	12.04	0.0118	8.822	8.81	43.2	0.64	78.1	14.5	60.08	0.26
Q	960	7.842	0.0088	4.886	13.5	58.2	0.98	81.3	16.4	40.89	0.17
R	1010	7.480	0.0064	4.151	17.6	79.8	0.70	83.3	18.8	39.98	0.16
S	1060	7.095	0.0052	3.892	20.0	98.2	0.91	83.4	21.5	38.01	0.12
T	1110	8.400	0.0049	4.963	25.4	103.8	0.84	82.2	25.1	44.29	0.14
U	1160	9.507	0.0054	5.372	27.2	95.0	1.7	83.0	28.8	50.52	0.16
V	1160	9.668	0.0048	5.346	39.9	105.3	0.87	83.4	34.4	51.59	0.17
W	1160	8.609	0.0059	4.110	41.7	86.3	2.0	85.6	40.1	47.21	0.13
X	1160	8.649	0.0093	4.050	35.9	55.2	2.5	85.9	45.1	47.57	0.13
Y	1160	9.423	0.0040	5.374	39.5	126.9	3.8	82.9	50.6	49.98	0.14
Z	1160	11.38	0.0025	7.947	52.4	203.1	3.8	79.1	57.8	57.52	0.18
ZA	1310	14.41	0.0006	4.997	144.5	906.6	1.4	89.6	77.8	81.91	0.23
ZB	1360	13.67	0.0006	5.360	125.7	844.5	0.27	88.2	95.2	76.62	0.22
ZC	1460	12.85	0.0014	5.547	21.2	355.0	1.2	87.0	98.1	71.18	0.20
ZD	1560	12.09	0.0022	5.110	11.5	237.0	0.90	87.3	99.7	67.25	0.21
ZE	1760	17.04	0.0027	10.19	1.92	189.8	2.3	82.2	100.0	88.65	0.63
total gas age			n=31		722.6	398.5				70.31	0.22
plateau			n=31	steps A-ZE	722.6	398.5			100.0	48.6	3.8

Appendix A. Argon geochronology analyses for the Victorio Granite biotite samples. Ages assigned to these samples are the plateau ages (Appendix A-1). Steps not used in the calculation of the age are in italics.

ID	Temp (°C)	$^{40}Ar/^{39}Ar$	$^{37}Ar/^{39}Ar$	$^{36}Ar/^{39}Ar$ (x 10^{-3})	$^{39}Ar_K$ (x 10^{-15} mol)	K/Ca	Cl/K (x 10^{-3})	$^{40}Ar^*$ (%)	^{39}Ar (%)	Age (Ma)	±2s (Ma)
GVM15 2402, Biotite											
A	*600*	*37.63*	*0.6703*	*80.03*	*2.91*	*0.76*	*36.6*	*37.2*	*0.4*	*88.6*	*4.2*
B	*670*	*11.08*	*0.5223*	*12.53*	*3.60*	*0.98*	*16.1*	*66.7*	*1.0*	*47.3*	*2.1*
C	*740*	*8.106*	*0.3873*	*6.111*	*14.4*	*1.3*	*7.3*	*77.8*	*3.1*	*40.44*	*0.64*
D	*820*	*5.921*	*0.0308*	*1.372*	*55.2*	*16.6*	*5.6*	*92.7*	*11.2*	*35.26*	*0.17*
E	900	5.625	0.0060	0.9890	114.3	85.2	5.7	94.3	28.0	34.08	0.11
F	950	5.433	0.0090	0.4372	94.0	56.4	5.2	97.1	41.8	33.90	0.11
G	1000	5.416	0.0104	0.3579	75.1	49.0	5.4	97.6	52.8	33.94	0.12
H	1050	5.432	0.0159	0.3755	53.8	32.0	5.6	97.5	60.7	34.01	0.17
I	1100	5.447	0.0119	0.6723	141.0	42.9	6.4	95.9	81.4	33.548	0.086
J	*1150*	*4.829*	*0.0618*	*0.5930*	*57.8*	*8.3*	*9.9*	*95.9*	*89.9*	*29.78*	*0.16*
K	*1200*	*4.952*	*0.1964*	*0.7037*	*28.9*	*2.6*	*80.2*	*95.6*	*94.2*	*30.44*	*0.26*
L	*1350*	*5.613*	*0.1432*	*0.5098*	*39.6*	*3.6*	*9.8*	*97.1*	*100.0*	*34.98*	*0.22*
total gas age			n=12		680.6	41.3				33.99	0.17
plateau			n=5	steps E-I	478.3	55.4			70.3	33.84	0.12
GVM9 2056, Biotite											
A	*600*	*39.47*	*0.5453*	*73.89*	*4.84*	*0.94*	*25.1*	*44.7*	*0.7*	*111.1*	*2.8*
B	*670*	*9.591*	*0.2258*	*12.72*	*10.9*	*2.3*	*8.4*	*60.7*	*2.3*	*37.43*	*0.84*
C	740	6.713	0.0417	4.070	31.0	12.2	6.2	81.7	6.9	35.27	0.30
D	820	5.915	0.0136	1.371	71.1	37.5	5.2	92.7	17.5	35.26	0.15
E	900	5.758	0.0095	0.8086	141.7	53.9	4.7	95.4	38.5	35.309	0.098
F	950	5.687	0.0103	0.7439	83.4	49.7	4.7	95.7	50.8	34.98	0.12
G	1000	5.738	0.0164	0.7462	54.4	31.0	5.0	95.7	58.9	35.30	0.17
H	1050	5.791	0.0103	0.8790	86.2	49.6	4.8	95.1	71.7	35.39	0.13
I	*1100*	*5.962*	*0.0317*	*1.061*	*102.4*	*16.1*	*4.6*	*94.3*	*86.9*	*36.14*	*0.11*
J	*1150*	*6.042*	*0.1618*	*1.168*	*28.0*	*3.2*	*73.0*	*94.1*	*91.0*	*36.52*	*0.28*
K	*1200*	*5.842*	*0.4324*	*0.1902*	*23.5*	*1.2*	*6.0*	*99.2*	*94.5*	*37.24*	*0.36*
L	*1350*	*7.543*	*0.2961*	*1.109*	*36.9*	*1.7*	*7.8*	*95.6*	*100.0*	*46.24*	*0.25*
M	*1650*	*90.84*	*0.2750*	*64.66*	*0.210*	*1.9*	*97.2*	*79.0*	*100.0*	*414.3*	*38.5*
total gas age			n=13		674.4	33.6				36.81	0.20
plateau			n=6	steps C-H	467.8	44.5			69.4	35.24	0.09

Appendix A. Argon geochronology analyses for the Victorio Granite muscovite samples. Ages assigned to these samples are the plateau ages (Appendix A-2). Steps not used in the calculation of the age are in italics.

ID	Temp (°C)	$^{40}Ar/^{39}Ar$	$^{37}Ar/^{39}Ar$	$^{36}Ar/^{39}Ar$ (x 10^{-3})	$^{39}Ar_K$ (x 10^{-15} mol)	K/Ca	Cl/K (x 10^{-3})	$^{40}Ar^*$ (%)	^{39}Ar (%)	Age (Ma)	±2s (Ma)
GVM15 2402, Muscovite											
A	*600*	*37.42*	*0.6797*	*100.9*	*2.86*	*0.75*	*29.5*	*20.4*	*0.3*	*48.9*	*4.2*
B	*700*	*8.477*	*0.1768*	*9.094*	*6.39*	*2.9*	*7.2*	*68.2*	*0.9*	*37.0*	*1.4*
C	*750*	*6.619*	*0.0290*	*3.007*	*8.28*	*17.6*	*3.9*	*86.2*	*1.8*	*36.6*	*1.1*
D	*800*	*6.625*	*0.0090*	*3.481*	*10.2*	*56.7*	*4.1*	*84.1*	*2.8*	*35.72*	*0.89*
E	850	6.775	0.0046	4.780	27.5	111.5	1.8	78.8	5.5	34.23	0.37
F	900	6.346	0.0023	2.973	56.5	222.9	1.2	85.7	11.2	34.89	0.20
G	940	5.722	0.0009	0.9327	175.3	539.0	0.56	94.7	28.7	34.761	0.082
H	980	5.623	0.0005	0.6341	179.6	1024.7	0.46	96.2	46.6	34.693	0.085
I	1020	5.600	0.0004	0.6036	257.3	1436.9	0.34	96.3	72.3	34.604	0.078
J	1060	5.564	0.0006	0.5170	94.0	837.1	0.41	96.8	81.7	34.54	0.12
K	*1100*	*5.558*	*0.0005*	*0.1952*	*109.7*	*1061.8*	*0.52*	*98.5*	*92.6*	*35.11*	*0.10*
L	*1200*	*6.013*	*0.0068*	*1.624*	*16.4*	*74.5*	*104.5*	*91.6*	*94.2*	*35.32*	*0.57*
M	*1350*	*5.918*	*0.0082*	*1.160*	*19.4*	*61.9*	*1.8*	*93.8*	*96.2*	*35.58*	*0.47*
N	*1650*	*5.741*	*0.0015*	*0.9487*	*38.2*	*349.3*	*1.1*	*94.7*	*100.0*	*34.85*	*0.25*
total gas age			n=14		1001.5	874.2				34.83	0.16
plateau			n=6 steps E-J		790.1	939.7			78.9	34.667	0.072
GVM9 2056, Muscovite											
A	*600*	*83.00*	*0.5411*	*159.0*	*1.89*	*0.94*	*42.1*	*43.4*	*0.2*	*218.8*	*6.7*
B	*700*	*9.175*	*1.092*	*15.58*	*2.49*	*0.47*	*16.8*	*50.5*	*0.5*	*29.7*	*3.5*
C	*750*	*8.137*	*1.213*	*9.879*	*4.03*	*0.42*	*7.3*	*65.0*	*1.0*	*33.9*	*2.1*
D	*800*	*6.948*	*0.0390*	*5.973*	*5.61*	*13.1*	*2.7*	*74.3*	*1.7*	*33.0*	*1.5*
E	*850*	*6.833*	*0.0081*	*3.505*	*16.4*	*63.2*	*2.5*	*84.5*	*3.6*	*36.86*	*0.50*
F	900	6.112	0.0025	1.869	50.8	206.9	0.89	90.5	9.7	35.35	0.19
G	940	5.688	0.0010	0.6097	149.2	519.7	0.41	96.4	27.6	35.023	0.079
H	980	5.616	0.0004	0.5029	123.2	1293.1	0.20	96.9	42.3	34.767	0.097
I	1020	5.602	0.0002	0.2730	175.9	2683.0	0.31	98.1	63.3	35.110	0.082
J	1060	5.530	0.0007	0.1340	95.2	766.4	0.36	98.8	74.7	34.91	0.11
K	*1100*	*5.531*	*0.0005*	*-0.0648*	*99.5*	*1071.1*	*0.68*	*99.9*	*86.6*	*35.29*	*0.10*
L	*1200*	*5.536*	*0.0038*	*0.1401*	*31.7*	*133.1*	*63.7*	*98.8*	*90.4*	*34.94*	*0.27*
M	*1650*	*5.601*	*0.0005*	*0.0520*	*80.2*	*1047.5*	*1.1*	*99.3*	*100.0*	*35.51*	*0.12*
total gas age			n=13		836.2	1181.9				35.50	0.16
plateau			n=5 steps F-J		594.3	1333.1			71.1	34.99	0.09

Appendix A. Argon geochronology analyses for the skarn alteration biotite samples (Fig.23, Appendix A-4) . Ages assigned to these samples are plateau ages. Steps not used in the age calculation are in itailics.

ID	Temp (°C)	$^{40}Ar/^{39}Ar$	$^{37}Ar/^{39}Ar$	$^{36}Ar/^{39}Ar$ (x 10^{-3})	$^{39}Ar_K$ (x 10^{-15})	K/Ca	Cl/K (x 10^{-3})	$^{40}Ar^*$ (%)	^{39}Ar (%)	Age (Ma)	±2s (Ma)
GVM 21 1278, 6.33 mg biotite											
A	*650*	*2894.3*	*-0.6036*	*9774.9*	*0.000*	*-*	*414.4*	*0.2*	*0.0*	*8.0*	*339.2*
AA	*650*	*1021.6*	*1.775*	*3251.3*	*0.043*	*0.29*	*3.0*	*6.0*	*0.3*	*82.7*	*14.4*
B	*750*	*152.9*	*1.311*	*411.4*	*0.135*	*0.39*	*-0.758*	*20.5*	*1.0*	*43.0*	*3.3*
C	*850*	*39.61*	*0.4768*	*42.57*	*0.704*	*1.1*	*0.75*	*68.3*	*5.1*	*37.14*	*0.56*
D	920	30.04	0.3724	13.29	1.94	1.4	0.65	87.0	16.3	35.88	0.20
E	1000	27.31	0.4709	4.431	4.07	1.1	0.60	95.3	39.8	35.74	0.15
F	1075	27.06	0.6193	3.439	3.56	0.82	0.69	96.4	60.3	35.82	0.15
G	*1110*	*29.57*	*1.351*	*4.147*	*2.28*	*0.38*	*0.61*	*96.2*	*73.5*	*39.05*	*0.18*
H	*1180*	*28.23*	*0.9910*	*3.018*	*2.36*	*0.51*	*0.62*	*97.1*	*87.2*	*37.62*	*0.17*
I	*1210*	*27.27*	*0.1273*	*2.380*	*0.516*	*4.0*	*1.2*	*97.5*	*90.1*	*36.46*	*0.33*
J	*1250*	*26.31*	*0.0668*	*1.625*	*1.09*	*7.6*	*0.33*	*98.2*	*96.4*	*35.45*	*0.20*
K	*1300*	*26.90*	*0.0445*	*2.901*	*0.430*	*11.5*	*1.1*	*96.8*	*98.9*	*35.73*	*0.37*
L	*1650*	*29.47*	*0.1430*	*12.74*	*0.186*	*3.6*	*0.13*	*87.3*	*100.0*	*35.30*	*0.71*
total gas age			n=13		17.3	1.7				36.69	0.26
plateau		MSWD = 0.15	n=3	steps D-F	9.6	1.0			55.2	35.80	0.19*
GVM 59 1702, 9.25 mg biotite											
A	*650*	*413.3*	*0.0674*	*1317.4*	*0.036*	*7.6*	*2.6*	*5.8*	*0.1*	*33.1*	*10.7*
B	*750*	*70.28*	*0.0185*	*134.2*	*0.195*	*27.6*	*-0.389*	*43.6*	*0.8*	*42.0*	*1.6*
C	*850*	*35.40*	*0.0052*	*29.26*	*1.39*	*98.1*	*0.88*	*75.6*	*5.3*	*36.80*	*0.33*
D	920	27.74	0.0028	6.212	3.51	183.5	0.66	93.4	16.6	35.63	0.16
E	1000	26.32	0.0058	1.784	3.35	88.5	0.62	98.0	27.5	35.49	0.15
F	1075	26.58	0.0122	2.201	2.91	41.8	0.47	97.6	36.9	35.68	0.17
G	1110	26.61	0.0112	2.690	2.40	45.4	0.49	97.0	44.6	35.52	0.16
H	1180	27.07	0.0121	4.140	3.58	42.0	0.46	95.5	56.2	35.56	0.18
I	1210	26.69	0.0130	2.745	4.45	39.2	0.58	97.0	70.7	35.61	0.15
J	1250	26.46	0.0320	2.180	4.33	15.9	0.37	97.6	84.7	35.52	0.14
K	1300	26.22	0.0576	1.338	3.39	8.9	0.74	98.5	95.7	35.54	0.14
L	*1650*	*27.12*	*0.0618*	*3.440*	*1.34*	*8.3*	*0.62*	*96.3*	*100.0*	*35.92*	*0.19*
total gas age			n=12		30.9	56.6				35.68	0.19
plateau			n=8	steps D-K	27.9	57.1			90.4	35.57	0.10

Appendix A. Argon geochronology analyses for the skarn alteration muscovite samples (Fig. 22). Ages assigned to these samples are the plateau ages. Steps not used in the calculation of the age are in italics.

ID	Temp (°C)	$^{40}Ar/^{39}Ar$	$^{37}Ar/^{39}Ar$	$^{36}Ar/^{39}Ar$ (x 10^{-3})	$^{39}Ar_K$ (x 10^{-15})	K/Ca	Cl/K (x 10^{-3})	$^{40}Ar^*$ (%)	^{39}Ar (%)	Age (Ma)	±2σ (Ma)
GVM 41 1925.5 9.53 mg muscovite											
A	*600*	*1742.9*	*0.6099*	*5827.1*	*0.038*	*0.84*	*3.6*	*1.2*	*0.1*	*28.9*	*16.8*
B	*650*	*113.1*	*3.259*	*320.4*	*0.052*	*0.16*	*9.7*	*16.5*	*0.2*	*25.8*	*3.7*
C	*700*	*70.68*	*5.751*	*0.0007*	*0.006*	*0.089*	*-34.703*	*100.7*	*0.2*	*96.5*	*23.6*
D	*775*	*113.1*	*1.057*	*292.5*	*0.504*	*0.48*	*0.003*	*23.6*	*1.4*	*36.7*	*1.3*
E	*825*	*48.10*	*0.0045*	*74.70*	*1.60*	*113.1*	*0.49*	*54.1*	*5.1*	*35.76*	*0.40*
F	875	28.03	0.0021	8.935	4.08	248.9	0.47	90.6	14.6	34.89	0.18
G	900	26.21	0.0015	2.922	3.94	333.2	0.41	96.7	23.8	34.83	0.14
H	925	26.17	0.0010	2.093	5.25	510.9	0.52	97.6	36.1	35.11	0.14
I	975	25.97	0.0006	2.385	10.0	826.9	0.41	97.3	59.5	34.72	0.14
J	1010	25.82	0.0004	1.634	7.90	1197.4	0.45	98.1	78.0	34.82	0.14
K	1050	26.26	0.0018	2.356	2.94	276.3	0.42	97.3	84.8	35.13	0.16
L	*1110*	*25.97*	*0.0026*	*1.134*	*3.38*	*197.7*	*0.62*	*98.7*	*92.7*	*35.23*	*0.16*
M	*1200*	*27.13*	*0.0168*	*4.585*	*0.609*	*30.4*	*0.28*	*95.0*	*94.1*	*35.41*	*0.35*
N	*1300*	*26.12*	*0.0249*	*0.8874*	*0.421*	*20.5*	*1.0*	*99.0*	*95.1*	*35.54*	*0.40*
O	*1650*	*26.04*	*0.0337*	*1.473*	*2.09*	*15.1*	*0.38*	*98.3*	*100.0*	*35.19*	*0.17*
total gas age			n=15		42.8	571.6				34.98	0.20
plateau			n=6	steps F-K	34.1	690.5			79.7	34.91	0.17
GVM 21 1490, 8.65 mg muscovite											
A	*600*	*6769.8*	*1.431*	*22602.2*	*0.005*	*0.36*	*32.2*	*1.3*	*0.0*	*122.1*	*116.7*
B	*650*	*152.1*	*5.963*	*454.7*	*0.035*	*0.086*	*-4.875*	*12.0*	*0.1*	*25.2*	*5.5*
C	*700*	*27.6295*	*0.6090*	*111.2*	*0.000*	*0.84*	*44.7*	*218.7*	*0.1*	*-85.8*	*220.9*
D	*775*	*135.0*	*9.056*	*366.1*	*0.341*	*0.056*	*0.25*	*20.4*	*1.0*	*38.1*	*2.0*
E	*825*	*61.05*	*0.0312*	*117.2*	*1.40*	*16.3*	*0.61*	*43.3*	*4.5*	*36.25*	*0.59*
F	*875*	*29.02*	*0.0070*	*11.59*	*3.91*	*73.1*	*0.51*	*88.2*	*14.4*	*35.14*	*0.18*
G	*900*	*26.51*	*0.0054*	*3.167*	*3.82*	*94.9*	*0.40*	*96.5*	*24.1*	*35.12*	*0.15*
H	925	26.01	0.0037	2.518	4.99	139.6	0.48	97.1	36.7	34.69	0.16
I	975	26.46	0.0020	3.360	8.46	260.8	0.53	96.2	58.2	34.97	0.16
J	1010	26.56	0.0004	4.004	7.98	1309.9	0.52	95.5	78.4	34.85	0.17
K	*1050*	*26.57*	*0.0003*	*3.491*	*4.20*	*1465.3*	*0.68*	*96.1*	*89.0*	*35.07*	*0.15*
L	*1110*	*25.95*	*0.0011*	*0.9232*	*3.46*	*473.8*	*0.61*	*98.9*	*97.8*	*35.25*	*0.15*
M	*1200*	*27.38*	*-0.0014*	*6.019*	*0.299*	*-*	*0.66*	*93.5*	*98.5*	*35.15*	*0.45*
N	*1300*	*26.25*	*-0.0066*	*-1.1958*	*0.130*	*-*	*2.3*	*101.3*	*98.9*	*36.52*	*0.80*
O	*1650*	*27.44*	*0.0017*	*3.401*	*0.453*	*296.0*	*1.2*	*96.3*	*100.0*	*36.29*	*0.39*
total gas age			n=15		39.5	556.0				35.07	0.22
plateau			n=3	steps H-J	21.4	623.3			54.3	34.83	0.20

Appendix A. 1. Argon geochronology analyses for the skarn alteration K-feldspar sample (Appendix A-4). No age assigned to this sample because of complexity of the age spectrum.

ID	Temp (°C)	$^{40}Ar/^{39}Ar$	$^{37}Ar/^{39}Ar$	$^{36}Ar/^{39}Ar$ (x 10^{-3})	$^{39}Ar_K$ (x 10^{-16} mol)	K/Ca	Cl/K (x 10^{-3})	$^{40}Ar^*$ (%)	^{39}Ar (%)	Age (Ma)	±2s (Ma)
GVM 21 1278 Kspar, K-feldspar											
A	505	1291.9	0.0091	1184.3	2.79	56.1	-1.526	72.9	0.5	968.7	3.4
B	505	95.49	0.0068	118.8	1.49	75.5	0.95	63.2	0.7	80.40	0.86
C	505	58.41	0.0059	57.54	1.24	86.6	0.71	70.9	0.9	55.51	0.71
D	555	333.7	0.0080	101.8	3.51	63.8	0.29	91.0	1.5	372.2	1.1
E	555	35.80	0.0090	14.30	2.77	56.7	-0.112	88.2	2.0	42.48	0.30
F	555	31.26	0.0151	8.096	2.19	33.9	-0.157	92.4	2.4	38.88	0.35
G	605	136.6	0.0119	28.83	4.49	43.0	0.36	93.8	3.2	166.46	0.46
H	605	31.09	0.0105	5.688	4.47	48.6	0.25	94.6	3.9	39.60	0.18
I	605	26.60	0.0071	3.158	3.83	72.0	0.51	96.5	4.6	34.61	0.20
J	655	71.25	0.0056	16.78	5.39	91.6	0.41	93.0	5.5	88.07	0.26
K	655	28.78	0.0027	3.284	6.08	187.3	0.26	96.6	6.5	37.47	0.14
L	655	26.27	0.0015	1.889	5.48	341.8	0.39	97.9	7.5	34.67	0.16
M	705	36.29	0.0014	5.477	6.78	364.0	0.56	95.5	8.6	46.59	0.17
N	705	24.45	0.0015	1.698	7.61	343.2	0.67	97.9	9.9	32.31	0.13
O	705	23.80	0.0009	0.8905	6.60	587.8	0.32	98.9	11.0	31.77	0.13
P	755	26.21	0.0008	0.5070	6.33	631.7	0.64	99.4	12.1	35.13	0.16
Q	755	23.51	0.0018	0.7880	8.12	284.5	0.47	99.0	13.5	31.41	0.11
R	755	23.03	0.0008	0.4571	7.08	635.0	0.90	99.4	14.7	30.90	0.12
S	805	24.23	0.0017	1.797	6.64	293.4	0.94	97.8	15.9	31.98	0.13
T	805	22.92	0.0013	0.9196	7.63	398.3	0.61	98.8	17.2	30.58	0.12
U	805	22.58	0.0010	-0.0930	6.60	506.9	0.77	100.1	18.3	30.52	0.12
V	855	25.06	0.0009	1.024	5.63	572.7	0.56	98.8	19.2	33.39	0.16
W	855	23.21	0.0002	-0.4148	6.85	2380.8	0.53	100.5	20.4	31.48	0.13
X	905	30.03	0.0009	2.787	7.86	591.3	0.69	97.3	21.8	39.33	0.12
Y	905	27.85	0.0010	1.892	8.72	521.2	0.48	98.0	23.3	36.78	0.12
Z	955	43.66	0.0008	8.101	10.2	641.9	0.79	94.5	25.0	55.32	0.13
ZA	955	39.49	0.0007	5.448	12.1	688.0	0.78	95.9	27.0	50.85	0.12
ZB	1005	56.80	0.0019	10.36	16.1	273.2	0.52	94.6	29.8	71.71	0.14
ZC	1005	48.22	0.0014	7.691	18.3	371.8	0.77	95.3	32.9	61.49	0.11
ZD	1055	59.81	0.0016	10.64	22.9	320.0	0.49	94.7	36.8	75.54	0.13
ZE	1055	47.37	0.0015	6.928	22.8	332.3	0.68	95.7	40.7	60.66	0.11
ZF	1105	58.82	0.0019	9.508	26.5	269.0	0.38	95.2	45.3	74.68	0.13
ZG	1105	47.36	0.0013	5.506	23.6	395.0	0.66	96.6	49.3	61.20	0.10
ZH	1155	52.48	0.0021	6.808	17.2	247.7	0.78	96.2	52.2	67.43	0.12
ZI	1155	53.66	0.0011	5.954	23.7	468.5	0.61	96.7	56.3	69.31	0.11
ZJ	1155	55.65	0.0007	6.436	59.7	738.9	0.63	96.6	66.5	71.724	0.084
ZK	1155	59.30	0.0007	7.061	42.7	765.2	0.39	96.5	73.7	76.25	0.11
ZM	1255	73.43	0.0005	7.492	63.2	1054.4	0.63	97.0	84.5	94.44	0.15
ZN	1355	69.98	0.0005	7.835	80.7	986.7	0.56	96.7	98.3	89.84	0.17
ZO	1455	61.50	0.0022	8.985	7.56	230.7	0.79	95.7	99.6	78.38	0.23
ZP	1750	58.25	0.0179	21.51	2.35	28.5	0.57	89.1	100.0	69.30	0.47
total gas age			n=41		585.8	613.6				74.79	0.16
plateau			n=41	steps A-ZP	585.8	613.6			100.0	53.2	3.4

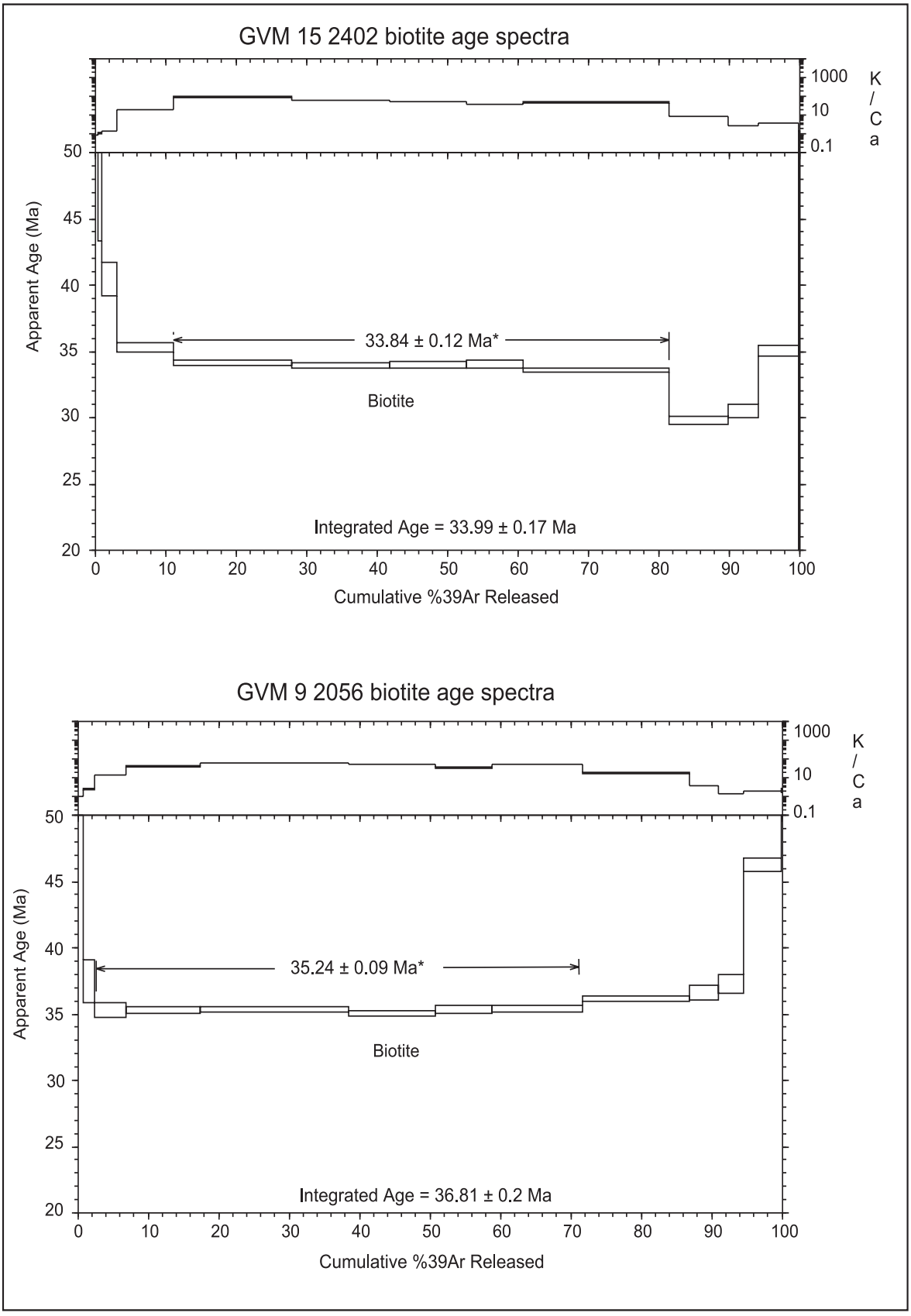

Appendix A-1 Age spectra for Victorio granite GVM 15 2402 and GVM 9 2056 biotite mineral samples.

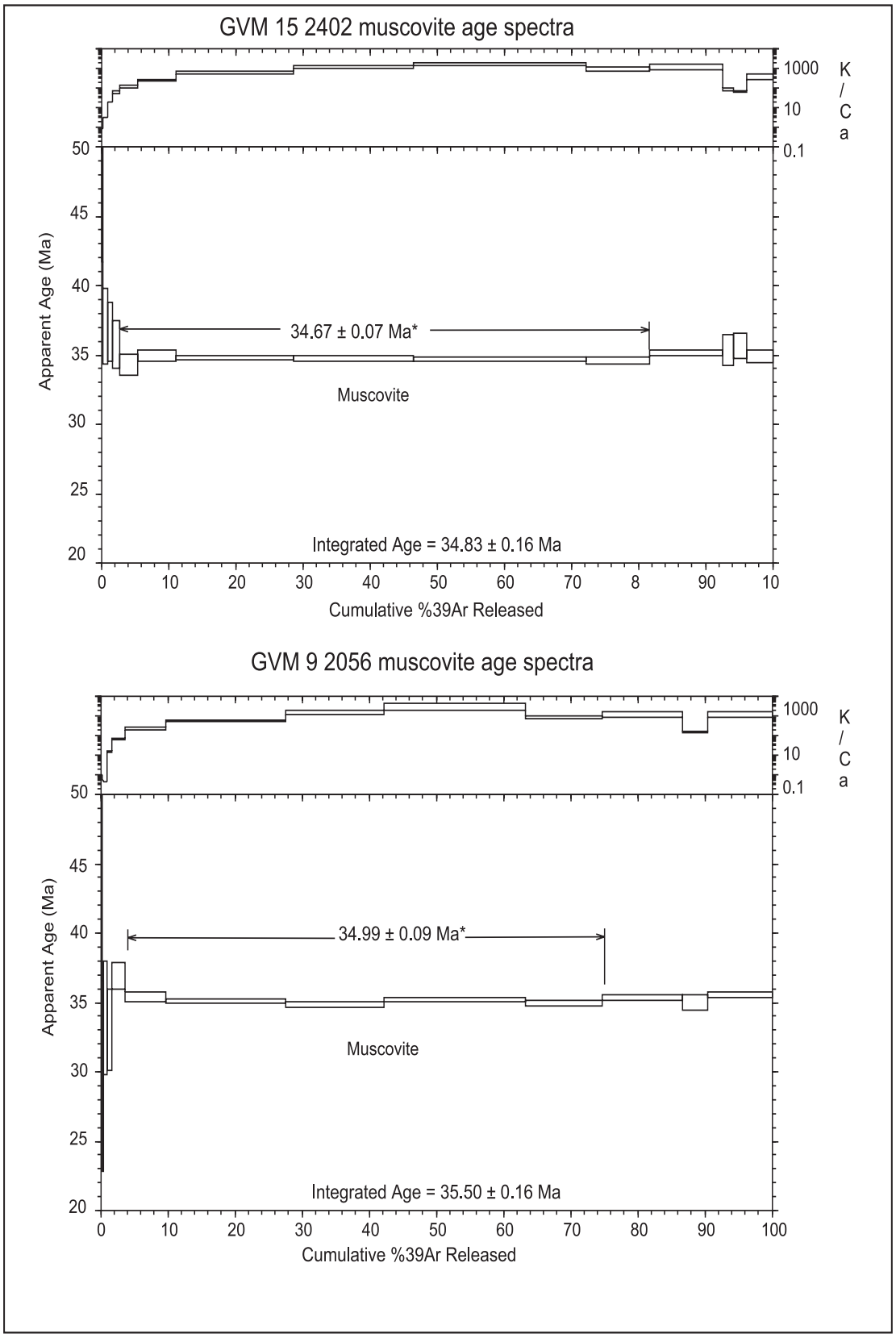

Appendix A-2. Age spectra for Victorio granite GVM 15 2402 and GVM 9 2056 muscovite mineral samples.

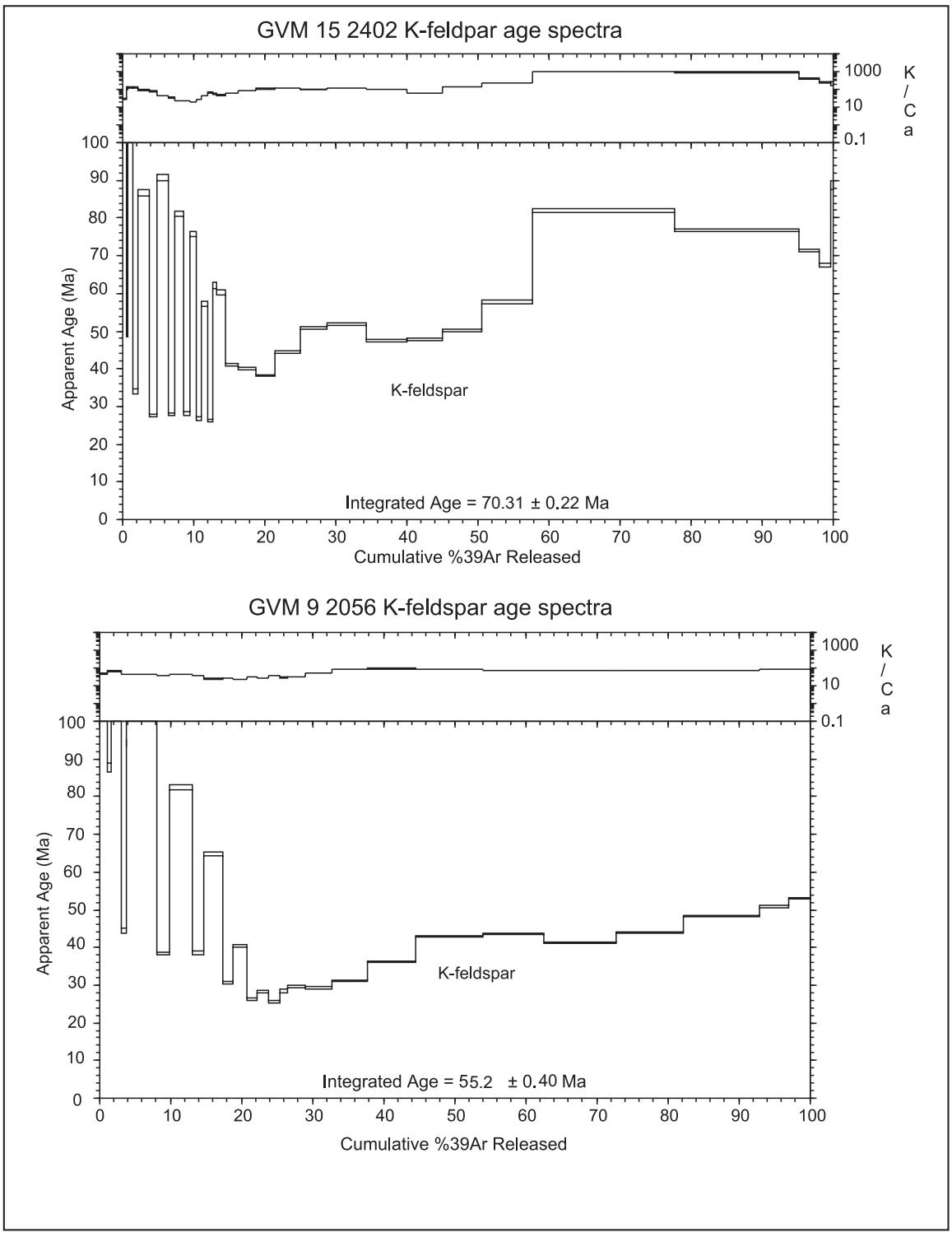

Appendix A-3. Age spectra for Victorio granite GVM 15 2402 and GVM 9 2056 K-feldspar mineral samples. The age spectra for GVM 9 2056 does not represent the entire age spectra because the gas was catastrophically lost during analysis.

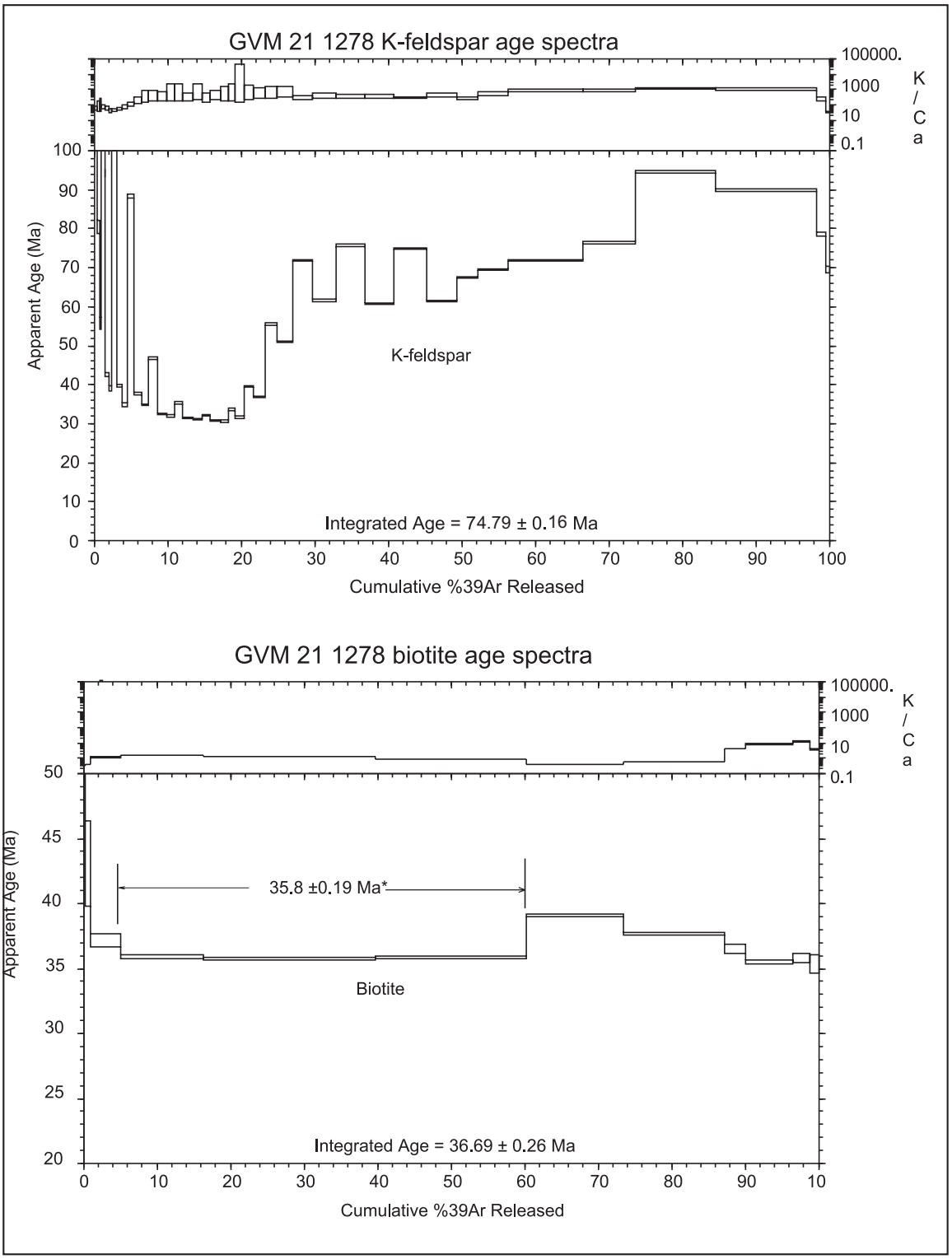

Appendix A-4. Age spectra for skarn alteration samples GVM 21 1278 K-feldspar and biotite. The K-feldspar age spectra was not assigned a plateau age

Appendix B: Fluid inclusion measurements and notes. P = primary, S = secondary, PS = psuedosecondary. Th= homogenization temperature
Tm clath = melting temp of clatherite, Tm ice = melting temp of ice, Tm CO2 = melting temp of CO2 ice, Th hh = homgenization temp of hydrohalite
Te = temp of first melting. All temperatures reported in degrees celsius. Values in parentheses are values entered into Flincor because measured values parameters were not within the program.

sample number	mineral	inclusion	% fill	P or S	phase	Th	Tm clath	Tm ice	Tm CO_2	Th hh	Th CO_2	Te
GVM 2 553	flourite	1	0.87	S	L + V + S -> L	180.7		-10.7				-46.9
chip #1		2	0.75	S	L + V + S -> L	190.1		-10.7				-38.5
		3	0.80	S	L + V + S -> L	181.3		-10.6				-41.5
		4	0.80	S	L + V + S -> L	180.9		-10.6				
		5	0.83	S	L + V + S -> L	184.2		-10.5				
		6	0.90	PS	L + V + S -> L	181.1		-4.9				
		7	0.87	PS	L + V + S -> L	186.7		-4.8				
GVM 2 1499	quartz	1	0.85	PS	LCO2 + L + V -> L	260.1	6.8		-56.6		33.2 (30.97)	-54.1
chip #1		2	0.85	PS	LCO2 + L + V -> L	221.2	8.4		-56.6		33.4 (30.97)	-53.3
		3	0.90	S	LCO2 + L + V -> L	285.0	6.8		-56.1		32.8 (30.97)	
		4	0.75	S	LCO2 + L + V -> L	285.0	7.3		-56.2		30.0	
		5	0.60	S	L +V -> L	285.0	6.0					
		6	0.95	S	L +V -> L	315.2	6.8					
GVM 8 1889	quartz	1	0.83	P	LCO2 + L + V -> L	334.0	7.2	-6.3	-56.2		31.4 (30.97)	
		2	0.77	P	LCO2 + L + V -> L	340.6	7.3		-56.3		31.4 (30.97)	
		3	0.68	P	LCO2 + L + V -> L	320.0	7.0	-8.6	-55.8		29.6	
		4	0.63	P/PS	LCO2 + L + V -> L	320.0	7.1	-9.1	-56.0		28.1	
		5	0.90	P	L + V -> L	219.0		-3.5				
		6	0.93	P	L + V -> L	199.3		-3.3				
		7	0.90	P	L + V -> L	200.9		-3.5				
GVM 8 2250	quartz	1	0.95	S	L + V ->.L	166.5		-4.6				
		2	0.90	S	L + V ->.L	244.9		-4.5				
		3	0.90	S	L + V ->.L	313.9		-4.6				
		4	0.93	S	L + V ->.L	185.7		-2.3				
		5	0.85	S	L + V ->.L			8.9				
GVM 15 2337	quartz	1	0.60	S	LCO2 + L + V -> L	291.2	7.0		-54.6		31.0	
chip #1		2	0.80	S	LCO2 + L + V -> L	223.2	6.8		-54.1		31.0	
		3	0.75	S	LCO2 + L + V -> L	195.8	5.3		-54.1		31.0	
		4	0.85	S	LCO2 + L + V -> L	181.2	5.0		-53.8		31.0	
		5	0.70	S	LCO2 + L + V -> L	266.2	4.3		-56.3		33.2 (30.97)	
		6	0.60	S	LCO2 + L + V -> L	272.0	5.2		-56.2		34.0 (30.97)	
chip#2		1	0.85	S	LCO2 + L + V -> L	271.8	6.8		-57.1		33.7 (30.97)	
		2	0.70	PS	L + V -> L	259.8	5.4					

Appendix B: Fluid inclusion measurements and notes. P = primary, S = secondary, PS = psuedosecondary. Th= homogenization temperature
Tm clath = melting temp of clatherite, Tm ice = melting temp of ice, Tm CO2 = melting temp of CO2 ice, Th hh = homgenization temp of hydrohalite
Te = temp of first melting. All temperatures reported in degrees celsius. Values in parentheses are values entered into Flincor because measured values parameters were not within the program.

sample number	mineral	inclusion	% fill	P or S	phase	Th	Tm clath	Tm ice	Tm CO_2	Th hh	Th CO_2	Te
GVM 21 1168.1	flourite	1	0.75	PS/P	L + V ->.L	193.2		-18.7				
		2	0.85	PS/P	L + V ->.L	192.7		-18.6				
		3	0.80	PS/P	L + V ->.L	193.7		-18.5				
		4	0.80	PS/P	L + V ->.L	193.1		-18.6				
		5	0.80	PS/P	L + V ->.L	188.8		-18.9				
GVM 21 1278	fluorite	1	0.80	S	LCO2 + L + V -> L	281.4	7.4		-59.7		31.5	
		2	0.75	S	LCO2 + L + V -> L	281.3	7.5		-59.7		31.3	
		3	0.73	S	LCO2 + L + V -> L	275.3	7.5		-59.6		31.1	
		4	0.83	S	LCO2 + L + V -> L	280.9	7.4		-59.7		31.1	
		5	0.40	S	LCO2 + L + V -> LCO2	208.1	10.1		-59.8		30.7	
		6	all co2	S	LCO2 + L + V -> L		7.4		-59.7		30.9	
		7	0.85	S	LCO2 + L + V -> L	280.1	7.4		-59.7		31.2	
		8	0.87	S	LCO2 + L + V -> L	280.5			-15.7		30.8	
GVM 21 1297	quartz	1	0.93	P(S)?	LCO2 + L + V -> L	171.2	7.1				31.3	
		2	0.90	P(S)?	LCO2 + L + V -> L	219.4	7.8				31.3	
		3	0.93	P(S)?	LCO2 + L + V -> L	235.6	7.8				30.3	
		4	0.91	P(S)?	LCO2 + L + V -> L	237.1	7.9				30.1	
		5	0.87	P(S)?	LCO2 + L + V -> L	248.5	7.2		-56.0		30.1	
		6	0.85	P(S)?	LCO2 + L + V -> L	236.5	8.0					
		7	0.70	P(S)?	LCO2 + L + V -> L						30.1	
GVM 21 1493.5	qtz grain	1	0.93	P	L + V -> L			-5.7		-7.1		
		2	0.78	P	L + V -> L	223.4						
		A	0.90	PS	L + V -> L	decrpt	5.3					
		B	0.87	P	L + V -> L	208.9	3.7					
		C	0.67	P	LCO2 + L + V -> L	275.2				-9.7		
		3	0.75	P	LCO2 + L + V -> L	300.0	3.5					
	veinlett	5	0.95	P	LCO2 + L + V -> L	178.6	9.0	-5.0				
		5a	0.97	P	L + V -> L	248.6		-5.0				
		6	0.75	PS	LCO2 + L + V -> L	215.0	8.3		-56.1		28.5	
		7	0.80	P	L + V -> L	decrpt		-5.3				
	vein qtz	8	0.77	P	LCO2 + L + V -> L	275.1	7.7		-60.3		31.3	
		9	0.55	P ?	LCO2 + L + V -> L	280.0	7.1		-60.4		22.9	
		10	0.75	P	LCO2 + L + V -> L	325.0	7.6		-60.4		30.5	
		11	0.85	PS/S	LCO2 + L + V -> L	decrpt	7.5		-60.4		30.4	

Appendix B: Fluid inclusion measurements and notes. P = primary, S = secondary, PS = psuedosecondary. Th= homogenization temperature
Tm clath = melting temp of clatherite, Tm ice = melting temp of ice, Tm CO2 = melting temp of CO2 ice, Th hh = homgenization temp of hydrohalite
Te = temp of first melting. All temperatures reported in degrees celsius. Values in parentheses are values entered into Flincor because measured values parameters were not within the program.

sample number	mineral	inclusion	% fill	P or S	phase	Th	Tm clath	Tm ice	Tm CO_2	Th hh	Th CO_2	Te
GVM 41 1925.5	quartz	1	0.70	P	L_{CO2} + L + V -> L	349.4	7.8	-6.0	-57.1		30.1	
chip #3		2	0.75	P	L_{CO2} + L + V -> L	> 360 (350)	8.2		-56.8		30.7	
		3	0.85	P	LCO2 + L + V -> L	293.8	9.7		-56.7		30.4	
		4	0.87	P	LCO2 + L + V -> L	306.2	7.4		-56.8		30.0	
chip #1	quartz	1	0.80	P	LCO2 + L + V -> L	280.9	8.1	-7.1	56.7		30.3	
		2	0.73	P	LCO2 + L + V -> L	290.1	9.3	-4.2	-56.4		30.8	
		3	0.75	P	LCO2 + L + V -> L	263.3	9.1	-4.1	-56.8		30.0	
		4	0.80	P	LCO2 + L + V -> L	276.8	8.9	-3.9	-57.1		30.1	
		5	0.80	P	LCO2 + L + V -> L	245.9	8.5	-3.4	56.0		30.9	
		6	0.85	P	LCO2 + L + V -> L	262.7	9.4	-3.8	-57.0	-4.0	30.1	
		1	0.82	P	LCO2 + L + V -> L	284.1	9.4		-57.1	-6.5		
		2	0.87	P	LCO2 + L + V -> L	281.0	7.3					
GVM 41 2073.10	quartz	1	0.75	P	LCO2 + L + V -> L	279.8	10.1 (10.0)		-56.9		30.8	
		2	0.77	P	LCO2 + L + V -> L	280.0	9.7		-56.6		29.9	
		3	0.87	P	LCO2 + L + V -> L	310.0	9.5		-56.6		30.6	
		4	0.83	P	LCO2 + L + V -> L	267.9	9.5	-4.8	-56.8		30.7	
		5	0.87	P	LCO2 + L + V -> L	234.9	9.8	-3.5			30.5	
		6	0.89	P	LCO2 + L + V -> L	273.3	5.8		-56.3		30.4	
		7	0.93	S	L + V -> L	195.8		-7.5				
		8	0.90	S	L + V -> L	195.7		-7.5				
		9	0.95	S	L + V -> L	196.4		-7.4				

sample number	mineral	inclusion	% fill	P or S	phase	Th	Tm clath	Tm ice	Tm CO_2	Th hh	Th CO_2	Te
GVM 59 1702	quartz	1	0.92	S	L + V -> L	214.8		-4.0				
		2	0.90	S	L + V -> L	215.9		-1.4				
		3	0.87	S	L + V -> L	218.1		-6.8				
		4	0.95	S	L + V -> L	178.2		-6.6				
		5	0.91	S	L + V -> L	207.8		-0.2				
		6	0.85	S	L + V -> L	227.5		-6.5				
		7	0.87	S	L + V -> L	223.3		-6.5				
		8	0.90	S	L + V -> L	232.3		-6.7				

Appendix B: Fluid inclusion measurements and notes. P = primary, S = secondary, PS = psuedosecondary. Th= homogenization temperature
Tm clath = melting temp of clatherite, Tm ice = melting temp of ice, Tm CO2 = melting temp of CO2 ice, Th hh = homgenization temp of hydrohalite
Te = temp of first melting. All temperatures reported in degrees celsius. Values in parentheses are values entered into Flincor because measured values parameters were not within the program.

sample number	mineral	inclusion	% fill	P or S	phase	Th	Tm clath	Tm ice	Tm CO_2	Th hh	Th CO_2	Te
GVM 65 1902	quartz	1	0.75	P	L + V -> L	253.2	6.3					
chip #1		2	0.93	PS/P	L + V -> L	233.5	-6.4					-55.2
		3	0.90	P	L + V -> L	235.8	5.8					
		4	0.85	P	L + V -> L	247.2	9.8					
		5	0.80	P	L + V -> L	237.1	4.1					
		6	0.85	P	L + V -> L	222.1						
		7	0.80	P	L + V -> L	210.3						
chip#2		1	0.90	P	L + V -> L	225.0	3.9					-17.3
		2	0.85	P	L + V -> L	237.4	5.9					-18.4
		3	0.90	P	L + V -> L	220.0	4.3					-22.1
		4	0.90	P	L + V -> L	226.1	3.4					-18.2
		5	0.80	P	L + V -> L	269.5	8.2					
		1	0.85	S	LCO2 + L + V -> L	273.6	6.4		-56.6	-5.0	31.3	
		2	0.87	S	L + V -> L	232.9		-4.7		-5.6		
		3	0.77	PS/P	LCO2 + L + V -> L	268.1				-5.8	31.8	
GVM A3 2007	quartz	1	0.80	P	LCO2 + L + V -> L	260.1	7.9				31.0 (30.97)	
chip # 1		2	0.85	P	LCO2 + L + V -> L	>200	6.0	-4.1			24.8	
		3	0.75	P	L + v -> L	258.8		-3.4				
		4	0.80	P	L + v -> L	187.2		-3.3				
		5	0.90	P	L + v -> L	182.3	8.1	-3.9				
		6	0.92	P	L + v -> L	184.9	8.3	-4.1				
		7	0.95	P	L + v -> L	151.1		-0.3				
VIC 12-99	quartz	1	0.90	PS	LCO2 + L + V -> L	250.1	10.7 (10.0)	-3.8	-56.7		31.0	
		2	0.80	PS	LCO2 + L + V -> L	230.1	9.2	-4.0			31.0	
		3	0.45	S	LCO2 + L + V -> L	263.5	10.7 (10.0)	-9.8	-58.1		23.0	
		4	0.87	S	L + V ->.L	249.3	9.4	-3.0				
		5	0.85	S	L + V ->.L	274.8	9.7	-5.1	-58.6		23.0	
		1	0.93	P	L + V ->.L	199.9	3.1	-6.9				
		2	0.85	P	L + V ->.L	264.1	8.9					
		3	0.85	P	L + V ->.L	258.0	9.2					
		4	0.75	P	L + V ->.L	270.1	9.4					
		5	0.73	P	L + V ->.L	263.1	7.9					
		6	0.55	P	LCO2 + L + V -> L	260.0	7.5					
		7	0.70	P	L + V ->.L	decrep	7.6					
		8	0.60	P	LCO2 + L + V -> L	decrep	9.1	-9.6	-55.6			

Appendix B: Fluid inclusion measurements and notes. P = primary, S = secondary, PS = psuedosecondary. Th= homogenization temperature
Tm clath = melting temp of clatherite, Tm ice = melting temp of ice, Tm CO2 = melting temp of CO2 ice, Th hh = homgenization temp of hydrohalite
Te = temp of first melting. All temperatures reported in degrees celsius. Values in parentheses are values entered into Flincor because measured values parameters were not within the program.

sample number	mineral	inclusion	% fill	P or S	phase	Th	Tm clath	Tm ice	Tm CO_2	Th hh	Th CO_2	Te
VIC 149-99	quartz	1	0.93	P/PS	L + V -> L	168.6		-1.0				
		2	0.95	P/PS	L + V -> L	109.1		-0.8				
	chip #2	1	0.85	P/PS	L + V -> L	207.2		-2.2				
		2	0.85	P/PS	L + V -> L	175.8		-2.3				
		3	0.83	S	L + V -> L	213.7		-1.7				
		4	0.90	S	L + V -> L	203.7		-2.4				
		5	0.85	P	L + V -> L	282.2		-1.4				
		6	0.80	P	L + V -> L	235.2		-2.3				
Vic 601	quartz	1	0.60	PS	LCO2 + VCO2 -> LCO2				-55.7		31.3	
		2	0.75	PS	LCO2 + VCO2 -> LCO2				-55.7		31.3	
		3	0.75	PS	LCO2 + VCO2 -> LCO2				-55.7		31.3	
		4	0.80	PS	LCO2 + VCO2 -> LCO2				-55.7		31.3	
		5	0.95	S	L + V -> L	157.9		-0.7				
		6	0.90	S	L + V -> L	178.5		-0.5				
VIC 605	quartz	1	0.93	P?	L + V -> L	217.9		-6.5				
		2	0.90	P?	L + V -> L	218.1		-6.5				
		3	0.93	PS	L + V -> L	198.9		-6.5				
		4	0.95	PS	L + V -> L	189.1		-6.5				
		5	0.93	PS	L + V -> L	205.7		-6.5				
		6	0.93	PS	L + V -> L	204.1		-6.5				
		7	0.90	S	L + V -> L	188.6		-3.8				
		8	0.92	S	L + V -> L	188.4		-3.5				
BRECCIA	quartz	1	0.93	S	L + V -> L	217.0		-7.0		-23.4		
		2	0.93	S	L + V -> L	217.1		-8.3		-23.0		
		3	0.95	S	L + V -> L	219.2		-7.3		-22.9		
		4	0.95	S	L + V -> L	219.9		-8.0		-23.4		
		5	0.90	S	L + V -> L	219.0		-7.0		-19.3		
		6	0.97	S	L + V -> L	187.9		-7.5		-18.5		
		7	0.90	S	L + V -> L	214.8		-6.5				
		8	0.95	S	L + V -> L	201.9		-4.9		-20.9		

Appendix B: Fluid inclusion measurements and notes. P = primary, S = secondary, PS = psuedosecondary. Th= homogenization temperature
Tm clath = melting temp of clatherite, Tm ice = melting temp of ice, Tm CO2 = melting temp of CO2 ice, Th hh = homgenization temp of hydrohalite
Te = temp of first melting. All temperatures reported in degrees celsius. Values in parentheses are values entered into Flincor because measured values parameters were not within the program.

sample number	mineral	inclusion	% fill	P or S	phase	Th	Tm clath	Tm ice	Tm CO_2	Th hh	Th CO_2	Te
Rambler	quartz	1	0.75	PS	L + V -> L	350.0		-0.5				
		2	0.95	PS	L + V -> L	152.0		-0.8				
		3	0.93	PS	L + V -> L	155.1		-0.8				
		4	0.50	PS	L + V -> L	336.9		-0.4				
E109 1935	calcite	1	0.93	P	L + V -> L	244.5		-6.8				
		2	0.90	P	L + V -> L	248.9		-6.8				
		3	0.87	P	L + V -> L	253.6		-6.8				
		4	0.91	P	L + V -> L	243.4		-6.9				
		5	0.90	P	L + V -> L	257.6		-6.8				
		6	0.92	P	L + V -> L	253.1		-6.8				
		7	0.90	P	L + V -> L	255.6		-6.8				
E109 1942	quartz	1	0.95	S	L + V -> L	206.9		-14.0				
		2	0.95	S	L + V -> L	179.9		-13.8				
		3	0.97	S	L + V -> L	154.5						
		4	0.90	S	L + V -> L	228.2		-15.9				
		5	0.80	S	L + V -> L	152.3		-8.3				
		6	0.90	S	L + V -> L	151.1		-7.6				
		7	0.85	S	L + V -> L	155.9		-8.9				
		8	0.85	S	L + V -> L	161.1		-9.0				
		9	0.95	S	L + V -> L	201.1		-15.7				

Appendix B2: Input and output data from the Flincor program used to calculate fluid salinity, density, and other chemical properties. Th = homogenization temperature, Tm = melt temperature, MV = molar volume, Den = density, Aqu = aqueous density. Th L-V = homogenization between the liquid and vapor phases, Th total = the final homogenization temperature for the fluid inclusion.

Sample	Inclusion	Tm ice/clath	Th L-V	Th Total	Th CO2 L-V	VolFrac Vap	CO2 VolFrac	CO2 Den	CO2 MV	Aqu. Den
GVM 2 553	1	-10.7	180.7			0.13				
GVM 2 553	2	-10.7	190.1			0.25				
GVM 2 553	3	-10.6	181.3			0.2				
GVM 2 553	4	-10.6	180.9			0.2				
GVM 2 553	5	-10.5	184.2			0.17				
GVM 2 553	6	-4.9	181.1			0.1				
GVM 2 553	7	-4.8	186.7			0.13				
GVM 2 1499	1	6.8		260.1	30.97		0.15	0.52	84.648	1.035
GVM 2 1499	2	8.4		221.2	30.97		0.15	0.52	84.648	1.013
GVM 2 1499	3	6.8		285	30.97		0.1	0.52	84.648	1.035
GVM 2 1499	4	7.3		285	30		0.25	0.596	73.894	1.029
GVM 2 1499	5	6		285	30.97		0.4	0.52	84.648	1.046
GVM 2 1499	6	6.8		315.2	30.97		0.05	0.52	84.648	1.035
GVM 7 1823	1	8.3		265.5	30.97		0.25	0.52	84.648	1.015
GVM 7 1823	2	3.7		226.69	30.97		0.1	0.52	84.648	1.073
GVM 7 1823	3	7.8		279.5	30.97		0.25	0.52	84.648	1.022
GVM 7 1823	4	6.7		219.2	30.97		0.07	0.52	84.648	1.037
GVM 7 1823	5	6.7		251.1	30.397		0.13	0.575	76.475	1.037
GVM 7 1823	6	6.5		251.8	30.97		0.13	0.52	84.648	1.039
GVM 7 1823	7	6.7		246.7	30.97		0.15	0.52	84.648	1.037
GVM 7 1823	8	6.8		244.4	30.97		0.1	0.52	84.648	1.035
GVM 8 1889	1	7.2		339	30.97		0.17	0.52	84.648	1.03
GVM 8 1889	2	7.3		340.6	30.97		0.23	0.52	84.648	1.029
GVM 8 1889	3	7		320	29.6		0.32	0.611	71.973	1.033
GVM 8 1889	4	7.1		320	28.1		0.37	0.654	67.267	1.032
GVM 8 1889	5	-3.5	219			0.1				
GVM 8 1889	6	-3.3	199.3			0.07				
GVM 8 1889	7	-3.5	200.9			0.1				
GVM 8 2250	1	-4.6	166.5			0.05				
GVM 8 2250	2	-4.5	244.9			0.1				
GVM 8 2250	3	-4.6	317.9			0.1				
GVM 8 2250	4	-2.3	185.7			0.07				

Appendix B2: cont. Input and output data from the Flincor program used to calculate fluid salinity, density, and other chemical properties. Th = homogenization temperature, Tm = melt temperature, MV = molar volume, Den = density, Aqu = aqueous density. Th L-V = homogenization between the liquid and vapor phases, Th total = the final homogenization temperature for the fluid inclusion.

Sample	Molal NaCl	Wt% NaCl	X(NaCl)	Crit.Temp.	Crit.Press.	Bulk XH2O	Bulk XCO2	Bulk XNaCl	Bulk Den	Bulk MV
GVM 2 553	2.94	14.67	0.05	509	582				0.997	20.1
GVM 2 553	2.94	14.67	0.05	509	582				0.988	20.28
GVM 2 553	2.92	14.57	0.05	508	579				0.996	20.12
GVM 2 553	2.92	14.57	0.05	508	579				0.996	20.11
GVM 2 553	2.89	14.47	0.05	507	577				0.992	20.19
GVM 2 553	1.42	7.68	0.02	445	408				0.944	19.94
GVM 2 553	1.39	7.54	0.02	444	404				0.937	20.08
GVM 2 1499	1.098	6.028	0.019			0.945	0.036	0.019	0.958	20.581
GVM 2 1499	0.556	3.147	0.01			0.954	0.037	0.01	0.939	20.603
GVM 2 1499	1.098	6.028	0.019			0.958	0.023	0.019	0.984	19.704
GVM 2 1499	0.93	5.154	0.016			0.909	0.076	0.015	0.921	22.375
GVM 2 1499	1.363	7.376	0.024			0.854	0.125	0.021	0.836	26.468
GVM 2 1499	1.098	6.028	0.019			0.97	0.011	0.019	1.01	18.898
GVM 7 1823	0.59	3.334	0.011			0.923	0.067	0.01	0.891	22.614
GVM 7 1823	2.095	10.91	0.036			0.941	0.023	0.036	1.018	19.7
GVM 7 1823	0.761	4.256	0.014			0.921	0.067	0.013	0.896	22.606
GVM 7 1823	1.131	6.2	0.02			0.964	0.016	0.02	1.001	19.212
GVM 7 1823	1.131	6.2	0.02			0.946	0.034	0.019	0.977	20.149
GVM 7 1823	1.197	6.541	0.021			0.948	0.031	0.02	0.972	20.218
GVM 7 1823	1.131	6.2	0.02			0.944	0.036	0.019	0.959	20.58
GVM 7 1823	1.098	6.028	0.019			0.958	0.023	0.019	0.984	19.704
GVM 8 1889	0.964	5.331	0.017			0.942	0.042	0.016	0.943	20.958
GVM 8 1889	0.93	5.154	0.016			0.924	0.06	0.015	0.912	22.165
GVM 8 1889	1.031	5.681	0.018			0.878	0.106	0.016	0.898	23.859
GVM 8 1889	0.997	5.507	0.018			0.848	0.137	0.015	0.892	24.859
GVM 8 1889	1.02	5.62	0.02	426	355				0.891	21.13
GVM 8 1889	0.96	5.32	0.02	423	348				0.907	20.75
GVM 8 1889	1.02	5.62	0.02	426	355				0.911	20.67
GVM 8 2250	1.34	7.25	0.02	441	397				0.955	19.71
GVM 8 2250	1.31	7.11	0.02	440	393				0.873	21.55
GVM 8 2250	1.34	7.25	0.02	441	397				0.764	24.63
GVM 8 2250	0.67	3.76	0.01	409	308				0.911	20.22

Appendix B2: cont. Input and output data from the Flincor program used to calculate fluid salinity, density, and other chemical properties. Th = homogenization temperature, Tm = melt temperature, MV = molar volume, Den = density, Aqu = aqueous density. Th L-V = homogenization between the liquid and vapor phases, Th total = the final homogenization temperature for the fluid inclusion.

Sample	Inclusion	Tm ice/clath	Th L-V	Th Total	Th CO2 L-V	VolFrac Vap	CO2 VolFrac	CO2 Den	CO2 MV	Aqu. Den
GVM 15 2337	1	7		291	30.97		0.4	0.52	84.648	1.033
GVM 15 2337	2	6.8		223.2	30.97		0.2	0.52	84.648	1.035
GVM 15 2337	3	5.3		195.8	30.97		0.25	0.52	84.648	1.055
GVM 15 2337	4	5		181.2	30.97		0.15	0.52	84.648	1.058
GVM 15 2337	5	4.3		266.2	30.97		0.3	0.52	84.648	1.067
GVM 15 2337	6	5.2		272	30.97		0.4	0.52	84.648	1.056
GVM 15 2337	7	6.8		271.8	30.97		0.15	0.52	84.648	1.035
GVM 15 2337	8	5.4		259.8	30.97		0.3	0.52	84.648	1.053
GVM 21 1168.1	1	-18.7	193.2			0.25				
GVM 21 1168.1	2	-18.6	192.7			0.15				
GVM 21 1168.1	3	-18.5	193.7			0.2				
GVM 21 1168.1	4	-18.6	193.1			0.2				
GVM 21 1168.1	5	-18.9	188.8			0.2				
GVM 21 1278	1	7.4		281.4	30.97		0.2	0.52	84.648	1.027
GVM 21 1278	2	7.5		281.3	30.97		0.25	0.52	84.648	1.026
GVM 21 1278	3	7.5		275.3	30.97		0.27	0.52	84.648	1.026
GVM 21 1278	4	7.4		280.9	30.97		0.17	0.52	84.648	1.027
GVM 21 1278	5	10		208.1	30.97		0.6	0.52	84.648	0.99
GVM 21 1278	6	-59.7		85.119128	0		30.9			
GVM 21 1278	7	7.4		280.1	30.97		0.15	0.52	84.648	1.027
GVM 21 1278	8	7.4		280.5	30.8		0.13	0.544	80.837	1.027
GVM 21 1297	1	7		171.2	30.97		0.07	0.52	84.648	1.033
GVM 21 1297	2	7.1		219.4	30.97		0.1	0.52	84.648	1.031
GVM 21 1297	3	7.8		235.6	30.97		0.07	0.52	84.648	1.022
GVM 21 1297	4	7.8		237.1	30.3		0.09	0.581	75.752	1.022
GVM 21 1297	5	7.9		248.5	30.1		0.13	0.591	74.462	1.021
GVM 21 1297	6	7.2		230	30.97		0.15	0.52	84.648	1.03
GVM 21 1297	7	8		236.5	30.1		0.3	0.591	74.462	1.019

Appendix B2: cont. Input and output data from the Flincor program used to calculate fluid salinity, density, and other chemical properties.
Th = homogenization temperature, Tm = melt temperature, MV = molar volume, Den = density, Aqu = aqueous density. Th L-V = homogenization between the liquid and vapor phases, Th total = the final homogenization temperature for the fluid inclusion.

Sample	Molal NaCl	Wt% NaCl	X(NaCl)	Crit.Temp.	Crit.Press.	Bulk XH2O	Bulk XCO2	Bulk XNaCl	Bulk Den	Bulk MV
GVM 15 2337	1.031	5.681	0.018			0.859	0.125	0.016	0.828	26.477
GVM 15 2337	1.098	6.028	0.019			0.931	0.051	0.018	0.932	21.54
GVM 15 2337	1.591	8.506	0.028			0.907	0.067	0.026	0.921	22.584
GVM 15 2337	1.687	8.975	0.029			0.935	0.036	0.028	0.978	20.573
GVM 15 2337	1.909	10.037	0.033			0.885	0.084	0.03	0.903	23.746
GVM 15 2337	1.623	8.663	0.028			0.85	0.125	0.025	0.842	26.465
GVM 15 2337	1.098	6.028	0.019			0.945	0.036	0.019	0.958	20.581
GVM 15 2337	1.558	8.347	0.027			0.891	0.084	0.025	0.893	23.745
GVM 21 1168.1	4.67	21.45	0.08	591	793				1.04	20.43
GVM 21 1168.1	4.65	21.38	0.08	590	790				1.04	20.43
GVM 21 1168.1	4.63	21.31	0.08	589	787				1.038	20.46
GVM 21 1168.1	4.65	21.38	0.08	590	790				1.04	20.44
GVM 21 1168.1	4.71	21.59	0.08	593	798				1.045	20.33
GVM 21 1278	0.896	4.976	0.016			0.934	0.051	0.015	0.926	21.547
GVM 21 1278	0.862	4.798	0.015			0.919	0.067	0.014	0.899	22.601
GVM 21 1278	0.862	4.798	0.015			0.912	0.074	0.014	0.889	23.052
GVM 21 1278	0.896	4.976	0.016			0.943	0.042	0.015	0.941	20.961
GVM 21 1278	0.004	0.021	0			0.756	0.244	0	0.708	34.417
GVM 21 1278										
GVM 21 1278	0.896	4.976	0.016			0.948	0.036	0.015	0.951	20.588
GVM 21 1278	0.896	4.976	0.016			0.952	0.032	0.015	0.965	20.197
GVM 21 1297	1.031	5.681	0.018			0.966	0.016	0.018	0.997	19.214
GVM 21 1297	0.997	5.507	0.018			0.959	0.023	0.017	0.98	19.707
GVM 21 1297	0.761	4.256	0.014			0.971	0.016	0.013	0.987	19.224
GVM 21 1297	0.761	4.256	0.014			0.964	0.023	0.013	0.982	19.497
GVM 21 1297	0.727	4.074	0.013			0.952	0.035	0.012	0.965	20.144
GVM 21 1297	0.964	5.331	0.017			0.947	0.036	0.016	0.954	20.585
GVM 21 1297	0.693	3.89	0.012			0.894	0.095	0.011	0.891	23.494

Appendix B2: cont. Input and output data from the Flincor program used to calculate fluid salinity, density, and other chemical properties. Th = homogenization temperature, Tm = melt temperature, MV = molar volume, Den = density, Aqu = aqueous density. Th L-V = homogenization between the liquid and vapor phases, Th total = the final homogenization temperature for the fluid inclusion.

Sample	Molal NaCl	Wt% NaCl	X(NaCl)	Crit.Temp.	Crit.Press.	Bulk XH2O	Bulk XCO2	Bulk XNaCl	Bulk Den	Bulk MV
GVM 21 1493.5	1	-5.7	223.4			0.07				
GVM 21 1493.5	A	3.7		208.9	30.97		0.1	0.52	84.648	1.073
GVM 21 1493.5	C	3.5		300	30.9		0.33	0.532	82.719	1.076
GVM 21 1493.5	3	6.5		312.4	30.97		0.25	0.52	84.648	1.039
GVM 21 1493.5	5	8.3		215	28.5		0.25	0.644	68.286	1.015
GVM 21 1493.5	6	9		178.6	30.97		0.05	0.52	84.648	1.004
GVM 21 1493.5	7	-5	248.6			0.03				
GVM 21 1493.5	8	7.7		275.1	30.97		0.23	0.52	84.648	1.023
GVM 21 1493.5	9	7.1		280	22.9		0.45	0.741	59.421	1.034
GVM 21 1493.5	10	7.6		325	30.5		0.25	0.569	77.338	1.025
GVM 21 1493.5	11	7.5		270	30.4		0.15	0.575	76.499	1.026
GVM 41 2037.1	1	10		279.8	30.8		0.25	0.544	80.837	0.99
GVM 41 2037.1	2	9.7		280	29.9		0.23	0.6	73.366	0.994
GVM 41 2037.1	3	9.5		310	30.6		0.13	0.562	78.299	0.997
GVM 41 2037.1	4	9.5		267.9	30.7		0.17	0.554	79.435	0.997
GVM 41 2037.1	5	9.8		234.9	30.7		0.13	0.554	79.435	0.993
GVM 41 2037.1	6	5.8		273.3	30.4		0.11	0.575	76.499	1.049
GVM 41 2037.1	7	-7.5	195.8			0.07				
GVM 41 2037.1	8	-7.5	195.7			0.1				
GVM 41 2037.1	9	-7.4	196.4			0.05				
GVM 59 1702	1	-4	214.8			0.08				
GVM 59 1702	2	-1.4	215.9			0.1				
GVM 59 1702	3	-6.8	218.4			0.13				
GVM 59 1702	4	-6.6	178.2			0.05				
GVM 59 1702	5	-0.2	207.8			0.09				
GVM 59 1702	6	-6.5	227.5			0.15				
GVM 59 1702	7	-6.5	223.3			0.13				
GVM 59 1702	8	-6.7	232.3			0.1				

Appendix B2: cont. Input and output data from the Flincor program used to calculate fluid salinity, density, and other chemical properties. Th = homogenization temperature, Tm = melt temperature, MV = molar volume, Den = density, Aqu = aqueous density. Th L-V = homogenization between the liquid and vapor phases, Th total = the final homogenization temperature for the fluid inclusion.

Sample	Molal NaCl	Wt% NaCl	X(NaCl)	Crit.Temp.	Crit.Press.	Bulk XH2O	Bulk XCO2	Bulk XNaCl	Bulk Den	Bulk MV
GVM 21 1493.5	1.65	8.78	0.03	455	436			0.913	21.07	
GVM 21 1493.5	2.095	10.91	0.036			0.941	0.023	0.036	1.018	19.7
GVM 21 1493.5	2.157	11.193	0.037			0.869	0.098	0.034	0.896	24.452
GVM 21 1493.5	1.197	6.541	0.021			0.914	0.067	0.02	0.91	22.59
GVM 21 1493.5	0.59	3.334	0.011			0.909	0.081	0.01	0.923	22.244
GVM 21 1493.5	0.35	2.004	0.006			0.983	0.011	0.006	0.98	18.93
GVM 21 1493.5	1.45	7.82	0.03	446			411	0.876	21.96	
GVM 21 1493.5	0.795	4.438	0.014			0.926	0.06	0.013	0.907	22.171
GVM 21 1493.5	0.997	5.507	0.018			0.786	0.2	0.014	0.902	26.359
GVM 21 1493.5	0.828	4.618	0.015			0.914	0.073	0.014	0.911	22.458
GVM 21 1493.5	0.862	4.798	0.015			0.945	0.04	0.015	0.958	20.506
GVM 41 2037.1	0.004	0.021	0			0.93	0.07	0	0.878	22.582
GVM 41 2037.1	0.108	0.626	0.002			0.929	0.069	0.002	0.904	22.003
GVM 41 2037.1	0.177	1.024	0.003			0.963	0.034	0.003	0.941	20.213
GVM 41 2037.1	0.177	1.024	0.003			0.952	0.045	0.003	0.922	20.941
GVM 41 2037.1	0.073	0.425	0.001			0.966	0.033	0.001	0.936	20.23
GVM 41 2037.1	1.428	7.704	0.025			0.947	0.028	0.024	0.997	19.808
GVM 41 2037.1	2.14	11.1	0.04	476	493				0.955	20.56
GVM 41 2037.1	2.14	11.1	0.04	476	493				0.955	20.56
GVM 41 2037.1	2.11	10.98	0.04	475	490				0.953	20.59
GVM 59 1702	1.16	6.37	0.02	433	375				0.902	20.87
GVM 59 1702	0.4	2.31	0.01	395	272				0.865	21.29
GVM 59 1702	1.95	10.23	0.03	468	472				0.929	20.7
GVM 59 1702	1.9	9.97	0.03	466	465				0.964	19.95
GVM 59 1702	0.06	0.33	0	377	225				0.858	20.99
GVM 59 1702	1.87	9.84	0.03	465	462				0.917	20.97
GVM 59 1702	1.87	9.84	0.03	465	462				0.921	20.87
GVM 59 1702	1.92	10.1	0.03	467	468				0.914	21.04

Appendix B2: cont. Input and output data from the Flincor program used to calculate fluid salinity, density, and other chemical properties. Th = homogenization temperature, Tm = melt temperature, MV = molar volume, Den = density, Aqu = aqueous density. Th L-V = homogenization between the liquid and vapor phases, Th total = the final homogenization temperature for the fluid inclusion.

Sample	Molal NaCl	Wt% NaCl	X(NaCl)	Crit.Temp.	Crit.Press.	Bulk XH2O	Bulk XCO2	Bulk XNaCl	Bulk Den	Bulk MV
GVM 65 1902	1	6.3		253.2	30.97		0.25	0.52	84.648	1.042
GVM 65 1902	2	6.4		233.5	30.97		0.07	0.52	84.648	1.041
GVM 65 1902	3	5.8		235.8	30.97		0.1	0.52	84.648	1.048
GVM 65 1902	4	9.8		247.2	30.97		0.15	0.52	84.648	0.993
GVM 65 1902	5	4.1		237.1	30.97		0.2	0.52	84.648	1.069
GVM 65 1902	6	3.9		225	30.97		0.1	0.52	84.648	1.071
GVM 65 1902	7	5.9		237.4	30.97		0.15	0.52	84.648	1.047
GVM 65 1902	8	4.3		220	30.97		0.1	0.52	84.648	1.067
GVM 65 1902	9	3.4		226.1	30.97		0.1	0.52	84.648	1.077
GVM 65 1902	10	8.2		269.5	30.97		0.2	0.52	84.648	1.016
GVM A3 2007	1	7.9		260.1	30.97		0.2	0.52	84.648	1.02
GVM A3 2007	2	6		200	30.97		0.15	0.52	84.648	1.046
GVM A3 2007	5	8.1		182.3	30.97		0.1	0.52	84.648	1.017
GVM A3 2007	6	8.3		184.9	30.97		0.08	0.52	84.648	1.015
GVM A3 2007	7	7		255	23.1		0.8	0.738	59.628	1.035
GVM A3 2007	8	8.2		215	30.97		0.15	0.52	84.648	1.016
GVM A3 2007	9	3.5		196	30.97		0.13	0.52	84.648	1.076
VIC 12-99	1	3.1		199.9	30.97		0.07	0.52	84.648	1.08
VIC 12-99	2	8.9		254.1	30.97		0.15	0.52	84.648	1.006
VIC 12-99	3	9.2		258	30.97		0.15	0.52	84.648	1.002
VIC 12-99	4	9.4		270.1	30.97		0.25	0.52	84.648	0.999
VIC 12-99	5	7.9		263.1	30.97		0.27	0.52	84.648	1.02
VIC 12-99	6	7.5		260	30.97		0.45	0.52	84.648	1.026
VIC 12-99	7	7.6		200	30.97		0.3	0.52	84.648	1.025
VIC 12-99	8	9.1		200	30.97		0.4	0.52	84.648	1.003
VIC 149-99	1	-2.2	207.2			0.15				
VIC 149-99	2	-2.3	175.8			0.15				
VIC 149-99	3	-1.7	213.7			0.17				
VIC 149-99	4	-2.4	203.7			0.1				
VIC 149-99	5	-1.4	282.1			0.15				
VIC 149-99	6	-2.3	235.2			0.2				
VIC 149-99	7	-1	168.6			0.07				
VIC 149-99	8	-0.8	109.1			0.05				

Appendix B2: cont. Input and output data from the Flincor program used to calculate fluid salinity, density, and other chemical properties. Th = homogenization temperature, Tm = melt temperature, MV = molar volume, Den = density, Aqu = aqueous density. Th L-V = homogenization between the liquid and vapor phases, Th total = the final homogenization temperature for the fluid inclusion.

Sample	Molal NaCl	Wt% NaCl	X(NaCl)	Crit.Temp.	Crit.Press.	Bulk XH2O	Bulk XCO2	Bulk XNaCl	Bulk Den	Bulk MV
GVM 65 1902	1.264	6.878	0.022			0.913	0.067	0.021	0.911	22.588
GVM 65 1902	1.231	6.71	0.022			0.963	0.016	0.021	1.004	19.209
GVM 65 1902	1.428	7.704	0.025			0.952	0.023	0.024	0.996	19.697
GVM 65 1902	0.073	0.425	0.001			0.962	0.037	0.001	0.922	20.633
GVM 65 1902	1.972	10.332	0.034			0.917	0.051	0.033	0.959	21.534
GVM 65 1902	2.034	10.623	0.035			0.942	0.023	0.035	1.016	19.699
GVM 65 1902	1.395	7.54	0.025			0.94	0.036	0.024	0.968	20.575
GVM 65 1902	1.909	10.037	0.033			0.944	0.023	0.032	1.012	19.697
GVM 65 1902	2.187	11.334	0.038			0.94	0.023	0.037	1.021	19.702
GVM 65 1902	0.624	3.521	0.011			0.939	0.051	0.011	0.917	21.559
GVM A3 2007	0.727	4.074	0.013			0.937	0.051	0.012	0.92	21.554
GVM A3 2007	1.363	7.376	0.024			0.94	0.036	0.023	0.967	20.575
GVM A3 2007	0.659	3.706	0.012			0.965	0.023	0.011	0.968	19.72
GVM A3 2007	0.59	3.334	0.011			0.971	0.018	0.01	0.975	19.393
GVM A3 2007	1.031	5.681	0.018			0.443	0.549	0.008	0.798	40.886
GVM A3 2007	0.624	3.521	0.011			0.953	0.037	0.011	0.942	20.6
GVM A3 2007	2.157	11.193	0.037			0.933	0.031	0.036	1.003	20.219
VIC 12-99	2.278	11.749	0.039			0.945	0.016	0.039	1.041	19.214
VIC 12-99	0.384	2.197	0.007			0.957	0.037	0.007	0.933	20.613
VIC 12-99	0.281	1.615	0.005			0.959	0.037	0.005	0.929	20.619
VIC 12-99	0.212	1.222	0.004			0.93	0.067	0.004	0.879	22.638
VIC 12-99	0.727	4.074	0.013			0.914	0.074	0.012	0.885	23.058
VIC 12-99	0.862	4.798	0.015			0.838	0.149	0.013	0.798	28.092
VIC 12-99	0.828	4.618	0.015			0.902	0.084	0.013	0.873	23.764
VIC 12-99	0.315	1.81	0.006			0.87	0.125	0.005	0.81	26.516
VIC 149-99	0.64	3.6	0.01	407	304				0.888	20.75
VIC 149-99	0.67	3.76	0.01	409	308				0.921	19.99
VIC 149-99	0.49	2.79	0.01	400	283				0.872	21.11
VIC 149-99	0.7	3.92	0.01	410	312				0.894	20.6
VIC 149-99	0.4	2.31	0.01	395	272				0.759	24.26
VIC 149-99	0.67	3.76	0.01	409	308				0.853	21.59
VIC 149-99	0.29	1.65	0.01	389	256				0.915	20.14
VIC 149-99	0.23	1.32	0	386	248				0.964	18.69

Appendix B2: cont. Input and output data from the Flincor program used to calculate fluid salinity, density, and other chemical properties. Th = homogenization temperature, Tm = melt temperature, MV = molar volume, Den = density, Aqu = aqueous density. Th L-V = homogenization between the liquid and vapor phases, Th total = the final homogenization temperature for the fluid inclusion.

Sample	Molal NaCl	Wt% NaCl	X(NaCl)	Crit.Temp.	Crit.Press.	Bulk XH2O	Bulk XCO2	Bulk XNaCl	Bulk Den	Bulk MV
VIC 601	5	-0.7	157.98			0.05				
VIC 601	6	-0.5	178.5			0.1				
VIC 605	1	-6.5	217.9			0.07				
VIC 605	2	-6.5	218.1			0.1				
VIC 605	3	-6.5	298.9			0.07				
VIC 605	4	-6.5	189.1			0.05				
VIC 605	5	-6.5	204.1			0.07				
VIC 605	6	-6.5	204.1			0.07				
VIC 605	7	-3.8	188.6			0.1				
VIC 605	8	-3.5	188.4			0.08				
BRECCIA	1	-7	217			0.07				
BRECCIA	2	-8.3	217.1			0.07				
BRECCIA	3	-7.3	219.2			0.05				
BRECCIA	4	-8	219.9			0.05				
BRECCIA	5	-7	219			0.1				
BRECCIA	6	-7.5	187.9			0.03				
BRECCIA	7	-6.5	214.8			0.1				
BRECCIA	8	-4.9	201.9			0.05				
RAMBLER	1	-0.5	350			0.25				
RAMBLER	2	-0.8	152			0.05				
RAMBLER	3	-0.8	155.1			0.07				
RAMBLER	4	-0.5	336.9			0.5				
E109 1935	1	-6.8	244.5			0.07				
E109 1935	2	-6.8	248.9			0.1				
E 109 1935	3	-6.9	253.6			0.13				
E109 1935	4	-6.9	243.4			0.09				
E109 1935	5	-6.8	257.6			0.1				
E109 1935	6	-6.8	253.1			0.1				
E109 1935	7	-6.8	255.6			0.1				

Appendix B2: cont. Input and output data from the Flincor program used to calculate fluid salinity, density, and other chemical properties. Th = homogenization temperature, Tm = melt temperature, MV = molar volume, Den = density, Aqu = aqueous density. Th L-V = homogenization between the liquid and vapor phases, Th total = the final homogenization temperature for the fluid inclusion.

Sample	Molal NaCl	Wt% NaCl	X(NaCl)	Crit.Temp.	Crit.Press.	Bulk XH2O	Bulk XCO2	Bulk XNaCl	Bulk Den	Bulk MV
VIC 601	0.2	1.16	0	385	244				0.922	19.54
VIC 601	0.14	0.83	0	382	236				0.898	20.05
VIC 605	1.87	9.84	0.03	465	462				0.926	20.76
VIC 605	1.87	9.84	0.03	465	462				0.926	20.76
VIC 605	1.87	9.84	0.03	465	462				0.83	23.17
VIC 605	1.87	9.84	0.03	465	462				0.952	20.2
VIC 605	1.87	9.84	0.03	465	462				0.939	20.47
VIC 605	1.87	9.84	0.03	465	462				0.939	20.47
VIC 605	1.11	6.08	0.02	430	367				0.925	20.36
VIC 605	1.02	5.62	0.02	426	355				0.921	20.43
BRECCIA	2	10.48	0.03	470	478				0.932	20.63
BRECCIA	2.35	12.06	0.04	484	517				0.944	20.81
BRECCIA	2.08	10.85	0.04	474	487				0.933	21.05
BRECCIA	2.27	11.7	0.04	481	508				0.938	20.92
BRECCIA	2	10.48	0.03	470	478				0.93	20.67
BRECCIA	2.14	11.1	0.04	476	493				0.963	20.39
BRECCIA	1.87	9.84	0.03	465	462				0.929	20.69
BRECCIA	1.42	7.68	0.02	445	408				0.925	20.34
RAMBLER	0.14	0.83	0	382	236				0.576	31.3
RAMBLER	0.23	1.32	0	386	248				0.929	19.39
RAMBLER	0.23	1.32	0	386	248				0.926	19.46
RAMBLER	0.14	0.83	0	382	236				0.611	29.48
E109 1935	1.95	10.23	0.03	468	472				0.902	21.31
E109 1935	1.95	10.23	0.03	468	472				0.898	21.42
E 109 1935	1.98	10.36	0.03	469	475				0.894	21.52
E109 1935	1.98	10.36	0.03	469	475				0.905	21.25
E109 1935	1.95	10.23	0.03	468	472				0.888	21.66
E109 1935	1.95	10.23	0.03	468	472				0.893	21.54
E109 1935	1.95	10.23	0.03	468	472				0.89	21.61

Appendix B2: cont. Input and output data from the Flincor program used to calculate fluid salinity, density, and other chemical properties. Th = homogenization temperature, Tm = melt temperature, MV = molar volume, Den = density, Aqu = aqueous density. Th L-V = homogenization between the liquid and vapor phases, Th total = the final homogenization temperature for the fluid inclusion.

Sample	Molal NaCl	Wt% NaCl	X(NaCl)	Crit.Temp.	Crit.Press.	Bulk XH2O	Bulk XCO2	Bulk XNaCl	Bulk Den	Bulk MV
E109 1942	1	-14	206.9			0.05				
E109 1942	2	-13.8	179.9			0.05				
E109 1942	3	-8.5	154.5			0.03				
E109 1942	4	-15.9	228.2			0.1				
E109 1942	5	-8.3	152.3			0.2				
E109 1942	6	-7.6	151.1			0.1				
E109 1942	7	-8.9	155.9			0.15				
E109 1942	8	-9	161.1			0.15				
E109 1942	9	-15.7	201.1			0.05				

Appendix B2: cont. Input and output data from the Flincor program used to calculate fluid salinity, density, and other chemical properties. Th = homogenization temperature, Tm = melt temperature, MV = molar volume, Den = density, Aqu = aqueous density. Th L-V = homogenization between the liquid and vapor phases, Th total = the final homogenization temperature for the fluid inclusion.

Sample	Molal NaCl	Wt% NaCl	X(NaCl)	Crit.Temp.	Crit.Press.	Bulk XH2O	Bulk XCO2	Bulk XNaCl	Bulk Den	Bulk MV
E109 1942	3.7	17.77	0.06	541	667				0.99	20.64
E109 1942	3.65	17.6	0.06	539	662				1.021	20.02
E109 1942	2.4	12.29	0.04	487	522				1.003	19.58
E109 1942	4.1	19.35	0.07	560	716				0.983	21.21
E109 1942	2.35	12.06	0.04	484	517				1.003	19.58
E109 1942	2.16	11.22	0.04	477	496				0.998	19.68
E109 1942	2.5	12.74	0.04	491	533				1.005	19.54
E109 1942	2.52	12.86	0.04	492	536				1.001	19.61
E109 1942	4.06	19.19	0.07	558	711				1.004	20.76

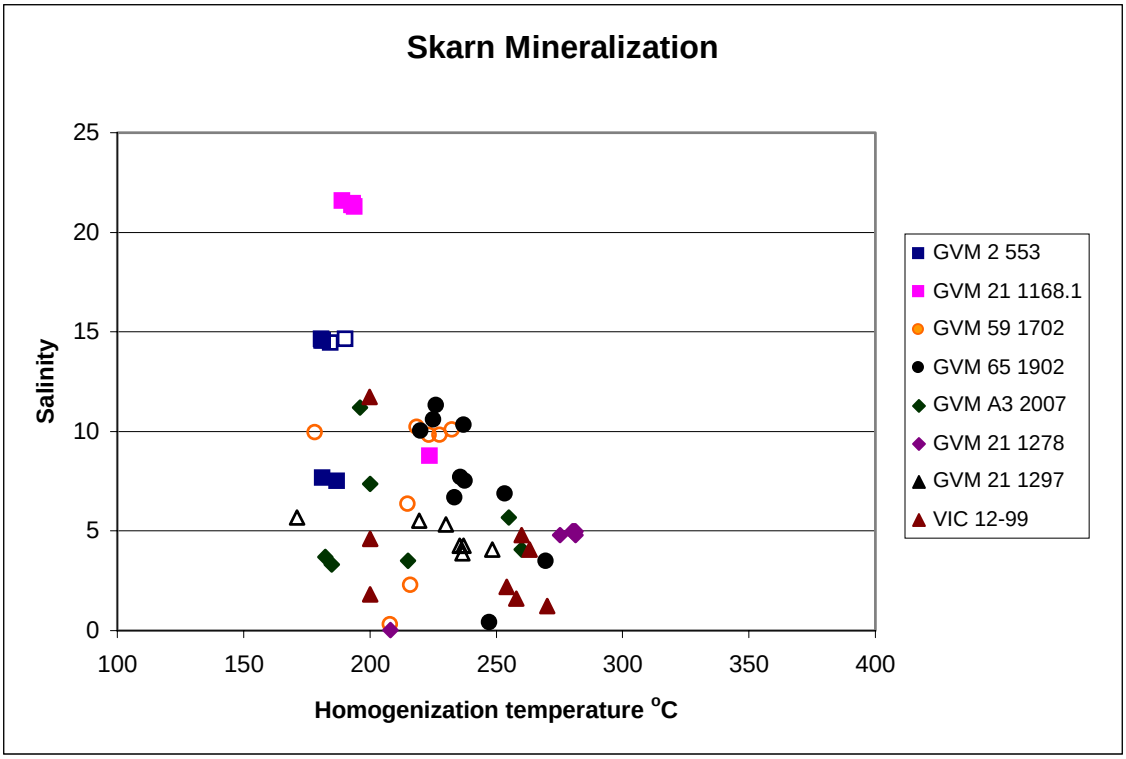

Appendix B-1. Graph of salinity verses homogenization temperature for samples from the skarn deposits. Open symbols = secondary, closed symbols = primary or psuedosecondary fluid inclusions.

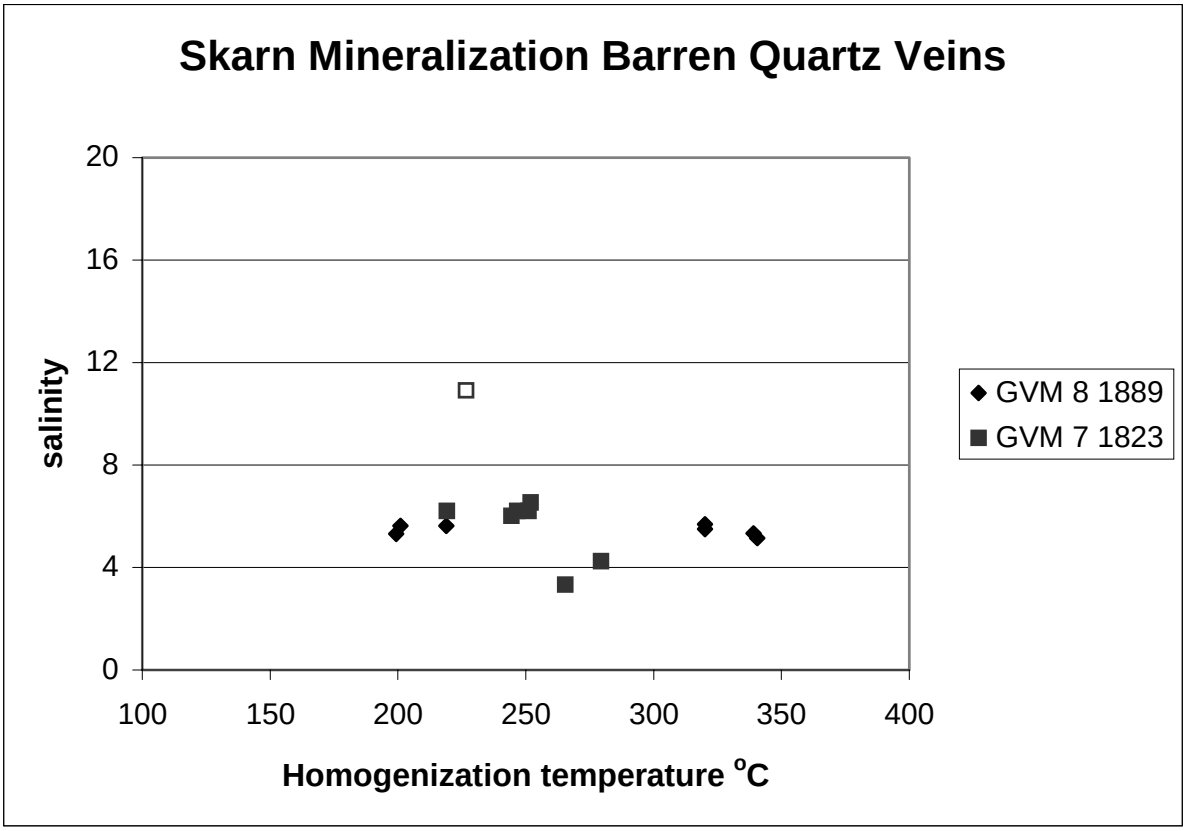

Appendix B-2. Graph of salinity verses homogenization temperature for the barren quartz veins from the skarn deposits. Open symbols = secondary, closed symbols = primary or psuedosecondary fluid inclusions.

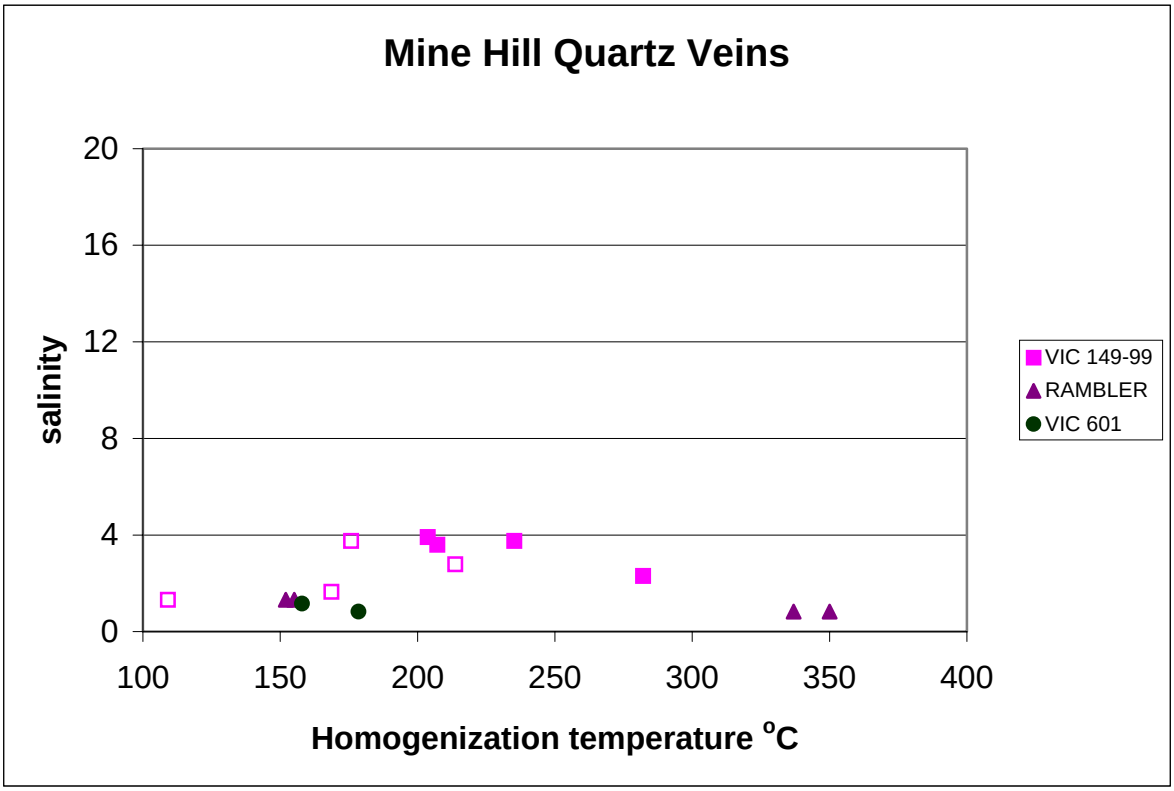

Appendix B-3. Graph of salinity verses homogenization temperature for samples from the carbonate-hosted replacement siliceous vein deposits. Open symbols = secondary, closed symbols = primary or psuedosecondary fluid inclusions.

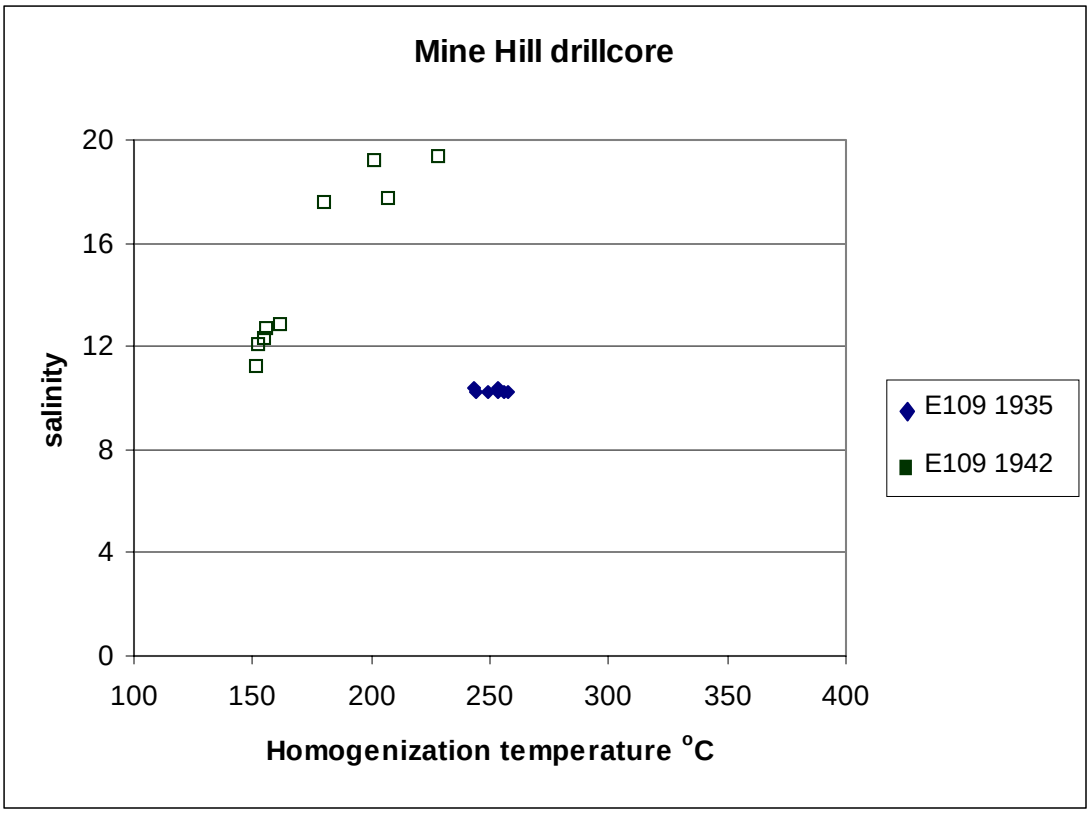

Appendix B-4. Graph of salinity verses homogenization temperature for samples from the carbonate-hosted replacement deposits deep drill hole samples. Open symbols = secondary, closed symbols = primary or psuedosecondary fluid inclusions.

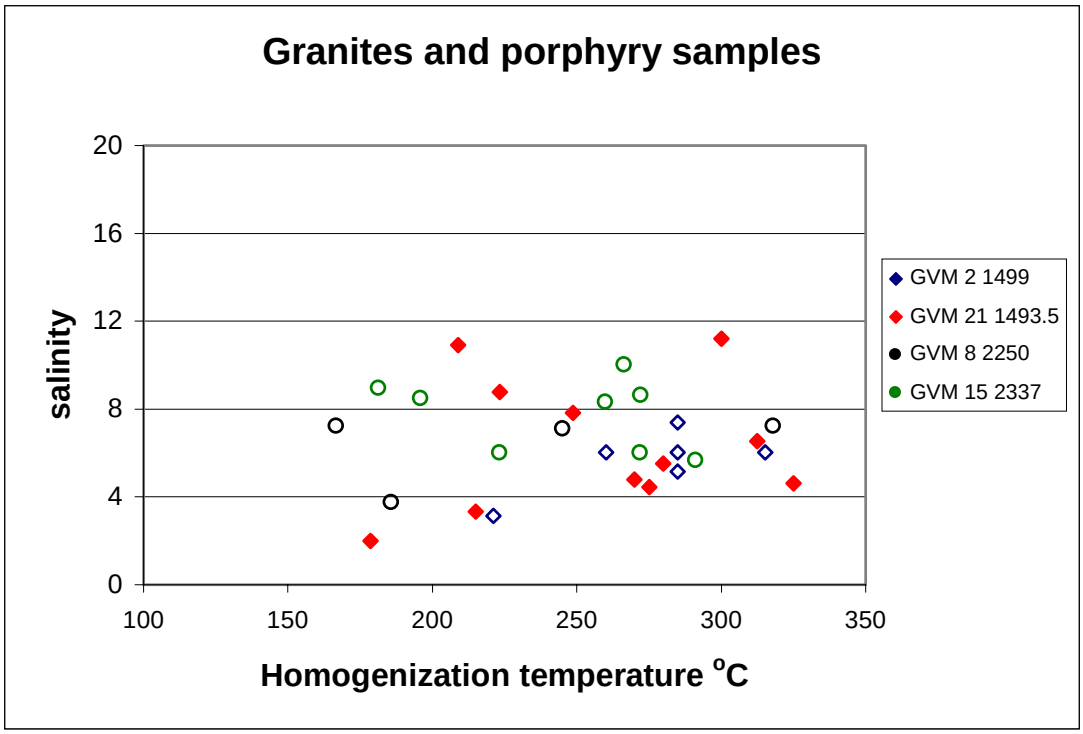

Appendix B-5. Graph of salinity verses homogenization temperature for the granite and porphyry samples. Open symbols = secondary, closed symbols = primary or psuedosecondary fluid inclusions.

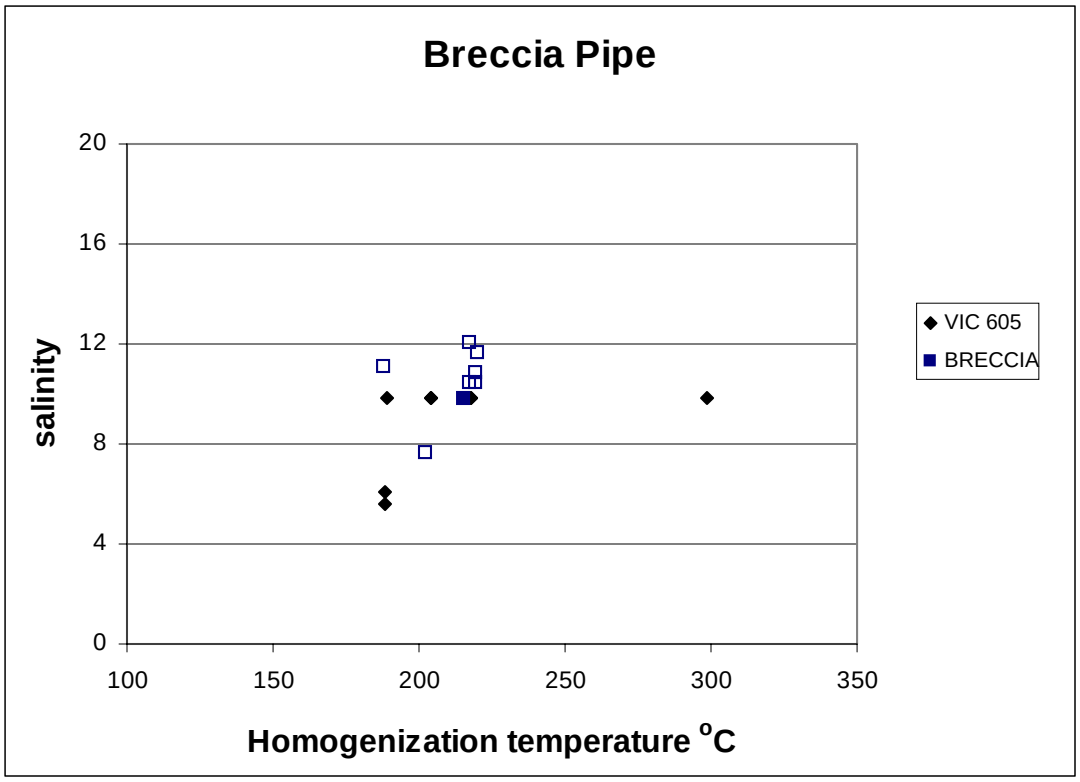

Appendix B-6. Graph of salinity verses homogenization temperature for vuggy quartz samples from the breccia pipe. Open symbols = secondary, closed symbols = primary or psuedosecondary fluid inclusions.

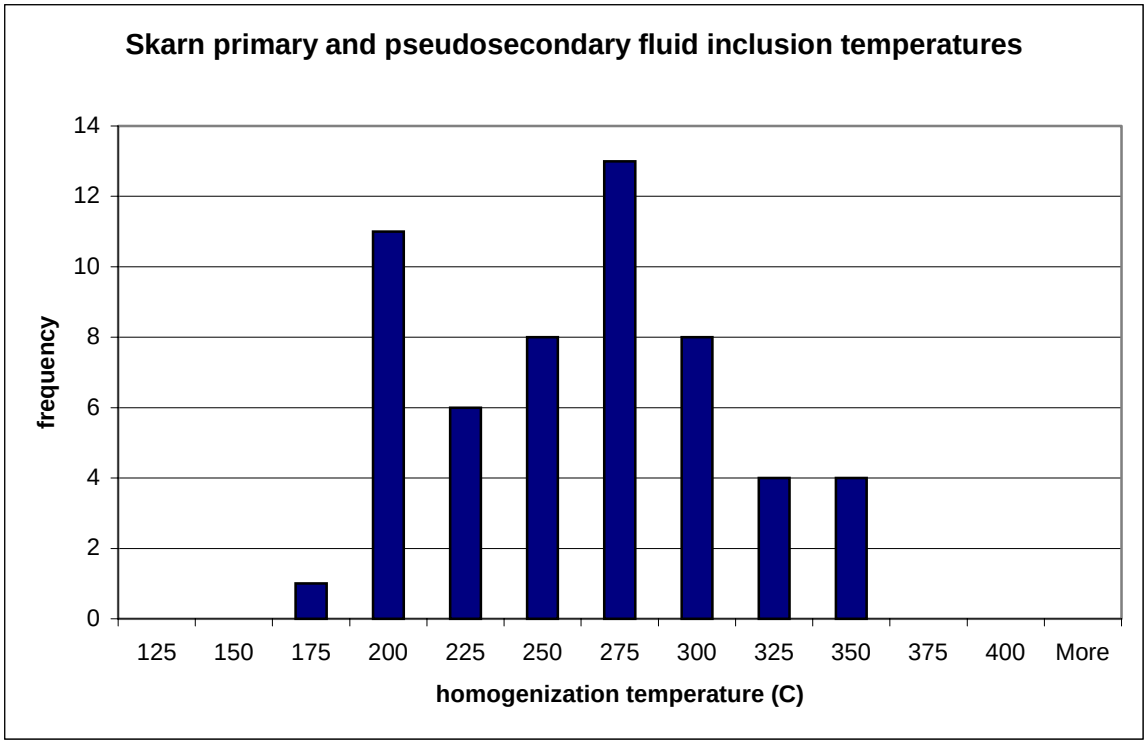

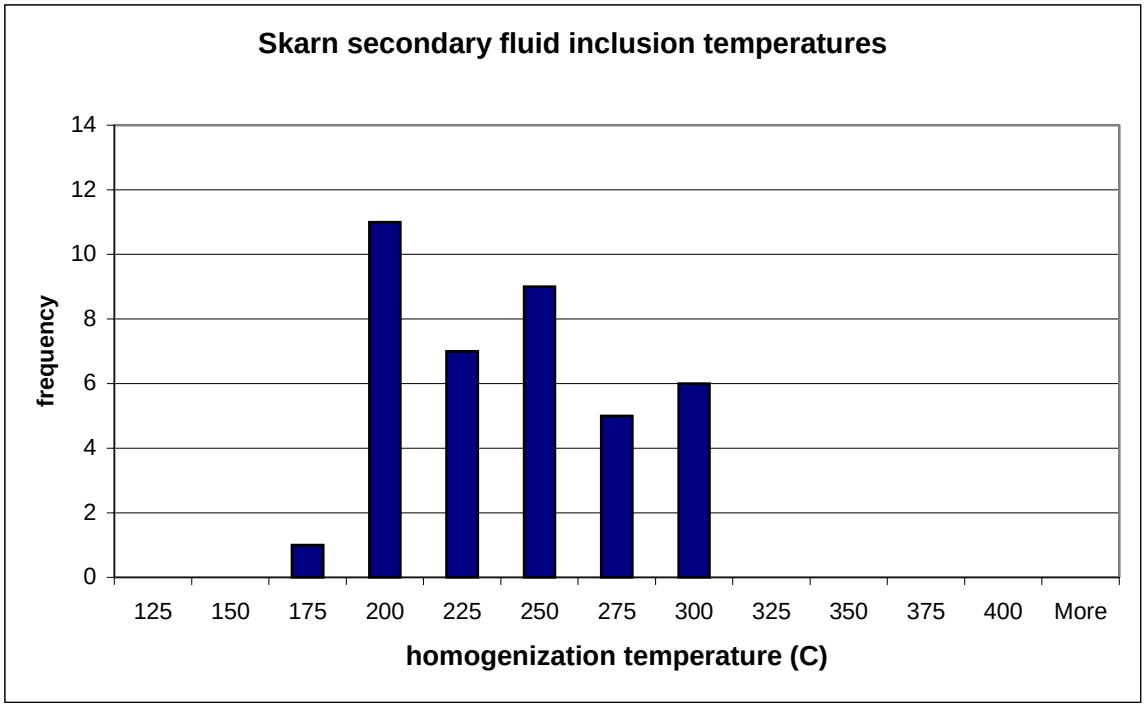

Appendix B-7. Histogram of the primary and pseudosecondary fluid inclusion homogenization temperatures for both the skarn and carbonate-hosted replacement deposits

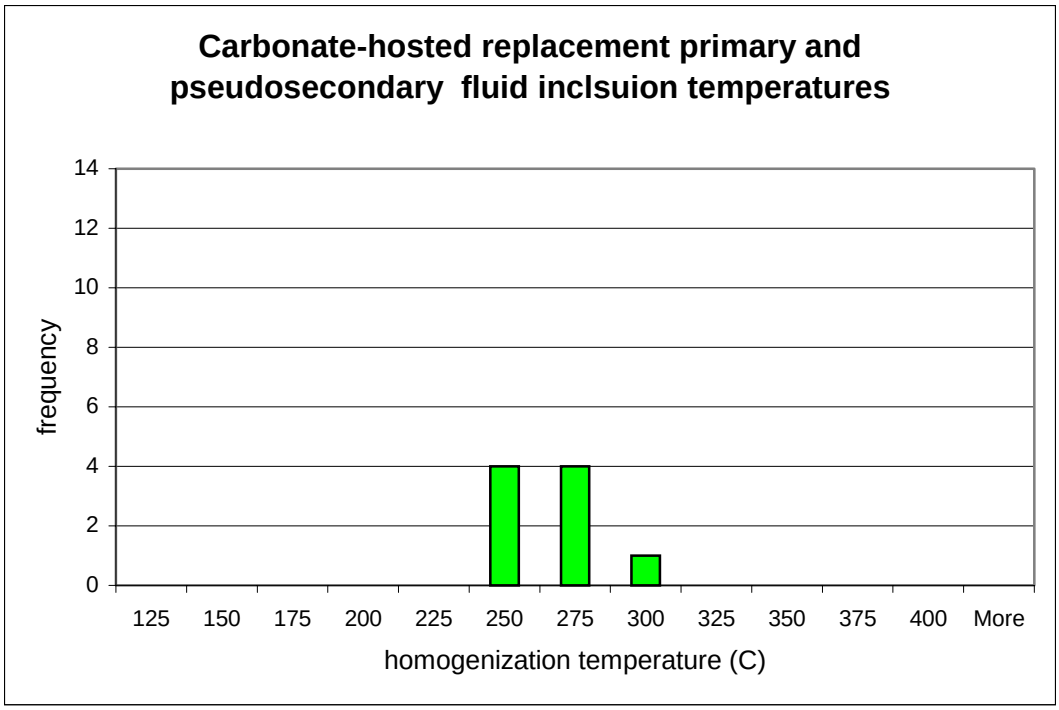

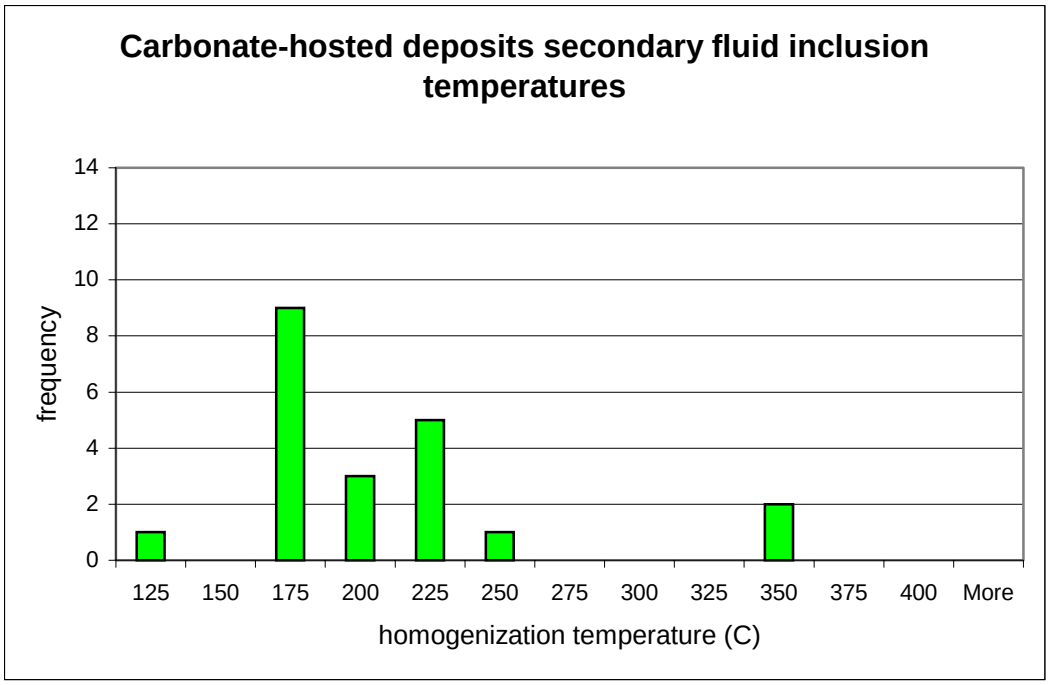

Appendix B-8. Histogram of the secondary fluid inclusion homogenization temperatures for both the skarn and carbonate-hosted replacement deposits

Appendix C: Fluid inclusion gas analyses results. Results are listed in ppm. A value of 0 means no detectable gas concentrations

sample	Crush	H2	He	CH4	H2O	N2	H2S	Ar	CO2	SO2	O2
GVM 59 1702	76850A	0.01125	0.00009	0.05957	93.37649	0.87597	0.00173	0.01249	5.49115	0.00058	0.12365
	6850B	0.01305	0.00037	0.08856	94.95108	0.29393	0.00124	0.00932	4.53802	0	0.06582
	6850C	0.00138	0.00009	0.02632	96.4625	0.36088	0.00114	0.00748	3.08225	0.00097	0.04397
	6850E	0.00644	0.00016	0.09563	95.89185	0.3358	0	0.00644	3.48374	0.00125	0.15094
	6850F	0.00037	0.00007	0.02267	96.38448	0.35882	0.00114	0.00617	3.11536	0.00101	0.08756
	6850G	0.00811	0.00005	0.03101	95.33363	0.2812	0.00164	0.00719	4.14688	0.00143	0.15415
	6850H	0.00091	0.00012	0.01392	96.79398	0.29945	0.00077	0.00431	2.79798	0.00089	0.07123
	6850I	0.02887	0.00013	0.02757	95.05625	0.32672	0.00181	0.00635	4.11622	0.00161	0.36869
	6850J	0.01078	0.00009	0.02953	95.35397	0.29188	0.00183	0.00647	4.15217	0.00123	0.12433
GVM 41 1925.5	96851A	0.12968	0.00038	0.05463	81.60102	0.43573	0.00188	0.01061	17.39612	0.00513	0.27596
	6851C	0.07844	0.00014	0.01474	90.79292	0.18914	0.00111	0.00425	8.75139	0.00276	0.12817
	6851D	0.145	0.00031	0.03087	84.62383	0.30676	0.00111	0.00837	14.54575	0.00463	0.2556
	6851E	0.02566	0.00014	0.04618	86.55197	0.54295	0.00212	0.0105	12.19187	0.00436	0.52707
	6851F	0.16481	0.00031	0.07188	82.69636	0.39646	0.00077	0.0077	16.34158	0.00479	0.24208
	6851G	0.01579	0.00007	0.03764	86.16202	0.33597	0.00306	0.00751	12.11884	0.00566	1.12645
	6851H	0.10458	0.00031	0.0341	92.22233	0.46041	0.00106	0.00636	7.03315	0.00059	0.10932
	6851I	0.15598	0.00037	0.04897	85.83903	0.29227	0.00118	0.00472	13.4122	0.00008	0.19265
GVM 21 1493.5	46852B	0.17694	0.0003	0.023	56.25427	1.01645	0.00509	0.01485	41.13927	0.00111	1.09975
	6852C	0.05293	0.00021	0.01733	70.46571	1.04888	0.00313	0.01065	27.50898	0.00116	0.72686
	6852D	0.21726	0.00044	0.03281	57.56311	2.95292	0.00388	0.01652	38.06661	0.00126	0.92881
	6852E	0.2729	0.00034	0.02041	57.46428	0.8736	0.00385	0.01149	40.22977	0.00093	0.91331
	6852F	0.29973	0.00041	0.03	51.17378	1.0716	0.00311	0.01245	46.1331	0.00069	1.03029
	6852G	0.23727	0.00037	0.02422	47.88427	1.05105	0.00258	0.01319	49.24339	0.00113	1.25665
	6852H	0.13435	0.00023	0.02357	65.42487	1.42387	0.00552	0.01204	31.92593	0.00089	0.85824
	6852I	0.24419	0.0004	0.02826	50.63457	1.17448	0.0046	0.01623	46.65549	0.00126	0.99811
E109 1942	26853B	0.00201	0.00039	0.35219	98.25766	1.24583	0.0005	0.01651	0.0566	0	0.04161
	6853C	0	0.00036	0.60538	98.68121	0.58087	0.00062	0.00837	0.06305	0.00023	0.02665
	6853D	0.00592	0.00054	0.58933	98.51955	0.72457	0.00074	0.01143	0.08402	0.00018	0.03029
	6853F	0.00315	0.00026	0.36068	98.80445	0.73036	0.00076	0.00903	0.04728	0	0.02069
	6853G	0	0.00061	0.54227	98.61443	0.74535	0.00049	0.01022	0.05162	0	0.02096
	6853H	0.00016	0.00056	0.57011	98.62299	0.67153	0.00088	0.00943	0.06957	0.00005	0.03507
	6853I	0.00006	0.00041	0.46646	98.76068	0.63646	0.00132	0.00837	0.07245	0.0002	0.04059
	6853J	0.00454	0.00045	0.46176	98.66928	0.61402	0.00132	0.00814	0.12358	0.0001	0.09572

Appendix C cont.: Fluid inclusion gas analyses results. Results are listed in ppm. A value of 0 means no detectable gas concentrations

sample	C2H4	C2H6	C3H6	C3H8	C4H8	C4H10	C5H12	C6H6	C7H8	N2/Ar	Ar/He	H2S/SO2
GVM 59 1702	59.9	294.5	91.8	0	5.3	0	0	18.6	0.3	70	142	2.982759
	53.1	234.8	64.8	0	2	13	0	18.4	0	32	25	
	0	78.3	49.5	0	0.1	0	0	2.3	0	48	80	1.175258
	0	201.2	66.7	0	2.2	2.5	0	4.8	0.2	52	41	
	0	144.6	48.5	0	3.3	7.9	6	13.2	0.2	58	94	1.128713
	0	237.8	74	0	6.2	9.3	0	19.6	0.2	39	144	1.146853
	0	103	44.3	0	2.6	4.9	0	9.7	0	69	35	0.865169
	0	489.8	72	14.2	10	20.1	7	44.2	0.9	51	49	1.124224
	0	185.7	47.3	0	6.4	18	3.2	16.2	0.2	45	76	1.487805
GVM 41 1925.5	0	554.1	316.4	0	3.5	0	7.8	6.6	0.1	41	28	0.366472
	0	222.2	140.5	0	0.2	0	0	6.7	0	45	31	0.402174
	0	488.7	282.8	0	0	0	0	5.7	0.4	37	27	0.239741
	0	704.1	233.5	0	7.7	8.9	0	16.8	0.6	52	75	0.486239
	0	454.8	267.5	0	3.3	0	0	6.5	0.5	51	25	0.160752
	0	1481.3	257.3	0	19.6	37.8	14.8	58.4	0.6	45	104	0.540636
	0	166.1	107.7	0	0.8	0	0	3.2	0	72	21	1.79661
	0	310.5	207.1	0	4.4	0	0	2	1.3	62	13	14.75
GVM 21 1493.5	0	1683.4	973.4	0	7	0	8.6	16.9	0.4	68	50	4.585586
	0	1037.9	552.1	0	6.9	14	17.1	12.9	0.6	99	51	2.698276
	0	1314.1	810.4	0	6.9	12.2	8.4	11.4	0.4	179	37	3.079365
	0	1400	657.4	0	5.2	6.8	9.7	11.7	0.4	76	33	4.139785
	0	1581	846.5	0	5.5	0	0	15.2	0.3	86	30	4.507246
	0	1844.7	970.6	0	10.3	3	11.3	18.7	0.2	80	35	2.283186
	0	1201.1	674.3	0	5.1	8.3	4.2	11.5	0.6	118	53	6.202247
	0	1435.6	956.4	0	6.1	5.6	5.1	14.9	0.5	72	41	3.650794
E109 1942	145.2	67.7	14.8	0	0	0	20.6	18.5	0	75	42	
	64.8	168.2	0	23.7	8.9	26.3	26.8	13.2	0.8	69	23	2.695652
	95.9	117.9	0	26	8.4	18.4	32.9	33.8	0.9	63	21	4.111111
	75.8	89.3	0	0	8.1	37.9	4.3	18	0	81	34	
	53.5	56.8	0	0	2.1	13.6	0	14.3	0.3	73	17	
	65.1	79.5	0	0	2.7	29.5	0.5	19.2	0	71	17	17.6
	36.9	59.4	10.7	0	3.3	0	0	19.5	0.1	76	20	6.6
	59.2	99.4	10.1	0	5.6	6.5	0	30	0.3	75	18	13.2

Appendix C cont.: Fluid inclusion gas analyses results. Results are listed in ppm. A value of 0 means no detectable gas concentrations

sample	Crush	H2	He	CH4	H2O	N2	H2S	Ar	CO2	SO2	O2
BRECCIA	6854A	0.27279	0.00002	0.51194	98.6131	0.36944	0.00099	0.00527	0.13466	0.0001	0.07519
	6854B	0.01723	0.00001	0.88103	98.52332	0.41096	0.0008	0.00545	0.09238	0	0.05632
	6854C	0.10062	0.00009	1.09196	98.24535	0.38616	0.0008	0.00621	0.15566	0	0.0032
	6854D	0.04528	0.00005	0.6787	98.92868	0.24027	0.00033	0.00356	0.09418	0.00057	0.0021
	6854E	0.00222	0.00002	0.68168	98.97682	0.27091	0.00041	0.00358	0.04647	0.00001	0.01211
	6854F	0.00427	0.00001	0.51395	98.99921	0.2916	0.00078	0.00403	0.11435	0.00013	0.06149
	6854G	0.00942	0.00002	0.2287	99.25739	0.29389	0.00106	0.00384	0.11386	0.00007	0.07909
	6854H	0.02871	0.00004	0.73632	98.8101	0.31482	0.00042	0.00464	0.09765	0	0.00123
	6854J	0	0	0.11185	99.82333	0.03934	0.00006	0.00096	0.02304	0	0.00011
RAMBLER	6855A	0.03578	0.00009	0.11391	89.54812	0.16392	0.00182	0.00723	9.82806	0.00387	0.20475
	6855B	0.05278	0.00024	0.05187	78.93251	0.31119	0.0018	0.00784	20.28994	0	0.26134
	6855C	0.04655	0.00019	0.07949	80.89221	0.32801	0.00196	0.00877	18.36276	0.00081	0.2033
	6855D	0.0111	0.00006	0.03515	91.25809	0.22723	0.00132	0.00528	8.22023	0.00009	0.19333
	6855E	0.041	0.00018	0.8455	90.74222	0.50728	0.00134	0.0037	7.65527	0	0.12555
	6855F	0.00693	0.00005	0.11115	94.83802	0.2508	0.00118	0.0046	4.66036	0	0.09436
	6855G	0.02706	0.00011	0.16392	91.17582	0.14734	0.00216	0.00448	8.29112	0.00235	0.13062
	6855H	0.00272	0.00002	0.19151	97.27644	0.07846	0.0008	0.0015	2.38169	0.00062	0.03834
	6855I	0.01239	0.00001	0.08757	95.50281	0.12369	0.00122	0.00298	4.05571	0.00128	0.1701
	6855J	0.03125	0.00014	0.22513	91.3397	0.11203	0.00223	0.00365	8.10061	0.00239	0.11637
GVM 8 1889	86857A	0.22019	0.00036	0.10162	57.2098	1.33262	0.00296	0.02386	40.29207	0.01265	0.55029
	6857B	0.24155	0.00033	0.1175	55.86726	1.05753	0.0016	0.01659	41.97116	0.00008	0.50067
	6857C	0.15914	0.00013	0.04491	70.91196	1.46886	0.00232	0.0165	26.87334	0.00054	0.37045
	6857D	0.15414	0.00018	0.04813	65.20479	0.60266	0.00247	0.01659	33.40412	0.00114	0.38992
	6857E	0.11276	0.0001	0.03067	78.39125	1.15363	0.00149	0.01182	19.94408	0.00084	0.24765
	6857F	0.10747	0.00011	0.02919	76.97794	1.17719	0.00241	0.01185	21.27137	0.00066	0.29868
	6857G	0.0288	0.0001	0.02586	79.25452	0.33225	0.00138	0.00933	19.87223	0.00097	0.33956
	6857H	0.11894	0.00019	0.03042	70.71425	0.53897	0.00303	0.01224	28.02501	0.00143	0.40019
	6857I	0.09245	0.00018	0.03697	77.40937	1.33519	0.00231	0.01155	20.61457	0.00091	0.35946
	6857J	0.18273	0.0003	0.03516	63.10262	0.88781	0.00255	0.01282	35.25434	0.00099	0.36634
VIC 12-99	96858A	0.13919	0.00018	1.9723	76.35397	0.34447	0.00518	0.00912	20.79157	0.00056	0.26479
	6858B	0.20324	0.00022	1.80567	66.48397	0.57717	0.00945	0.01238	30.32454	0.00082	0.41445
	6858C	0.0148	0.00003	1.65903	85.35991	1.28012	0.00612	0.00703	11.34493	0.00057	0.23417
	6858E	0.04182	0.00004	1.48159	83.7005	0.81815	0.008	0.00742	13.59733	0.00067	0.24695
	6858F	0.23026	0.00022	1.32294	74.19573	0.80206	0.01223	0.00953	23.00679	0.00064	0.30554
	6858G	0.07492	0.00007	0.98845	81.24917	0.73953	0.00954	0.00822	16.49745	0.00069	0.31233
	6858H	0.0572	0.00002	2.07481	83.3494	0.83831	0.00868	0.00669	13.37521	0.00052	0.20795

Appendix C cont.: Fluid inclusion gas analyses results. Results are listed in ppm. A value of 0 means no detectable gas concentrations

sample	C2H4	C2H6	C3H6	C3H8	C4H8	C4H10	C5H12	C6H6	C7H8	N2/Ar	Ar/He	H2S/SO4
BRECCIA	28.4	87	7.7	0	2.5	9.8	8.7	20.5	0.3	70	239	9.9
	31.1	58.6	0	0	1.2	14.9	1.3	17.8	0.1	75	395	
	0	75.1	13.1	5.6	0	1.5	0	4	0.4	62	71	
	14.2	35.3	5.4	0.3	0	0	0	7.1	0.6	67	70	0.578947
	15.9	24.2	0.1	0	0	4.3	7.5	5.6	0	76	170	41
	10	64	9.5	0	3.3	1.5	0	13.3	0.2	72	599	6
	7.5	78.5	0	0	4.1	15.3	4.4	16.4	0.2	77	210	15.14286
	1	44.1	0	1.4	2.8	3.5	4.1	3.6	0	68	107	
	1.5	4.7	0	0.6	0.3	3.3	2.7	0	0	41	0	
RAMBLER	0	667.9	216.7	0	1.4	0	0	38.4	0	23	83	0.470284
	0	593.9	266.4	0	0	18.1	3.9	22.3	0.2	40	32	
	0	472.7	260.4	0	6.1	0	0	20.4	0	37	47	2.419753
	0	332.2	129.3	0	2.5	2.6	0	14.3	0.2	43	85	14.66667
	0	490.7	22.9	184.6	33.3	0	0	46.4	1.7	137	20	
	0	225.2	65.6	0	5.1	14.4	0	15.1	0	54	102	
	0	372.9	119.1	0	6.7	17.1	13.2	21.1	0.1	33	39	0.919149
	0	176.5	0	15.3	12.2	46.6	11	17.3	0	52	62	1.290323
	0	314.1	55.9	0	8.4	19.3	4.3	20.3	0.4	41	284	0.953125
	0	479.5	31.5	0.2	21.2	85.8	26.8	19.7	0.4	31	27	0.933054
GVM 8 1889	0	1774.1	714.4	0	18.1	0	0	29	0	56	66	0.233992
	0	1564.3	667.8	0	5	0	0	18.9	1.3	64	50	20
	0	1020.4	474.3	0	6.2	0.5	5.9	10.7	0.5	89	130	4.296296
	0	1128.7	590.9	0	8	11	5.7	14	0.3	36	94	2.166667
	0	737.7	286.2	0	5	5.8	8.2	13.8	0.4	98	118	1.77381
	0	827.7	379.7	0	4.7	3.6	2.8	12.1	0.4	99	107	3.651515
	0	923.5	373.8	0	6.6	16.5	6.4	23.1	0.4	36	94	1.42268
	0	1055.1	475.3	0	5.3	0	3.1	14	0.6	44	64	2.118881
	0	916.3	418.3	0	6	9.1	7.2	13.2	0.4	116	63	2.538462
	0	1028	491.4	0	6	6	1.1	10.6	0.4	69	43	2.575758
VIC 12-99	0	868	297.9	0	3.1	5.2	0	12.1	0.4	38	50	9.25
	0	1220.9	420.9	0	5.5	17.6	0	15.5	0.6	47	56	11.52439
	0	680.7	214.5	0	5	9.8	5.4	17.2	0.3	182	224	10.73684
	0	713.6	217.6	0	4.4	14.7	6.5	18.4	0.3	110	166	11.9403
	0	813.1	292.6	0	6	15	0	13.3	0.5	84	44	19.10938
	0	884.6	270.9	0	5.3	10.9	7.9	16.7	0.1	90	121	13.82609
	0	578.6	205.4	0	4	7.8	2.4	13.6	0.1	125	335	16.69231

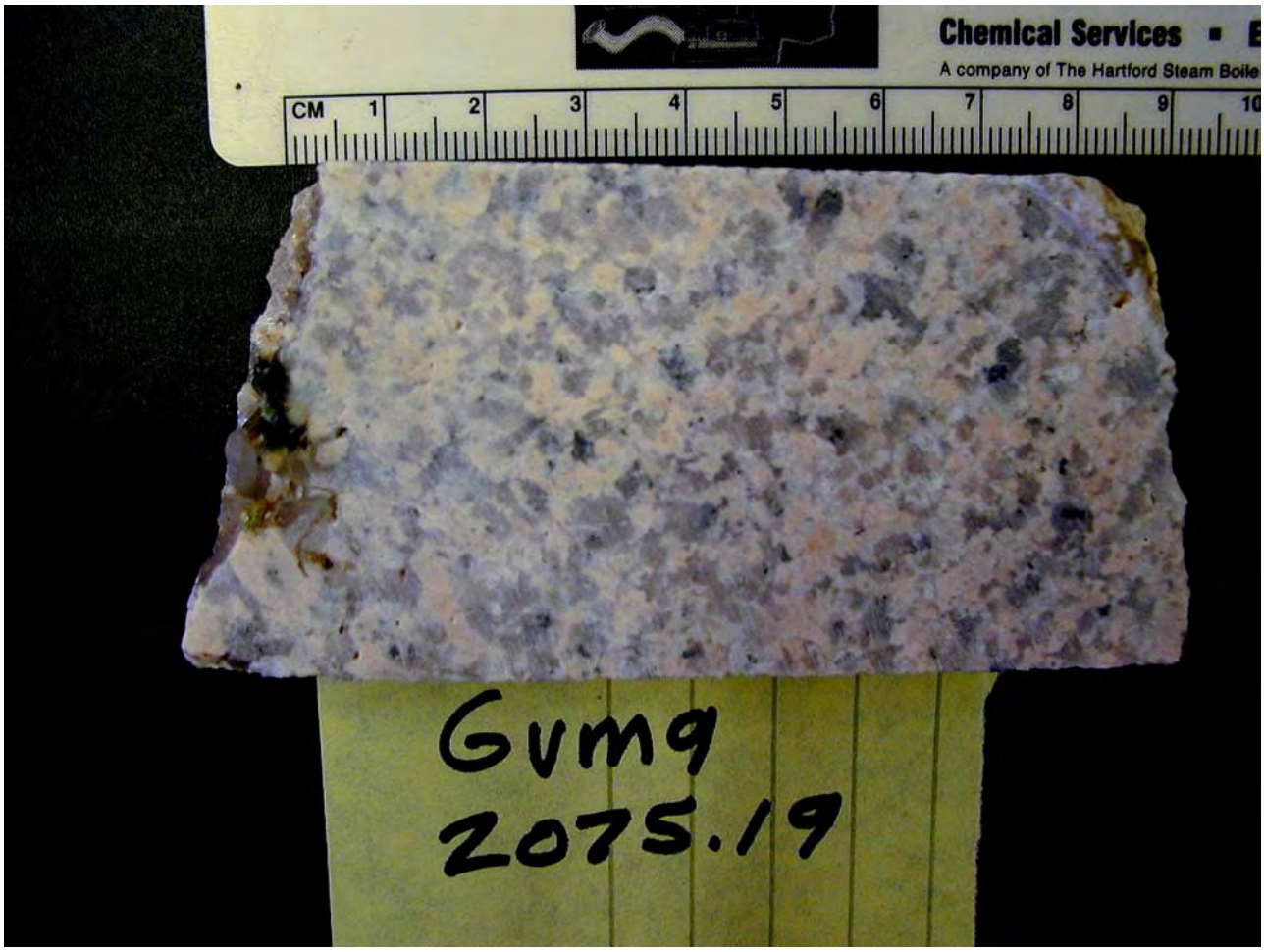

Appendix D-1.Photograph of Victorio Granite sample GVM 9 2075.19 showing the feldspar-quartz-biotite mineral assemblages. The biotite mineral grains on the left hand side of the photo show minor amounts of chlorite alteration. This sample also contains igneous muscovite, which is difficult to see in the photograph.

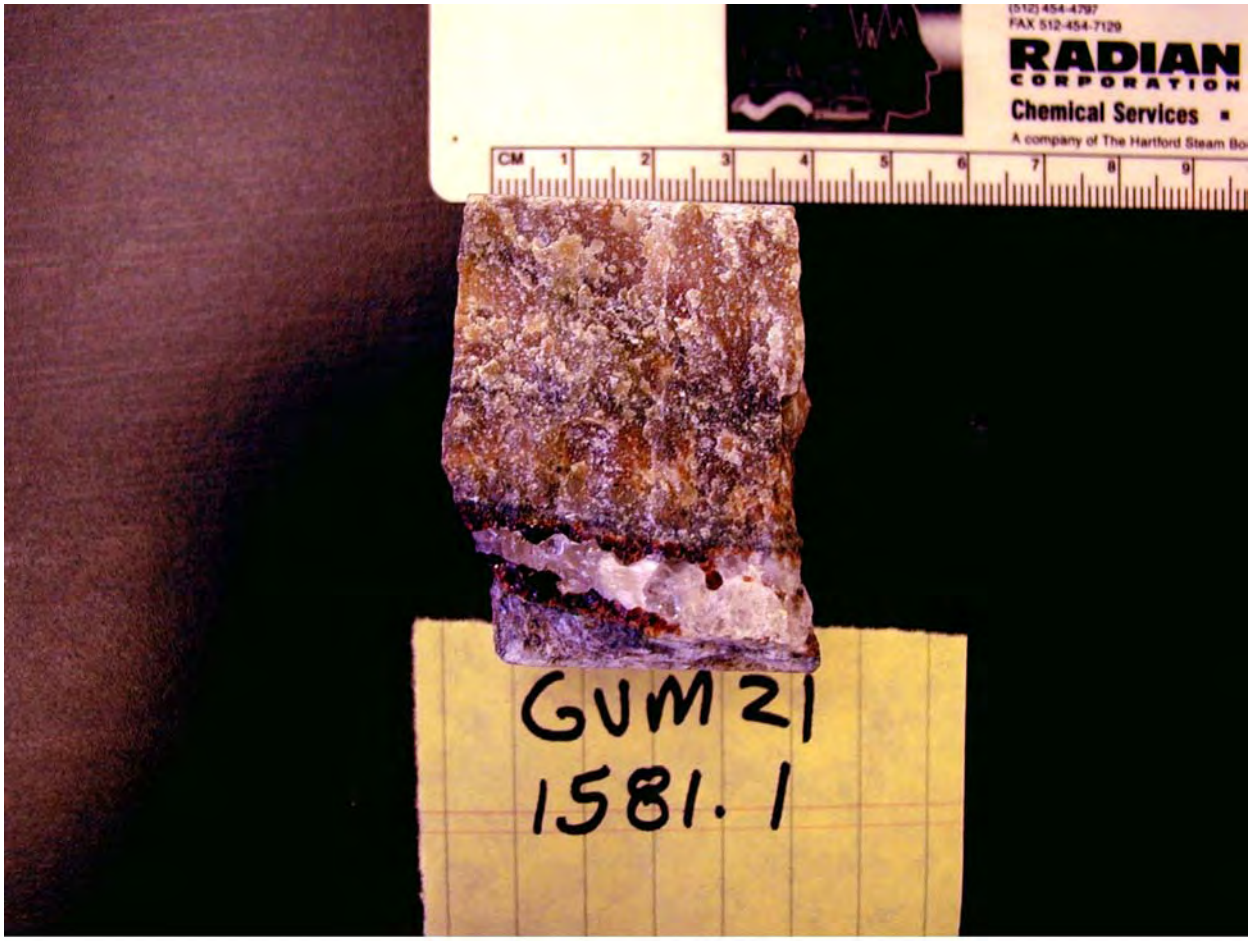

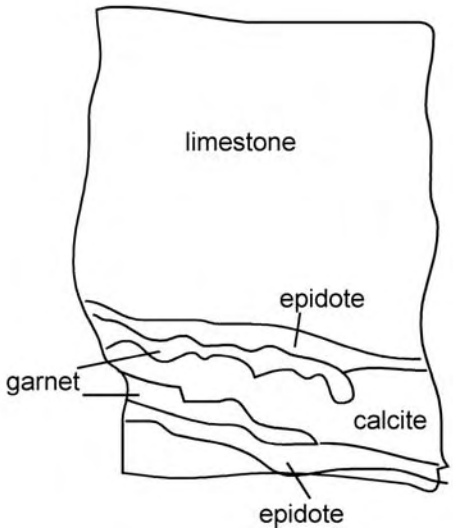

Appendix D-2. Photograph of skarn sample GVM 21 1581.1 showing contact metasomatic alteration of calcite-garnet-epidote mineralization. The minerals from this sample are considered to be from the Stage 1 of the paragenetic sequence.

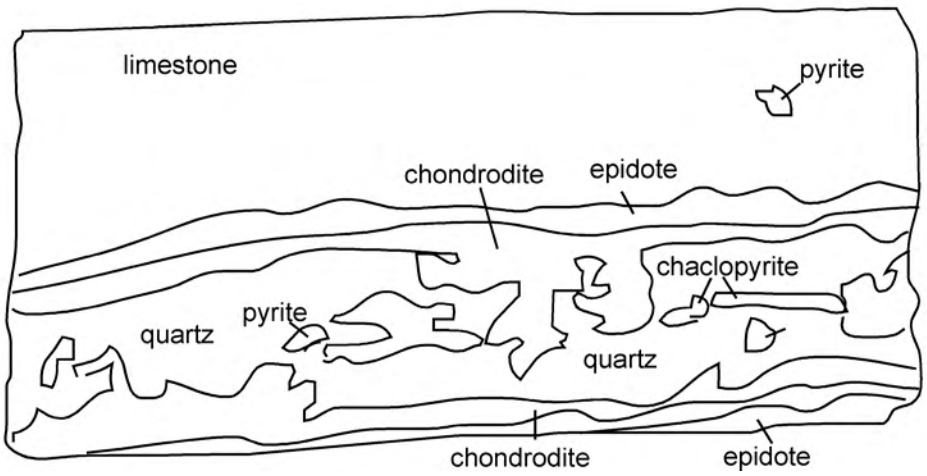

Appendix D-3. Photograph of skarn sample GVM 21 1168.2 showing quartz-chondrodite-chalcopyrite-pyrite vein with epidote rim and disseminated pyrite. The minerals in this sample are from the end of Stage 1 and the beginning of sub-stage 1.

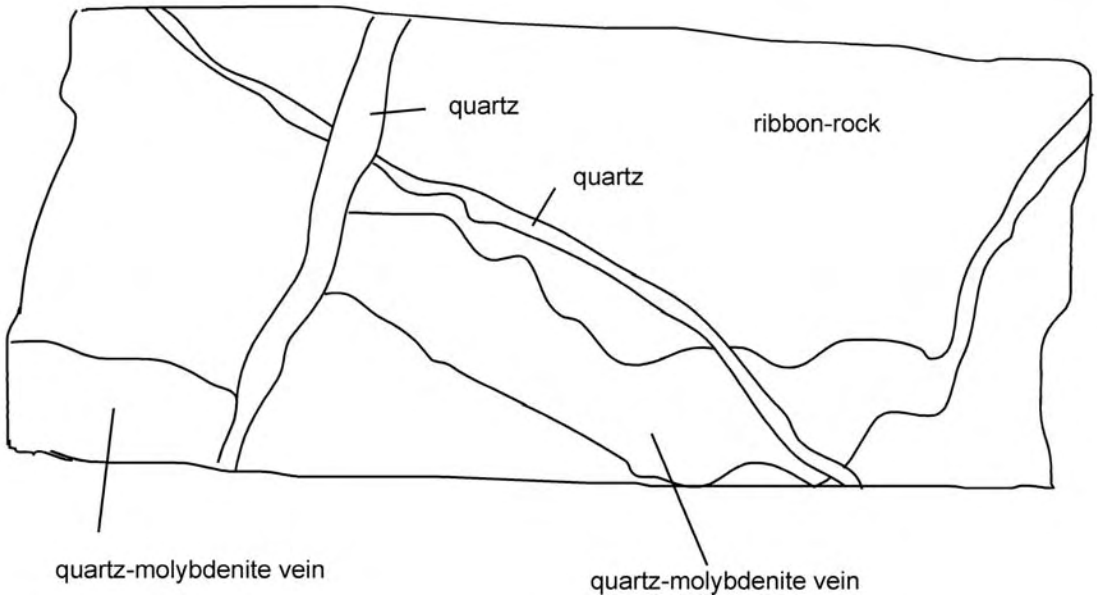

Appendix D-4. Photograph of skarn sample GVM 18 1651 showing ribbon-rock alteration, quartz-molybdenite veins, and quartz veins. The minerals from this sample are considered to be from beginning of sub-stage 1.

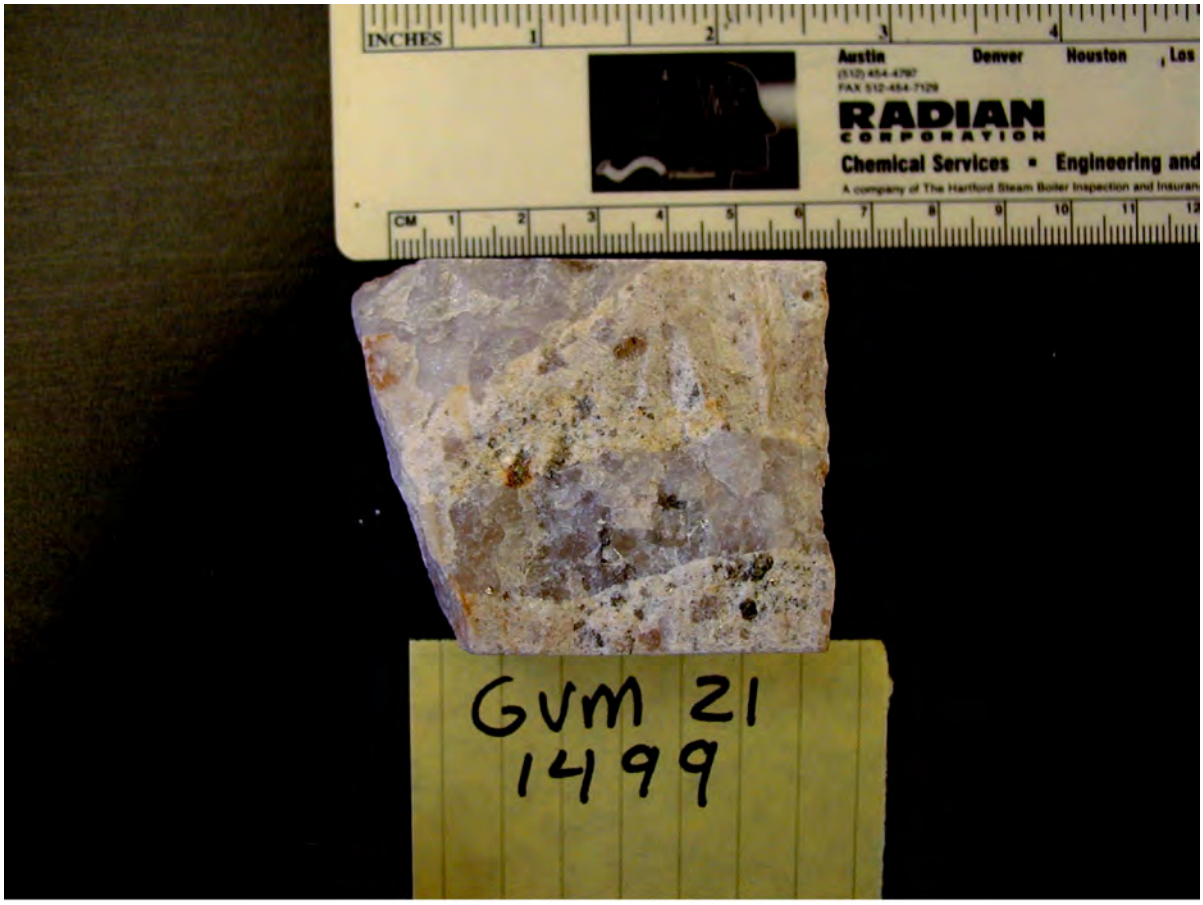

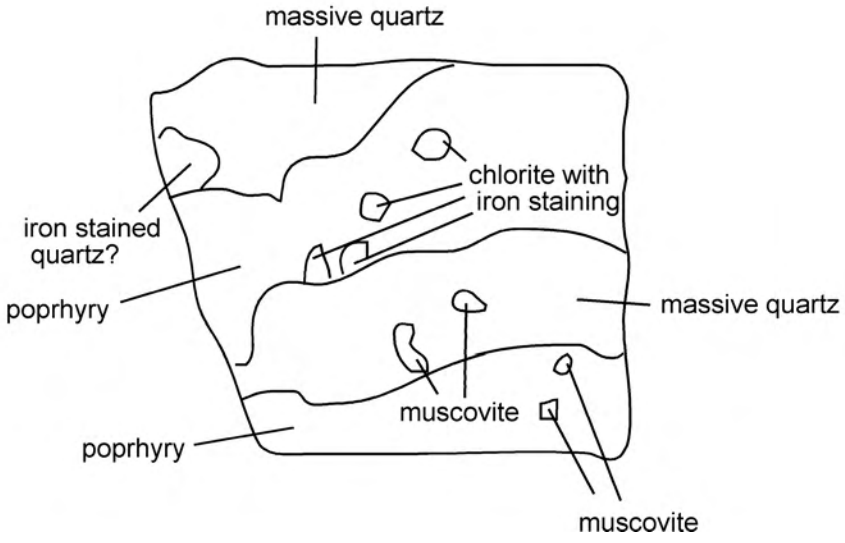

Appendix D-5. Photograph of porphyry sample GVM 21 1499 showing muscovite and chlorite with some iron staining and quartz veins. The minerals in this sample are considered to be from Stage 1. The quartz veins appear to have been deposited after the formation of the porphyry.

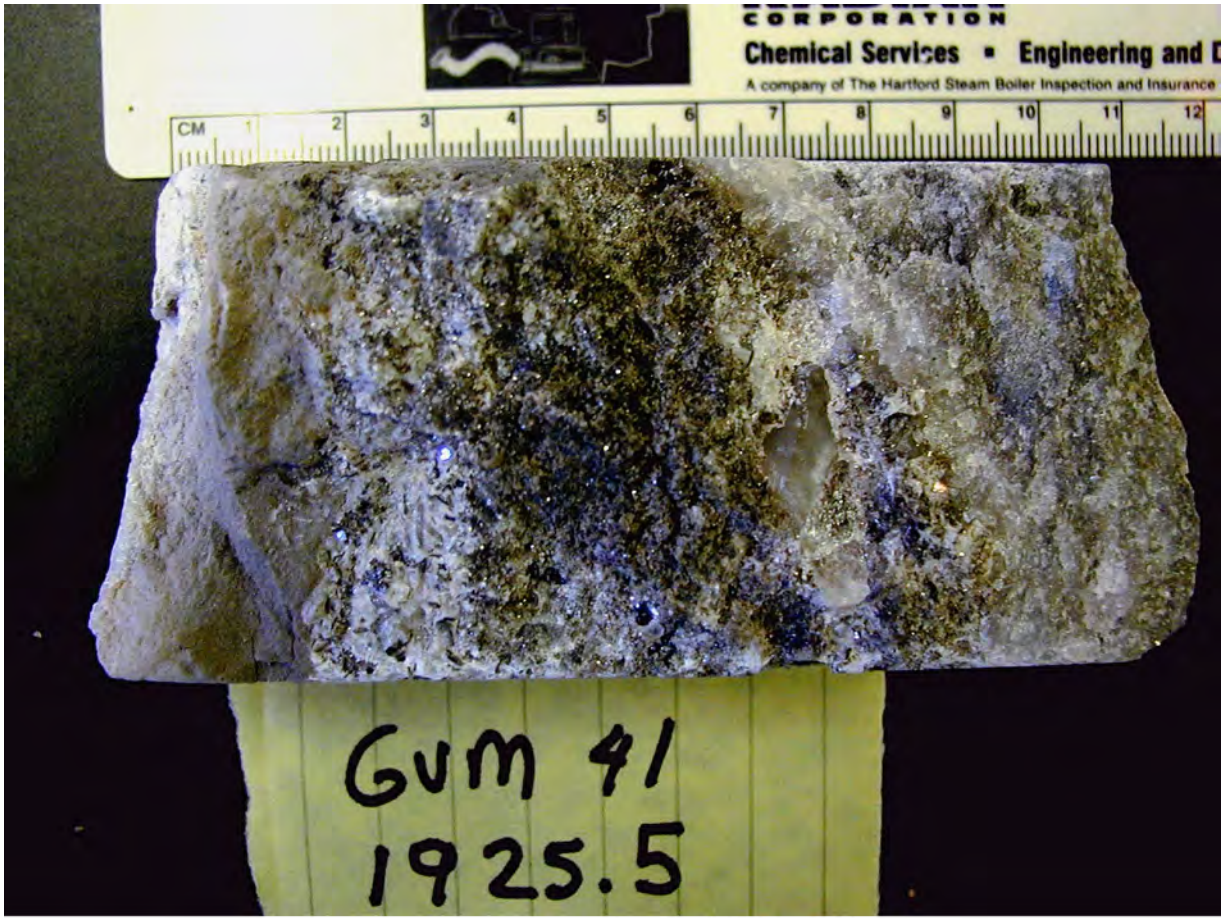

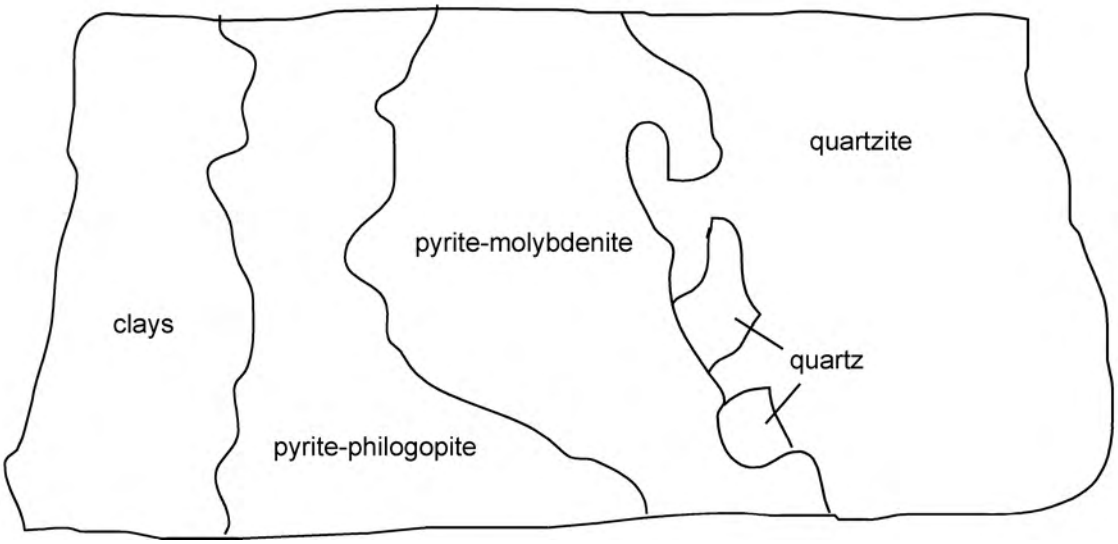

Appendix D-6. Photograph showing skarn sample GVM 41 1925.5 the pyrite-molybdenite, pyrite-muscovite veins with clay alteration and quartzite host rock. The minerals from this sample are from the second sub-stage, with later sericitic/argillic alteration (possibly from the third sub-stage).

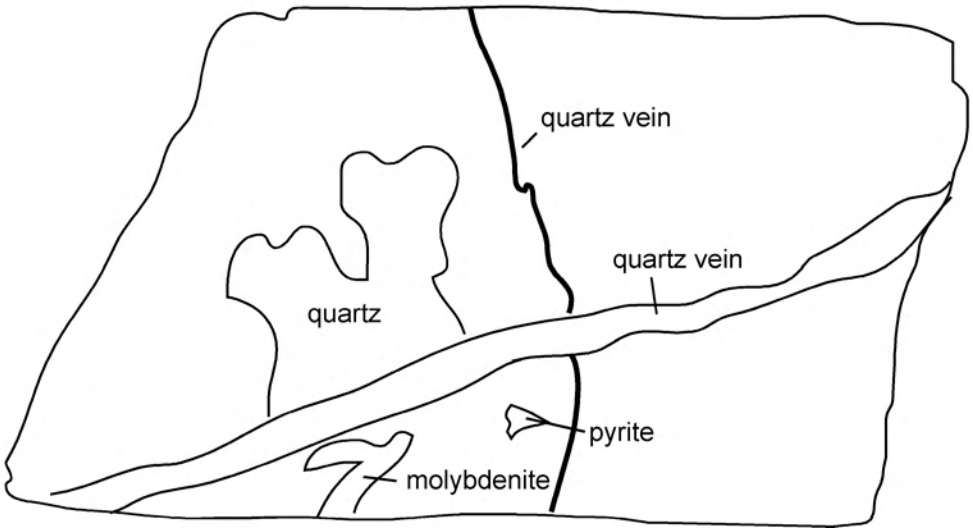

Appendix D-7. Photograph of a porphyry sample GVM 21 1862 showing quartz veins and mineralization with molybdenite and pyrite minerals. The minerals in this sample are from Stage 1 of the paragenetic sequence.

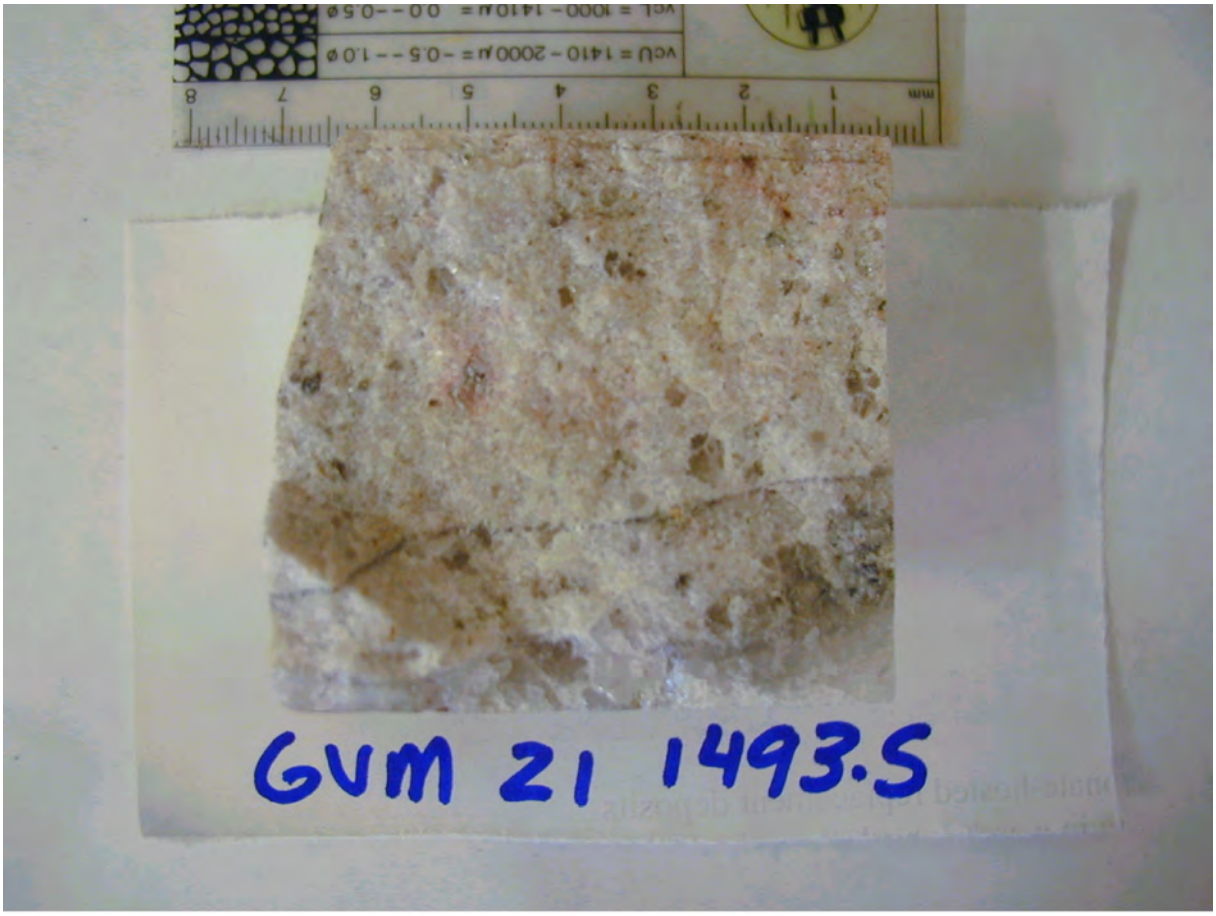

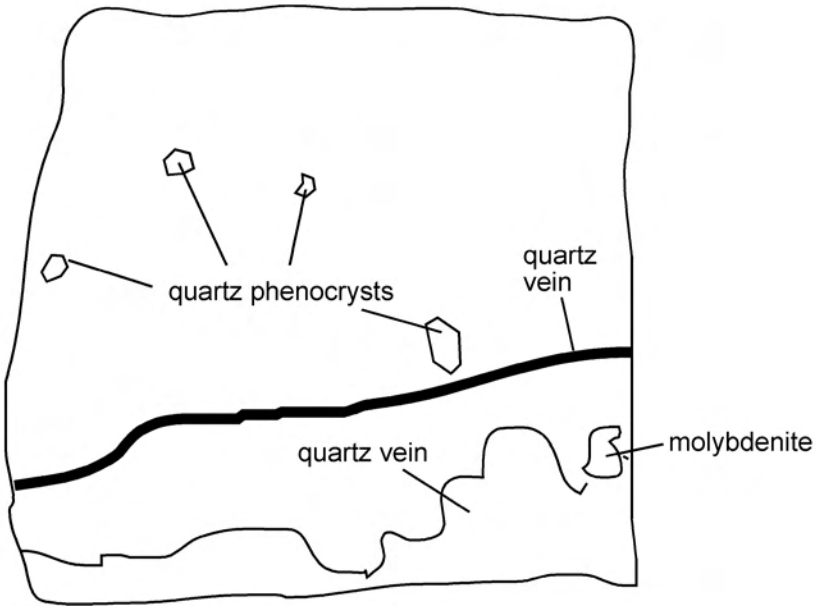

Appendix D-8. Photograph of skarn sample GVM 21 1493.5 showing a porphyry molybdenite sample with quartz veins. The minerals from this sample are from Stage 1 of the paragenetic sequence.

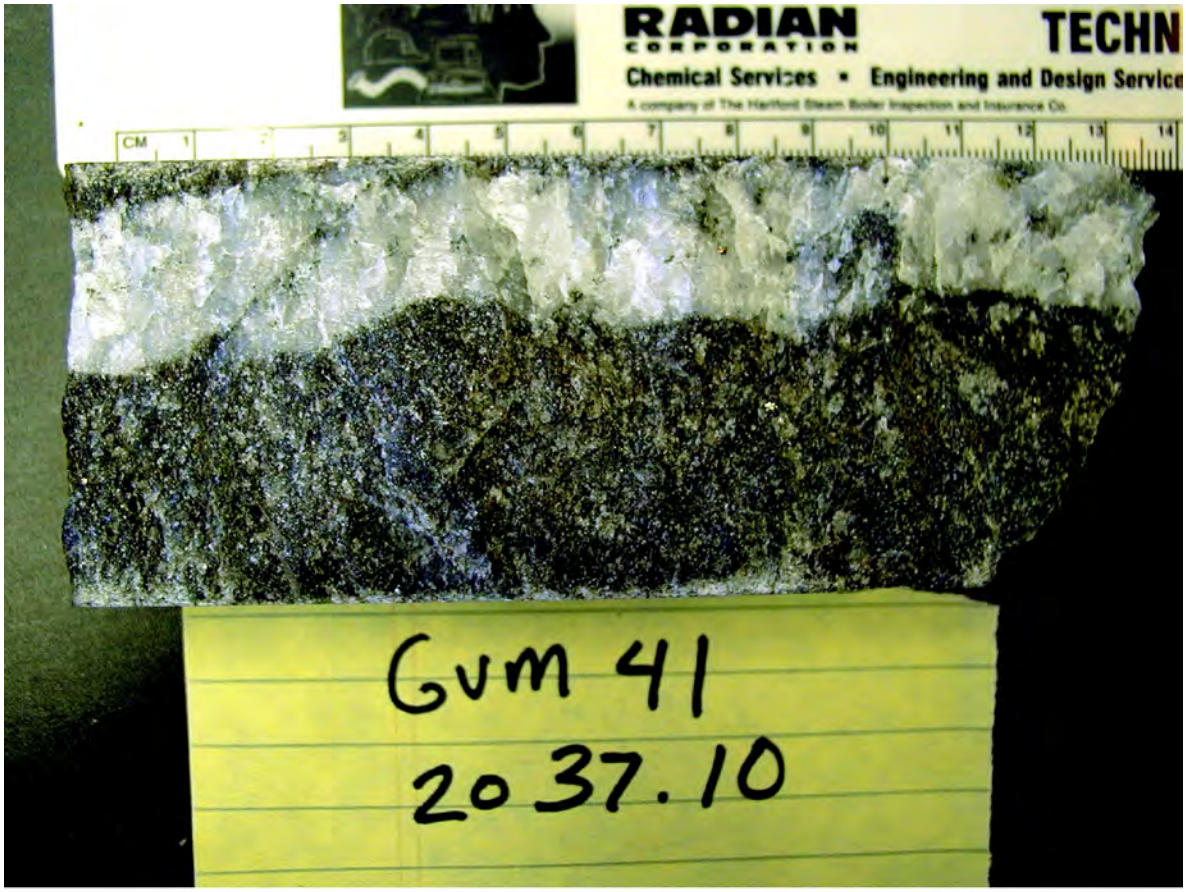

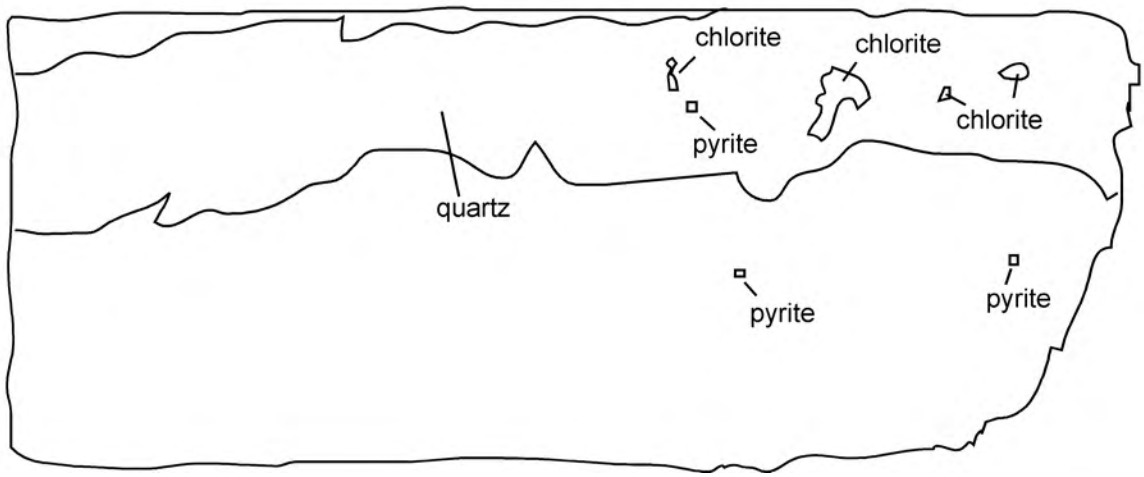

Appendix D-9. Photograph of skarn sample GVM 41 2037.10 with quartz-chlorite-pyrite vein disseminated pyrite. The minerals in this sample are from Stage 1 of the paragenetic sequence.

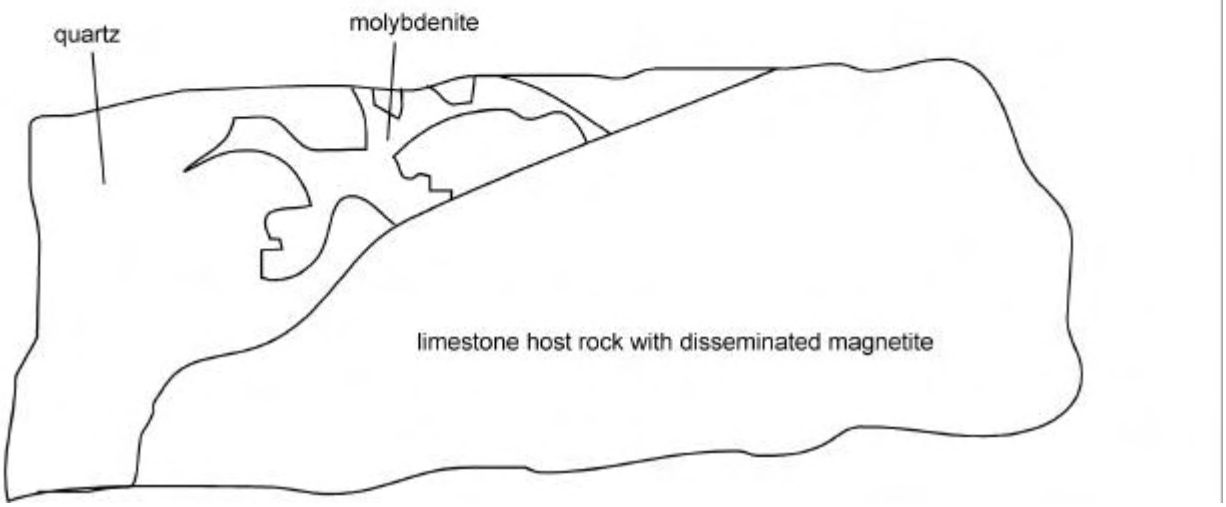

Appendix D-10 Photograph of skarn sample GVM 65 1902.8 showing quartz-molybdenite vein in a limestone host rock with disseminated magnetite. The minerals in this sample are from Stage 1 of the paragenetic sequence.

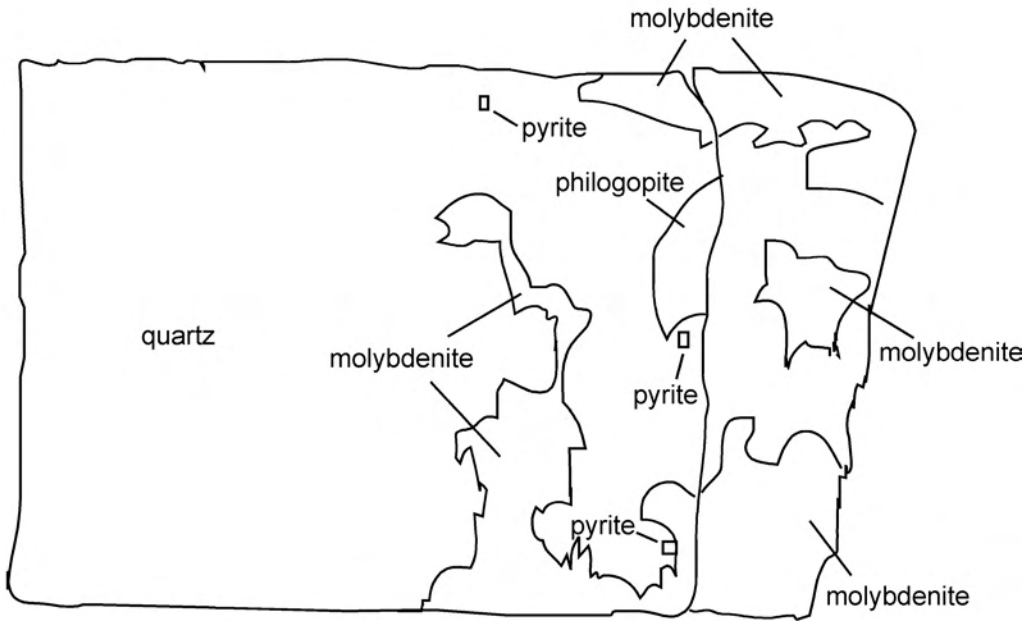

Appendix D-11. Photograph of skarn sample GVM 211297 showing quartz-molybdenite-pyrite-philogopite vein. Not shown in this photograph are K-feldspar minerals in this sample. The minerals in this sample are from the end of Stage 1 and the beginning of sub-stage 1.

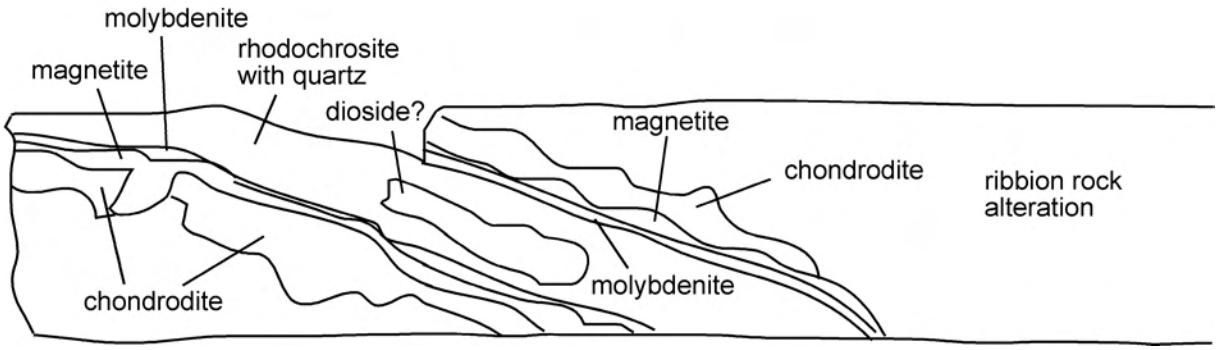

Appendix D-12. Photograph of skarn sample GVM 17 1420 showing quartz-rhodochrosite-diopside, molybdenite, chondrodite, magnetite vein in a host rock that has evidence of ribbon-rock alteration the minerals in this sample are from sub-stage 2 and this sample is representative of the dominant ore veins.

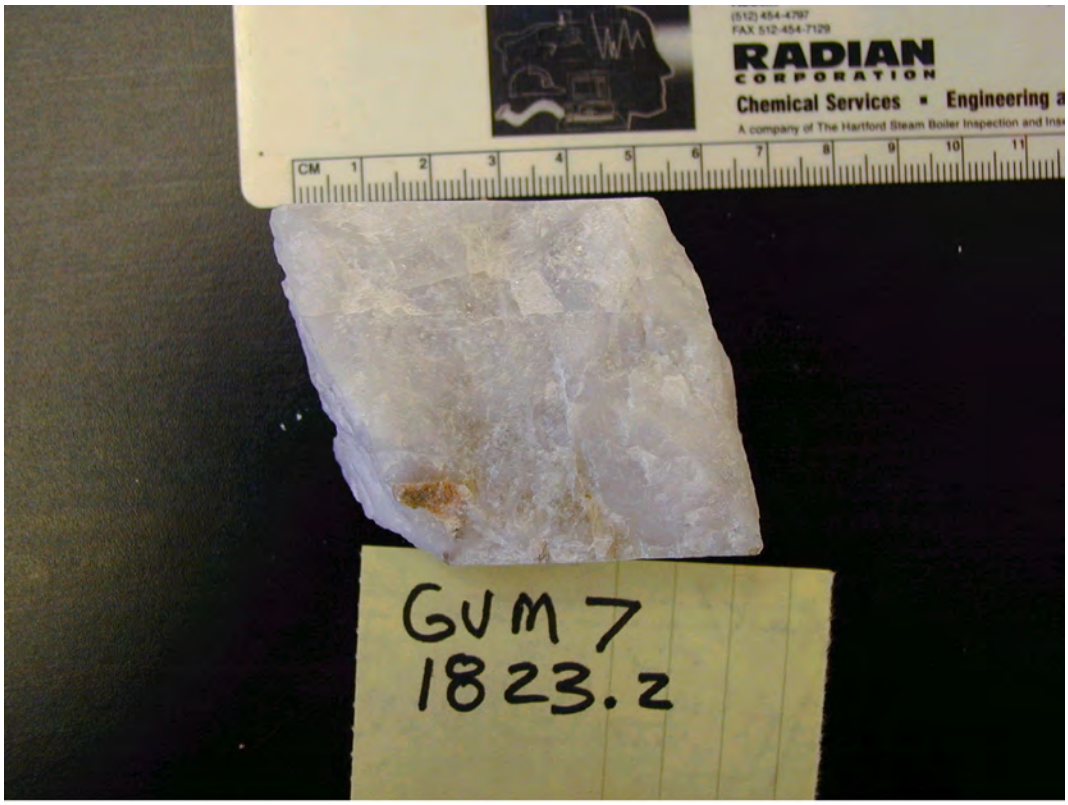

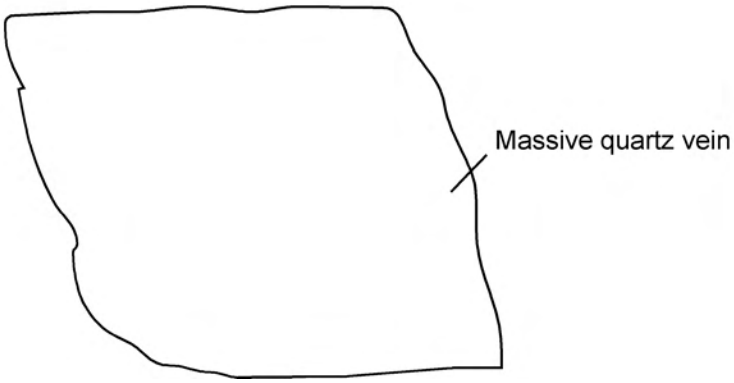

Appendix D-13. Photograph of skarn sample GVM 7 1823.2 barren quartz vein representing the first stages of skarn mineral alteration. This sample represents the quartz mineralization from sub-stage 1.

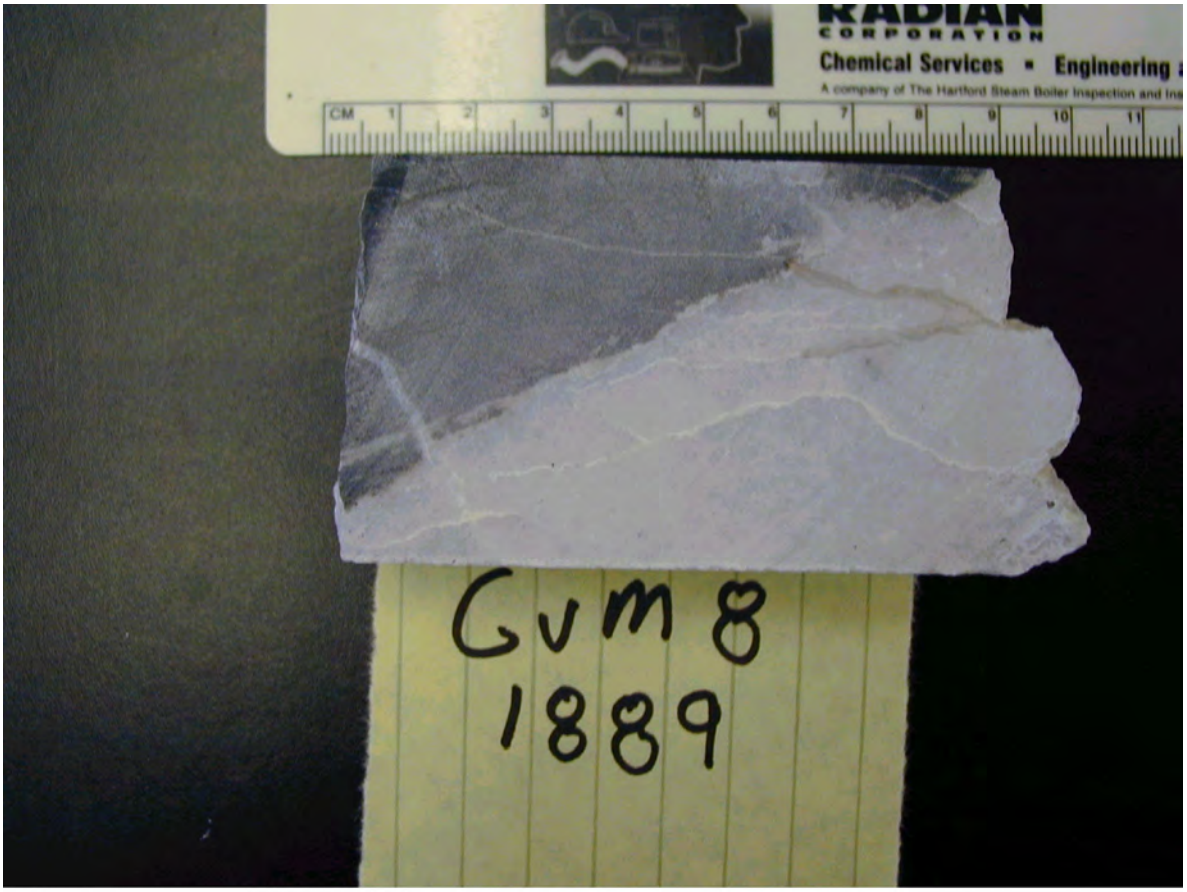

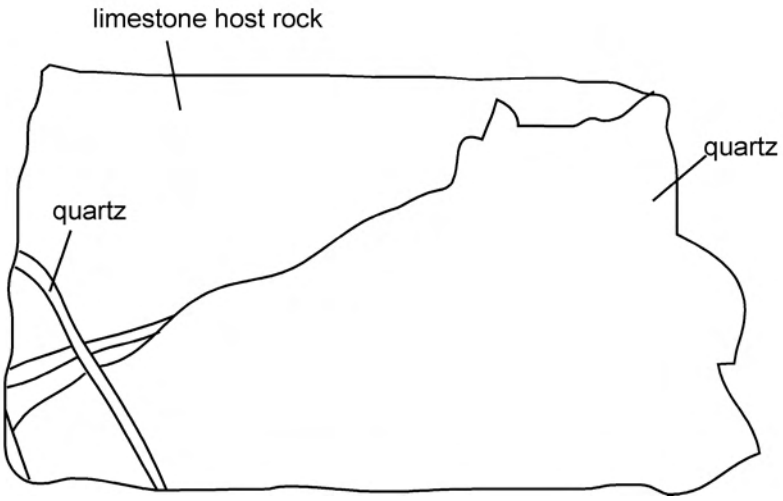

Appendix D-14. Photograph of skarn sample GVM 8 1889 barren quartz vein showing multiple quartz veins representing the first stages of skarn vein alteration. The multiple, cross-cutting quartz veins are from sub-stage 1.

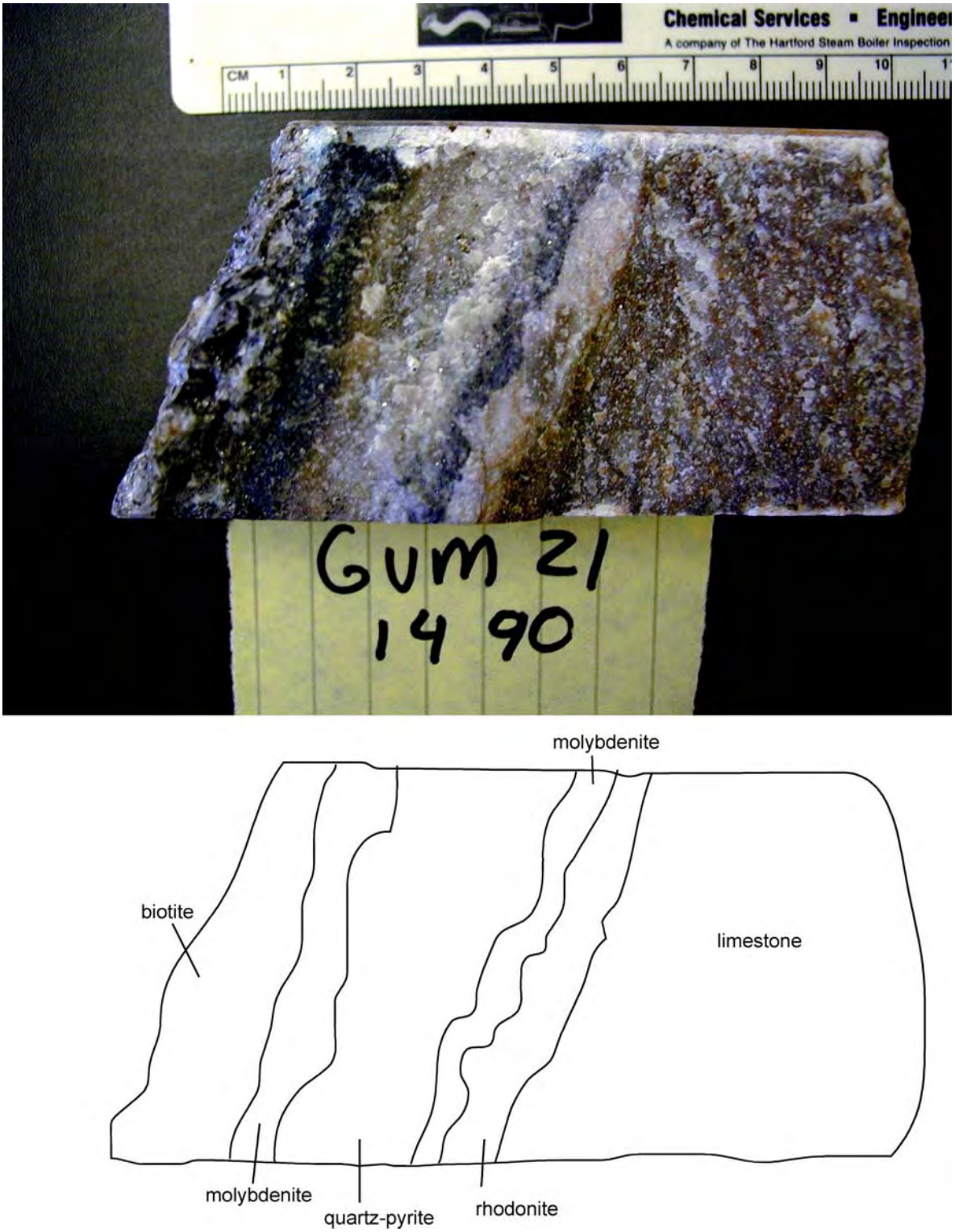

Appendix D-15. Photograph of skarn sample GVM 21 1490 showing biotite-molybdenite-quartz-pyrite-rhodonite vein. Not pictured is fluorite mineralization associated with the biotite. The minerals from this sample are from sub-stage 2 and sub-stage 3.

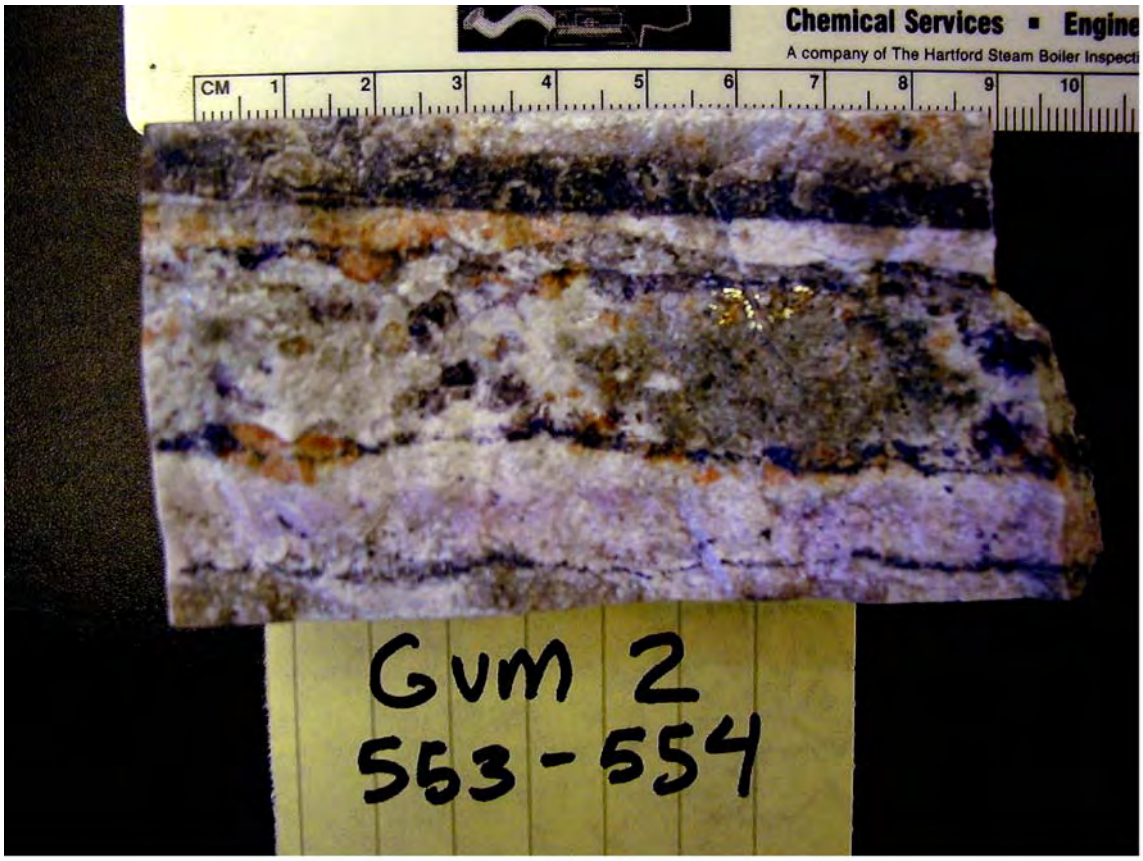

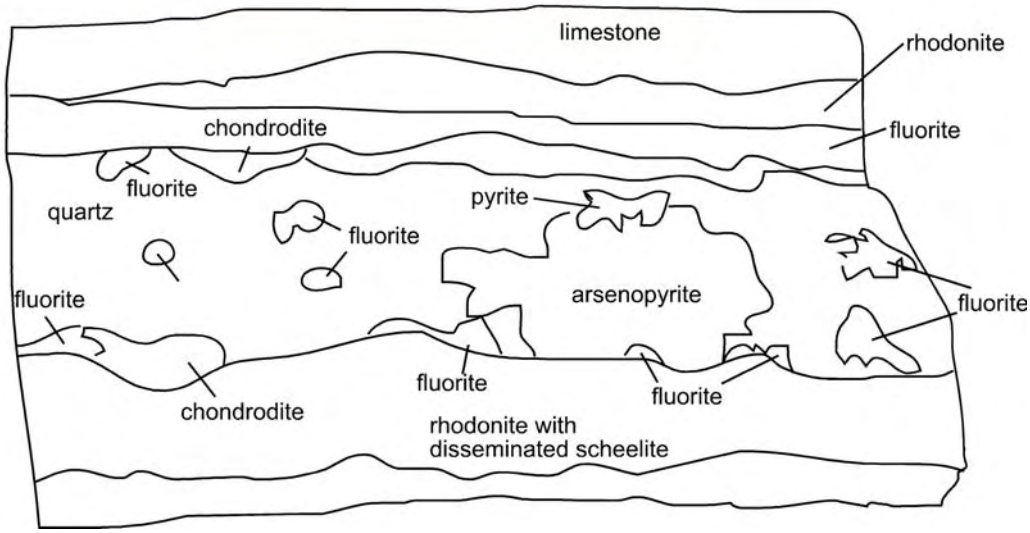

Appendix D-16. Photograph of skarn sample GVM 2 553-554 showing quartz-fluorite-pyrite-arsenopyrite-chondrodite vein with rhodonite and disseminated scheelite vein representing late-stage vein alteration. This minerals from this sample are from sub-stage 3.

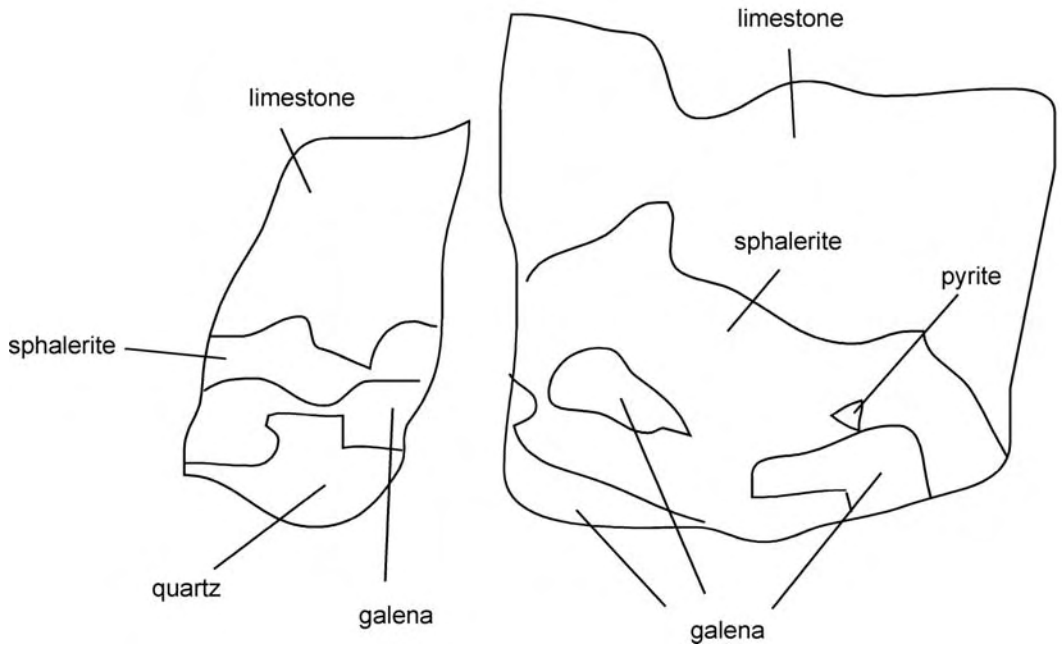

Appendix D-17. Photograph of carbonate-replacement sample E109 1942 showing galena-sphalerite-pyrite-quartz vein mineralization. The minerals from this sample are from sub-stage 3.

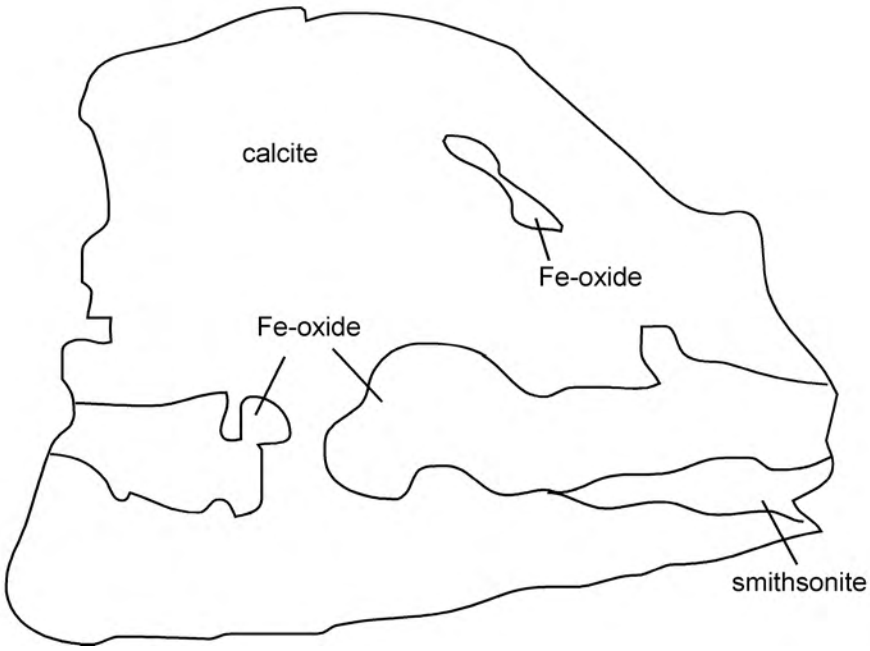

Appendix D-18. Photograph of sample VIC 67-99 a sample from the carbonate-hosted replacement deposit showing calcite, Fe-oxides, and smithsonite alteration This sample is from the last stage of the paragentic sequence.

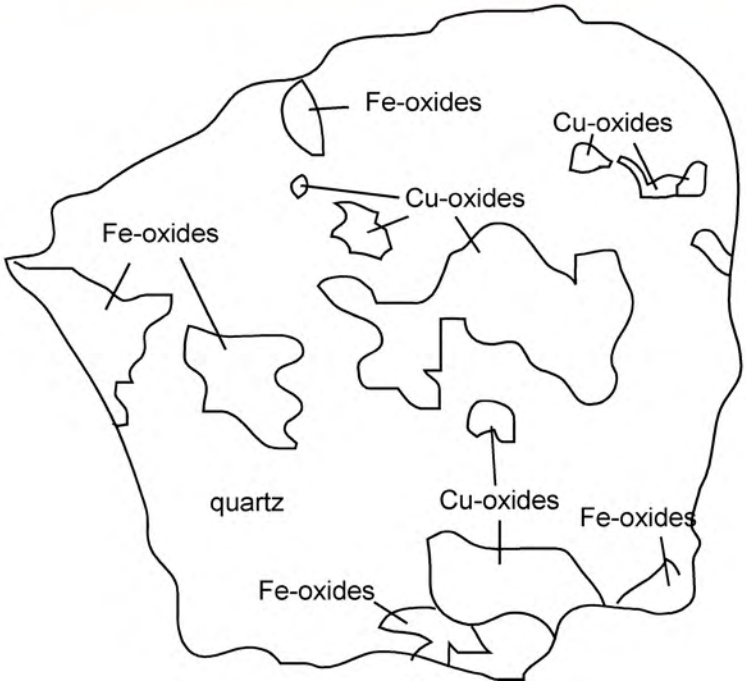

Appendix D-19. Photograph of carbonate-hosted replacement sample VIC 149-99showing quartz, Fe and Cu-oxides. This sample is from the last stage of the paragentic sequence.

Appendix D-20. Photograph of skarn sample GVM 21 1278 showin the K-feldspar, quartz, fluorite, molybdenite and biotite mineral assemblage. This sample is from sub-stage 1. The molybdenite appears to be intergrown with the K-feldspar and quartz vein, and also is found as veins along the edge of the K-feldspar-quartz vein. The black veins are where the biotite sample from argon geochronology analysis was taken.

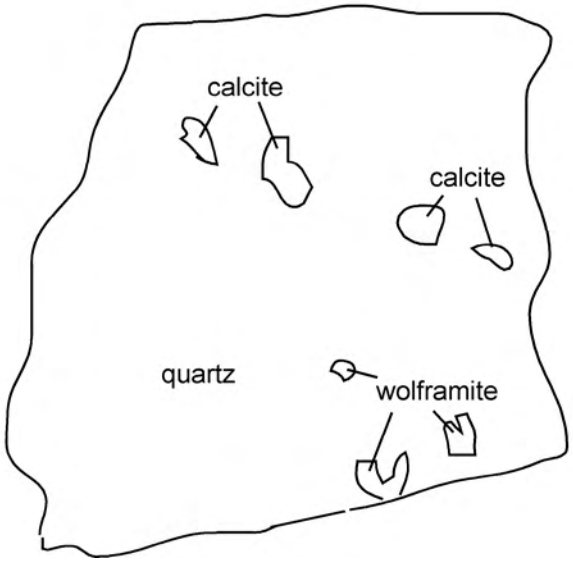

Appendix D-21. Photograph of skarn sample VIC 12-99 a quartz-wolframite skarn vein with black calcite minerals taken from the surface near the Middle Hills area. The minerals from this sample are from sub-stage 2.